NDOT Research Report

Report No. 032-10-803

Unbonded Prestressed Columns for Earthquake Resistance

May 2012

Disclaimer

This work was sponsored by the Nevada Department of Transportation. The contents of this report reflect the views of the authors, who are responsible for the facts and the accuracy of the data presented herein. The contents do not necessarily reflect the official views or policies of the State of Nevada at the time of publication. This report does not constitute a standard, specification, or regulation.

Report Number CCEER-12-02

Unbonded Prestressed Columns for Earthquake Resistance

Alexander S. Larkin
David H. Sanders
M. Saiid Saiidi

_____

Abstract

Modern structures are able to survive significant shaking caused by earthquakes. By implementing unbonded post-tensioned tendons in bridge columns, the damage caused by an earthquake can be significantly lower than that of a standard reinforced concrete bridge column, by reducing residual displacement. Reducing residual displacement will reduce the amount of damage and allows for faster repairs and minimal closure time of the bridge. The objective of this research was to investigate new construction details for unbonded post-tensioned bridge columns that will reduce damage caused by an earthquake. Two 0.4-scale columns containing unbonded tendons were selected for testing. The two columns were identical except for the amount of longitudinal reinforcement crossing the joint between the column base and the footing. SAP2000 was used to model each column, showing a close correlation between the calculated and measured results. A parametric study was conducted on the specimens investigating various axial dead loads, initial post-tensioning force, tendon location, and increase in the concrete strength. For the specimens to be true scale models, the amount of post-tensioning required in a full-scale column was taken into consideration. The large amount of prestress needed in a full-scale column requires separate tendons being spread around the center of the column cross section. Greased and sheathed strands were incorporated for their additional corrosion protection. The introduction of the unbonded tendons showed a significant reduction in residual displacements. The re-centering effect was not as dominant with an increase in longitudinal reinforcement. A smaller longitudinal reinforcement ratio also produced a larger displacement ductility.

Acknowledgments

Table of Contents

List of Tables

List of Figures

CHAPTER 1

Introduction

1.1　Introduction

Maintaining life safety in seismic engineering design is the number one concern. After a structure can maintain life safety, the next goal is to reduce the amount of damage in the structure following large lateral deformations. Reducing the amount of damage to the structure will allow for rapid repairs and a reduction in closure time. Damage may be in the form of spalling concrete, buckling or fracture of column longitudinal reinforcement, and permanent lateral displacement. One way to reduce permanent lateral displacements in bridge columns is to introduce unbonded post-tensioned tendons.

Unbonded post-tensioned columns have shown reductions in residual column displacements following lateral deformations. Further research is desired to better develop construction methods for unbonded post-tensioned columns. Past research has primarily focused on the use of a single tendon, centrally located at the center of the column cross section. The use of a single tendon is not a realistic option in relatively large full-scale columns. The high tendon force required for re-centering, and the large tendon area is too much for one centrally located tendon. To provide a more realistic construction method for large scale columns, several tendons should be used, so the total post-tensioning force and tendon area required for re-centering can be dispersed equally among several tendons. Additionally, there is still question as to the amount of prestress, initial level of stress, and amount of longitudinal reinforcement crossing the joint between the column base and the footing needed to provide the best overall column performance.

Following large lateral deformations that would come from earthquake excitation, it is necessary to have the option of inspecting and, if necessary, replacing the tendons. An improved construction method from prior research is to anchor the tendons in the corners of the footing as opposed to the base of the footing. This modification creates the possibility of accessing the tendons, and is made possible with several smaller tendons equally spaced around the center of the column cross section, instead of one large tendon centrally located in the center of the column cross section. The use of greased and sheathed strands also creates additional corrosion protection, which is especially important in bridge columns.

1.2　Literature Review

Many researchers have used unbonded post-tensioning in columns for the re-centering benefits following a large seismic event. The introduction of unbonded post-tensioning for seismic column design has been shown to reduce the amount of residual displacement compared to a conventionally reinforced column. The primary focus of prior research was to investigate the magnitude of the re-centering effects. To focus more closely on the re-centering effect of the tendon, most columns had a small longitudinal reinforcement ratio that crossed the joint between the footing and the base of the column, and some columns had zero longitudinal reinforcement crossing the joint. The majority of

past researchers also used only one tendon that was centrally located within the column cross section. The following sections describe previous research that focused on post-tensioning columns:

1.2.1   Segmental Unbonded Post-Tensioned Columns

Research conducted by Hewes and Priestley focused on segmental column construction with a single tendon centrally located within the column cross section (Hewes & Priestley, 2002). Column parameters from this experiment are shown in Table 1-1. The single tendon used for re-centering purposes was anchored in the base of the footing. Several test specimens were constructed, each being made up of four segments. The upper three segments were lightly reinforced in the longitudinal direction and were reinforced with spirals in the transverse direction. The lowermost segment contained a steel jacket to provide transverse reinforcement and no longitudinal reinforcement. For all columns, there was no longitudinal reinforcement crossing the column footing interface, except for the post-tensioned tendon. If the tendon failed, there would not be any connectivity between the column base and the footing. The tendon used was made of 27 $\frac{1}{2}$" (12.7 mm)-diameter grade 270 ksi (1860 MPa) low-relaxation strands. Each column was tested by cyclic loading. Throughout the testing procedures, the columns experienced very little residual drift. By utilizing unbonded tendons, inelastic straining of the tendon did not occur and the original prestress force was maintained throughout testing. Each column in this experiment was tested twice; once with an initial prestress level, and a second time following repairs and an increased prestress level.

This report elaborates on the importance of the initial tendon force. The axial load ratio, defined as the sum of the initial prestress force and the axial dead load divided by the product of the gross cross sectional area and concrete compressive strength, was used to help determine the initial tendon force. A range of axial load ratios was used in a parametric study to help determine the optimal initial tendon force. The axial load ratio was adjusted by keeping the area of prestress constant and adjusting the initial force. The study found that a low axial load ratio of 0.10 was desirable because of the low initial tendon force, making it less likely that the tendons will yield with large lateral displacements. However, the negative effect of a low axial load ratio was the low column strength, especially when no other longitudinal reinforcement was crossing the column footing interface. A high axial load ratio of 0.35 was not desirable because it resulted in a less ductile member and a negative post-elastic stiffness. For columns of similar construction, it is recommended that the axial load ratio be at a maximum of 0.20 to maximize the benefits of post-tensioning. Test one pushed the columns out to 3%-4% drift, depending on the observed damage. Following repairs and an increased prestress level, the columns were pushed to lateral drifts on the order of 5%-6% (depending on damage), without significant strength degradation, making them functional in regions of high seismicity. Following drifts of 5%-6%, residual drifts of 0.7% and 0.2% were recorded. However, the report does not indicate that the columns were pushed to greater drift levels, which is of importance to monitor tendon stresses at high drift levels. The report indicates that the selection of the prestressing steel area and initial stress can be selected by a trial and error method and checked with an analytical model. It was noted in

the report that if a similar post-tensioning system were to be used in actual bridge projects, multiple tendons distributed around the section may be used.

1.2.2   Partially Prestressed Columns

Research conducted by Jeong et al. investigated the use of unbonded post-tensioning in four lightly reinforced circular columns (Jeong et al., 2008). Column parameters from this experiment are shown in Table 1-1. Each column was lightly reinforced in the longitudinal direction, resulting in a longitudinal reinforcement ratio of 0.66%. The first post-tensioned column was used as a base model, with only light reinforcement in the longitudinal direction and no post-tensioning. The second column was similar to the first, but had unbonded mild-longitudinal reinforcement in the plastic hinge region, and an initial prestress force of 6.3% of f'_cA_g. The third column was similar to the second with unbonded mild longitudinal reinforcement, but had a higher initial prestress force of 9.3% of f'_cA_g. The fourth and final column contained a steel jacket at the expected plastic hinge location in addition to the unbonded mild longitudinal reinforcement. The axial dead load applied to each column was set at 5.7% of f'_cA_g. The tendon that supplied the prestress force was composed of a single bar, which was centrally located within the column cross section and was anchored in the base of the footing.

All columns exhibited an impressive re-centering ability following shake table testing. The tendon in all four columns also remained elastic, indicating that the initial prestress force selected was satisfactory. The third column, which had a higher initial prestress force, showed a decrease in residual displacement and an increase in damage due to the increased compression force on the column. The fourth column, which contained the steel jacket located at the base of the column, showed the least amount of damage, as expected. All of the columns used a single tendon, centrally located within the column cross section. The single tendon was anchored in the base of the footing.

Following shake table testing, the four columns showed a similar maximum cumulative response displacement (SRSS) of about 4.8" (122 mm), leading to a ductility of about 5. These results were from a test run at the design level earthquake, corresponding to a scaling factor of 50% of the earthquake record used. When the ground motion was increased to the maximum level, 75% scaling factor, the maximum cumulative response displacements (SRSS) increased to 10" (254 mm). Following the maximum level excitation, residual displacements remained low in all four columns, with a maximum residual displacement of 2.3" (58 mm) from column PRC-U (lowest post-tensioning force).

1.2.3   Segmental Hollow-Core Square Post-Tensioned Columns

Research conducted by Ou et al. investigated construction methods and detailing in segmental column construction for the mild longitudinal bars that are continuous across segment joints (Ou et al., 2009). Column parameters from this experiment are shown in Table 1-1. The benefit from mild-longitudinal reinforcement that crosses the segmental joints is the connectivity between the column base and the footing in case of a tendon failure, and also an increase in energy dissipation. This research also investigated

the effect of varying the energy dissipating bar ratio, as well as the initial post-tensioning force.

Each of the four square columns had four post-tensioned tendons made of (2) 0.6" (15.2 mm) grade 270 ksi (1860 MPa) strands that were placed inside the hollow column core. External tendons can be inspected more easily for corrosion problems, but would be difficult to remove as they are anchored at the base of the footing. Additionally, inspection would require the removal of other bridge components. The longitudinal reinforcement ratio in each of the four columns varied from 0% to 1%. The mild longitudinal reinforcement crossing the joint between the footing and the first segment was unbonded a distance into the footing by wrapping the bars with duct tape. The unbonded bars were used to avoid premature failure from low cycle fatigue. The post-tensioning force was held constant in three of the columns $(0.07f'_cA_g)$, but was significantly reduced in the fourth column to $(0.021f'_cA_g)$ to determine the effect of post-tensioning force on energy dissipation and residual displacement. The only segment with unbonded mild longitudinal reinforcement was the first segment due to expected repetitive gap opening between the footing and the first segment. Bonded mild longitudinal reinforcement was connected between the other segments with threaded receivers.

Test results showed that the columns displayed excellent drift capacities suitable for seismic regions. The mild reinforcement was effective in ensuring a large ductility and high levels of energy dissipation. The column that did not have mild reinforcement at the column footing interface displayed a drift capacity of 4.6%, while those with mild steel reinforcement displayed drift capacities of 5%. The column responses were mostly dominated by the joint opening between the foundation and the first segment.

1.2.4   Square Post-Tensioned Columns

Palermo et al. conducted research on square post-tensioned columns to investigate "controlled rocking," where the inelastic demand is focused at the section interface to minimize damage within the structural elements (Palermo et al., 2007). Column parameters from this experiment are shown in Table 1-1. Energy dissipating elements were provided by mild longitudinal reinforcement used within the section interface. The objective of the research was to better develop construction techniques so these methods can be adopted by the construction practice, and not just the scientific community.

Five columns were constructed, one monolithic column as a benchmark, two post-tensioned columns, and two hybrid columns. The post-tensioned columns contained only post-tensioning crossing the column footing interface, and the hybrid columns consisted of post-tensioning along with mild longitudinal reinforcement crossing the column footing interface. The prestressed (unbonded tendons) portion of the reinforcement provides a re-centering effect, while the mild reinforcement provides additional moment capacity along with energy dissipation. In this experiment, the post-tensioning was used to carry the axial dead load along with the initial post-tensioning force. Columns PT1 and HBD1 were considered to have zero initial post-tensioning force (just tied up tendons) because of design constraints, but it was noted that this could be a realistic design choice to provide additional redundancy in a severe earthquake.

4

The four prestressed columns were designed to have the same nominal moment capacity as the benchmark column. However, due to the limitations of prestressing with only two tendons in the first hybrid model (HBD1), it was required to be designed for a slightly lower capacity than the benchmark. Due to this constraint, the second set of specimens (PT2 & HBD2) had an alternative configuration that doubled the amount of post-tensioning. In all four post-tensioned columns, the tendons were anchored in the base of the footing.

The columns performed very well with high energy dissipation from the mild reinforcement, re-centering capabilities from the unbonded tendons, and a stable hysteretic behavior up to high ductility levels. These all contribute to a reduction in damage following large lateral displacements. The hybrid models had the lowest amount of damage, as the majority of damage was focused on the mild reinforcement. Columns PT1, PT2, HBD1, and HBD2 reached ultimate drift ratios of 3.5%, 4%, 3%, and 3.5%, respectively. The ultimate drift in all of the cases corresponded to the drift level at the end of the test, prior to yielding the tendon.

1.2.5   Unbonded Prestressed Hollow Concrete Columns with Precast Segments

Yamishita and Sanders constructed an unbonded hollow concrete column with precast segments, in which the main objectives were; to evaluate the seismic performance, confirm that residual displacements were small following lateral drifts, check the energy dissipation, find an equation to check the stress in the prestressing steel, and develop a simplified load-displacement calculation model (Yamishita & Sanders, 2005). Column parameters from this experiment are shown in Table 1-1. The test model was based on a prototype model, and consisted of three segments. The loading protocol was produced by shake table testing using the Kobe Earthquake motion.

Throughout testing, the column behaved very well with essentially no residual displacement and minor spalling at the base. The concrete damage could be easily repairable, but it was noted in the report that a system would need to be developed to replace the tendons in an actual bridge. During run 14 (out of 15), the column reached a maximum drift of 2.8" (71.1 mm) corresponding to a drift ratio of 3.9%. At this time, the anchorage of one of the strands popped out, possibly due to too large of an initial prestress force. During the final run (15), the column reached a maximum displacement of 6.96" (177 mm) corresponding to a drift ratio of 9.7%. At this time, the cover concrete was completely spalled on both sides of the column and two more additional anchorages popped out. All of the column rotation took place between the column base and footing. The joints between the first and second segment, and the second and third segment remained closed. An equation was developed to estimate the strain in the prestressing steel in terms of the drift.

1.2.6   Unbonded Post-Tensioned Bridge Columns in Full System Simulation

Cruz-Noguez and Saiidi tested several different column bents in a four-span bridge earthquake simulation study. Two bents were constructed using unbonded post-tensioning in the columns (Cruz-Noguez & Saiidi, 2010), one with conventional reinforced concrete and the other with innovative details incorporating rubber layers. The

objective was to determine how the unbonded post-tensioned columns would behave in a full system interaction, specifically the re-centering capabilities. Columns in each bent were post-tensioned with a single tendon bar, which was anchored in the base of the footing. Column parameters from this experiment are shown in Table 1-1.

The unbonded post-tensioned columns displayed enhanced re-centering capabilities. It was also noted that the initial post-tensioning force selected was appropriate since the tendons did not reach yielding values at large drift ratios. The maximum forces developed in the tendons were found to be 80% of the calculated yielding force of the tendons. It was noted that the construction process of incorporating unbonded post-tensioning in the columns did not deviate far from the base model, of which conventional reinforced columns were constructed. While constructing unbonded post-tensioned columns did not require a lot of additional time, and the columns were efficient in reducing residual displacements, it was noted that the columns might not remain serviceable following a strong earthquake because they are vulnerable to spalling of concrete and fracture of steel due to the high axial load ratio.

1.2.7   Precast Columns with Energy Dissipating Joints

Motaref et al. tested several precast segmental columns with energy dissipating joints (Motaref et al., 2011). Four cantilever columns were tested by shake table excitation. One benchmark column (SC-2) was constructed and tested to evaluate the performance three other cantilever columns with energy dissipating joints. The three columns were; SBR-1 that utilized an elastomeric bearing pad at the column base for energy dissipation, SE-2 that used ECC (engineered cementitious composite) in the plastic hinge region for energy dissipation, and SF-2 that used a CFRP jacket in the plastic hinge region. All column parameters are shown in Table 1-1.

All of the columns performed very well through shake table testing. The benchmark column (SC-2) had the most extensive damage, as expected. Column SBR-1 containing the elastomeric bearing pad was free of damage at the column bearing interface, and showed the best performance of all of the columns. Column SC-2 had a peak lateral force occur at a drift of 4.2% and the column strength began to decrease with further lateral displacement. Column SBR-1 was able to maintain the peak lateral force through a drift level of 14%. All of the columns utilized post-tensioning for re-centering benefits. A single steel rod was used for the post-tensioning force and was anchored in the base of the footing in each column.

1.3   Motivation

Based on the literature review, it was noted that there are several parameters that require more investigation. Much of the previous research investigates re-centering capabilities of unbonded post-tensioned columns with very little to no longitudinal reinforcement crossing the column footing interface. Reinforcement ratios greater than 1.0% should be tested to gain a better perspective of the effect of the reinforcement on re-centering. Developing tendon details requires further investigation to develop a realistic full-scale configuration. Prestress area and initial force has been tested with a wide range of values without a definite value for the best all-around column performance. Not only

should re-centering be further investigated, but tendon strains at large lateral displacements, even beyond column failure should also be looked at. A wide range of axial dead load has been investigated because the axial load can vary significantly in modern bridge columns. Axial load should be investigated to provide the best all-around column performance, and an accurate unbonded post-tensioned analytical model is required for further investigation, since only a few columns can be tested at a time.

1.3   Objectives & Scope

The primary objective of this research was to investigate the cyclic lateral load performance of unbonded post-tensioned columns. It was critical to determine the effect of the longitudinal reinforcement ratio on re-centering capabilities, and an appropriate initial post-tensioning force that will not yield the tendons at large drift ratios. In addition, the research was used to investigate new and improved construction methods for unbonded post-tensioned concrete columns, specifically developing a constructible full-scale column, including the tendon details. Anchoring the tendons at the corners of the footing was introduced to evaluate the possibility of removing tendons, following a seismic event. The tendons were also greased and sheathed to help protect the strands against corrosion, of which bridges are highly susceptible.

To accomplish these objectives, two columns were constructed and tested under cyclic loading. The columns were constructed side by side, and cast at the same time to ensure similar properties between the two specimens. Throughout testing, strain gauges, displacement transducers, and load cells were used to measure behavior.

An analytical model was developed to determine the column behavior. After the experimental program, the analytical model was updated with the actual material properties. The analytical model proved to be accurate. With an accurate correlation between the measured and calculated results, a parametric study was conducted. The parametric study was used to evaluate a wide range of parameters so design recommendations could be made.

CHAPTER 2

Specimen Design and Construction

2.1   Introduction

Two columns were constructed and tested to better understand the performance of unbonded post-tensioned columns using new construction methods for seismic application. This chapter focuses on the selection, design, construction, and material properties of the specimens. The one parameter varied between the two specimens was the amount of longitudinal reinforcement crossing the interface between the column base and footing. All the other parameters including the initial post-tensioned force were specified to be the same for the two specimens so the effect on the amount of longitudinal steel on re-centering could be investigated.

2.2   Selection of Experimental Specimens

Column dimensions were based on a (60"-diameter (1524 mm)) prototype column. Columns of this size are typical for the state of Nevada and surrounding regions. The specimens selected were 0.4-scale, leading to a scaled column diameter of 24" (610 mm) (Figure 2-1). The largest possible column diameter that testing equipment could support was selected so a realistic tendon configuration would be possible. The aspect ratio was chosen as 4.5, leading to a flexure dominated failure as opposed to shear failure. The scaled column height was 108" (2743 mm) (Figure 2-2).

The first specimen was called "PT-LL," for unbonded post-tensioned with low longitudinal reinforcement. From the literature review, it was concluded that previously tested post-tensioned columns for seismic application contained very little to no longitudinal reinforcement crossing the joint between the column base and footing. The low amounts of longitudinal reinforcement demonstrated excellent re-centering capabilities. Columns without any longitudinal reinforcement crossing the joint between the column base and footing also showed excellent re-centering capabilities, but did not provide energy dissipation. To provide re-centering capabilities and some energy dissipation, column PT-LL was designed with 10-#5 ASTM 706 grade 60 ksi (414 MPa) reinforcing bars, resulting in a longitudinal reinforcement ratio of 0.685%.

The second specimen was called "PT-HL," for post-tensioned with high longitudinal reinforcement. To achieve a better understanding of the effect of longitudinal reinforcement on column re-centering, PT-HL was selected with nearly twice the amount of longitudinal reinforcement crossing the joint between the column base and footing. Column PT-HL was designed with 10-#7 ASTM 706 grade 60 ksi (414 MPa) reinforcing bars, resulting in a longitudinal reinforcement ratio of 1.33%. PT-HL cross section and elevation are shown in Figure 2-3 and Figure 2-4, respectively. Column parameters for both PT-LL and PT-HL are shown in Table 2-1.

The axial load index is defined as the axial load divided by the product of the concrete compressive strength and column cross sectional area. The axial load index will be referred to as a percentage of $f'_c A_g$. Typical values for the axial load index range between 0.05 and 0.1 for bridges. The dead load was set to be 6% of the axial load index,

or 6% of f'$_c$A$_g$, which is relatively small for typical bridges. This lower value was selected because there would be an additional axial load from the post-tensioning force. The initial post-tensioning force was selected based on the analytical model and literature review. The initial post-tensioning force was set to be 10% of f'$_c$A$_g$. Initial post-tensioning stress was selected to be around 20% of f$_{pu}$ to insure that the tendons would not yield during testing. Concrete strength at test day was specified at 4500 ksi (31 MPa), leading to an initial tendon force of 203.5 kips (905 kN) for 10% of f'$_c$A$_g$. Based on 0.6" (15.2 mm) diameter 270 ksi (1862 MPa) low-relaxation strands, to achieve an initial tendon stress of approximately 20% of f$_{pu}$, the required tendon area was 3.769 in^2 (2432 mm^2). The area of one 0.6" (15.2 mm) diameter 270 ksi (1862 MPa) low-relaxation strand is 0.217 in^2 (140 mm^2), therefore, 17.37 strands would be needed to satisfy this requirement. For this experiment, to maintain a symmetrical layout, sixteen strands were selected leading to an initial tendon stress of 21.7% of f$_{pu}$.

The prototype column of 60" (1524 mm) diameter constructed with 4500 ksi (31 MPa) concrete would need one hundred strands to fulfill this same requirement. One hundred strands would be far too many for one centrally located tendon. The most realistic option would be to have four separate tendons evenly spaced around the center of the column cross section. To determine how close the anchorages could be to the center of the column cross section, a prototype anchorage was selected that could hold twenty-five stands. Using four anchorages, each holding twenty-five strands, the one hundred strand requirement would be satisfied. For the selected anchorage, the outer diameter of the local reinforcing spiral was 17" (432 mm). With 2" (50.8 mm) of clear cover between spirals, a distance of 13.5" (343 mm) out from the center of the column cross section was calculated as the location for each of the four anchorages. For the scale models, the scaled distance out from the center of the column cross section to the center of the anchor was 5.4" (137 mm) (see Figure 2-1 and Figure 2-3). Each anchor contained four 0.6" (15.2 mm) 270 ksi (1862 mm) low-relaxation strands. It was decided to use unbonded tendons in this study because the literature review concluded that unbonded tendons evenly distributes the strain over the entire length of the tendon, reducing inelastic strains in the unbonded tendons.

Post-tensioned columns constructed for seismic application have the possibility of damaging tendons during a seismic event. Therefore, it is necessary to be able to inspect, and if needed, replace tendons. Replacing tendons requires having access to an anchored end. Anchoring tendons in the base of the footing has been the traditional method in prior research, but does not make it possible to replace or inspect the tendons if necessary. In this project the tendons were anchored on the side of the footing as shown in Figure 2-5 and Figure 2-6, making it possible to access the tendons after construction is complete. Additionally, to better protect the tendons from corrosion, greased and sheathed strands were used.

2.3   Design of Experimental Specimens

Footing dimensions were governed by overturning, actuator height, and tendon anchorage locations. The plan view footing dimensions were 84"x84" (2134 mm x 2134 mm), and the height of the footing was 32" (813 mm) (see Figure 2-5 and Figure 2-6). Six 2-^{1}/$_2$" (64 mm) schedule 40 PVC pipes were used as tie down holes through the

footing, with three located at 24" (610 mm) away from the east side of the column, and three located at 24" (610 mm) away from the west side of the column. One 2-$^1/_2$" (64 mm) schedule 40 PVC pipe was located 24" (610 mm) to the north and south of the column to allow the axial load rods to pass through the footing and anchor in the strong floor. All PVC pipe locations were selected according the available strong floor hole locations. The overall hole pattern dimension in the strong floor used to tie down the footing was 48"x48" (1219 mm x 1219 mm). The additional length in the footing dimensions was used to provide additional moment arm length to resist the predicted overturning moment, and additional straight length for the tendon once it exits the bottom of the steel pipe.

Tendons were designed to exit diagonally through the corners of the footing for ease of replacement. Exiting the tendons to the north, east, south, and west sides of the footing would not work since the footing tie down holes were directly in the way, so each tendon was required to exit toward one of the four corners of the footing. Anchoring the tendons in the corners of the footing also allows for a longer straight length between the footing corner and the steel pipe, helping reduce any unwanted rotational forces at the tendon anchor. Due to this configuration, 13-$^3/_4$"x13-$^3/_4$"x19.45" (349 mm x 349 mm x 494 mm) triangular sections were removed from each of the four corners in the footing (see Figure 2-6). This allowed for a level interface between the footing and tendon anchor head. Sending the tendons to the corners of the footing required using a 3" (76 mm) diameter steel pipe with a 20" (508 mm) radius to complete a 90-degree bend that the tendon could travel through. The tendons were anchored in the corners of the footing, centered at a height of 5-$^1/_2$" (140 mm) above the base of the footing.

The footings were designed to be very stiff and rigid. The footing reinforcement consisted of two mats of 14-#6 grade 60 ksi (414 MPa) reinforcing bars spaced at approximately 6" (152 mm) in each direction. Footing shear reinforcement was provided by 58 vertical #3 grade 60 ksi (414 MPa) reinforcing bars. All concrete clear cover in the footing was set at 1" (25.4 mm). Figure 2-7 shows the reinforcement layout with anchorages.

Column PT-LL was reinforced with 10-#5 grade 60 ksi (414 MPa) reinforcing bars evenly spaced in a circular pattern resulting in a longitudinal reinforcement ratio of 0.685%. The bars began near the top of the loading head, continued through the column, and extended into the footing where they were fully developed with a 90-degree hook. The transverse spiral reinforcement consisted of #3 grade 60 ksi (414 MPa) reinforcing bars with a 2" (50.8 mm) pitch, resulting in a transverse reinforcement ratio of 1.00%. The spiral reinforcement continued 23" (584 mm) into the footing with a double spiral at the end. The steel pipes used to send the tendons out to the corners of the footing all began inside the spiral reinforcement. The bottoms of the steel pipes were located 4" (102 mm) above the base of the footing to avoid interference with the bottom mat of footing reinforcement.

Column PT-HL was identical to column PT-LL in design, except for the amount of longitudinal reinforcement. Column PT-HL was reinforced longitudinally with 10-#7 grade 60 ksi (414 MPa) reinforcing bars, resulting in a longitudinal reinforcement ratio of 1.33%. All column concrete clear cover was 1" (25.4 mm). The tendon ducts within each column consisted of 2-$^1/_2$" (64 mm) diameter schedule 40 PVC pipe. Each duct was

attached to the column rebar cage with tie wire to maintain proper positioning throughout construction and pouring.

Loading heads for column PT-LL and column PT-HL were identical. The plan view dimensions of the leading heads were 36"x40" (914 mm x 1016 mm), with an overall depth of 30" (762 mm) as shown in Figure 2-8 and Figure 2-9. The loading head dimensions were governed by the mid-stroke length of the actuator. Since the actuator position was fixed due to the hole location in the reaction wall, and the column position was fixed due to the hole location in the strong floor, the loading head was designed to position the actuator right at mid-stoke when connected to the loading head and strong wall. The actuator connects to the reaction wall and loading head by four threaded rods on an 11-$^3/_4$" (298 mm) square pattern. Since the loading head in each column had four tendons located in the direct path for actuator connection, a steel adapter plate was used. The steel adapter plate connected to the actuator on one side, and the loading head on the opposite side with a different hole pattern than that of the actuator. The threaded rod pattern on the loading head side was spread out to a rectangular pattern of 11-$^3/_4$"x26" (298 mm x 660 mm). The increase from 11-$^3/_4$" (298 mm) to 26" (660 mm) in the horizontal direction allowed for the threaded rods to be sent through the column head without interference from the tendons.

From the plan view of the loading head, a 22"x22" (559 mm x 559 mm) square recess, with a depth of 5-$^1/_4$" (133 mm) was embedded to provide a space for the tendon anchor heads (see Figure 2-9). This recess allowed for the spreader beam that carried the axial load to be placed directly over the top of the column, without interference from the anchor heads. A wood jig with the recess dimensions was made so each of the four anchor heads could be bolted into their proper position. Once the anchor heads were connected, the wood jig was coated in wax for easy release following the concrete pour. The jig was fastened to the loading head formwork once it was centered in the proper position.

The loading head general zone reinforcement was designed to withstand the gross ultimate tensile strength from the tendons. The loading heads were reinforced with two mats of 6-#7 grade 60 ksi (414 MPa) reinforcing bars in each direction. This configuration was determined to be sufficient for the general zone reinforcement. The four anchor heads were locally confined with supplied spirals and also received additional confinement from the column spiral.

2.4   Construction of Test Specimens

The first step in constructing each test specimen was to assemble the column reinforcement. The longitudinal and transverse reinforcements were connected using tie wires to construct the column rebar cage. Once the rebar cage was complete, strain gauges were applied to both longitudinal and transverse reinforcement. The strain gauges were attached in the region of the lower quarter of the column, where maximum strains were expected.

Once the column rebar cages were complete, footing construction began by placing the plywood formwork. The lower mat of footing reinforcement was set into place inside the formwork. Each of the four anchor heads with their local reinforcing spiral were attached to the footing formwork as shown in Figure 2-10. At this point, the

3" (76 mm) diameter steel pipes used to send the tendons to the corners of the footing were set and secured into position as shown in Figure 2-11. The steel pipes were required to be placed at this time because the placement of the column rebar cage and upper mat of footing reinforcement would inhibit access to the location of the steel pipes. The steel pipes were designed to terminate 2" (50.8 mm) below the top of the footing, underneath the column. Tendon duct, consisting of 2-$^1/_2$" (64 mm) schedule 40 PVC pipe was then placed inside the first two inches of steel pipe and secured with a coupler. The PVC duct continued 24" (610 mm) out of the top of the footing, where it was outfitted with another coupler. The reason for not continuing the PVC duct all the way to the top of the column was because the equipment used to place the column rebar cage over the top of the duct was unable to reach a height of that magnitude. The column rebar cage was then placed over the steel pipes and duct where it was set into position. PVC duct was also connected between the bottom of the steel pipes and the footing anchor heads with couplers.

Once the steel pipes and column rebar cage were in position, hairpin reinforcement was placed throughout the curvature of each pipe for additional anchorage as shown in Figure 2-12. In a full-scale column, the radius of curvature for each tendon would be much greater and a standard bendable duct would be used in place of the steel pipe which would require hairpin reinforcement. For this project, the steel pipes were required due to the tight radius required by the footing dimensions. Footing reinforcement was completed with the installation of the upper mat of reinforcement and vertical shear reinforcement as shown in Figure 2-13. Upon completion of footing construction, concrete was poured before column construction continued (see Figure 2-14).

Tendon duct was then placed in each of the couplers extending from the footing and continuing up to a height above the top of the column. Each duct would later be cut to its proper length, which had to be measured once the loading head was constructed. Sonotube, used as formwork for the column, was placed over each rebar cage following a 7-day cure of the footing. Test results would later indicate that the rebar cage for PT-LL was not exactly vertically straight. An exaggerated "S" would be descriptive in defining the shape of the end result of the rebar cage in PT-LL. Due to this, cover concrete within the first 24" (610 mm) of column above the top of the footing was 1" (25.4 mm) on the east side, and 2" (50.8 mm) on the west side, instead of the specified 1" (25.4 mm) on both sides. Within the lower quarter of the column, it appeared that the rebar cage was short by 1" (25.4 mm) in the transverse direction. Once the Sonotube was in place, a deck was built and loading head construction began (see Figure 2-15).

Loading head construction began by placing and securing the bottom mat of reinforcement. Due to heavy congestion in the loading head, this step took place before the plywood formwork was placed. A plywood box with the anchor heads and spiral reinforcement attached was placed and secured to the loading head formwork to provide the recess for the anchor heads. At this point, the top mat of loading head reinforcement was placed. Vertical shear reinforcement was then placed and concrete was placed in the loading head and column.

2.4.1   Tendon Installation

Strands were installed using two tools: Cable Gripper and Pushing Bullet. The Cable Gripper is similar to a Chinese finger trap, when a strand is inserted into the gripper, the opposite end of the gripper can be pulled with a large force without losing the strand (see Figure 2-16). The Pushing Bullet is a 3" (76 mm) long steel tube with a round end that fits snugly over the strand as shown in Figure 2-17.

Installing up to three strands in each duct was not a problem, but installing the fourth required using the Cable Gripper due to the 90-degree turn each strand had to go through. Prior to placing any of the strands through the duct, a $^1/_4$" (6.4 mm) cable with the Cable Gripper attached to one end was placed through the entire length of the duct with the gripper end exiting the top of the column. Strands one through three were then individually pushed through the duct from bottom to top with the Pushing Bullet. The fourth strand was then connected to the $^1/_4$" (6.4 mm) cable with the Cable Gripper. At this point, the fourth and final strand was pulled through the duct from top to bottom. Pulling the last strand from the top allowed for a connection between the end of the cable and a forklift so the forklift could slowly drive away from the base of the footing, pulling the strand through.

Strain gauges were then attached to the strands near the top of the column. Prior to installing the strain gauges, a portion of the strand sheathing was removed so the strand could be de-greased for the secure placement of strain gauges. Tendons were required to have a minimum free length exiting the anchor head of 36" (914 mm) to allow space for stressing. Strain gauges were placed 36" (914 mm) below the anchor head, so 72" (1829 mm) of sheathing was removed from each strand. The degreased installed strands are shown in Figure 2-18.

2.4.2   Stressing of Tendons

The tendons were stressed in PT-LL and PT-HL on the same day. Column and loading head concrete had cured for 28 days at the time of stressing. The tendons were stressed in two stages. First, the tendons were stressed to 75% of their ultimate strength in order to properly seat the wedges in the strands. Second, steel shims that were placed under the anchor heads prior to stressing were removed in order to reach the proper initial tendon stress.

Prior to stressing, two $^1/_2$" (12.7 mm) thick steel shims were placed under each anchor head as shown in Figure 2-19. Wedges were then set in place at each strand/anchor head interface. A steel pipe was then place over the strand to deliver impact to the wedge to help minimize the anchorage slip that would take place during stressing. With all of the wedges in place, each strand was individually stressed to 75% of its ultimate strength (see Figure 2-20). The stressing sequence began by stressing one strand from tendon one using a monostrand jack. The tendon arrangement for each column was identical, as shown in Figure 2-21. Following the stressing of one strand from tendon one, one strand from tendon three was stressed. Following the stressing of one strand from tendon three, one strand from tendon two was stressed, and then one strand from tendon four was stressed. This circular pattern continued until all sixteen strands were

stressed. The objective of this stressing sequence was to minimize the amount of elastic shortening on the column and to also reduce unwanted moments on the column.

Following the initial tendon stressing to seat the wedges, steel shims had to be removed to achieve the desired initial stresses for testing. To remove the steel shims, a multistrand jack was placed on a jack chair which was placed over each anchor head one by one (see Figure 2-22). Once the jack chair was in place, the stressed tendon with anchor head was lifted so one of the $^1/_2$" (12.7 mm) steel shims could be removed and replaced with one $^1/_4$" (6.4 mm) steel shim. At this point, the multistrand jack was released so the anchor head could bear against the anchor plate. A second liftoff was then performed at a very slow rate on the same anchor head until the point was reached when the steel shims became movable, at which point the force required to hold the anchor head in place was read from the multistrand jack gauge which corresponded to the force in the tendon. Each tendon varied slightly from one another, so $^1/_8$" (3.2 mm) shims were also available to try and make up for these differences. Once all four tendons had been stressed, the remaining strand was removed.

2.5   Material Properties

2.5.1   Steel

The average tensile reinforcing bar stresses were measured by testing three #3, #5, and #7 reinforcing bar samples. Reinforcement properties were determined by following ASTM A706 testing standards. Each reinforcing bar was placed in an Instron tensile testing machine controlled by the computer program Partner. While testing the reinforcement, Partner recorded both the yield and ultimate stresses. The average yield stress for the #3, #5, and #7 reinforcing bars were 71.3 ksi (491.6 MPa), 71.8 ksi (495.1 MPa), and 69.8 ksi (481.3 MPa), respectively. The specified yield strength was 60 ksi (414 MPa). The reinforcement steel properties are shown in Table 2-2.

The properties of the 0.6" (15.2 mm) 7-wire 270 ksi (1862 MPa) low-relaxation strand stresses were measured by testing three samples. Determining the yield and ultimate strengths of the 0.6" (15.2 mm) 7-wire 270 ksi (1862 MPa) low-relaxation strands followed ASTM A370-03a standards. The tensile test was carried out on an Instron tensile testing machine run by the computer program Partner. An initial load of 10% of the minimum breaking load specified for the strands was applied, resulting in 58.6 kips (261 kN). A Class B-1 extensometer was then attached to the specimen and adjusted until a gage length reading of 0.001 in./in. was attained. Once the extensometer was adjusted, the load was then increased until an extension of 1.00% was read. The load corresponding to this extension was then read as the yield strength which corresponded to an average from the three specimens of 247 ksi (1703 MPa). The specified yield strength of 0.6" (15.2 mm) 7-wire 270 ksi (1862 MPa) low-relaxation strand is 243 ksi (1675 MPa). The load continued to increase until the specimen reached failure, at which point the ultimate load was taken. The average ultimate load from the three specimens was 281 ksi (1937 MPa). To increase the accuracy of the measured yield and ultimate stresses, a micrometer was used to determine the exact area of the 0.6" (15.2 mm) 7-wire 270 ksi (1862 MPa) strand. The end of the tested specimen was unwound so each of the seven wires could individually be measured with the micrometer. Using the total measured area

14

of the strand with the measured yield and ultimate strengths, the yield and ultimate stresses were calculated. The measured strand properties are shown in Table 2-2, and the average stress-strain curve is shown in Figure 2-23. The two column specimens both contained steel from the same lot, so measured results represent that of both column PT-LL and PT-HL.

2.5.2 Concrete

Column PT-LL and PT-HL were cast simultaneously. The footing for each specimen was cast first. Once the footings were cast, the column formwork was placed and the loading head construction began. Upon completion of the loading head construction, the column and loading head of each specimen was cast in one lift. Formwork for the footing, column, and loading head was removed after 7 days of curing for both specimens.

The specified concrete strength was 4.5 ksi (31 MPa) with a maximum aggregate size of $^3/_8$" (9.5 mm). Slump was measured using a slump cone before each concrete casting. The measured slump for the footing concrete was 3-$^3/_4$" (95.3 mm). Each concrete pour had a specified amount of "trim" water that could be added to increase workability without decreasing the specified strength. The footing concrete did not require adding any trim water since workability was not an issue in the footing. The measured slump for the column/loading head pour was 4" (102 mm). This measurement was too low since the column and loading head were very congested and required more workable concrete. Additionally, the column and loading head concrete was cast 17 days after the footing was cast, and the 14-day compressive strength of the footing concrete had already reached 4735 psi (32.6 MPa). Since the specified concrete compressive strength was 4500 psi (31 MPa), and the mix design for the footing and column/loading head were identical, it was considered safe to add as much of the trim water needed to improve workability. Six out of the eleven allowed gallons of trim water were added to the mix. Another slump test was measured at 4-$^3/_4$" (121 mm). This value was still too low and trim water was available so another three gallons were added to the mix. Another slump test was measured at 5-$^1/_2$" (140 mm). At this point, the concrete had become more workable so it was placed in the columns and loading heads.

Eighteen 6" (152 mm) by 12" (305 mm) cylinders were taken from the footing and column/loading head casting. Three cylinders were each tested on day 7, 14, 28, and the test day of each column. This left extra cylinders in case of mishandling. Each cylinder was tested on a SATEC MKIII-C testing machine. Table 2-3 shows the average compressive strengths of three cylinders measured at day 7, 14, 28, and test day. The table includes results for both the footing, and column/loading head of each specimen.

CHAPTER 3

Experimental Procedure

3.1   Introduction

Two unbonded post-tensioned bridge columns using modified tendon details were tested in the outdoor lab at UNR. The main focus was to investigate the seismic behavior of these columns by subjecting them to cyclic loading. Throughout the experiment, data was gathered through strain gauges, Novotechnik displacement transducers, string POTs, and load cells. The test setup consisted of a strong floor, 220-kip actuator, spreader beam with hydraulic rams and accumulator, and a reaction block system. This chapter describes the details of the instrumentation, test setup, and loading protocol.

3.2   Instrumentation

The first step in instrumentation was to strain gauge each column. A detailed drawing of the strain gauge plan was developed to place the strain gauges on the longitudinal and transverse reinforcement in the area where the highest strains were expected. The instrumentation plan for conventional reinforcement is shown in Figure 3-1. A total of six layers of strain gauges in each column were installed. A plastic hinge length was calculated using the California Department of Transportation Seismic Design Criteria (2006). The plastic hinge length equation is shown here as Equation 3-1.

$$L_p = 0.08L + 0.15f_{ye}d_{bl} \geq 0.3f_{ye}d_{bl} \quad \text{(in, ksi)} \qquad\qquad \text{Eqn. 3-1}$$

$$L_p = 0.08L + 0.022f_{ye}d_{bl} \geq 0.044f_{ye}d_{bl} \quad \text{(mm, MPa)}$$

L_p = plastic hinge length, in (mm)

L = column length, in (mm)

f_{ye} = yield stress of the longitudinal reinforcing bar, ksi (MPa)

d_{bl} = diameter of one longitudinal reinforcing bar, in (mm)

The calculated plastic hinge length for PT-LL and PT-HL was 14.3" (363.2 mm) and 16.5" (419.1 mm), respectively. The first layer was placed 4" (101.6 mm) below the column footing interface, the second layer was placed $^1/_2$" (12.7 mm) above the column footing interface, and the next four layers were evenly spaced above the second layer at 6" (152.4 mm) intervals. This arrangement allowed for full coverage of the calculated plastic hinge length. Column PT-LL and PT-HL used the same instrumentation plan for ease of comparisons.

The loading direction of cyclic motion was to the east and west, bending the column about the north-south axis. The east and west ends will be considered the extreme ends of the column. Two longitudinal bars from each extreme end had one strain gauge

attached at each layer. Starting with the first layer above the footing, the transverse reinforcement from each layer had four strain gauges attached at the north, east, south, and west locations. Each column had a total of forty-four TML YFLA-2-5LT strain gauges attached to the conventional reinforcement. At the time of testing, column PT-LL had two faulty gauges, #3 and #5, and column PT-HL had four faulty gauges, #4, #5, #24, and #38. Most likely, these gauges were damaged while casting the column concrete. Figure 3-2 shows strain gauges attached to the conventional reinforcement. The strain gauge wires ran down the north and south face of the column to prevent any interference they might have with the extreme longitudinal reinforcement.

Strain gauges were also attached to the post-tensioning tendons in each column to monitor their behavior throughout testing. It was assumed that the strain in the tendons near the top of the column and the plastic hinge region would be the same since the tendons were unbonded. Therefore, a single layer of strain gauges were installed 36" (914 mm) below the anchor heads at the top of the column. The tendon strain gauge plan is shown in Figure 3-3. The same configuration was used in each column for ease of comparison.

Each tendon, consisting of four strands, had six gauges attached to two of the four strands. Three gauges were placed on a strand on different wires so a more precise average strain could be measured. This configuration resulted in a total of twenty-four TML FLK-1-11-5LT strain gauges for tendon monitoring in each column. These strain gauges were specified differently from the conventional reinforcement strain gauges due the very small surface area on each of the seven wires that make up one strand. Since the 7-wire strands were encapsulated in a plastic sleeve and greased, application at the strain gauges required the removal of sheathing and grease from the end of the strand at the top of the column to the desired gauge location. In order to reach to proper desired strain gauge location, the strand was pushed through the column until 108" (2743 mm) extended beyond the loading head. Sheathing was then removed from the strand to a distance of 72" (1829 mm) from the top of the strand. This allowed a 36" (914 mm) clear length for stressing, and another 36" (914 mm) to the layer of strain gauges. Grease was removed from the strand by unwinding the end of each strand to the location of strain gauge placement. Large amounts of grease could then be effectively removed with a rag, followed by several passes over each wire with a clean rag and Acetone until all grease was removed. The strand was then wound back into its original shape and strain gauges were applied to their designated locations as shown in Figure 3-4.

Following the installation of all tendon strain gauges, the strands were carefully pulled back into the column until the gauges reached their specified depth of 36" (914 mm) below the top anchor heads. Strain gauge wires traveled through the grout tube entrance on the anchor plate to avoid the possibility of being fractured by the anchor head. Since the tendons were unbonded, the grout tube was free to use. Figure 3-5 shows the strain gauge wires exiting the anchor plate in place of the grout tube.

Column curvature was measured by Novotechnik displacement transducers. Each column utilized a total of ten transducers at five different layers. Five of the transducers were placed on the east side of the column, and the other five were placed on the west side of the column. The transducers were attached to the columns using $5/16$" (8 mm) all-thread horizontal rods that ran in the east-west direction of the column, and were set prior to casting. The threaded rods were only able to be embedded into the east and west sides

of the column to a depth of 5-$^1/_4$" (133 mm), due to interference with the post-tensioning ducts. The first transducer layer was located $^1/_2$" (12.7 mm) above the column and footing interface. The remaining four layers were equally spaced at 7" (178 mm) intervals above the column and footing interface. Towards the end of each experiment, severe spalling at the base of each column prevented further gathering of data from the first layer of transducers. The instrumentation plan for the Novotechnik displacement transducers is shown in Figure 3-6, and is identical for each column.

Three Unimeasure PA-40 stringpots were attached between the loading head and a reference frame to measure the absolute lateral column displacement at the level of the applied lateral load (Figure 3-6). The 220-kip (979 kN) actuator that was used to produce the cyclic loading protocol was equipped with a load cell used to measure the magnitude of the lateral force. A load cell was also used to measure the magnitude of the axial load in each column. The load cell was placed between one of the vertical hydraulic rams and the anchor plate at the end of the axial load rod. This configuration will be explained in more detail in Section 3.3. Column drift levels were controlled by the actuator.

3.3   Test Setup

Reaction wall construction was the first step in preparing the outdoor lab for testing. A total of seven 48"x48"x96" (1219 mm x 1219 mm x 2438 mm) concrete blocks were used to assemble the reaction wall. Six out of the seven blocks were stacked on top of each other side by side to form two columns, each three blocks tall. The final concrete block was placed on top of the east side of the stack to reach the proper height for the actuator to meet the loading head. The complete reaction wall is shown in Figure 3-7. Between the strong floor and the first two concrete blocks, and between each concrete block thereafter, $^3/_4$" (19 mm) thick plywood pieces were placed along with numerous 5"x5" (127 mm x 127 mm) dollops of hydrostone between the concrete blocks. The plywood and hydrostone were used to create a level surface between the blocks to prevent any rocking that might occur throughout the experiment.

Once all blocks were in place, 1-$^1/_4$" (32 mm) post-tensioning bars were placed in the horizontal direction to hold the stack together throughout the experiment. Post-tensioning bars also ran in the vertical direction and were anchored in the base of the 36" (914 mm) deep strong floor to prevent the reaction wall from overturning. Each post-tensioning bar was stressed to 100 kips (445 kN). Hole locations for securing the actuator to the reaction wall were positioned at 24" (610 mm) on center, requiring an adapter plate since the hole pattern on the actuator was set at 11-$^3/_4$" (298 mm).

Before each column was set into testing position, several 1-$^1/_2$" (38 mm) thick wood blocks were set under the column footing footprint. Form release was then sprayed on the strong floor where the footing would be placed. Once the column was set, a 2"x4" (51 mm x 102 mm) wood form was built around the base of the footing, leaving a 3" (76 mm) gap between the edges of the footing and the form. The form was sealed to the strong floor using fast dry caulk. Grout was then poured in the gap between the formwork and the footing until it reached a level of 1-$^1/_2$" (38 mm) above the base of the footing. The grout was placed to ensure a level surface between the footing and strong floor to prevent any rocking that might occur while testing. After allowing the grout to cure for 24 hours, six 1-$^1/_4$" (31.8 mm) post-tensioned bars connecting the footing to the strong

18

floor were stressed to 100 kips (445 kN). Each column was painted with white primer at this time to help identify cracks throughout the experiment.

The axial dead load in each column was maintained by an accumulator, which held equal and constant load between two hydraulic rams that rested on top of a 60" (1524 mm) steel spreader beam. The spreader beam was bolted to the top of the loading head with $^1/_2$" (12.7 mm) threaded rods that were embedded into the loading head prior to casting. The spreader beam extended beyond the loading head by 10" (254 mm) on the north and south sides, allowing 1-$^3/_8$" (35 mm) high strength threaded rods to run through the hydraulic rams, spreader beam, and footing to transfer the axial dead load from the hydraulic rams to the column. Between one of the hydraulic rams and the anchor plate of the high strength rod a load cell was placed, to measure the axial load representing the gravity load on the column. The axial gravity load for this experiment was selected based on the axial load index. The axial load index is defined as the axial load, divided by the product of the concrete compressive strength and the gross cross-sectional area of the column. For bridges, this value is typically between 0.05 and 0.1. A value from the lower end of this range was selected, since the columns would undergo additional axial load from the post-tensioning. Based on the specified concrete strength of 4500 psi (31 MPa), and an axial load index of 0.06, the axial dead load resulted in a value of 122 kips (543 kN). While the axial dead load was specified to be 122 kips (543 kN), variations through the experiment were observed, ranging from 95 kips (423 kN) to 132 kips (587 kN) for PT-LL, and 104 kips (463 kN) to 134 kips (596 kN) for PT-HL. A leaking valve in the hydraulic line was fixed between testing PT-LL and PT-HL, reducing the range in axial dead load for PT-HL. The complete test setup is shown in Figure 3-8 and Figure 3-9.

3.4   Loading Protocol

The loading protocol for cyclic testing consisted of two push-pull cycles at increasing drift ratios (defined as the lateral displacement at mid height of the loading head, divided by the height above the footing to the lateral loading point). Drift ratios were initially set at 0.25%, 0.5%, and 1%, then up to 6% in 1% intervals. Once a drift of 6% was attained, drift levels would continue in 2% increments up to failure. Column PT-LL had a longitudinal reinforcing bar fail during the last cycle of 6% drift, leading to a change the initial protocol to a drift of 7% for the next cycle. The modified loading protocol for PT-LL and PT-HL is shown in Figure 3-10 and Figure 3-11, respectively, and the displacement at each drift ratio is summarized in Table 3-1. The protocol change from a 6% drift to a 7% drift was implemented to help build a smooth pushover curve since the column had already had a longitudinal reinforcing bar fail at 6%. Following two cycles at 7% drift, the column was pulled once to -10% from -7% drift, and then pushed once to +10% drift. Even though the column had already failed, this additional pull and push to 10% drift was used to see how the tendons would respond to a drift of that magnitude. Due to the failure at 6% for column PT-LL, and to keep a consistent loading program between the two specimens, column PT-HL followed the same modified loading protocol. Column PT-HL failed at 8%, and again was pushed to a drift of 10% to monitor tendon strains. The load rate for each specimen was 1" (25.4 mm) per minute through the 3% drifts, and increased to 5" (127 mm) per minute for all of the following drifts. These values were essentially near static.

19

CHAPTER 4

Experimental Results

4.1 Introduction

Two post-tensioned bridge columns were tested under cyclic loading. Column PT-LL and PT-HL were nearly identical except for the amount of longitudinal reinforcement crossing the joint between the column base and footing. This chapter presents results that focus on the general test observations, hysteretic response, the pushover curves, strains in reinforcing bars and post-tensioning strands, and column curvature, and compares the two test specimen results.

4.2 PT-LL Results

4.2.1 General Observations

Cyclic testing consisted of a push and pull (referred to as a cycle) motion from an actuator at a given drift ratio. Two cycles were applied at each drift ratio. The push was toward the east direction and will be considered positive, and the pull was toward the west direction and will be considered negative. Table 4-1 designates the load numbers with the corresponding drift ratio. Each load number, corresponding either to a push or a pull at a given drift ratio will be shown in the pictures presented in this chapter. The height of the column is 108" (2743 mm), therefore ±1% drift is ±1.08" (27.4 mm) of displacement.

The first small cracks appeared after the first pull cycle to -0.25% drift as shown in Figure 4-1. As loading continued, cracks increased in length and width, and many new cracks formed within the lower fourth of the column. The first spalling at the base of the column formed on the west side following the first pull to -2% drift, as shown in Figure 4-2. The first spalling on the east side of the column occurred shortly thereafter, following the first push to 3% as shown in Figure 4-3. As mentioned in Chapter 2, cover concrete on the east side of the column was 1" (25.4 mm) less than that on the west side, leading to a visible spiral on the east side after the first push to 3% drift (see Figure 4-3). At this point, it was apparent that the cover concrete on the east side of the column was around 1" (25.4 mm). Roughly 1-$^3/_4$" (44.5 mm) of cover concrete had spalled on the west side at this time, and the west spiral was still not visible. Spiral reinforcement became visible on the west side after the second push to 3% drift, shown in Figure 4-4. The visible spiral indicated that the cover concrete on the west side of the column was 2" (50.8 mm). The first longitudinal bar began to buckle on the east side of the column after the second push to 6% drift, as shown in Figure 4-5. Figure 4-6 shows the same longitudinal reinforcing bar after fracture, which took place on the way to the second pull of -6% drift. The longitudinal bar fractured at column displacement of -5.46" (-138.7 mm), equal to a drift of 5.1%. Loading continued up to 10% drift to attain a complete pushover curve, and to monitor tendon strains at large drift levels.

4.2.2   Hysteretic Response

The hysteretic response is shown in Figure 4-7. The force shown in the hysteresis curve was measured directly from a load cell connected in line with the actuator. It is assumed that the axial dead load force acts through the column base, at the point at which the column is rotated about, creating no additional moments or base shear on the system. The column displacement in the hysteresis curve was measured by the Unimeasure PA-40 stringpots described in Chapter 2. Figure 4-8 shows the absolute force-displacement values from the negative envelope of the hysteresis curve, superimposed over the positive envelope of the hysteresis curve. From this figure, the maximum difference in lateral force between the positive and negative envelope is nearly 10 kips (44.5 kN), at a displacement of 6" (152.4 mm). Force-displacement relationships between the positive and negative envelopes are very similar up to 2% drift. Around 2% drift and beyond, severe spalling on the west side of the column begins. Once the severe spalling onset occurs on the west side of the column, the center of gravity of the column section begins to shift to the east. While the center of gravity of the section is shifting to the east, the post-tensioning center of gravity stays at the location of the original center of gravity. The difference between the centers of gravity creates a vertical force at an eccentricity. The force is equivalent to the post-tensioning force, and the eccentricity is equivalent to the distance between the columns new center of gravity and the post-tensioning center of gravity. This force and eccentricity can be thought of as an equivalent horizontal force acting towards the west at the top of the column. Therefore, more force is needed to push the column towards the east, explaining why the positive (push) envelope has greater forces compared to the negative (pull) envelope. This will be discussed further and modeled in Chapter 5 (Analytical Model).

Table 4-2 displays the positive, negative, and average residual displacements from the hysteresis curve at each drift level. The residual displacement is notably small for drifts up to 3%, resulting in a residual displacement of less than 25% of the maximum lateral column drift for each cycle. Continuing up to a drift of 7%, residual displacements are still less than 40% of the maximum lateral drift. The small residual displacement values indicate that the unbonded post-tensioning force helps reduce residual displacements.

4.2.3   Cyclic Response

The pushover curve was created by averaging the positive and negative envelopes of the hysteretic response (see Figure 4-8). The average pushover curve is shown in Figure 4-9, where the "X" indicates the first reinforcing bar fracture, occurring at a displacement of 6.6" (167.6 mm), at a drift of 6.1%. The maximum average lateral force in the column was 53.4 kips (237.5 kN) at a drift of 6.6" (167.6 mm).

By evaluating the measured strains from the experimental results, strain gauge #6 was on the first longitudinal bar to yield, at a column displacement of 0.65" (16.5 mm). This value was then used to plot a straight line on the average pushover curve, beginning at zero force and displacement, and continuing through the point of force and displacement at first yield. A horizontal line was then plotted near the top of the pushover curve, where the area above the horizontal line bounded by the pushover curve was equal

21

to the area under the horizontal line bounded by the pushover curve and the straight line running through the point of first yield. The location where the two plotted straight lines intersect is the effective yield displacement of the column (see Figure 4-9). The effective yield displacement of the column was 0.95" (24.1 mm).

Two different ductility displacements were then defined. The first ductility was termed "ductility displacement capacity," and is defined as the ultimate displacement (displacement at 80% of the peak lateral force in the column) divided by the effective yield displacement. The ultimate displacement at 80% of the peak load was measured at 9.1" (231.1 mm) at a drift of 8.4%, leading to a ductility displacement capacity of 9.6. The second ductility was termed "ductility at first fracture," and is defined as the lateral column displacement at the time of the first longitudinal reinforcing bar fracture, divided by the effective yield displacement. The column displacement when the first longitudinal reinforcing bar fractured was measured at 6.6" (167.6 mm) at a drift of 6.1%, leading to a ductility at first fracture of 6.9.

4.2.4   Measured Strains

Strain gauges were attached to the conventional reinforcement and post-tensioning strand as shown in Chapter 3 in Figure 3-1 and Figure 3-3, respectively. Material properties from Chapter 2 indicate that the yield strain in the longitudinal reinforcement was 2480 microstrain. Strain-drift hysteresis curves for the longitudinal reinforcing bars within the first two layers are shown in Figure 4-10 through Figure 4-15. In all tables and figures presenting strain gauge results, negative strain corresponds to tension. The first layer of strain gauges were located $^1/_2$" (12.7 mm) below the column footing interface, and the second layer of strain gauges were located 7-$^1/_2$" (190.5 mm) above the column footing interface. Within the strain-drift hysteresis curves, the location of longitudinal reinforcement fracture is shown as a deviation away from the smooth strain-drift hysteresis curves. The first occurrence of this is shown in Figure 4-10. In this figure, the reinforcement fractures on the way to its first push to 7% drift. Following the 7% drift, the reinforcing bar goes into compression for the first pull to -7%. From this point on forward, it is shown in the figure that the strain does not go below zero microstrain again, indicating that the reinforcement can no longer support tensile forces. Strain-drift hysteresis curves for strain gauges 3 and 5 are not included since these strain gauges were not functioning at the time of the experiment. All other conventional reinforcing strain-drift hysteresis curves are shown in Appendix A.

Table 4-3 through Table 4-6 show the maximum strains at each drift level for the conventional reinforcement. These figures will be referred to as "strain gauge charts." Several of the strain gauges were not functioning prior to testing, likely due to severed wires from casting the column concrete. The non-functional gauges are marked as "faulty" in the strain gauge charts. Additionally, several strain gauges became detached during the experiment and are marked as "slipped" at the corresponding drift level in the strain gauge charts. It was determined that a strain gauge had slipped when the recorded data displayed a very large jump in value, at which point that value remained constant.

Strain-drift hysteresis curves from tendons 1 and 4 are shown in Figure 4-16 through Figure 4-25. Tendons 1 and 4, (Figure 2-21), do not show any yielding strains from any of the measured strain gauge data. The tested strand results (see Table 2-2) and

measured modulus of elasticity (E_{ps}=28,667 ksi, 197,700 MPa), indicate that the tendons yield strain is 8600. Tendons 1 and 3 were on the east-west axis, where the highest tendon strains were measured, and tendons 2 and 4 were on the north-south axis, where lower maximum strains were measured. The strain-drift hysteretic curves of tendons 1 and 4 are representative of all four tendons since tendon number 1 is located on the east-west axis, and tendon number 4 is located on the north-south axis. Strain-drift hysteresis curves for tendons 2 and 3 are shown in Appendix A. Table 4-7 and Table 4-8 show the maximum strains at each drift for the post-tensioning strands.

4.2.5   Moment Curvature Relationship

Column curvature was measured by Novotechnik displacement transducers. The transducers were located across five different layers as shown in the curvature instrumentation plan (Figure 3-6). To calculate the average curvature over the length of each layer, Equation 4.1 was used.

$$\varphi = \frac{\frac{\Delta W}{lw} - \frac{\Delta E}{le}}{ld} \qquad\qquad \text{(Eq. 4.1)}$$

φ = Average Curvature

ΔW, ΔE = Measured transducer displacement at the west and east locations, respectively

lw, le = Gauge length of transducers at the west and east locations, respectively

l_d = Horizontal distance between the pair of transducers on opposite sides of the column

Moment was measured as the product of the horizontal force in the actuator and the height from the top of the footing to the location of that force.

Moment curvature hysteresis curves are shown in Figure 4-26 through Figure 4-30. All of the curves are plotted with the same scale for ease of interpretation and comparison. The graphs indicate that the majority of the columns curvature took place within the bottom two layers. The bond slip layer shows the column curvature with respect to the footing surface, and layers 1 through 4 show the column curvature of that section. Bond slip and layer 1 both display a curvature greater than twice that of layer two. Continuing up the column to the location of layer four, there is virtually no curvature, with values less than 0.0006 $^{\text{rad.}}/_{\text{in}}$ (0.00002 $^{\text{rad.}}/_{\text{mm}}$).

To summarize the curvature results, the average height of each layer above the footing was plotted against the maximum curvature at each drift level. For ease of interpretation, these results were broken up into two separate plots for drift ratios of 0.25% through 2%, and 3% through 7%, as shown in Figure 4-31 and Figure 4-32, respectively. These two plots also indicate that the majority of the columns curvature took place near the column base, and reduced significantly to nearly zero curvature in layer four.

4.3   PT-HL Results

4.3.1   General Observations

Table 4-9 designates the cycle number with the corresponding drift ratio. The cycle numbers are shown in each of the experimental pictures presented in this section. During one of the cycles, a reinforcing bar fractured; the test was momentarily stopped so pictures could be taken along with notes and observations of the damage. This differs from Table 4-1 representing PT-LL, where cycle numbers indicated the target drift ratio, even if the test was stopped at mid drift to observe damage. The cycle numbers in Table 4-9 indicate the exact drift ratio when a picture was taken. The test cycles for PT-HL followed that of PT-LL, beginning with a 0.25% drift ratio, and ending at a 10% drift ratio. Following the two cycles at 8% drift, the column had reached failure. Testing continued from the final pull at -8% drift, and went directly on to one pull to -10% drift, and one push to 10% drift. The complete cycle at 10% drift was used to determine if the initial tendon force was adequate to prevent tendon yielding at large drift ratios.

Figure 4-33 shows the first crack, which appeared after the second cycle of 0.25% drift. As testing proceeded, the cracks grew in length and width while many new cracks formed. The first spalling at the base of the east side of the column occurred after the first cycle of 3% drift, as shown in Figure 4-34. Figure 4-35 shows the first spalling at the base of the west side of the column after the first cycle of -3% drift. Figure 4-36 shows the first visible spiral on the east side of the column, also taking place after the first cycle of -3% drift. The first spiral to become visible on the west side of the column took place after the second cycle to 3% drift, as shown in Figure 4-37. The first longitudinal reinforcing bars to become visible on the west and east sides of the column appeared after the first cycle to 5% and -5% drift, as shown in Figure 4-38 and Figure 4-39, respectively. The first longitudinal reinforcing bar to buckle was on the west side of the column after the second cycle of -7% drift, as shown in Figure 4-40. The first transverse reinforcement to fracture occurred right at the end of the first cycle of 8% drift, as shown in Figure 4-41. The west side longitudinal reinforcing bar that was beginning to buckle in Figure 4-40, fractured at a drift of 2.92%, on the way to the second cycle of 8% drift, as shown in Figure 4-42.

4.3.2   Hysteretic Response

The hysteretic response is shown in Figure 4-43. The force shown in the hysteresis curve was measured directly from a load cell connected in line with the actuator. It is assumed that the axial dead load force acts through the column base, at the point at which the column is rotated about, creating no additional moments or base shear on the system, similar to column PT-LL. The column displacement in the hysteresis curve was measured by the Unimeasure PA-40 stringpots, also similar to column PT-LL. Table 4-10 displays the positive, negative, and average residual displacements from the hysteresis curve at each drift level. For drift ratios up to 3%, the average residual displacement is less than 25% of the maximum lateral drift. Beyond drift ratios of 3%, the average residual displacement increases quickly, up to 55% of the lateral drift at 10%

drift. The increased longitudinal reinforcement ratio increases the magnitude of residual displacement for drifts that exceed 3%.

4.3.3 Cyclic Response

The absolute force and displacement from the negative envelope of the hysteresis curve was plotted and superimposed over the positive envelope, shown in Figure 4-44. An average curve was then calculated from the positive and negative envelope of the hysteresis curve and is considered the pushover curve, shown in Figure 4-45. The "X" on the pushover curve represents the first reinforcing bar fracture, occurring at a displacement of 8.56" (217.4 mm) at a drift of 7.9%.

Strain gauge 6 measured the first longitudinal reinforcing bar yield at a displacement of 1.02" (25.9 mm). A straight line was then plotted on the pushover curve beginning at zero force and zero displacement, and continuing through the force and displacement at first yield. A straight horizontal line was then plotted near the top of the pushover curve. This straight line was positioned such that the area above the straight line bounded by the pushover curve was equal to the area under the straight line bounded by the pushover curve and the straight line running through the point of first yield. The intersection of the two straight lines is the effective yield displacement and was measured at 1.42" (36.1 mm). Column displacement when the first reinforcing bar fractured was 8.56" (217.4 mm) at a drift ratio of 7.9%. Ultimate displacement was 9.87" (250.7 mm) at a drift of 9.1% and was calculated as the column displacement at 80% of the peak force.

Two ductility displacements were calculated from the pushover results; ductility at first fracture, and ductility displacement capacity. Ductility at first fracture was 6.0 and was calculated as the displacement at first fracture divided by the effective yield displacement. Ductility displacement capacity was 7.0 and was calculated as the ultimate displacement divided by the effective yield displacement.

4.3.4 Measured Strains

Strain gauges were attached to the conventional reinforcement and post-tensioning strand with the identical layout of column PT-LL. Prior to testing, four strain gauges on the conventional reinforcement were non-functional, and five strain gauges on the post-tensioning strand were non-functional. Most likely, casting the column concrete and stressing the strands damaged these gauges.

Figure 4-46 through Figure 4-51 show the strain-drift relationship of strain gauges 1 through 8 from the conventional reinforcement. These strain gauges measured the highest strains and were located within the lower two strain gauge layers (Figure 3-1). The first strain gauge layer was located $^1/_2$" (12.7 mm) below the column footing interface, and the second layer was located 7-$^1/_2$" (190.5 mm) above the column footing interface. Strain gauges 4, 5, 24, and 38 were the four non-functional strain gauges on the conventional reinforcement. All other conventional reinforcement strain-drift relationships are shown in Appendix A. The yield strain was obtained from the measured results presented in Chapter 2, and resulted in 2410 microstrains. Table 4-11 through Table 4-14 display the maximum strains from the conventional reinforcement at each

drift level. Strain values in the tables are displayed in bold print following yielding. Non-functional strain gauges are marked as "faulty" in the tables. During the experiment, specifically at high drift levels, several strain gauges slipped and are marked as "slipped" in the tables at the corresponding location of slip. It was determined that a strain gauge had slipped when the recorded data displayed a very large jump in value, at which point that value remained constant.

Strain-drift relationships for tendons 1 and 4 are shown in Figure 4-52 through Figure 4-60. Identical to column PT-LL, these two tendons represent the extreme east-west axis, and the north-south axis. Tendon 1 is located on the west side of the column and tendon 4 is located on the south side of the column (Figure 2-21). Strain-drift relationships for the remaining two tendons are shown in Appendix A. Results from testing the strand indicate that the strands yield at a microstrain of 8600. The strain-drift relationships for the tendons indicate that all of the strands were well below this value throughout testing. The maximum strain at each drift level for all strand strain gauges are shown in Table 4-15 and Table 4-16. Strain gauges 5, 8, 12, 19, and 24 were non-functional and are marked as "faulty" in the strain gauge tables. Strain gauge 6 was the only strain gauge from the strand to slip during testing and is marked as "slipped" at the corresponding location in the tables.

4.3.5   Moment Curvature Relationship

Column curvature was measured using Novotechnik displacement transducers. The instrumentation plan for column PT-HL was identical to that of column PT-LL (Figure 3-6). Equation 4.1 was used to calculate the average curvature over each gauge length. Moment-curvature hysteresis curves are shown in Figure 4-61 through Figure 4-65, where all of the figures are plotted with the same scale limits for ease of comparison and interpretation. A total of five layers were used to measure the column curvature. The first layer, termed "bond slip" was used to measure the column curvature with respect to the footing surface, and layers 1 through 4 were used to measure the curvature of that section. From the figures, it is evident that the majority of the column curvature was within the bond slip layer and layers 1 through 3. Layer 4 indicates nearly zero curvature, with peak values of 0.0006 $^{\text{rad.}}/_{\text{in}}$ (0.00002 $^{\text{rad.}}/_{\text{mm}}$), even at the maximum drift of 10% (Figure 4-61).

To summarize the moment-curvature results, the average height of each layer was plotted against the curvature at each drift level. For ease of interpretation, Figure 4-66 displays the column height vs. curvature for drifts 0.25% through 2%, and Figure 4-67 displays the column height vs. curvature for drifts 3% through 8%. These figures also show that nearly all column curvature took place at the bond slip and first three layer levels. Layer 4 shows nearly zero curvature for all drift levels.

4.4   PT-LL and PT-HL Response Comparison

4.4.1   General Observations

Figure 4-68 through Figure 4-72 display pictures of column PT-LL and column PT-HL throughout the experiment at various drift levels. In all of these figures, column

26

PT-LL is displayed on the left hand side and column PT-HL is displayed on the right hand side. The figures show damage for drifts of 3%, 4%, 5%, 6%, and 7%. Visible damage is greater in column PT-LL at 3% drift, and seems to be similar for drifts of 4%, 5%, and 6%. At 7% drift, a larger amount of longitudinal reinforcement is visible in PT-LL.

4.4.2   Cyclic Response

Effective yield displacement was greater for column PT-HL, resulting in a value of 1.42" (36.1 mm), compared to 0.95" (24.1 mm) for column PT-LL. Column displacement at first fracture was greater for column PT-HL, resulting in a value of 8.6" (218.4 mm), compared to 6.6" (167.6 mm) for column PT-LL. Ultimate column displacement capacity was also greater for column PT-HL, resulting in a value of 9.9" (251.5 mm), compared to 9.1" (231.1 mm) for column PT-LL. While calculating the displacement ductility capacities, column PT-LL had greater values than column PT-HL. The ductility at first fracture was 6.9 for column PT-LL, and 6.0 for column PT-HL. Ductility displacement capacity was 9.6 for column PT-LL, and 7.0 for column PT-HL. While the damage levels were greater for column PT-LL, especially at lower drift levels, the ductility capacities were also greater for column PT-LL.

4.4.3   Residual Displacement

Table 4-17 summarizes the residual displacement at each drift level for the two columns. The average residual displacements for the two cycles at each drift level for the positive side of the hysteresis curve are displayed under the positive table column. The average of the two cycles at each drift level for the negative side of the hysteresis curve is shown under the negative table column. The overall average residual displacement between the positive and negative sides of the hysteresis curve is shown under the average table column.

The results indicate that the uneven amount of cover concrete on column PT-LL significantly affected the residual displacements, as they vary greatly between the positive and negative side of the hysteresis curve. On the positive side of the hysteresis curve, the residual displacement is nearly equal between the two columns for drifts up to 1%. Beyond drifts of 1%, the residual displacement for column PT-HL steadily increases, to over double the residual displacement of column PT-LL at 7% drift. On the negative side of the hysteresis curve, residual displacements for drifts of 0.25% and 0.5% are identical for the two columns. For drifts of 1% to 6% the residual displacement in column PT-LL is greater than that of column PT-HL. At 7% drift, the residual displacement for column PT-LL is slightly less than that of column PT-HL. To make a reasonable comparison due to the uneven cover concrete of column PT-LL, the average residual displacement should be examined.

Average residual displacement of column PT-LL was slightly greater than or equal to the residual displacement of column PT-HL for drifts of 0.25% to 2%. For drifts of 3% to 7%, the average residual displacement for column PT-LL is less than that of column PT-HL, by as much as 1" (25.4 mm) at a drift of 7%. The normalized residual

displacement at 7% drift, taken as the ratio of the residual drift to the column displacement at 7% drift, is 39% for column PT-LL and 52% for the column PT-HL.

4.4.4   Moment Curvature Relationships

Moment curvature results indicate that nearly all of the column rotation took place near the column footing intersection for both columns. For each column, layer 4 was located at a height of 25" (635 mm) above the column footing intersection. At this location, the measured curvature at the largest drift was only 0.0006 $^{rad.}/_{in}$ (0.00002 $^{rad.}/_{mm}$) for each column. Moving down the column to the location of layer three at a height of 18" (457.2 mm) above the column footing intersection, the curvature was 0.0007 $^{rad.}/_{in}$ (0.00003 $^{rad.}/_{mm}$) for column PT-LL and 0.0023 $^{rad.}/_{in}$ (0.00009 $^{rad.}/_{mm}$) for column PT-HL. At layer 2 at a height of 11" (279.4 mm) above the column footing intersection, the curvature was 0.0019 $^{rad.}/_{in}$ (0.000075 $^{rad.}/_{in}$) for column PT-LL and 0.0027 $^{rad.}/_{in}$ (0.000011 $^{rad.}/_{in}$) for column PT-HL. These comparisons indicate substantially higher peak curvature in PT-HL than PT-LL throughout the 25" (635 mm) height above the footing. These results indicate that the higher longitudinal reinforcement ratio in PT-HL lead to a stronger section, and the post-tensioning force is not large enough for rigid rotation.

4.4.5   Post-Tensioning Forces

Table 4-18 displays the initial post-tensioning forces for each tendon for the two columns. Each tendon was to be stressed so that the final total tendon force would be equal to 10% of f'$_c$A$_g$. As shown in the table, the measured initial tendon force was 7.7% of f'$_c$A$_g$ for column PT-LL, and 9.6% of f'$_c$A$_g$ for column PT-HL. The stressing procedure described in section 2.4.2 was followed. It was difficult to achieve an identical overall tendon force between the two columns because the pressure gauge on the stressing jack was used to determine the overall force, and this is not the most accurate measurement. Variations in the steel shim size are most likely the cause of the difference in tendon forces between the two columns. If room had allowed, load cells between the bearing plates and anchor heads would have been the best source for measuring the force.

Table 4-19 displays the maximum tendon forces at each drift level. The values were taken from tendons 1 and 3, since these two displayed the highest forces from the four tendons. Each drift level alternates between tendon 1 and 3. For example, the push portion of each cycle displays the tendon force from tendon 1, since this tendon was located on the tension side of the column cross section for push cycles. The pull cycles display the tendon force from tendon 3, since this tendon was located on the tension side of the column cross section for pull cycles. The largest tendon force measured in column PT-HL (which was stressed closest to the specified initial tendon force of 10% f'$_c$A$_g$) was 147.2 kips (654.8 kN), corresponding to 169.6 ksi (1169.3 MPa). The yield stress of each tendon is 243 ksi (1675 MPa), and the measured maximum tendon stress of 169.6 ksi (1169.3 MPa), measured at 10% drift is right at 70% of the yield stress. This indicates that the initial tendon stress selected is very safe and will not yield the tendons, even at large drift ratios.

28

One tendon was removed from column PT-HL following testing, and is shown in Figure 4-73 and Figure 4-74. The tendon selected was one of the extreme tendons that experienced the most significant stresses. Column PT-HL was selected for tendon inspection because the tendons from PT-HL were initially stressed closer to the specified level compared to column PT-LL. As shown in the figure, the tendons experienced very minor damage at the location of the bend in the steel pipe following twenty cycles of various drift levels, all the way up to 10% drift. Only one of the four strands from the tendon inspected showed minor damage, all other strands were essentially unaffected.

CHAPTER 5

Analytical Model

5.1 Introduction

The analytical model was initially created to assist in the selection of test specimens. From the analytical model, projected column behavior, such as pushover response and residual displacements from cyclic loading could be analyzed to help select the test specimens. Once the experiment was complete, the analytical predictions were compared with the experimental results. The computer program SAP2000 was used to generate the analytical model. This chapter describes the modeling methods used, pushover analysis, cyclic analysis, tendon forces, and the analytical model validation with the experimental results.

5.2 Modeling Methods

Fiber models were used to model column PT-LL and PT-HL in the analytical model as shown in Figure 5-1 and Figure 5-2, respectively. Within the fiber models, the measured material data was used to define the steel and concrete properties. The fiber model for each column consisted of a cross section, divided into six sections in the radial direction, and twenty-four sections in the transverse direction. As shown in the figures representing the fiber models, the only difference between the two models is the longitudinal reinforcement. Each fiber within the section was modeled as either unconfined or confined concrete. The unconfined concrete stress-strain curved used in the model is shown in Figure 5-3, and the confined concrete stress-strain curve used in the model is shown in Figure 5-4. The confined concrete stress-strain curve was developed by Mander's model, which is a built-in feature in SAP2000. The original column models were created with a specified concrete strength of 4.5 ksi (31 MPa) for the unconfined concrete. This value was later changed to the measured concrete strengths (shown in Table 2-3) of each column following material testing.

Steel reinforcement properties were represented by a built-in model in SAP2000, as shown in Figure 5-5. The initial specimen steel reinforcement model utilized the default yield and ultimate stresses of 60 ksi (414 MPa) and 90 ksi (621 MPa), respectively. Following material testing, the model was modified by inserting the measured yield and ultimate stresses (shown in Table 2-2) for the steel reinforcement.

The two columns were modeled using nodes and frame elements. An elevation view of the analytical model is shown in Figure 5-6. The plastic hinge length was calculated using the California Department of Transportation Seismic Design Criteria (2006). The plastic hinge length equation is shown here as Equation 3-1, previously identified in Chapter 3 where it was used to determine instrumentation placement.

$$L_p = 0.08L + 0.15f_{ye}d_{bl} \geq 0.3f_{ye}d_{bl} \ \text{(in, ksi)} \qquad \text{Eqn. 3-1}$$

$$L_p = 0.08L + 0.022f_{ye}d_{bl} \geq 0.044f_{ye}d_{bl} \ \text{(mm, MPa)}$$

L_p = plastic hinge length, in (mm)

L = column length, in (mm)

f_{ye} = yield stress of the longitudinal reinforcing bar, ksi (MPa)

d_{bl} = diameter of one longitudinal reinforcing bar, in (mm)

Plastic hinge length for column PT-LL and PT-HL was calculated as 14.3" (363 mm) and 16.5" (419 mm), respectively. Once the plastic hinge length was established, a frame element with fiber hinge properties was inserted into the model over the plastic hinge length. Another frame element was then attached to the top of the fiber hinge and extended along the height of the column, to the location of horizontal actuator force (a height of 108" (2743 mm), including the plastic hinge length). The overall column height was the same for each specimen, 108" (2743 mm), including the difference in plastic hinge length between the two. The base of the fiber hinge, also the location of the base of the column, was assigned a fixed constraint. A vertical force at the top of the column was assigned as the axial dead load. The dead load was specified at 0.06 of the axial load index, defined earlier in Chapter 4, resulting in a force of 122 kips (543 kN).

Post-tensioned tendons were modeled using link elements. Figure 5-6 shows two of the tendons. The other two are in line with the element representing the column itself and are not shown for clarity. The parameters used to model the link elements were force and displacement. The measured stress-strain curve for the 7-wire 270 ksi (1862 MPa) strand was used to calculate the force-displacement curve for the link elements. The stress was multiplied by the area of one tendon, 0.868 in^2 (560 mm^2) to obtain the force, and the strain was multiplied by the length of one tendon, 200" (5080 mm) to obtain the displacement. A link element was then placed at the tendon location within the model. The tendons began below the fixity representing the base of the column, at the approximate location of the start of the bend in the steel pipe, located 5" (127 mm) below the column-footing interface. The tendons continued along the length of the column and were anchored at the location of the top of the loading head. A body constraint was then used to connect the top of the column with the end of the four tendons, to insure that the tendons and column moved together as one unit.

To initially stress the tendons (link elements), a frame element was created and referred to as a "Tendon Bar" in the model (see Figure 5-6). The tendon bar was connected between the base of each tendon, and a point 25" (635 mm) below the footing. The base of this frame element was assigned a pinned constraint. To apply the initial prestress force to the link element, the tendon bar was assigned a negative deformation in the axial direction. To insure that the tendon bar would not elongate after the initial deformation was specified, the area property modifier was greatly increased, producing a very high axial stiffness.

5.3   Pushover Analysis

A pushover analysis was used to investigate the peak lateral force and displacement each column would undergo. Tendon forces and stresses could also be

monitored, and more specifically the displacement at which point the tendons would yield. Prior research had shown that finite element models tend to over predict tendon forces, so predicted tendon forces that were close to or at the yield point were not considered a high risk.

Figure 5-7 and Figure 5-8 display the calculated pushover curve for column PT-LL and PT-HL, respectively. The measured material properties were used in the analysis (see Table 2-2 and Table 2-3). As described in Chapter 4, concrete cover was uneven in PT-LL. This specimen was modified, adjusting the fiber element representing the column cross section to correlate with the actual dimensions of the tested column. The modified pushover response is shown in Figure 5-9. The modified pushover response of column PT-LL was taken as the average of the positive and negative envelope of the hysteresis, described in further detail in section 5.3.2, and shown in Figure 5-12. A more detailed account of the modeling method used for the modified pushover response of PT-LL will also be discussed in greater detail in section 5.3.2.

5.3.1   Pushover Validation with Experimental Results

5.3.2   Column PT-LL

Column PT-LL was constructed with a rebar cage of a diameter 1" (25.4 mm) smaller than specified. The smaller rebar cage was found to be off-center in the plastic hinge region during testing, resulting in 2" (50.8 mm) of cover concrete on the west side of the column, and 1" (25.4 mm) of cover concrete on the east side of the column. Due to the uneven concrete cover, the calculated analytical model pushover curve showed large differences against the measured pushover curve as shown in Figure 5-10. A second analytical model representing column PT-LL was created to better characterize the specimen.

The second analytical model was developed with cover concrete (unconfined concrete) to match the tested specimen. Additionally, the five longitudinal reinforcing bars on the west side of the column were moved in closer to the core of the column, representing the actual specimen. These modifications to the analytical model displayed similar pushover results to that of the specimen. Figure 5-11 displays the positive and negative envelopes from the measured hysteresis curve. Figure 5-12 displays the modified calculated positive and negative envelopes from the hysteresis curve. From these two figures, it can be seen that the positive and negative envelopes begin to deviate from each other near a displacement of 2" (51 mm), for both the calculated and measured results. Figure 5-13 and Figure 5-14 display the positive measured and calculated response, and the negative measured and calculated response, respectively. The modified calculated analytical model displays more accurate results when the positive and negative envelopes are averaged and plotted with the measured average pushover response, as shown in Figure 5-15.

The original calculated analytical model of column PT-LL compared to the measured results, displayed a maximum difference in lateral force of 10.7 kips (47.6 kN). The original analytical model maximum lateral force was 63.7 kips (283.4 kN), compared to the measured maximum lateral force of 53.4 kips (237.5 kN). The modified calculated analytical model compared to the measured results displays a maximum difference in

32

lateral force of nearly half of the original analytical model comparison, with a maximum difference in peak lateral force of 5.3 kips (23.6 kN). The modified analytical model maximum lateral force was 50.3 kips (223.7 kN), compared to the measured maximum lateral force of 53.4 kips (237.5 kN).

5.3.3   Column PT-HL

The calculated and measured pushover results for PT-HL are shown in Figure 5-16. The calculated pushover curve displays very similar results to the measured pushover curve. In both cases, the column begins to yield near the same point, shows a peak force at similar displacements, and has a lateral force difference of less than 5 kips (22 kN) at peak force. This model appears to be more accurate than PT-LL, even though identical modeling methods were used. Most likely, the cause of the difference is because PT-LL did not have symmetrical cover concrete.

5.4   Cyclic Load Analysis

A cyclic displacement history identical to the cyclic loading protocol presented in Chapter 3 was used in the analytical model to estimate energy dissipation and residual displacements. Positive and negative lateral loads were created in the model. These lateral loads were then assigned as forces near the top of the column at the location of the horizontal actuator force, 108" (2743 mm) above the base of the column. To create a displacement controlled analysis, each load case was assigned a displacement according to the loading protocol. To reach the specified positive or negative displacement, the positive and negative loads assigned near the top of the column were used to push and pull the column.

The analytical hysteresis curves of column PT-LL and PT-HL are shown in Figure 5-17 and Figure 5-18, respectively. Cyclic loading was created by first assigning a load case called push 1 with a positive lateral load located at the top of the column. Push 1 was applied following the application of the axial dead load and initial tendon force, which were both assigned to the dead load load case. Load case push 1 was the first step in the loading protocol, pushing the column out to a displacement of 0.27" (6.9 mm), or 0.25% drift. The next load case was called push 2, which applied a negative lateral load at the top of the column to pull the model to a displacement of -0.27" (-6.9 mm), or -0.25% drift, following push 1. This sequence continued through the cyclic loading protocol up to 10% drift.

Residual displacements from the analytical model of column PT-LL and PT-HL were measured and recorded in Table 5-1 and Table 5-2, respectively. The tables display the residual displacement from the positive and negative side of the hysteresis curve, as well as the average residual displacement between the two following the first cycle at each drift level. These values were recorded as the column displacement at zero force, following the first push and first pull at each load cycle. The first push and pull at each cycle was used for the residual displacement comparison between the analytical and experimental results.

Tendon forces from column PT-LL and PT-HL at the peak push and pull displacement during the first cycle of each drift ratio were recorded from the analytical

model and are shown in Table 5-3 and Table 5-4, respectively. These tendon forces were compared with the experimental first push and pull at each cycle. The tendon forces were found by averaging the measured strains recorded by the strain gauges from each strand. The average strain was multiplied by the measured strand modulus of elasticity and the strand area to obtain the tendon force.

5.4.1   Comparison of Measured and Calculated Cyclic Load Results

5.4.2   Column PT-LL

Hysteretic behavior of the modified calculated analytical model was superimposed over the measured results and is shown in Figure 5-19. The modified calculated analytical model shows similar forces to the measured results, specifically on the negative side of the hysteresis curve. The calculated forces do not quite reach the measured forces on the positive side of the hysteresis curve. Average residual displacements for drifts up to 7% are very similar between the calculated and measured results and are shown in Table 5-5. The largest difference in residual displacement between the calculated and measured results is only 0.48" (12.19 mm) at a drift of 7%, corresponding to 16.3% difference. The calculated column forces and residual displacements matched closely with measured results.

Measured tendon forces were monitored throughout testing and are compared with the calculated tendon forces in Table 5-6. The tendon forces show close correlation for small drift ratios. For drift ratios through 2%, the maximum difference between the measured and calculated tendon forces is less than 10%. As the drift ratio increases, the tendon force difference between the measured and calculated results also increases. At maximum horizontal load, the difference in the analytical and experimental tendon force was less than 15%. Note that the specimen reached its peak load at 6.1% drift, and was at 80% of its peak load at 8.4% drift. Considering these values, the difference between the calculated and measured tendon forces were less than 25% throughout the ultimate capacity of the column.

5.4.3   Column PT-HL

The calculated hysteretic response was plotted with the measured hysteretic response in Figure 5-20. The calculated force envelope follows nearly exactly that of the calculated force envelope. It can be seen that the residual displacements are also very close, especially for smaller drift ratios. Average calculated residual displacements for drifts up to 7% were recorded and compared with the measured residual displacements in Table 5-7. The results in the table show a very close correlation of the maximum difference between the calculated and measured residual displacements, where the maximum difference is 0.69" (17.53 mm) occurring at a drift of 4%, corresponding to 46% difference.

Measured tendon forces were monitored throughout testing and compared with the calculated tendon forces in Table 5-8. The difference between the calculated and measured tendon force is minimal for small drifts through 2%, where the difference between forces is less than 10%. As the drift ratio increases, differences between the

calculated and measured tendon forces also increase. At maximum horizontal load, the difference in the analytical and experimental tendon force was less than 35%. Note that the specimen reached its peak load at 7.1% drift, and was at 80% of its peak load at 9.1% drift. Considering these values, the difference between the calculated and measured tendon forces was less than 36% throughout the ultimate capacity of the column. This difference at ultimate capacity for PT-HL is higher than the maximum difference of PT-LL, most likely because the initial tendon force in this column was higher. The calculated and measured results of column PT-HL show close correlation.

CHAPTER 6

Parametric Study

6.1   Introduction

A parametric study was conducted using the prototype column to determine the full-scale behavior. The basic geometric properties of the two columns, PT-LL and PT-HL, were used as the basis for this study. The same loading protocol as the scaled models was used to investigate the pushover response, hysteretic behavior, residual displacements, and tendon stresses at various drift levels. An initial base model was created to make comparisons with the scaled results. A parametric study was then conducted, investigating changes in axial load, initial post-tensioning forces, concrete strength, tendon location, and the longitudinal reinforcement ratio.

6.2   Prototype Modeling

6.2.1   Introduction

A column model was created following the prototype dimension. The prototype dimensions resulted in a column of 60" (1524 mm) diameter with a height of 270" (6858 mm). Grade 60 ksi (414 MPa) steel was used for both longitudinal and transverse reinforcement. Column PT-LL longitudinal reinforcement consisted of 12-#11's resulting in a reinforcement ratio of 0.66%, and column PT-HL longitudinal reinforcement consisted of 24-#11's resulting in a reinforcement ratio of 1.32%. Unconfined concrete strength was set a 4500 psi (31 MPa). Axial dead load was maintained at 6% of the axial load index (defined in Chapter 2), resulting in a value of 763 kips (3394 kN). Initial tendon force was set at 10% of the axial load index (ALI), resulting in a total force of 1272 kips (5658 kN), or 318 kips (1415 kN) in each of the four tendons. Referring back to section 2.2 of Chapter 2, in order to maintain an initial tendon stress of 21.7% of f_{pu}, one hundred strands would be needed to fulfill this requirement. Therefore, twenty-five strands were used at each of the four tendon locations, resulting in a single tendon area of 5.43 in^2 (3503 mm^2), and an area of 21.72 in^2 (14012 mm^2) for all four tendons.

6.2.2   Pushover Response

The pushover responses of column PT-LL and PT-HL are shown in Figure 6-1 and Figure 6-2. Each column was pushed to a drift of 10%, similar to each scaled column specimen. Since the column height of the prototype models was 270" (6858 mm), a drift of 1% corresponded to a displacement of 2.7" (68.6 mm). Column PT-LL reached a peak force of 350 kips (1557 kN) at a displacement of 13.05" (332 mm), corresponding to 4.8% drift. Column PT-HL reached a peak force of 435 kips (1935 kN) at a displacement of 13.5" (343 mm), corresponding to 5% drift. The ultimate force and displacement of column PT-LL, defined as the force and displacement at 80% of the peak force, was 280 kips (1246 kN) and 19.9" (506 mm), respectively. The ultimate force and displacement for column PT-HL was 348 kips (1548 kN) and 22.5" (572 mm), respectively.

36

6.2.3   Hysteretic Response

The hysteretic responses of column PT-LL and PT-HL are shown in Figure 6-3 and Figure 6-4. The figures reflect behavior for cycles through 8% drift. The residual displacements for column PT-LL and PT-HL were measured during the first cycle at each drift level, and are shown in Table 6-1 and Table 6-2. Residual displacements from the positive and negative sides of the hysteresis curve are presented in the tables, as well as the average. Column PT-LL shows strong re-centering capabilities, with a residual displacement of 0.94" (23.88 mm) at 4% drift, and a residual displacement of 11.80" (299.72 mm) at 8% drift. These calculated residual displacements correspond to 8.7% of the lateral drift at 4% drift, and 54.6% of the lateral drift at 8% drift. Column PT-HL showed a residual displacement of 4.53" (115.16 mm) at 4% drift, and a residual displacement of 16.47" (418.25 mm) at 8% drift. These calculated residual displacements correspond to 41.9% of the lateral drift at 4% drift, and 76.3% of the lateral drift at 8% drift. Similar to the scaled models tested, the longitudinal reinforcement ratio plays a significant role in re-centering capabilities.

6.2.4   Tendon Stresses

Tendon forces were measured in the model throughout the cyclic motion. The forces were converted to stresses based on the area of each prototype tendon, 5.43 in^2 (3500 mm^2), and are presented in Table 6-3 and Table 6-4 for columns PT-LL and PT-HL, respectively. The table displays the largest tendon stress following each push-pull cycle. All values in the table corresponding to push cycles (positive), are recorded from tendon 1, and all values in the table corresponding to pull cycles (negative), are recorded from tendon 3. This approach was taken for ease of comparison with results presented in Chapter 4. All tendon stresses in this chapter are presented in this manner. Tendons do not begin to yield until a stress of 243 ksi (1675 MPa) is reached. From the tables, it can be seen that all tendon stresses were kept below the yield stress.

6.2.5   Comparison with Scaled Model

The pushover and hysteretic behavior of each column follows a very similar trend to the results presented in Chapters 4 and 5. Tendon stresses are also very close to the scaled model results, but do show small differences. The scaled analytical tendon stresses are higher than the prototype analytical stresses, indicating that the model is sensitive to tendon length. As presented in Chapter 5, the analytical model over predicted the tested tendon stresses by up to 25% for column PT-LL, and 34% for column PT-HL, through drifts of 7%. The difference between the two tested specimens is caused by different initial tendon forces. Column PT-LL had an initial tendon force of 7.7% of the ALI, and column PT-HL had an initial tendon force of 9.6% of the ALI. The prototype models presented within this section display tendon stresses slightly lower than that of the scaled analytical models, bringing them closer to the measured stresses. The scaled stresses of column PT-LL and PT-HL were 167.7 ksi (1156.3 MPa) and 168.5 ksi (1161.8 MPa),

respectively, at 7% drift. The prototype stresses of column PT-LL and PT-HL were 166.1 ksi (1145.3 MPa) and 165.5 ksi (1141.1 MPa), respectively, at 7% drift.

With close correlation between the scaled and prototype analytical models, a parametric study was conducted. The following sections in this chapter report the prototype behavior when the axial load, initial post-tensioning force, concrete strength, and tendon location is varied, while all other parameters are held constant. Table 6-5 shows the values used in each parametric study. Study I investigated the axial dead load by varying the axial dead load from the original value of 6% of the ALI, to 10%, 15%, and 20% of the ALI. Study II investigated the initial post-tensioning force by varying the original initial force of 10% of the ALI, to 15% and 20% of the ALI. Study III investigated the concrete strength by increasing the concrete strength to 10 ksi (69 MPa). In study III, the axial dead load and initial post-tensioning force were increased according to the ALI. The original axial dead load of 6% of f'$_c$A$_g$ was 763 kips (3396 kN), and the initial post-tensioning force of 10% of f'$_c$A$_g$ was 1272 kips (5660 kN). By increasing the concrete strength from 4.5 ksi (31 MPa) to 10 ksi (69 MPa), this lead to an axial dead load of 6% of f'$_c$A$_g$ equal to 1696 kips (7546 MPa), and an initial post-tensioning force of 10% f'$_c$A$_g$ equal to 2827 kips (12577 MPa). Study III' is an additional study on the concrete strength, where the axial dead load and initial post-tensioning force were held at the original values of 763 kips (3396 kN), and 1272 kips (5660 kN), respectively. Study IV investigated the tendon location with respect to column diameter. The original tendon location was set at 22.5% of the column diameter, resulting in a value of 13.5" (343 mm) out from the center of the column cross section. The fourth study investigated increasing this value to 30% of the column diameter, resulting in a location of 18" (457 mm) out from the center of the column cross section. The fifth and final study investigated a decrease in the longitudinal reinforcement ratio to 0.34%. The results are summarized in the following sections, and recommendations are presented at the end of the chapter based on the parametric study.

6.3   Axial Dead Load

6.3.1   Introduction

The axial dead load of the scaled and prototype columns was set at 6% of the ALI. In practice, the ALI can have a wide range of values, and therefore was investigated in the parametric study. Parametric study I investigated varying the axial dead load from the tested 6%, to 10%, 15%, and 20% of the ALI. The pushover and hysteretic responses are presented in this section, along with residual displacements and tendon stresses.

6.3.2   Pushover Response

The pushover response for column PT-LL and PT-HL with a dead load of 10%, 15%, and 20% of the (ALI) are shown in Figure 6-5, Figure 6-6, Figure 6-7, Figure 6-8, Figure 6-9, and Figure 6-10, respectively. As the axial dead load increased, the column displacement at the peak lateral force decreased. The peak lateral force and corresponding displacement of column PT-LL and column PT-HL with a dead load of 10% of the ALI was 359 kips (1597 kN) at 12.6" (320 mm), and 444 kips (1975 kN) at

38

12.2" (310 mm), respectively. Peak lateral force and corresponding displacement of column PT-LL and PT-HL with a dead load of 15% of the ALI was 371 kips (1650 kN) at 11.3" (287 mm), and 456 kips (2028 kN) at 11.3" (287 mm), respectively. Peak lateral force and the corresponding displacement of column PT-LL and PT-HL with a dead load of 20% of the ALI is 384 kips (1708 kN) at 10.4" (264 mm), and 467 kips (2077 kN) at 11.3" (287 mm), respectively. The original prototype columns, PT-LL and PT-HL, with a dead load of 6% of the ALI showed the best performance. Column PT-LL and PT-HL reached the largest displacement at peak lateral force, resulting in values of 13.5" (343 mm) at 350 kips (1557 kN), and 13.1" (333 mm) at 435 kips (1935 kN), respectively.

6.3.3   Hysteretic Response

        The hysteretic responses of column PT-LL and PT-HL with a dead load of 10%, 15%, and 20% of the ALI are shown in Figure 6-11, Figure 6-12, Figure 6-13, Figure 6-14, Figure 6-15, and Figure 6-16, respectively. As the dead load increased from the original prototype value of 6% of the ALI, the column capacity decreased. The original prototype columns were able to withstand cyclic loading through 8% drift. Each increase of axial dead load resulted in failure at lower drifts. At a dead load of 10% of the ALI, columns PT-LL and PT-HL failed after cycles of 7% drift. At a dead load of 15% of the ALI, columns PT-LL and PT-HL failed after cycles of 5% and 6% drift, respectively. At a dead load of 20% of the ALI, columns PT-LL and PT-HL failed after cycles of 5% and 6% drift, respectively.
        Residual displacements for column PT-LL and PT-HL at 10%, 15%, and 20% of the ALI are presented in Table 6-6, Table 6-7, Table 6-8, Table 6-9, Table 6-10, and Table 6-11, respectively. The tables show a large impact on residual displacement as the ALI increases. A drift level of 5% will be used for comparison purposes, since all columns made it to this drift level. Column PT-LL had a residual displacement of 1.75" (44.45 mm) at 5% drift for the original prototype model with an ALI of 6%. The residual displacement at 5% drift increases as the ALI increases to 10%, 15%, and 20%, to residual displacements of 2.22" (56.39 mm), 3.41" (86.69 mm), and 5.76" (146.36 mm), respectively. Column PT-HL had a residual displacement of 6.43" (163.44 mm) at 5% drift for the original prototype model with an ALI of 6%. The residual displacement at 5% drift increases as the ALI increases to 10%, 15%, and 20%, to residual displacements of 6.45" (163.80 mm), 6.63 (168.45 mm), and 7.90" (200.59 mm), respectively. The original prototype columns with a dead load of 6% of the ALI showed the best performance, both in capacity and residual displacement.

6.3.4   Tendon Stresses

        Tendon stresses from column PT-LL and PT-HL with an axial dead load of 10%, 15%, and 20% of the ALI are presented in Table 6-12, Table 6-13, Table 6-14, Table 6-15, Table 6-16, and Table 6-17, respectively. Tendons do not begin to yield until a stress of at least 243 ksi (1675.5 MPa) is reached. For all cases presented in this section, the tendons do not yield during the cyclic loading. In each case of increasing the dead load, the tendon stress decreases. For comparison purposes, tendon stresses at 5% drift will be examined. Tendon stresses for column PT-LL with a dead load of 10%, 15%, and

20% of the ALI, resulted in tendon stresses of 147.7 ksi (1018.7 MPa), 137.8 ksi (950.4 MPa), and 121.4 ksi (837.1 MPa), respectively. Tendon stresses for column PT-HL with a dead load of 10%, 15%, and 20% of the ALI, resulted in tendon stresses of 143.9 ksi (992.2 MPa), 136.9 ksi (943.7 MPa), and 124.8 ksi (860.2 MPa), respectively. The only benefit of increasing the axial deal load in the first parametric study is the decrease in tendon stresses.

6.4 Initial Post-Tensioning Force

6.4.1 Introduction

The initial post-tensioning force in the scaled and prototype columns was set at 10% of the ALI. Parametric study II investigated increasing the initial post-tensioning force from 10%, up to 15% and 20% of the ALI. Pushover and hysteretic behavior is presented in this section, along with residual displacements and tendon stresses throughout testing.

6.4.2 Pushover Response

The pushover response for columns PT-LL and PT-HL with an initial post-tensioning force of 15% and 20% of the ALI are presented in Figure 6-17, Figure 6-18, Figure 6-19, and Figure 6-20, respectively. As the initial post-tensioning force increased, the displacement at the peak lateral force decreased. The peak lateral force and corresponding displacement of column PT-LL and PT-HL with an initial tendon force of 15% of the ALI was 363 kips (1615 kN) at 12.6" (320.0 mm), and 446 kips (1984 kN) at 12.2" (309.9 mm), respectively. Peak lateral force and corresponding displacement of column PT-LL and PT-HL with an initial tendon force of 20% of the ALI was 374 kips (1664 kN) at 10.4" (264.2 mm), and 458 kips (2037 kN) at 11.3" (287.0 mm), respectively. Similar to the axial load parametric study, the original prototype columns showed the best performance. The original prototype columns; PT-LL and PT-HL, showed a peak lateral force and displacement of 350 kips (1557 kN) at 13.5" (342.9 mm), and 435 kips (1935 kN) at 13.1" (332.7 mm), respectively.

6.4.3 Hysteretic Response

The hysteretic response of columns PT-LL and PT-HL with an initial post-tensioning force of 15% and 20% of the ALI are presented in Figure 6-21, Figure 6-22, Figure 6-23, and Figure 6-24, respectively. Similar to the axial dead load parametric study, as the initial post-tensioning force increases, the columns hysteretic capacity decreases. The original prototype columns were able to withstand cyclic loading through drifts of 8%. At an initial post-tensioning force of 15% of the ALI, column PT-LL fails after drifts of 7%, while column PT-HL was able to undergo drifts of 8%. At an initial post-tensioning force of 20% of the ALI, column PT-LL and PT-HL both failed following drifts of 6%.

Residual displacements of column PT-LL and PT-HL from cases with an initial post-tensioning force of 15% and 20% of the ALI are presented in Table 6-18, Table

6-19, Table 6-20, and Table 6-21, respectively. The tables show a significant impact on residual displacement as the initial post-tensioning force increases from 10% of the ALI to 15% and 20% of the ALI. A drift level of 5% will be used for discussion comparison purposes. Column PT-LL had a residual displacement of 1.75" (44.45 mm) at 5% drift for the original prototype model with an initial post-tensioning force of 10% of the ALI. The residual displacement at 5% drift increases as the initial post-tensioning force increases to 15% and 20% of the ALI, to residual displacements of 2.46" (62.48 mm), and 3.67" (93.22 mm), respectively. Column PT-HL had a residual displacement of 6.43" (163.44 mm) at 5% drift for the original prototype model with an initial post-tensioning force of 10% of the ALI. The residual displacement at 5% drift slightly decreases to 6.37" (161.80 mm) with an initial post-tensioning force of 15% of the ALI, and increases to a residual displacement of 6.65" (168.91 mm) with an initial post-tensioning force of 20% of the ALI. Comparing all drift levels at each initial post-tensioning force gives a better perspective of the residual displacement capabilities of each column. For column PT-LL, the lowest residual displacements all occurred when the initial post-tensioning force was set at 10% of the ALI. For column PT-HL, the lowest residual displacements through 4% drift all occurred with an initial post-tensioning force of 20% of the ALI. At 5% drift, the lowest residual displacement occurred with an initial post-tensioning force of 15% of the ALI. Drifts of 6% and greater showed the lowest residual displacements with an initial post-tensioning force of 10% of the ALI.

The original prototype columns with an initial post-tensioning force of 10% of the ALI showed the beast all-around performance, both in capacity and residual displacement. Column PT-HL showed lower residual displacements with an increase in the initial post-tensioning force at lower drift levels, but residual displacements quickly increased at drifts beyond 4%. The increased initial post-tensioning force decreases each columns capacity, especially column PT-LL, developing higher levels of damage at lower drift levels, and therefore increases residual displacements.

6.4.4   Tendon Stresses

Tendon stresses from column PT-LL and PT-HL with an initial post-tensioning force of 15% and 20% of the ALI are presented in Table 6-22, Table 6-23, Table 6-24, and Table 6-25, respectively. Tendons do not begin to yield until a stress of at least 243 ksi (1675.5 MPa) is reached. For all cases presented in this section, the tendons do not yield during the cyclic loading. For comparison purposes, tendon stresses at 5% drift will be examined. Tendon stresses for column PT-LL with an initial post-tensioning force of 15% and 20% of the ALI, resulted in tendon stresses of 175.0 ksi (1206.8 MPa), and 191.8 ksi (1322.4 MPa), respectively. Tendon stresses for column PT-HL with an initial post-tensioning force of 15% and 20% of the ALI, resulted in tendon stresses of 172.4 ksi (1188.5 MPa), and 191.7 ksi (1321.8 MPa), respectively. The only benefit of increasing the initial post-tensioning force in the second parametric study is the slight increase in lateral force in the pushover curve. However, the displacement corresponding to the peak lateral force in the pushover curve decreases from the original prototype model for both columns.

6.5   Concrete Strength

6.5.1   Introduction

Concrete strength in the scaled and prototype columns was set at 4.5 ksi (31 MPa). In practice, this value can take on a wide range of values. Parametric study III and III' investigated the behavior of the columns where the concrete strength was increased to 10 ksi (69 MPa). As mentioned in section 6.2.5, parametric study III focuses on column behavior with an increase in concrete strength and corresponding axial dead load and initial post-tensioning force due to the concrete strength effect on the ALI. Parametric study III' focuses on increasing only the concrete strength in each column, and leaving the axial dead load and initial post-tensioning force at the same values of the original prototype columns. Pushover and hysteretic responses are presented in this section, along with residual displacements and tendon stresses throughout cyclic loading.

6.5.2   Pushover Response

The pushover response of columns PT-LL and PT-HL with a concrete strength of 10 ksi (69 MPa) for parametric study III are presented in Figure 6-25, and Figure 6-26, respectively. Pushover responses of column PT-LL and PT-HL with a concrete strength of 10 ksi (69 MPa) for parametric study III' are presented in Figure 6-27, and Figure 6-28, respectively. As previously stated, the difference between parametric study III and III', is that study III follows an ALI corresponding to the increase in f'$_c$, and study III' follows an ALI according to the original prototype. As the concrete strength, axial dead load, and initial post-tensioning force increased in study III, the displacement at the peak lateral force decreased. The peak lateral force and corresponding displacement of column PT-LL and PT-HL with a concrete strength of 10 ksi (69 MPa) was 542 kips (2411 kN) at 8.6" (218.4 mm), and 622 kips (2766 kN) at 8.6" (218.4 mm), respectively. As only the concrete strength increased in study III', the displacement at peak force increased. Peak lateral force and corresponding displacement of column PT-LL and PT-HL with an increase in concrete strength was 411 kips (1828 kN) at 15.3" (388.6 mm), and 505 kips (2244 kN) at 13.5" (342.9 mm), respectively. The original prototype columns; PT-LL and PT-HL, showed a peak lateral force and displacement of 350 kips (1557 kN) at 13.5" (342.9 mm), and 435 kips (1935 kN) at 13.1" (332.7 mm), respectively. Parametric study III did not show any advantages of increasing the concrete strength, axial dead load, and initial post-tensioning force. Parametric study III' did show performance improvements from the original prototype columns, increasing the column displacement at peak lateral force from 13.5" (342.9 mm) to 15.3" (388.6 mm) for column PT-LL, and 13.1" (332.7 mm) to 13.5" (342.9 mm) for column PT-HL.

6.5.3   Hysteretic Response

The hysteretic response of columns PT-LL and PT-HL from parametric study III, with an increase in concrete strength, axial dead load, and initial post-tensioning force are presented in Figure 6-29, and Figure 6-30, respectively. Hysteretic responses of column PT-LL and PT-HL from parametric study III', where only the concrete strength was

increased, is presented in Figure 6-31, and Figure 6-32, respectively. The original prototype columns were able to withstand cyclic loading through drifts of 8%. Column PT-LL and PT-HL from parametric study III both failed following drifts of 6%. Column PT-LL and PT-HL from parametric study III' were able to withstand the same cyclic loading used with the original prototype columns, maintaining capacity through 8% drift.

Residual displacements of column PT-LL and PT-HL from parametric study III are presented in Table 6-26, and Table 6-27, respectively. Residual displacements of column PT-LL and PT-HL from parametric study III' are presented in Table 6-28, and Table 6-29, respectively. The tables show a significant impact on residual displacement from the increase in concrete strength. A drift level of 5% will be used for discussion comparison purposes. Column PT-LL had a residual displacement of 1.75" (44.45 mm) at 5% drift for the original prototype model with a concrete strength of 4.5 ksi (31 MPa). The residual displacement at 5% drift increased in parametric study III to a residual displacement of 2.37" (60.24 mm). Residual displacement for column PT-LL in parametric study III' showed an improvement, decreasing to 1.68" (42.79 mm). Column PT-HL had a residual displacement of 6.43" (163.44 mm) at 5% drift for the original prototype model with a concrete strength of 4.5 ksi (31 MPa). The residual displacement at 5% drift in parametric study III, decreased to a residual displacement of 4.30" (109.33 MPa). Residual displacement for column PT-HL in parametric study III' also showed an improvement, decreasing to a residual displacement to 4.57" (116.08 MPa). Column PT-LL and PT-HL both show all-around reductions in residual displacement from an increase in concrete strength.

6.5.4   Tendon Stresses

Tendon stresses from column PT-LL and PT-HL from parametric study III were calculated and are presented in Table 6-30, and Table 6-31, respectively. Tendon stresses from column PT-LL and PT-HL in parametric study III' (increased concrete strength only) are presented in Table 6-32, and Table 6-33, respectively. Tendons do not begin to yield until a stress of at least 243 ksi (1675.5 MPa) is reached. For all cases presented in this section, the tendons do not yield during the cyclic loading. For discussion comparison purposes, tendon stresses at 5% drift from the tables will be examined. Tendon stresses for column PT-LL and PT-HL in parametric study III, resulted in tendon stresses of 170.9 ksi (1178.1 MPa), and 166.0 ksi (1144.6 MPa), respectively. Tendon stresses for column PT-HL in parametric study III', resulted in tendon stresses of 137.2 ksi (946.2 MPa), and 137.7 ksi (949.3 MPa), respectively. The original prototype columns, PT-LL and PT-HL, resulted in stresses of 154.4 ksi (1064.6 kN) and 149.9 ksi (1033.4 kN), respectively. There is no tendon stress benefit from parametric study III, as the tendon stresses increased in the study. However, parametric study III' presents several benefits; tendon stresses decrease in each column compared to the original prototype columns, residual displacements decrease in each column, and column displacement at peak force increased in each column.

6.6   Tendon Location

6.6.1   Introduction

Tendon location in the scaled and prototype columns was set at 22.5% of the column cross section diameter, resulting in a location 13.5" (343 mm) out from the center of the column cross section. This value was initially chosen as the closest location the four tendons could be placed to the center of the column cross section. For parametric study IV, the four tendons were moved out to a location of 30% of the diameter of the column cross section. This resulted in a location 18" (457 mm) out from the center of the column cross section. The pushover and hysteretic behavior, as well as residual displacements and tendon stresses throughout cyclic loading are presented in this section.

6.6.2   Pushover Response

The pushover responses of columns PT-LL and PT-HL, with four tendons located at 30% of the column diameter, are presented in Figure 6-33, and Figure 6-34, respectively. As the tendon location out from the center of the column cross section increased, the displacement at the peak lateral force slightly increased. The peak lateral force and corresponding displacement of column PT-LL and PT-HL with a tendon location of 30% of the column diameter was 372 kips (1655 kN) at 14.0" (356 mm), and 459 kips (2042 kN) at 14.0" (356 mm), respectively. The original prototype columns; PT-LL and PT-HL, showed a peak lateral force and displacement of 350 kips (1557 kN) at 13.5" (342.9 mm), and 435 kips (1935 kN) at 13.1" (332.7 mm), respectively.

6.6.3   Hysteretic Response

The hysteretic response of columns PT-LL and PT-HL, with four tendons located at 30% of the column diameter, are presented in Figure 6-35, and Figure 6-36, respectively. The original prototype columns were able to withstand cyclic loading through drifts of 8%. Increasing the tendon location reduced the cyclic capacity of column PT-LL, producing failure following 7% drift. Column PT-HL was able to withstand cyclic loading through drifts of 8%.

Residual displacements of column PT-LL and PT-HL from the change in tendon location are presented in Table 6-34, and Table 6-35, respectively. The tables show a small impact on residual displacement as the tendon location out from the center of the column cross section is increased. A drift level of 5% will be used here for discussion comparison purposes. Column PT-LL and PT-HL had a residual displacement of 1.75" (44.45 mm) and 6.43" (163.44 mm) at 5% drift for the original prototype models, respectively. The residual displacement at 5% drift for each column decreased as the tendon location out from the center of the column cross section was increased to 30% of the column diameter. Column PT-LL and PT-HL showed residual displacements of 1.57" (39.86 mm), and 5.71" (145.05 mm), respectively. Increasing the distance out from the center of the column cross section shows an improvement by slightly reducing the residual displacements.

44

6.6.4 Tendon Stresses

Tendon stresses from column PT-LL and PT-HL were calculated from the models with an increased distance out from the center of the column cross section to each tendon and are presented in Table 6-36 and Table 6-37, respectively. Tendons do not begin to yield until a stress of at least 243 ksi (1675.5 MPa) is reached. For all cases presented in this section, the tendons do not yield during the cyclic loading, although they do become very close. For discussion comparison purposes, tendon stresses at 5% drift will be examined. Tendon stresses from column PT-LL and PT-HL with an increased tendon location resulted in stresses of 174.0 ksi (1199.7 kN) and 169.5 ksi (1168.5 kN), respectively. The original prototype columns; PT-LL and PT-HL, showed tendon stresses at 5% drift of 154.4 ksi (1064.6 kN) and 149.9 ksi (1033.4 kN). Increasing the distance of the tendon location from the center of the column cross section shows benefits in re-centering capabilities, but results in tendon stresses that are very close to the yield stress.

6.7   Extra Low Longitudinal Reinforcement

6.7.1 Introduction

Column PT-LL was designed with a longitudinal reinforcement ratio of 0.69%. A parametric study was conducted on a specimen named PT-EL (post-tensioned extra low longitudinal reinforcement) with a reinforcement ratio of 0.34%. This parametric study was used to determine if a very low reinforcement ratio would help reduce residual displacements even greater than column PT-LL. The pushover and hysteretic behavior, as well as residual displacements and tendon stresses throughout cyclic loading are presented in this section.

6.7.2 Pushover Response

The pushover response of column PT-EL, with a longitudinal reinforcement ratio of 0.34% is presented in Figure 6-37. As the longitudinal reinforcement ratio decreased, the displacement at the peak lateral force remained the same as column PT-LL, and increased slightly from that of column PT-HL. The peak lateral force and corresponding displacement of column PT-EL with a reinforcement ratio of 0.34% was 296 kips (1317 kN) at 13.5" (343 mm). The original prototype columns; PT-LL and PT-HL, showed a peak lateral force and displacement of 350 kips (1557 kN) at 13.5" (342.9 mm), and 435 kips (1935 kN) at 13.1" (332.7 mm), respectively.

6.7.3 Hysteretic Response

The hysteretic response of column PT-EL with a longitudinal reinforcement ratio of 0.34% is presented in Figure 6-38. The original prototype columns were able to withstand cyclic loading through drifts of 8%. Decreasing the longitudinal reinforcement ratio produced failure following the first push to 8% drift.

Residual displacements of column PT-EL from the change in longitudinal reinforcement ratio is presented in Table 6-38. The tables show a small impact on

45

residual displacement as the longitudinal reinforcement ratio is decreased. A drift level of 5% will be used here for discussion comparison purposes. Column PT-LL and PT-HL had a residual displacement of 1.75" (44.45 mm) and 6.43" (163.44 mm) at 5% drift for the original prototype models, respectively. The residual displacement at 5% drift for column PT-EL decreased with the reduction in longitudinal reinforcement. Column PT-EL showed a residual displacement of 0.81" (20.45 mm). It should be noted that there was a large increase in residual displacement from 5% drift to 6% drift. At 6% drift, column PT-EL had a residual displacement of 2.15" (54.61 mm), compared to 3.72" (94.49 mm) and 9.21" (233.97 mm) for the original columns PT-LL and PT-HL, respectively.

6.7.4   Tendon Stresses

Tendon stresses from column PT-EL were calculated from the model with a decreased amount of longitudinal reinforcement and is presented in Table 6-39. Tendons do not begin to yield until a stress of at least 243 ksi (1675.5 MPa) is reached. For all cases presented in this section, the tendons do not yield during the cyclic loading. For discussion comparison purposes, tendon stresses at 5% drift will be examined. Tendon stresses from column PT-EL with a decrease in longitudinal reinforcement resulted in a stress of 154.9 ksi (1067.7 kN). The original prototype columns; PT-LL and PT-HL, showed tendon stresses at 5% drift of 154.4 ksi (1064.6 kN) and 149.9 ksi (1033.4 kN). Decreasing the amount of longitudinal reinforcement reduced residual displacements at low drift levels, but decreased the columns cyclic capacity.

6.8   Design Recommendations

Based on the parametric study, the original prototype columns and the columns from parametric study III' showed the best overall performance. These observations are based on an overall assessment of ductility, tendon stresses, and re-centering capabilities, and do not go to great lengths to distinguish one parametric study from the other. The columns from parametric study III', increasing the concrete strength to 10 ksi (69 MPa) from 4.5 ksi (31 MPa) displayed two benefits; a reduction in residual displacement, and an increase in column displacement at peak lateral force. The original columns were able to maintain lower tendon stresses throughout cyclic loading. Parametric study I, varying the axial dead load from 6% of the ALI up to 10%, 15%, and 20% of the ALI, displayed the benefit of a reduction in tendon stresses throughout testing. Parametric study II, varying the initial post-tensioning force from 10% of the ALI up to 15% and 20% of the ALI, showed the benefit of an increase in the lateral force on the column from the pushover response. Parametric study III, increasing the concrete strength to 10 ksi (69 MPa) from 4.5 ksi (31 MPa), along with the axial dead load and initial post-tensioning force corresponding to the ALI, did display any benefits. Parametric study IV, increasing the distance out from the center of the column cross section to the tendons from 22.5% to 30% of the column diameter, showed a slight improvement on residual displacements, but resulted in a large increase in tendon stresses, bringing them very close to the yield stress a drift of 8%. Parametric study V, decreasing the amount of longitudinal reinforcement to 0.34% did reduce residual displacements but did not have as much

46

cyclic capacity as the original columns. Column PT-EL failed following the first push to 8% drift during cyclic loading.

Based on these observations, the axial dead load and initial post-tensioning force should be set at 6% and 10% of the ALI, respectively, the values of the original prototype columns. Increasing the amount of axial dead load and initial post-tensioning force in parametric study I and II, respectively, resulted in columns with less cyclic capacity, lower column displacements at peak lateral force, and increased residual displacements from the overall results, looking at all drift levels. The ALI should use a concrete strength of 4.5 ksi (31 MPa) while considering the magnitude of the axial dead load and initial post-tensioning force according to the ALI. The actual concrete strength for the column construction can be increased, up to 10 ksi (69 MPa) to improve overall performance, based on the results presented from parametric study III'. Although column performance was not checked with a concrete strength between 4.5 ksi (31 MPa) and 10 ksi (69 MPa), it is assumed that a concrete strength between these values will produce reasonable results, within the performance values of the results from 4.5 ksi (31 MPa) concrete and 10 ksi (69 MPa) concrete.

CHAPTER 7

Summary and Conclusions

7.1   Summary

During large earthquakes, bridge columns undergo large lateral displacements. These large displacements can cause damage and residual displacements that require closure of the bridge until repairs can be made. In order to reduce damage and residual displacements in bridge columns, unbonded post-tensioned tendons have been introduced to promote a re-centering in the columns. A reduction in residual displacement helps reduce the damage level in bridge columns, therefore shortening the amount of time required for repairs. Two similar unbonded post-tensioned bridge columns were tested using cyclic loading, each column having a different longitudinal reinforcement ratio.

The primary objective of this study was to investigate the re-centering capabilities of two unbonded post-tensioned columns under cyclic loading with an improved tendon design. The 0.4-scale columns, PT-LL and PT-HL, had longitudinal reinforcement ratios of 0.69% and 1.33%, respectively. Aside from the longitudinal reinforcement ratio, each column maintained similar properties. Each column had a diameter of 24" (610 mm), and a height of 108" (2743 mm). The concrete strength was specified as 4.5 ksi (31 MPa), and reinforcing steel was specified as Grade 60 ksi (414 MPa). Each column was subject to a cyclic motion, beginning with two cycles at 0.25% and 0.5% drift. Cyclic motion then increased to 1% drift, and continued in 1% increments to failure.

The large tendon force required for re-centering capabilities can be provided with one tendon in a scaled column, but will result in too large of a tendon area and force for a single tendon when designed at prototype dimensions. To account for this, four separate tendons were located around the center of the column cross section. This configuration allowed for the required re-centering force and high tendon area to be equally spread out to four separate tendons, making a realistic design for a full-scale column. Following a large seismic event, there is a possibility of the tendons yielding due to large lateral displacements. To provide access to the tendons, each of the four tendons were anchored in the four corners of the footing. This configuration allows for access to the anchor heads following construction. To help prevent any corrosion in the tendons, each strand was encapsulated in a greased plastic sleeve. Following testing, one of the extreme tendons was removed for inspection and showed no serious damage, proving that the sheathing provides a sufficient protection for severe shaking.

Pushover and hysteretic responses, as well as residual displacements and tendon stresses were analyzed from each column following testing. The results were used to analyze the column behavior from the varying amount of longitudinal reinforcement within each column. Tendon stresses were measured and used to determine if the initial tendon force and stress were appropriate for large lateral displacements.

Following experimental testing, it was determined that the analytical model gave a close prediction of the measured results. Using the analytical model, a parametric study was conducted. The parametric study consisted of four separate studies: Study I varied the amount of axial dead load while all other parameters were held constant. Study II varied the initial post-tensioning force while all other parameters were held constant.

Study III increased the concrete strength and corresponding axial load and initial post-tensioning force, according to the axial load index (ALI). Study III' increased the concrete strength and held the axial dead load and initial post-tensioning force at the original values used in the test. Study IV, the final study, investigated the column behavior when the distance to the tendon from the center of the column cross section was increased. The parametric study was used to determine design recommendations for unbounded post-tensioned bridge columns.

7.2   Conclusions

Experimental and analytical results were used to determine the following conclusions:

1) Constructing each column with four separate tendons centrally located within the column cross section provided sufficient area and spacing for the tendons in the experimental specimens. The area and spacing of tendons would also work in a full-scale design. Exiting the tendons out of the corners of the footing provided the possibility of removing the tendons, and did not display any negative effects. Encapsulating the tendons in greased sleeves provided corrosion protection and held up well with minimal damage following many cycles at large drift ratios. Therefore, the encapsulated tendons should be sufficient in preventing corrosion.

2) Selecting an initial tendon force of 10% of the axial load index (ALI), and an initial tendon stress of 21% of f_{pu}, provided re-centering capabilities and did not yield the tendons. Once the columns reached failure (8.4% drift for PT-LL, and 9.1% drift for PT-HL at 80% of maximum load), they were pushed to a drift ratio of 10% (10.8" (274 mm) of displacement) to measure the tendons stresses. At a large drift ratio of 10%, the tendon stresses remained below the yield stress, with a maximum stress of 151 ksi (1041 MPa) for column PT-LL, and 169 ksi (1165 MPa) for column PT-HL. The yield stress of the tendons was 247 ksi (1703 MPa), and 70% of the yield stress (a good target to stay below) was 173 ksi (1192 MPa). These maximum stresses were measured in the tendons located on the extreme sides of the column, where the highest tendon stresses were measured. The initial post-tensioning force in column PT-LL resulted in a force of 7.7% of the ALI, and the initial post-tensioning force in column PT-HL resulted in a force of 9.6% of the ALI. Since column PT-HL was initially stressed to a force (9.6% ALI) that was very close to the specified initial force (10% ALI), the specified initial tendon force of 10% of the ALI would be recommended. Even at large column displacements of 10% drift, the maximum tendon stress in column PT-HL remained just under 70% of f_{pu}.

3) Minimizing column residual displacements was the primary motive of using unbonded post-tensioning. Using unbonded tendons in each column helped minimize residual displacements. Column PT-LL showed an average residual displacement between the positive and negative sides of the hysteresis response of 0.32" (8.0 mm) at a drift ratio of 2% (2.16" (54.9 mm)). At larger drift ratios, the residual displacement remained low, with measured residual displacements of 1.85" (47.0 mm) at 5% drift (5.4" (137 mm)),

2.50" (63.6 mm) at 6% drift (6.48" (165 mm)), and 2.94" (74.6 mm) at 7% drift (7.56" (192 mm)). These residual displacements corresponded to 34.3% of the lateral drift at 5% drift (5.4" (137 mm)), 38.6% of the lateral drift at 6% drift (6.48" (165 mm)), and 38.9% of the lateral drift at 7% drift (7.56" (192 mm)). Column PT-HL showed an average residual displacement between the positive and negative sides of the hysteresis response of 0.30" (7.7 mm) at a drift of 2% (2.16" (54.9 mm)). At larger drift ratios, the residual displacement increased beyond the values of column PT-LL, with measured residual displacements of 2.26" (57.4 mm) at 5% drift (5.4" (137 mm)), 3.07" (77.9 mm) at 6% drift (6.48" (165 mm)), and 3.94" (100.0 mm) at 7% drift (7.56" (192 mm)). These residual displacements corresponded to 41.9% of the lateral drift at 5% drift (5.4" (137 mm)), 47.4% of the lateral drift at 6% drift (6.48" (165 mm)), and 52.1% of the lateral drift at 7% drift (7.56" (192 mm)). Note the lower residual displacements of column PT-LL compared to column PT-HL, even when column PT-LL had an initial tendon force of 7.7% of the ALI, and PT-HL had an initial tendon force of 9.6% of the ALI. The longitudinal reinforcement ratio had a large impact on the column re-centering capabilities, and the lower reinforcement ratio resulted in significantly smaller residual displacements.

4) Pushover curves were created by averaging the positive and negative envelopes of the hysteresis curve of each column. The pushover curve from each column was then used to calculate the elasto-plastic column behavior, from which ductility capacities were determined. Two separate ductility capacities were established: ductility at first fracture and ductility displacement capacity. The ductility at first fracture was defined as the column displacement when the first longitudinal rebar fractured, divided by the effective yield displacement. Column PT-LL and PT-HL resulted in a ductility at first fracture of 6.9 and 6.0, respectively. Ductility displacement capacity was defined as the column displacement at 80% of the peak lateral force, divided by the effective yield displacement. Column PT-LL and PT-HL resulted in a ductility displacement capacity of 9.6 and 7.0, respectively. Visible damage was greater in column PT-LL compared to PT-HL for drifts up to 3%. Visible damage was similar between the two columns for drifts of 4%, 5%, and 6%. At a drift of 7%, the visible damage became slightly greater in column PT-LL. While damage was similar and slightly higher in column PT-LL, column PT-LL had a greater ductility for both the ductility at first fracture, and the displacement ductility capacity.

5) Column PT-LL contained a longitudinal reinforcement ratio of 0.69%, and column PT-HL contained a longitudinal reinforcement ratio of 1.33%. The benefits of the lower reinforcement ratio are; smaller residual displacements, and larger ductility displacement capacity and ductility at first fracture. The benefits of having a higher longitudinal reinforcement ratio are; a slight reduction in damage compared to the lower reinforced column, and a larger column displacement at the first longitudinal reinforcement fracture. Column PT-LL had a column displacement at first fracture of 6.6" (168 mm), corresponding to a drift ratio of 6.1%, and column PT-HL had a column displacement at first fracture of 8.56" (217 mm), corresponding to a drift ratio of 7.9%.

6) Using fiber elements to model each column, with link elements used to model the tendons, provided a close correlation between the measured and calculated results. Measured pushover and hysteretic responses of each column matched up well with the analytical model, indicating that the model can be used to make close predictions of actual column behavior. Column PT-LL was found to have uneven concrete cover following testing. When the column was modified with uneven concrete cover, the model showed a close correlation to the actual column behavior. Residual displacements also showed a close correlation between the measured and calculated results. Column PT-LL had a maximum difference in residual displacement between the analytical and measured results of 0.48" (12.19 mm) at 7% drift, corresponding to 16.3% difference. Column PT-HL had a maximum difference in residual displacement between the analytical and measured results of 0.69" (17.53 mm) at 4% drift, corresponding to 46% difference.

7) Close correlation between the analytical and measured results allowed for a parametric study to be conducted on the prototype columns to gain a perspective of full-scale behavior. Parametric study I focused on increasing the axial dead load, while all other parameters maintained original values. Increasing the axial dead load to 10%, 15%, and 20% of the ALI did not show any benefits. Parametric study II investigated each columns behavior following an increase in the initial post-tensioning force from 10% of the ALI, up to 15% and 20% of the ALI. Increasing the initial post-tensioning force did not improve the re-centering capabilities of column PT-LL for drifts of 1% through 8%. Increasing the initial post-tensioning force reduced the ductility, and therefore brought on failure at an earlier point, allowing cycles only through 7% drift when the initial force was increased to 15% of the ALI. When the initial force was increased to 20% of the ALI, failure initiated following cycles of 6% drift. The original initial post-tensioning force of 10% of the ALI provided the best overall behavior for column PT-LL. Increasing the initial post-tensioning force did improve the re-centering capabilities of column PT-HL at certain drift levels. An initial post-tensioning force of 20% of the ALI provided the best re-centering capabilities for drifts through 4%. An initial post-tensioning force of 15% of the ALI provided the best re-centering capabilities at 5% drift. The original initial post-tensioning force of 10% of the ALI provided the best re-centering capabilities for drifts of 6% and higher. Based on parametric study II, the original initial tendon force of 10% of the ALI provided the best all around re-centering capabilities for both columns. Parametric study III investigated the column behavior when the concrete strength was increased from 4.5 ksi (31 MPa) to 10 ksi (69 MPa), and the axial dead load and initial post-tensioning force increased according to the ALI. This study did not show any benefits, making each column less ductile, and increasing residual displacements. Parametric study III' investigated the column behavior when the concrete strength was increased from 4.5 ksi (31 MPa) to 10 ksi (69 MPa), and the axial dead load and initial post-tensioning force remained at their original values of 6% and 10% of the ALI ($f'_c = 4.5$ ksi (31 MPa)), respectively. Increasing only the concrete strength showed several benefits, including a reduction in residual displacements, increased column displacement at the peak lateral force, and a decrease in tendon stress at high drift levels. Parametric study IV investigated the column behavior when the tendon location was increased to 30% of the column diameter out from the center of the

column cross section. Increasing the distance out from the center of the column cross section improved column performance. The displacement at peak lateral force increased, residual displacements decreased, but the tendon forces increased to values very close to the tendon yield stress at high drift ratios. With tendon stresses nearly reaching their yield stress, the tendon location increase to 30% of the column diameter is not recommended. Based on the parametric study, the original columns showed the best overall performance, aside from increasing the concrete strength. Increasing the original concrete strength showed improvements in the residual displacements and an increase in the column displacement at peak lateral force, all without increasing the tendon stresses.

7.3   Design Recommendations

Based on the analytical and test results, the following design recommendations have been made:

1) Four separate tendons shall be used and located at 22.5% of the column diameter out from the center of the column cross section. Tendons should be composed of encapsulated greased and sheathed strands and should be anchored in the corners of the footing.

2) The overall initial tendon force should be set at 10% of the axial load index (ALI). The tendon area should be selected by dividing the initial tendon force (10% ALI) by 20% of f_{pu}.

3) The longitudinal reinforcement ratio should be kept below 1.0%. The lower reinforcement ratio tested (0.69% as opposed to 1.33%) provided lower residual displacements and larger ductility levels.

4) Columns should be modeled using fiber elements, and tendons should be modeled using link elements. Tested material properties and actual column geometries can be used for more accurate modeling.

5) Columns should be designed to have a maximum axial dead load of 6% of the ALI, as this showed the best ductility and re-centering capabilities in a parametric study. The ALI used to determine the initial post-tensioning force and dead load should assume a concrete strength of 4.5 ksi (31 MPa). The actual concrete strength used in the columns can be increased up to 10 ksi (69 MPa) to improve re-centering capabilities.

References

1) Hewes, J. T., and Priestley, M. J. N. (2002). "Seismic Design and Performance of Precast Concrete Segmental Bridge Columns." Structural Systems Research Project, *Rep. No. SSRP-2001/25*, University of California, San Diego, La Jolla, California.

2) Jeong, H. I., Sakai, J., and Mahin, S. A. (2008). "Shaking Table Tests and Numerical Investigation of Self-Centering Reinforced Concrete Bridge Columns." Pacific Earthquake Engineering Research Center, *Rep. No. PEER 2008/06,* University of California, Berkeley, Berkeley, California.

3) Ou, Y., Wang, P.-H., Tsai, M.-C., Chang, K.-C., and Lee, G. C. (2009). "Large-scale experimental study of precast segmental unbonded post-tensioned concrete bridge columns for seismic regions." *Journal of Structural Engineering, ASCE,* Published online; 10.1061 /(ASCE)ST.1943-541X. 0000110. National University of Science and Technology, Taiwan.

4) Palermo, A., Marriot, D. and Pampanin, S. (2007) *Design, Modeling, and Experimental Response of Seismic Resistant Bridge Piers with Posttensioned Dissipating Connections.* Journal of Structural Engineering (ASCE), 133, 11, 1648-1661. University of Canterbury, New Zealand.

5) Yamashita, R., and Sanders, D. (2005). "Shake Table Testing and an Analytical Study of Unbonded Prestressed Hollow Concrete Columns Constructed with Precast Segments." *Report No. CCEER 05-09.* University of Nevada, Reno. Pages, 204.

6) Cruz-Noguez, C. A., and Saiidi, M. S. (2010). "Experimental and Analytical Seismic Studies of a Four-Span Bridge System with Innovative materials." *Report No. CCEER-10-04*, University of Nevada, Reno. Pages, 655.

7) Motaref, S., Saiidi, M., and Sanders, D. (2011). "Seismic Response of Precast Bridge Columns with Energy Dissipating Joints" *Report No. CCEER 11-01.* University of Nevada, Reno. Pages 707.

8) California Department of Transportation (2006). "Seismic Design Criteria (SDC)," Division of engineering services, Sacramento, California.

Table 1-1: Literature Review Parameters

Section	Column	Height, in (mm)	Diameter, in (mm)	ρ_l	Initial PT, kips (kN), %f'$_c$A$_g$	Dead Load, kips (kN), %f'$_c$A$_g$	Concrete Strength, psi (MPa)
1.2.1	JH1	145 (3683)	24 (610)	0%	604.5 (2689), 18.8% 734.5 (3267), 19.6%	200 (890), 6.2% 200 (890), 5.3%	Test 1: 7.1 (48.7) Test 2: 8.3 (57.0)
	JH2	145 (3683)	24 (610)	0%	479.9 (2135), 14.3% 566.8 (2521), 15.7%	200 (890), 6.0% 200 (890), 5.5%	Test 1: 7.4 (50.8) Test 2: 8.0 (55.5)
	JH3	72.5 (1842)	24 (610)	0%	463.1 (2060), 12.3% 611.1 (2718), 16.3%	200 (890), 5.3% 200 (890), 5.3%	Test 1: 8.3 (57.3) Test 2: 8.3 (57.1)
	JH4	72.5 (1842)	24 (610)	0%	466.7 (2076), 12.3% 600.3 (2670), 15.8%	200 (890), 5.3% 200 (890), 5.3%	Test 1: 8.4 (58.1) Test 2: 8.4 (57.8)
1.2.2	PRC-2	203 (2440)	16 (406)	0.66%	49.4 (220), 5.6%	54.0 (240), 6.0%	4.7 (32.6)
	PRC-U	203 (2440)	16 (406)	0.66%	46.6 (207), 5.3%	54.0 (240), 6.0%	4.7 (32.2)
	PRC-U2	203 (2440)	16 (406)	0.66%	77.9 (346), 8.8%	54.0 (240), 6.0%	4.7 (32.5)
	PRC-UJ	203 (2440)	16 (406)	0.66%	48.7 (217), 5.5%	54.0 (240), 6.0%	4.7 (32.1)
1.2.3	COC	160 (4064)	34x34 (864x864)	0%	234.3 (1042), 7%	327.3 (1456), 10%	4.6 (32)
	C5C	160 (4064)	34x34 (864x864)	0.50%	234.3 (1042), 7%	327.3 (1456), 10%	4.6 (32)
	C8C	160 (4064)	34x34 (864x864)	1.0%	234.3 (1042), 7%	327.3 (1456), 10%	4.6 (32)
	C5C-1	160 (4064)	34x34 (864x864)	0.50%	70.1 (312), 2%	327.3 (1456), 10%	4.6 (32)
1.2.4	MON1	63 (1600)	13.75x13.75 (350x350)	1.0%	0	45.0 (200), 2.5%	9.6 (65.9)
	PT1	63 (1600)	13.75x13.75 (350x350)	0.0%	0	45.0 (200), 3.1%	7.8 (54.1)
	PT2	63 (1600)	13.75x13.75 (350x350)	0.0%	22.5 (100), 1.5%	45.0 (200), 3.1%	7.8 (54.1)
	HBD1	63 (1600)	13.75x13.75 (350x350)	0.66%	0	45.0 (200), 3.1%	7.8 (54.1)
	HBD2	63 (1600)	13.75x13.75 (350x350)	1.0%	22.5 (100), 1.5%	45.0 (200), 3.1%	7.8 (54.1)
1.2.5	HRU	72 (1829)	40x18 (1016x457)	0.0%	400 (1779), 21.1%	95 (423), 5%	5 (35)
1.2.6	PT Bent	72 (1829)	12 (305)	0.78%	55 (245), 9.2%	50.4 (224) 8.4%	5.3 (36.5)
1.2.7	SC-2	72 (1829)	16 (406)	1.0%	100 (444.8), 11%	80 (356), 9%	4.5 (31)
	SBR-1	72 (1829)	16 (406)	1.2%	100 (444.8), 11%	80 (356), 9%	4.5 (31)
	SE-2	72 (1829)	16 (406)	1.0%	100 (444.8), 11%	80 (356), 9%	4.5 (31)
	SF-2	72 (1829)	16 (406)	1.0%	100 (444.8), 11%	80 (356), 9%	4.5 (31)

Table 2-1: Column Parameters

Column	ρ_l	ρ_s	Initial PT, kips (kN)	Dead Load, kips (kN)	Height, in (mm)	Diameter, in (mm)	Aspect Ratio	Concrete Cover, in
PT-LL	0.685% (10 #5's)	1.00%	7.7%fcAg, 157 (698)	6%fcAg, 122 (543)	108 (2743)	24 (610)	4.5	1 (25.4)
PT-HL	1.33% (10 #7's)	1.00%	9.6%fcAg, 194 (868)	6%fcAg, 122 (543)	108 (2743)	24 (610)	4.5	1 (25.4)

Table 2-2: Steel Properties

Tested Bar	Sample	f_y, ksi (MPa)	f_u, ksi (MPa)	Elongation (%)
Transverse Bars: #3	1	68.4 (471.6)	98.4 (678.5)	17
	2	71.3 (491.6)	110.3 (760.5)	15
	3	74.2 (511.6)	104.7 (721.9)	16
	Average:	**71.3 (491.6)**	**104.5 (720.3)**	**16**
Longitudinal Bars: #5	1	71.5 (493.0)	95.8 (660.5)	19
	2	71.8 (495.1)	111.7 (770.2)	15
	3	72.1 (497.1)	97.4 (671.6)	17
	Average:	**71.8 (495.1)**	**101.6 (700.8)**	**17**
Longitudinal Bars: #7	1	69.3 (477.8)	112.1 (772.9)	20
	2	70 (482.7)	112.1 (772.9)	18
	3	70.1 (483.3)	112.3 (774.3)	14
	Average:	**69.8 (481.3)**	**112.2 (773.4)**	**17.3**
Post-Tensioning Strand: 0.6"	1	245.9 (1695.5)	281.6 (1941.6)	7.1
	2	247.7 (1707.9)	281.1 (1938.2)	6.8
	3	247.7 (1707.9)	280.4 (1933.4)	6.4
	Average:	**247.1 (1703.8)**	**281.0 (1937.7)**	**6.8**

Table 2-3: Average Concrete Compressive Strengths

Column	Segment	7-Day, psi (MPa)	14-Day, psi (MPa)	28-Day, psi (MPa)	Test Day, psi (MPa)
PT-LL	Footing	4361 (30.1)	4735 (32.6)	5384 (37.1)	5384 (37.1)
	Column & Loading Head	3380 (23.3)	3746 (25.8)	4489 (31.0)	4510 (31.1)
PT-HL	Footing	4361 (30.1)	4735 (32.6)	5384 (37.1)	5384 (37.1)
	Column & Loading Head	3380 (23.3)	3746 (25.8)	4489 (31.0)	4570 (31.5)

Table 3-1: Drift Displacements

Drift	Δ, in (mm)
0.25%	0.27 (6.9)
0.50%	0.54 (13.7)
1%	1.08 (27.4)
2%	2.16 (54.9)
3%	3.24 (82.3)
4%	4.32 (109.7)
5%	5.40 (137.2)
6%	6.48 (164.6)
8%	8.64 (219.5)
7%	7.56 (192.0)
10%	10.80 (274.3)

Table 4-1: PT-LL Load Numbers

Load No.	Drift Ratio (%)	Load No.	Drift Ratio (%)	Load No.	Drift Ratio (%)
1	0.25	14	-2	27	5
2	-0.25	15	2	28	-5
3	0.25	16	-2	29	6
4	-0.25	17	3	30	-6
5	0.5	18	-3	31	6
6	-0.5	19	3	32	-6
7	0.5	20	-3	33	7
8	-0.5	21	4	34	-7
9	1	22	-4	35	7
10	-1	23	4	36	-7
11	1	24	-4	37	7
12	-1	25	5	38	9
13	2	26	-5	39	10

Table 4-2: PT-LL, Residual Displacements

PT-LL, in (mm)			
Drift (%)	Positive	Negative	Average
0.25	0.05 (1.27)	0.03 (0.76)	0.04 (1.02)
0.5	0.06 (1.52)	0.06 (1.52)	0.06 (1.52)
1	0.08 (2.03)	0.12 (3.05)	0.10 (2.54)
2	0.20 (5.08)	0.43 (10.92)	0.32 (8.12)
3	0.37 (9.40)	1.00 (25.40)	0.69 (17.53)
4	0.66 (16.76)	1.84 (46.74)	1.25 (31.75)
5	0.98 (24.89)	2.71 (68.83)	1.85 (46.99)
6	1.51 (38.35)	3.50 (88.90)	2.50 (63.50)
7	1.84 (46.74)	4.04 (102.62)	2.94 (74.68)

Table 4-3: PT-LL Maximum Microstrains, Longitudinal Reinforcement

Strain Gauge	Cycle	0.25%	0.50%	1%	2%	3%	4%	5%	6%	7%	10%
SG01	Push 1	-203	-858	-1945	**-2828**	**-7196**	**-10404**	**-13992**	**-17612**	**-9579**	
	Pull 1	674	1008	1709	2403	**3719**	**4511**	**4832**	**5120**	**4157**	**3627**
	Push 2	-236	-864	-1971	**-3005**	**-7876**	**-11274**	**-14941**	**-18372**	-20	537
	Pull 2	681	1021	1774	**2508**	**3771**	**4518**	**4734**	**4924**	**3365**	
SG02	Push 1	-125	-583	-1618	**-2495**	**-2921**	**-5612**	**-8833**	**-12219**	**-14209**	
	Pull 1	648	753	1126	2010	2331	**4033**	**4662**	**4616**	**4210**	**3817**
	Push 2	-118	-622	-1670	**-2593**	**-3117**	**-6751**	**-9842**	**-13227**	**-12461**	**-3575**
	Pull 2	655	772	1165	2089	**2606**	**4387**	**4610**	**4263**	**3739**	
SG03	Push 1										
	Pull 1						Faulty				
	Push 2										
	Pull 2										
SG04	Push 1	623	958	1549	2238	**2940**	**4751**	**5604**	**6004**	**-2605**	
	Pull 1	-171	-748	-1824	**-2586**	**-4502**	**-7579**	**-10828**	**-16038**	**-4541**	**-4370**
	Push 2	689	997	1706	**2526**	**3983**	**5125**	**5899**	**5617**	**-3767**	**-4010**
	Pull 2	-190	-768	-1811	**-2605**	**-5276**	**-8327**	**-12140**	**-8196**	**-4377**	
SG05	Push 1										
	Pull 1						Faulty				
	Push 2										
	Pull 2										
SG06	Push 1	-636	-2031	**-8871**	**-22289**	**-28991**	**-36951**	**-36067**	**-21208**	**-9546**	
	Pull 1	662	904	-1841	**-4305**	**-4737**	**-1409**	**-4953**	**-2097**	**-1022**	**-3053**
	Push 2	-813	-1926	**-8517**	**-21109**	**-28179**	**-36709**	**-25754**	**-15049**	**-7384**	**-7744**
	Pull 2	662	904	-1992	**-4573**	**-3250**	**-2601**	**-4147**	**-550**	**-2837**	
SG07	Push 1	811	1177	1903	**3642**	**4244**	**6461**	**9096**	**10391**	**19696**	
	Pull 1	-667	-1576	**-6944**	**-15353**	**-18976**	**-26143**	**-25521**	**-6395**	**1759**	**-18401**
	Push 2	844	1210	759	2335	**4434**	**6977**	**8573**	**7252**	**19329**	**16688**
	Pull 2	-614	-1478	**-6480**	**-13287**	**-18891**	**-24521**	**-17452**	**-1497**	**-20349**	
SG08	Push 1	857	1348	2310	**6693**	**9846**	**14132**	**15610**	**14897**	**-16624**	
	Pull 1	-975	-1969	**-8387**	**-16153**	**-20150**	**-27223**	**-32155**	**-39509**	**-15656**	**-13359**
	Push 2	923	1354	1479	**5816**	**10546**	**13935**	**14910**	**2689**	**-11966**	**-13405**
	Pull 2	-916	-1858	**-7870**	**-14007**	**-19699**	**-25875**	**-32142**	**-16716**	**-13556**	
SG13	Push 1	-137	-648	**-2787**	**-13851**	**-7302**	**-4881**	**-4966**	**-5143**	**-2460**	
	Pull 1	726	1047	2179	**5614**	**-3762**	**-4842**	**-4933**	**-4940**	**-2146**	**-7380**
	Push 2	-124	-713	**-2931**	**-11483**	**-5162**	**-4842**	**-5064**	**-5267**	**-8493**	**-7629**
	Pull 2	733	1047	2414	**5686**	**-3873**	**-4842**	**-5005**	**-5241**	**-7648**	
SG14	Push 1	-66	-472	-2207	**-11546**	**-20000**	**-25580**	**-31310**	**-36228**	**-45724**	
	Pull 1	511	609	1074	1205	**4080**	**6824**	**9542**	**8297**	**-21651**	**211777**
	Push 2	-72	-511	-2299	**-11565**	**-18795**	**-24093**	**-29562**	**-35940**	**-41284**	**-69523**
	Pull 2	517	616	1126	1984	**4453**	**7636**	**8992**	**3654**	**-95620**	
SG15	Push 1	707	1092	1760	**4860**	**8334**	**12134**	**-2845**	**-5567**	**-5528**	
	Pull 1	-203	-1047	**-2473**	**-11552**	**-20789**	**-22797**	**-6188**	**-6038**	**-6070**	**-6025**
	Push 2	700	1119	1910	**3860**	**8040**	**3925**	**-5639**	**-5501**	**-6031**	**212611**
	Pull 2	-216	-1034	**-2479**	**-12233**	**-19317**	**-14097**	**-6051**	**-5822**	**-6103**	
SG16	Push 1	732	1184	2001	**5192**	**11318**	**16569**	**22526**			
	Pull 1	-353	-1432	**-2746**	**-10233**	**-15863**	**-20440**	**-24892**		Slipped	
	Push 2	713	1197	2086	**4584**	**11044**	**16772**	**-215494**			
	Pull 2	-353	-1393	**-2779**	**-10076**	**-14803**	**-20093**	**-215494**			

58

Table 4-4: PT-LL Maximum Microstrains, Longitudinal Reinforcement

Strain Gauge	Cycle	0.25%	0.50%	1%	2%	3%	4%	5%	6%	7%	10%
SG21	Push 1	-510	-2002	**-3952**	**-13309**	**-21508**	**-26592**	**-5372**	**-4908**	**-3632**	
	Pull 1	733	1224	2179	**3481**	**10018**	9933	**-4312**	**-3049**	**-2225**	**-1590**
	Push 2	-589	-1989	**-4018**	**-12890**	**-20088**	**-10901**	**-5182**	**-4018**	**-2572**	**-1832**
	Pull 2	720	1224	2316	**6262**	**10744**	**-1250**	**-4050**	**-2565**	**-2401**	
SG22	Push 1	-373	-1663	**-3110**	**-11110**	**-17944**	**-22409**	**-26998**	**-29983**	**-18101**	
	Pull 1	556	884	1191	1277	4903	7332	10645	8229	**-8249**	**-10926**
	Push 2	-439	-1663	**-3018**	**-11070**	**-16785**	**-21859**	**-26704**	**-20825**	**-16759**	**-11313**
	Pull 2	583	897	1218	**3123**	**5473**	7790	11411	**-4229**	**-10894**	
SG23	Push 1	674	1047	1635	**2689**	**4396**	3847	5574	7229	12809	
	Pull 1	-203	-942	-2322	**-7863**	**-16289**	**-22301**	**-29183**	**-35522**	**-35247**	**-47153**
	Push 2	661	1086	1734	**3186**	**3500**	3500	5436	7602	14778	**-30079**
	Pull 2	-216	-935	-2250	**-8969**	**-16217**	**-22451**	**-28954**	**-34377**	**-36503**	
SG24	Push 1	818	1348	2206	**4569**	**5564**	6015	8522	10656	**-15147**	
	Pull 1	-203	-1132	-2415	**-10486**	**-21280**	**-28788**	**-37429**	**-45578**	**-18210**	**6788**
	Push 2	916	1407	2297	**4287**	**4680**	5682	8765	7744	**-16253**	Slipped
	Pull 2	-216	-1146	-2389	**-11743**	**-21005**	**-29122**	**-37416**	**-27106**	**-18119**	
SG29	Push 1	-190	-982	**-2756**	**-8164**	**-11915**	**-15156**	**-18894**	**-23038**	**-12459**	
	Pull 1	700	995	1630	1905	**4164**	5787	6822	7980	4465	3987
	Push 2	-190	-1061	**-2750**	**-8354**	**-12040**	**-15424**	**-19752**	**-23817**	**-1152**	**98**
	Pull 2	714	1015	1663	2422	**4517**	5918	6966	7162	3817	
SG30	Push 1	-98	-753	-2153	**-3508**	**-5091**	**-7434**	**-9947**	**-11766**	**-10477**	
	Pull 1	471	615	955	1394	**2650**	3959	4685	5569	6263	5661
	Push 2	-98	-785	-2068	**-3632**	**-5818**	**-7977**	**-10235**	**-11688**	**-9607**	**-1283**
	Pull 2	471	622	975	1636	**2997**	4149	4895	5693	5575	
SG31	Push 1	752	1125	1635	**2433**	**2746**	1785	1824	1988	1648	
	Pull 1	-314	-1151	**-2550**	**-9645**	**-14621**	**-17387**	**-20408**	**-22415**	**-17766**	**-18596**
	Push 2	785	1112	1661	2027	1517	1563	1746	1883	2210	**-7748**
	Pull 2	-301	-1098	-2491	**-10089**	**-13836**	**-17504**	**-19708**	**-19028**	**-15942**	
SG32	Push 1	772	1250	1957	**3507**	**3416**	2958	2833	2519	**-4705**	
	Pull 1	-497	-1381	**-3023**	**-8788**	**-14972**	**-18506**	**-21614**	**-24316**	**-9573**	**-8592**
	Push 2	798	1250	1983	**2807**	**2585**	2598	2473	2343	**-5817**	**-6053**
	Pull 2	-465	-1341	**-3095**	**-9390**	**-14507**	**-18388**	**-21241**	**-14664**	**-8500**	
SG37	Push 1	-255	-1315	**-2793**	**-8400**	**-10134**	**-11920**	**-14026**	**-16146**	**-9362**	
	Pull 1	720	1047	1531	1629	1747	2309	**2486**	2637	**1753**	**1151**
	Push 2	-255	-1308	**-2735**	**-8204**	**-9905**	**-12195**	**-14569**	**-16486**	**-3507**	**-2159**
	Pull 2	693	1047	1524	1125	1793	2283	2316	2296	962	
SG38	Push 1	-222	-955	-2224	**-3055**	**-4894**	**-7177**	**-9415**	**-11103**	**-9565**	
	Pull 1	406	595	870	1354	1701	1780	1780	1904	1531	1524
	Push 2	-229	-994	-2211	**-3036**	**-5842**	**-7995**	**-9951**	**-11325**	**-7596**	**-2885**
	Pull 2	412	595	890	1348	1636	1668	1695	1688	1367	
SG39	Push 1	602	883	1295	1825	2119	2426	**2995**	3571	3342	
	Pull 1	-6	-464	-1347	-1903	-2321	**-2688**	**-3518**	**-4505**	**-3956**	**-4002**
	Push 2	602	883	1328	1851	2204	**2583**	3283	3590	3159	**1942**
	Pull 2	-6	-464	-1334	-1909	-2302	**-2877**	**-3780**	**-4205**	**-3753**	
SG40	Push 1	798	1191	1826	**2539**	**3063**	4397	4888	5202	3200	
	Pull 1	-65	-608	-1721	-2231	**-3089**	**-4672**	**-5536**	**-6701**	**-1093**	Slipped
	Push 2	792	1211	1845	**2500**	**3599**	4496	4960	5189	2055	
	Pull 2	-59	-608	-1701	-2290	**-3468**	**-4751**	**-5667**	**-2984**	**-314**	

Table 4-5: PT-LL Maximum Microstrains, Transverse Reinforcement

Strain Gauge	Cycle	0.25%	0.50%	1%	2%	3%	4%	5%	6%	7%	10%
SG09	Push 1	-7	-46	-52	-52	-85	-98	-59	0	46	
	Pull 1	13	20	33	-46	-105	-105	-157	-157	131	124
	Push 2	-13	-39	-46	-33	-65	-91	20	7	92	124
	Pull 2	0	26	39	-39	-65	-78	-111	-20	157	
SG10	Push 1	118	249	-308							
	Pull 1	0	-72	-229			Slipped				
	Push 2	144	262	-334							
	Pull 2	7	-59	-216							
SG11	Push 1	-26	-26	-46	-20	-26	-46	-39	-72	-72	
	Pull 1	-39	-52	-20	7	0	-7	-7	-13	-33	-33
	Push 2	-26	-46	-46	-46	-33	-52	-52	-79	-85	-72
	Pull 2	-33	-46	-20	-13	-20	-20	-26	-46	-20	
SG12	Push 1	52	33	7	-39	98	124	92	52	-229	
	Pull 1	39	26	105	111	105	190	281	288	150	-150
	Push 2	46	46	20	0	124	144	111	98	-85	209
	Pull 2	33	39	105	105	111	209	242	196	33	
SG17	Push 1	-7	13	0	-79	-46	26	59	105	98	
	Pull 1	-13	-7	-111	-26	39	7	20	111	98	-157
	Push 2	-13	20	-20	-33	-33	33	105	92	131	-340
	Pull 2	-26	-7	-118	-7	13	20	111	334	-72	
SG18	Push 1	-92	-124	-216	-458	-366	-308	-550			
	Pull 1	-39	-157	-275	-465	-517	-595	-870		Slipped	
	Push 2	-92	-124	-216	-373	-294	-432	-694			
	Pull 2	-33	-164	-281	-275	-465	-635				
SG19	Push 1	-59	-13	-26	-183	-360	-556	-530	-301	-700	
	Pull 1	-26	-59	-98	-216	-242	-314	-347	-327	-13	268
	Push 2	-46	-20	-46	-229	-419	-543	-419	-406	-308	700
	Pull 2	-46	-72	-111	-118	-249	-347	-327	-183	229	
SG20	Push 1	78	72	52	26	-222	-98	-59	157	-203	
	Pull 1	-33	-20	-65	-307	-516	-798	-830	-1203	-889	163
	Push 2	65	78	33	-150	-144	-85	124	-26	1151	1288
	Pull 2	-20	-46	-65	-294	-490	-758	-726	-954	543	
SG25	Push 1	-52	-33	-26	-39	-111	-170	-170	-137	-118	
	Pull 1	-59	-33	-20	-111	-111	-209	-530	-746	-628	-641
	Push 2	-59	-26	-26	-92	-137	-164	-111	-131	-301	-648
	Pull 2	-59	-33	-39	-105	-118	-308	-556	-595	-504	
SG26	Push 1	-137	-177	-249	-386	-412	-373	-936	-1204	-1001	
	Pull 1	-92	-137	-144	-92	-373	-458	-981	-870	-870	-896
	Push 2	-137	-157	-249	-360	-504	-432	-1060	-1152	-857	-1001
	Pull 2	-105	-137	-164	-20	-412	-465	-962	-975	-877	

Table 4-6: PT-LL Maximum Microstrain, Transverse Reinforcement

Strain Gauge	Cycle	0.25%	0.50%	1%	2%	3%	4%	5%	6%	7%	10%
SG27	Push 1	-105	-105	-170	-177	-334	-373	-524	-602	-674	
	Pull 1	-98	-92	-137	-85	13	144	288	321	268	-33
	Push 2	-98	-131	-170	-242	-347	-491	-517	-759	-805	-471
	Pull 2	-118	-98	-124	-39	13	183	288	268	170	
SG28	Push 1	-52	-242	-321	-360	-366	-386	-327			
	Pull 1	-118	-151	-209	-432	-890	-1093				
	Push 2	-79	-236	-281	-327	-347	-347		Slipped		
	Pull 2	-118	-164	-216	-517	-831	-1034				
SG33	Push 1	-137	-105	-111	-72	-13	-20	-7	-98	-59	
	Pull 1	-131	-111	-85	-98	-164	-170	-170	-203	-170	-170
	Push 2	-118	-92	-118	-66	-20	-20	-52	-170	-59	-281
	Pull 2	-137	-105	-79	-118	-151	-164	-177	-170	-151	
SG34	Push 1	-210	-262	-367	-511	-635	-766	-851	-930	-943	
	Pull 1	-183	-288	-432	-589	-818	-930	-805	-799	-517	-543
	Push 2	-223	-288	-399	-563	-668	-766	-845	-1034	-858	-1218
	Pull 2	-210	-314	-426	-556	-851	-818	-746	-478	-530	
SG35	Push 1	7	39	52	-13	13	20	20	0	0	
	Pull 1	7	0	-85	-236	-432	-491	-530	-582	-334	-262
	Push 2	0	20	13	20	20	20	13	13	-65	-196
	Pull 2	33	7	-111	-294	-393	-478	-497	-366	-222	
SG36	Push 1	-7	-7	-85	-105	-294	-464	-667	-831	-746	
	Pull 1	-85	-98	-157	-229	-484	-674	-798	-889	-778	-634
	Push 2	7	-26	-78	-157	-353	-510	-713	-961	-425	-229
	Pull 2	-85	-98	-150	-288	-504	-687	-765	-759	-628	
SG41	Push 1	-13	-33	-26	-59	-59	-124	-170	-216	-98	
	Pull 1	-20	13	0	7	-46	-26	-26	-13	52	46
	Push 2	-20	-20	-7	-65	-79	-131	-177	-268	20	46
	Pull 2	-13	7	20	0	-13	-20	-13	46	65	
SG42	Push 1	-164	-196	-262	-334	-366	-393	-458	-478		
	Pull 1	-52	-59	-105	-131	-150	-170	-170	-196		
	Push 2	-124	-183	-255	-347	-360	-412	-458	-497	Slipped	
	Pull 2	-52	-59	-118	-150	-157	-177	-190	-209		
SG43	Push 1	-39	-52	-151	-242	-268	-334	-367	-399	-321	
	Pull 1	-26	0	-26	-46	-52	-59	-39	-33	0	0
	Push 2	-33	-52	-157	-262	-275	-334	-360	-419	-242	-137
	Pull 2	-13	-7	-33	-39	-65	-52	-33	-13	-7	
SG44	Push 1	-33	-46	-13	0	-13	-98	-177	-255	-288	
	Pull 1	-105	-105	-131	-183	-236	-288	-321	-360	-373	-327
	Push 2	-39	-20	-26	-13	-72	-151	-229	-301	-295	-262
	Pull 2	-92	-124	-137	-177	-236	-281	-321	-327	-327	

Table 4-7: PT-LL Maximum Microstrain, Post-Tensioning

Strain Gauge	Cycle	0.25%	0.50%	1%	2%	3%	4%	5%	6%	7%	10%
PT-01	Push 1										
	Pull 1					Faulty					
	Push 2										
	Pull 2										
PT-02	Push 1	-1067	-1218	-1519	-2095	-2508	-2888	-3261	-3608		
	Pull 1	-878	-845	-799	-766	-642	-517	-380	-262		Slipped
	Push 2	-1067	-1218	-1519	-2076	-2495	-2875	-3235			
	Pull 2	-891	-838	-792	-714	-590	-472	-341			
PT-03	Push 1	-1035	-1199	-1507	-2070	-2503	-2883	-3282	-3610	-3872	
	Pull 1	-839	-819	-767	-734	-616	-491	-367	-256	-144	111
	Push 2	-1029	-1179	-1494	-2064	-2476	-2876	-3230	-3590	-3610	-4527
	Pull 2	-845	-819	-753	-681	-583	-459	-341	-210	-105	
PT-04	Push 1										
	Pull 1					Faulty					
	Push 2										
	Pull 2										
PT-05	Push 1	-1993	-2137	-2464	-3087	-3454	-3834	-4227	-4587	-4882	
	Pull 1	-1822	-1763	-1737	-1665	-1482	-1324	-1134	-938	-748	-256
	Push 2	-1986	-2150	-2478	-3028	-3415	-3814	-4161	-4581	-4568	-5505
	Pull 2	-1822	-1783	-1731	-1606	-1442	-1272	-1075	-898	-663	
PT-06	Push 1	-1689	-1833	-2166	-2781	-3193	-3592	-4031	-4456	-4796	
	Pull 1	-1499	-1479	-1420	-1355	-1178	-1028	-871	-720	-570	-243
	Push 2	-1695	-1865	-2179	-2768	-3161	-3586	-4018	-4476	-4528	-5706
	Pull 2	-1505	-1473	-1420	-1303	-1146	-982	-838	-688	-511	
PT-07	Push 1	-946	-986	-1095	-1352	-1550	-1729	-1872	-2011	-2060	
	Pull 1	-951	-976	-1055	-1229	-1288	-1367	-1417	-1456	-1456	-1605
	Push 2	-951	-986	-1095	-1337	-1521	-1704	-1833	-1981	-1852	-2021
	Pull 2	-946	-971	-1045	-1174	-1224	-1323	-1347	-1412	-1382	
PT-08	Push 1	-1000	-1019	-1150	-1438	-1654	-1869	-2033	-2190	-2236	
	Pull 1	-974	-1019	-1124	-1294	-1359	-1444	-1510	-1556	-1575	-1732
	Push 2	-987	-1033	-1163	-1405	-1621	-1824	-1994	-2144	-2020	-2190
	Pull 2	-987	-1013	-1111	-1248	-1301	-1405	-1451	-1503	-1477	
PT-09	Push 1	-439	-511	-641	-982	-1257	-1499	-1728	-1905	-1964	
	Pull 1	-452	-484	-589	-818	-903	-1034	-1087	-1139	-1172	-1375
	Push 2	-439	-491	-641	-962	-1231	-1460	-1669	-1872	-1702	-1912
	Pull 2	-445	-478	-576	-766	-851	-969	-1015	-1106	-1087	
PT-10	Push 1	-2828	-2867	-2979	-3280	-3470	-3686	-3804	-3928	-3928	
	Pull 1	-2861	-2920	-3083	-3391	-3588	-3764	-3869	-3961	-3915	-4157
	Push 2	-2835	-2867	-2966	-3260	-3450	-3646	-3745	-3882	-3607	-3607
	Pull 2	-2861	-2920	-3070	-3339	-3509	-3705	-3771	-3843	-3823	
PT-11	Push 1	-2454	-2493	-2592	-2880	-3076	-3253	-3364	-3508	-3495	
	Pull 1	-2461	-2533	-2696	-2997	-3168	-3325	-3449	-3514	-3469	-3691
	Push 2	-2448	-2480	-2579	-2860	-3010	-3194	-3331	-3442	-3207	-3161
	Pull 2	-2480	-2520	-2683	-2925	-3096	-3266	-3318	-3423	-3370	
PT-12	Push 1	-2675	-2715	-2826	-3107	-3310	-3500	-3644	-3775	-3775	
	Pull 1	-2708	-2760	-2931	-3245	-3422	-3585	-3683	-3788	-3749	-3978
	Push 2	-2675	-2708	-2813	-3081	-3271	-3448	-3579	-3716	-3448	-3435
	Pull 2	-2701	-2754	-2885	-3160	-3350	-3526	-3592	-3670	-3638	

Table 4-8: PT-LL Maximum Microstrain, Post-Tensioning

Strain Gauge	Cycle	0.25%	0.50%	1%	2%	3%	4%	5%	6%	7%	10%
PT-13	Push 1										
	Pull 1					Faulty					
	Push 2										
	Pull 2										
PT-14	Push 1	-1421	-1362	-1316	-1329	-1309	-1283	-1192	-1100	-897	
	Pull 1	-1578	-1722	-2023	-2507	-2906	-3240	-3541	-3796	-3985	-4888
	Push 2	-1408	-1355	-1303	-1303	-1264	-1218	-1120	-1009	-642	-158
	Pull 2	-1578	-1722	-1996	-2448	-2847	-3200	-3442	-3691	-3881	
PT-15	Push 1	-1315	-1283	-1237	-1250	-1224	-1184	-1119	-1021	-824	
	Pull 1	-1499	-1662	-1950	-2448	-2861	-3221	-3515	-3817	-4000	-4936
	Push 2	-1328	-1269	-1217	-1217	-1184	-1145	-1047	-949	-602	-163
	Pull 2	-1505	-1662	-1931	-2402	-2802	-3168	-3417	-3679	-3902	
PT-16	Push 1	-1742	-1683	-1630	-1545	-1434	-1329	-1198	-1067	-844	
	Pull 1	-1938	-2069	-2416	-2979	-3379	-3726	-4046	-4374	-4564	-5553
	Push 2	-1742	-1683	-1591	-1467	-1381	-1277	-1139	-975	-668	-196
	Pull 2	-1931	-2095	-2403	-2907	-3293	-3680	-3942	-4269	-4479	
PT-17	Push 1										
	Pull 1					Faulty					
	Push 2										
	Pull 2										
PT-18	Push 1	-1479	-1426	-1348	-1276	-1151	-1046	-902	-772	-549	
	Pull 1	-1681	-1832	-2153	-2696	-3076	-3423	-3724	-4031	-4221	-5203
	Push 2	-1479	-1413	-1328	-1197	-1073	-988	-844	-673	-372	47
	Pull 2	-1668	-1812	-2120	-2618	-2997	-3370	-3626	-3914	-4136	
PT-19	Push 1	-1466	-1519	-1656	-1996	-2219	-2448	-2585	-2716	-2749	
	Pull 1	-1493	-1565	-1761	-2121	-2376	-2579	-2723	-2860	-2919	-3344
	Push 2	-1473	-1532	-1663	-1964	-2199	-2389	-2500	-2657	-2461	-2657
	Pull 2	-1499	-1578	-1748	-2062	-2317	-2513	-2644	-2762	-2867	
PT-20	Push 1	-1407	-1453	-1584	-1905	-2140	-2356	-2500	-2644	-2684	
	Pull 1	-1421	-1493	-1669	-2042	-2311	-2513	-2664	-2808	-2860	-3286
	Push 2	-1401	-1440	-1578	-1879	-2101	-2317	-2435	-2585	-2383	-2599
	Pull 2	-1427	-1486	-1682	-1983	-2232	-2448	-2585	-2723	-2795	
PT-21	Push 1	-1479	-1532	-1656	-1964	-2206	-2402	-2533	-2684	-2743	
	Pull 1	-1486	-1558	-1741	-2095	-2383	-2553	-2703	-2841	-2874	-3306
	Push 2	-1473	-1519	-1643	-1944	-2160	-2343	-2487	-2625	-2442	-2644
	Pull 2	-1512	-1558	-1735	-2049	-2284	-2474	-2605	-2749	-2841	
PT-22	Push 1	-1951	-1997	-2134	-2455	-2704	-2914	-3110	-3254	-3352	
	Pull 1	-1971	-2049	-2200	-2547	-2743	-2894	-2979	-3071	-3084	-3470
	Push 2	-1951	-1984	-2128	-2429	-2665	-2900	-3044	-3215	-3090	-3418
	Pull 2	-1957	-2043	-2193	-2475	-2665	-2822	-2907	-2999	-3025	
PT-23	Push 1										
	Pull 1					Faulty					
	Push 2										
	Pull 2										
PT-24	Push 1	-1538	-1591	-1722	-2049	-2298	-2514	-2677	-2848	-2946	
	Pull 1	-1545	-1604	-1794	-2141	-2330	-2468	-2573	-2651	-2684	-3064
	Push 2	-1525	-1584	-1715	-2016	-2272	-2481	-2638	-2808	-2671	-2998
	Pull 2	-1551	-1610	-1787	-2049	-2265	-2409	-2481	-2579	-2619	

Table 4-9: PT-HL Load Numbers

Load No.	Drift Ratio (%)	Load No.	Drift Ratio (%)	Load No.	Drift Ratio (%)
1	0.25	16	-2	31	6
2	-0.25	17	3	32	-6
3	0.25	18	-3	33	7
4	-0.25	19	3	34	-7
5	0.5	20	-3	35	7
6	-0.5	21	4	36	-7
7	0.5	22	-4	37	8
8	-0.5	23	4	38	-8
9	1	24	-4	39	2.92
10	-1	25	5	40	8
11	1	26	-5	41	-8
12	-1	27	5	42	-10
13	2	28	-5	43	10
14	-2	29	6		
15	2	30	-6		

Table 4-10: PT-HL, Residual Displacements

PT-HL, in (mm)			
Drift (%)	Positive	Negative	Average
0.25	0.04 (1.02)	0.03 (0.76)	0.04 (1.02)
0.5	0.06 (1.52)	0.06 (1.52)	0.06 (1.52)
1	0.11 (2.79)	0.09 (2.29)	0.10 (2.54)
2	0.30 (7.62)	0.31 (7.87)	0.30 (7.62)
3	0.75 (19.05)	0.85 (21.59)	0.80 (20.32)
4	1.42 (36.07)	1.58 (40.12)	1.50 (38.10)
5	2.17 (55.12)	2.35 (59.69)	2.26 (57.40)
6	2.94 (74.68)	3.19 (81.03)	3.07 (77.98)
7	3.80 (96.52)	4.08 (103.63)	3.94 (100.08)

Table 4-11: PT-HL Maximum Microstrain, Longitudinal Reinforcement

Strain Gauge	Cycle	0.25%	0.50%	1%	2%	3%	4%	5%	6%	7%	8%	10%
SG01	Push 1	-302	-1043	-2387	-7724	-13488	-19062	-25475	-10039	-5685	-5554	
	Pull 1	616	977	1659	4262	4793	6065	6892	-3679	-3180	-4151	-4629
	Push 2	-315	-1049	-2636	-8203	-13718	-19554	-26163	-6183	-5456	-4701	-4747
	Pull 2	616	1003	1902	4367	4990	6151	6557	-3364	-3449	-4603	
SG02	Push 1	-177	-726	-1865	-3410	-9797	-16590	-18331	-23940	-22245	-24248	
	Pull 1	452	661	995	1774	1806	857	3063	2251	151	-52	-4097
	Push 2	-183	-713	-2304	-3763	-12487	-15890	-19110	-23907	-20949	-21937	-9457
	Pull 2	452	681	1224	1846	111	3043	2775	1531	-92	-3658	
SG03	Push 1	471	746	1197	1805	2080	2341	3250	3276	3133	2930	
	Pull 1	-65	-425	-1347	-2106	-2805	-8018	-10974	-14342	-17834	-20934	-22281
	Push 2	504	798	1478	1942	2126	3191	3257	3205	3133	2322	-11091
	Pull 2	-65	-432	-1347	-2151	-2975	-8417	-11458	-15048	-18305	-20110	
SG04	Push 1											
	Pull 1					Faulty						
	Push 2											
	Pull 2											
SG05	Push 1											
	Pull 1					Faulty						
	Push 2											
	Pull 2											
SG06	Push 1	-425	-1256	-2459	-12282	-17154	-22660	-27814	-31790	-33255	-23380	
	Pull 1	464	713	1131	-333	65	4284	7645	11026	11229	5062	-3610
	Push 2	-432	-1210	-7416	-12066	-16958	-22000	-27016	-30626	-28389	-18161	-13727
	Pull 2	464	719	-922	-471	1092	4473	7410	10444	7946	-4486	
SG07	Push 1	838	1283	2127	7167	5276	7292	9039	8738	13876	7206	
	Pull 1	-308	-1093	-2330	-12973	-17273	-23328	-20081	-12344	-2769	-2153	-4058
	Push 2	903	1348	3417	3358	6218	6467	6774	12672	10119	-59	43409
	Pull 2	-308	-1021	-2448	-12161	-16894	-21842	-14576	-6670	-563	-4006	
SG08	Push 1	687	1139	1970	4051	5222	6656	8122	9470	4457	-9712	
	Pull 1	-406	-1054	-2277	-7788	-11675	-17578	-22598	-25104	-18658	-21884	-11623
	Push 2	733	1165	2232	3861	5615	6760	8423	8521	-6976	-11145	-10818
	Pull 2	-406	-1027	-2140	-7663	-11917	-17401	-22054	-20667	-21982	-11610	
SG13	Push 1	-281	-831	-2165	-2813	-9576	-15293	-19793	-24117	-29147	-36322	
	Pull 1	471	805	1504	2878	8000	9910	12349	14024	13710	-3035	-12912
	Push 2	-275	-883	-2250	-3768	-10341	-15090	-19257	-24110	-29716	-20094	-27583
	Pull 2	471	824	1629	3656	7607	9707	12022	13272	6868	-11859	
SG14	Push 1	-216	-694	-1813	-2415	-8863	-13910	-8398	-2952	-2985	-2887	
	Pull 1	353	517	1028	1879	4949	5858	3332	275	20	-700	-8955
	Push 2	-216	-733	-2121	-2533	-9151	-13877	-2939	-2756	-2651	-2690	-4104
	Pull 2	353	537	1145	2010	4831	5662	975	347	-275	-7593	
SG15	Push 1	792	1139	1806	7232	9745	7205	-2834	-2794	-3122	-4686	
	Pull 1	-131	-674	-2055	-9077	-14967	-5216	-3423	-3390	-3442	-3612	-5268
	Push 2	707	1099	2559	5792	8344	-2271	-2520	-2722	-3593	-5196	-4555
	Pull 2	-131	-667	-2022	-8586	-12899	-3698	-3429	-3396	-3429	-5314	
SG16	Push 1	812	1237	2174	9965	13631	18757	-3392	-3457	-3025	-5434	
	Pull 1	-249	-864	-2259	-7431	-13919	-7464	-4662	-4570	-4563	-4708	-4825
	Push 2	720	1231	4760	8852	13834	-3110	-3536	-3339	-5676	-5264	211982
	Pull 2	-249	-884	-2193	-7313	-13762	-4740	-4596	-4563	-4832	-4832	

Table 4-12: PT-HL Maximum Microstrain, Longitudinal Reinforcement

Strain Gauge	Cycle	0.25%	0.50%	1%	2%	3%	4%	5%	6%	7%	8%	10%
SG21	Push 1	-308	-1158	-2493	-7447	-11413	-15294	-18972	-14927	-3855	-3711	
	Pull 1	609	988	1577	2965	5936	8868	13095	-3292	-3383	-2938	Slipped
	Push 2	-321	-1165	-2978	-7120	-10791	-14633	-17853	-3697	-3796	-3815	
	Pull 2	609	975	1643	2880	6165	9110	11112	-3351	-3023	-3220	
SG22	Push 1	-242	-1093	-2336	-7492	-11568	-15331	-19276	-22960	-25950	-27704	
	Pull 1	530	831	1263	1950	3226	4050	4894	6079	9213	12792	3383
	Push 2	-262	-1066	-2794	-7525	-10940	-15016	-18916	-22201	-24812	-28122	-26526
	Pull 2	530	811	1322	1858	3252	3978	4816	6144	9874	0	
SG23	Push 1	654	988	1446	2773	5226	7051	8412	-1681	-3297	-3467	
	Pull 1	-190	-844	-1949	-6626	-10374	-13186	-10433	-3774	-3938	-3944	-4108
	Push 2	628	955	1851	2440	5037	7326	497	-3388	-3427	-3624	-3728
	Pull 2	-190	-818	-1923	-6384	-9752	-12460	-6430	-3846	-3957	-3970	
SG24	Push 1											
	Pull 1					Faulty						
	Push 2											
	Pull 2											
SG29	Push 1	-249	-1028	-2495	-5167	-12068	-16279	-12075	-5442	-5337	-5252	
	Pull 1	714	1113	1807	3608	4577	5625	-1552	-4204	-4780	-4872	Slipped
	Push 2	-262	-1028	-3097	-5965	-12009	-15722	-7851	-5180	-5199	-5147	
	Pull 2	714	1106	1866	3948	4394	5101	-3169	-4256	-4918	-5167	
SG30	Push 1	942	255	-878	-1899	-10062	-12438	-12988	-7084	-4027	-3712	
	Pull 1	1675	1957	2434	3253	4117	2925	994	-2194	-1847	-1519	-2770
	Push 2	935	241	-1362	-2063	-10121	-11136	-12216	-4131	-3791	-3267	-4020
	Pull 2	1675	2035	2480	3390	3868	2094	97	-2253	-2037	-2456	
SG31	Push 1	635	929	1407	2087	2499	2833	3252	3985	4292	3841	
	Pull 1	-39	-628	-1760	-3167	-8152	-9572	-11973	-14918	-18739	-22697	-23881
	Push 2	648	949	1695	2081	2486	2800	3481	4174	4181	2748	-12536
	Pull 2	-39	-615	-1747	-3232	-7969	-9631	-12085	-15258	-19543	-20675	
SG32	Push 1	615	988	1557	2368	3264	4860	6090	6783	7064	2714	
	Pull 1	-131	-687	-1694	-2656	-6691	-9262	-13513	-16947	-20649	-22690	Slipped
	Push 2	608	968	1930	2296	3689	5135	6011	6731	6639	-7483	
	Pull 2	-131	-674	-1642	-2845	-6861	-9641	-13494	-17176	-20656		
SG37	Push 1	-203	-988	-2455	-3136	-6062	-9380	-12248	-15553	-18578	-21046	
	Pull 1	563	903	1479	2049	2867	4072	5204	5813	5963		
	Push 2	-209	-1034	-2802	-3266	-6684	-9767	-12680	-16005	-18990	Slipped	
	Pull 2	563	890	1447	2134	3018	4229	5276	5649	5040		
SG38	Push 1											
	Pull 1					Faulty						
	Push 2											
	Pull 2											
SG39	Push 1	569	883	1322	1878	2114	2186	2821	2343	2094	1754	
	Pull 1	-79	-517	-1420	-2415	-2749	-7552	-10327	-12768	-14783	-15987	-14345
	Push 2	569	851	1577	1898	2061	2742	2343	2160	1937	1132	-4849
	Pull 2	-79	-524	-1427	-2389	-2847	-8023	-10667	-12977	-14960	-13304	
SG40	Push 1	485	773	1166	1651	1637	1657	1382	1159	2476		
	Pull 1	-46	-373	-1022	-1841	-2175	-6511	-9013	-10775	-12007	Slipped	
	Push 2	491	714	1552	1520	1592	1421	1068	989			
	Pull 2	-46	-406	-1120	-1854	-2339	-6891	-9105	-9354			

Table 4-13: PT-HL Maximum Microstrain, Transverse Reinforcement

Strain Gauge	Cycle	0.25%	0.50%	1%	2%	3%	4%	5%	6%	7%	8%	10%
SG09	Push 1	-39	-92	-131	-124	-144	-131	-98	-65	-52	-33	
	Pull 1	-26	-59	-79	-98	-131	-124	-111	-72	-59	-46	-255
	Push 2	-72	-85	-131	-124	-137	-105	-65	-52	-39	-72	-281
	Pull 2	-26	-46	-79	-118	-131	-124	-105	-46	-72	-111	
SG10	Push 1	46	59	46	0	-13	-20	-13	-7	13	-33	
	Pull 1	-13	-7	26	72	0	-46	20	92	137	301	190
	Push 2	33	52	59	20	-7	39	-7	-52	26	406	157
	Pull 2	-13	-26	59	39	-20	-7	72	98	308	229	
SG11	Push 1	20	33	78	52	13	-13	-33	59	131	118	
	Pull 1	-20	-7	-33	-137	-177	-360	-307	-222	-150	-170	-523
	Push 2	7	46	85	46	26	-26	13	144	137	131	-78
	Pull 2	-20	0	-26	-144	-235	-281	-222	-157	-216	-255	
SG12	Push 1	7	33	7	26	46	33	-7	-33	-78	-170	
	Pull 1	7	33	20	105	98	78	65	52	-118	-347	-438
	Push 2	-7	33	26	33	46	13	-13	-20	-124	-177	-105
	Pull 2	7	20	33	85	105	98	46	-39	-183	-386	
SG17	Push 1	7	65	-85	-164	-59	-190	-308	-380	-497	-700	
	Pull 1	-7	26	13	-72	-46	-190	-314	-419	-694	72	2618
	Push 2	7	59	-137	-157	-118	-262	-327	-393	-596	-537	-504
	Pull 2	-7	13	7	-65	-98	-223	-308	-445	-615	1708	
SG18	Push 1	-59	-92	-183	-445	-1027	-1576	-2322	-2486	-2564	-11094	
	Pull 1	-13	-7	-26	-46	-262	-641	-1190	-1524	-1903	-11270	-6456
	Push 2	-72	-111	-235	-497	-962	-1629	-2244	-2316	-2558	-9380	-8078
	Pull 2	-13	-20	-33	-46	-301	-700	-1249	-1531	-2309	-6260	
SG19	Push 1	13	59	39	13	-33	-150	-164	-301	-484	-706	
	Pull 1	46	52	-85	-209	-294	-491	-726	-674	-582	-347	-693
	Push 2	26	39	7	33	-78	-105	-170	-419	-458	-654	-556
	Pull 2	46	39	-85	-183	-281	-497	-693	-595	-412	-523	
SG20	Push 1	13	-7	-20	-39	-65	-216	-223	-216	-262	-380	
	Pull 1	-59	-79	-124	-275	-772	-929	-877	-1034	-1296	602	Slipped
	Push 2	7	-13	-39	-59	-170	-236	-183	-255	-458	-13	
	Pull 2	-59	-92	-124	-275	-733	-805	-844	-1054	-1348		
SG25	Push 1	-7	-20	-52	-183	-353	-511	-517	-530	-550	-295	
	Pull 1	-20	-13	0	-59	-131	-281	-360	-465	-609	-936	-1034
	Push 2	7	-33	-65	-223	-393	-491	-484	-478	-399	-137	-825
	Pull 2	-20	-7	-20	-79	-183	-275	-373	-491	-700	-877	
SG26	Push 1	-46	-72	-111	-190	-373	-556	-766	-903	-962	-995	
	Pull 1	-13	0	46	59	131	144	111	170	216	393	Slipped
	Push 2	-52	-65	-124	-203	-393	-582	-792	-851	-877	-497	
	Pull 2	-13	13	39	46	124	124	92	151	196		

Table 4-14: PT-HL Maximum Microstrain, Transverse Reinforcement

Strain Gauge	Cycle	0.25%	0.50%	1%	2%	3%	4%	5%	6%	7%	8%	10%
SG27	Push 1	-39	-33	0	-85	-151	-327	-386	-452	-478	-491	
	Pull 1	-39	-52	-72	-190	-281	-321	-373	-432	-478	-667	-681
	Push 2	-26	-13	-33	-98	-183	-308	-399	-406	-380	-353	-294
	Pull 2	-39	-46	-85	-190	-268	-294	-366	-419	-537	-543	
SG28	Push 1	-13	-65	-92	-92	-137	-216	-294	-216	-131	-308	
	Pull 1	-72	-92	-124	-190	-491	-635	-864	-1021	-1191	Slipped	
	Push 2	0	-59	-79	-98	-164	-236	-196	-105	-59		
	Pull 2	-72	-79	-118	-177	-458	-667	-870	-1008	-1374		
SG33	Push 1	-46	0	-46	-262	-511	-661	-655	-596	-583	-805	
	Pull 1	-52	-46	-157	-281	-550	-720	-687	-733	-785	-910	-910
	Push 2	-39	-7	-177	-275	-511	-687	-563	-504	-576	-844	-1008
	Pull 2	-52	-46	-183	-334	-609	-713	-648	-707	-759	-812	
SG34	Push 1	-72	-98	-137	-216	-308	-373	-432	-471	-491	-445	
	Pull 1	-20	-26	-59	-105	-124	-190	-190	-183	-190	-222	Slipped
	Push 2	-65	-92	-164	-222	-294	-360	-406	-419	-445	-334	
	Pull 2	-20	-33	-79	-92	-131	-177	-157	-170	-196		
SG35	Push 1	-20	-13	-124	-177	-262	-275	-288	-360	-393	-386	
	Pull 1	0	13	-105	-223	-393	-419	-406	-439	-425	-445	-556
	Push 2	-13	-13	-137	-203	-262	-262	-314	-340	-353	-255	-275
	Pull 2	0	-20	-79	-242	-399	-386	-419	-412	-393	-439	
SG36	Push 1	-26	-26	-59	-59	-33	-85	-222	-380	-432	-445	
	Pull 1	-65	-85	-111	-98	-124	-222	-347	-399	-327	-170	Slipped
	Push 2	-26	-39	-65	-26	13	-124	-275	-347	-373	-131	
	Pull 2	-65	-92	-92	-65	-98	-203	-327	-334	-222	-164	
SG41	Push 1	-39	-13	-33	-105	-236	-308	-353	-406	-497	-582	
	Pull 1	-39	-33	-13	-13	-92	-170	-203	-262	-353	-458	-478
	Push 2	-33	-33	-39	-131	-249	-301	-353	-432	-517	-530	-543
	Pull 2	-39	-46	-7	-20	-124	-183	-249	-301	-386	-471	
SG42	Push 1	-39	-52	-92	-131	-157	-196	-282	-301	-308	-249	
	Pull 1	-7	-13	-20	-46	-52	-59	13	79	157	190	Slipped
	Push 2	-33	-59	-111	-138	-144	-242	-288	-295	-275	-216	
	Pull 2	-7	-7	-39	-52	-72	0	20	124	177		
SG43	Push 1	-52	-26	-13	-92	-223	-334	-399	-452	-504	-602	
	Pull 1	-33	0	-33	-203	-327	-419	-497	-556	-596	-615	-615
	Push 2	-52	-46	-20	-124	-268	-334	-412	-458	-543	-622	-648
	Pull 2	-33	0	-59	-236	-367	-439	-504	-563	-602	-583	
SG44	Push 1	-20	-72	-177	-288	-327	-367	-354	-399	-432	-432	
	Pull 1	-92	-105	-151	-210	-262	-314	-340	-386	-426	-439	Slipped
	Push 2	-39	-85	-242	-308	-334	-334	-367	-373	-439	-203	
	Pull 2	-92	-118	-111	-203	-242	-301	-347	-393	-426	-373	

Table 4-15: PT-HL Maximum Microstrain, Post-Tensioning

Strain Gauge	Cycle	0.25%	0.50%	1%	2%	3%	4%	5%	6%	7%	8%	10%
PT-01	Push 1	-2089	-2246	-2554	-3006	-3412	-3778	-4125	-4452	-4714	-4865	
	Pull 1	-1912	-1834	-1768	-1585	-1441	-1304	-1212	-1048	-891	-695	-394
	Push 2	-2089	-2246	-2711	-2993	-3372	-3739	-4086	-4367	-4596	-4708	-5127
	Pull 2	-1912	-1847	-1723	-1585	-1402	-1277	-1146	-996	-845	-616	
PT-02	Push 1	-1689	-1833	-2101	-2494	-2867	-3175	-3463	-3731	-3967	-4085	
	Pull 1	-1532	-1493	-1427	-1290	-1152	-1041	-943	-799	-661	-498	-255
	Push 2	-1689	-1840	-2245	-2481	-2841	-3155	-3430	-3646	-3843	-3941	-4255
	Pull 2	-1532	-1499	-1381	-1277	-1133	-1021	-890	-766	-622	-419	
PT-03	Push 1	-1930	-2074	-2394	-2813	-3199	-3552	-3860	-4147	-4409	-4533	
	Pull 1	-1746	-1681	-1596	-1432	-1282	-1131	-1007	-857	-693	-477	-202
	Push 2	-1923	-2087	-2545	-2793	-3147	-3513	-3814	-4082	-4291	-4370	-4789
	Pull 2	-1746	-1688	-1544	-1406	-1223	-1086	-961	-817	-634	-392	
PT-04	Push 1	-1951	-2101	-2383	-2841	-3188	-3535	-3862	-4137	-4425	-4563	
	Pull 1	-1767	-1735	-1649	-1558	-1446	-1361	-1276	-1152	-1021	-825	-445
	Push 2	-1944	-2101	-2559	-2828	-3155	-3483	-3803	-4091	-4321	-4406	-4779
	Pull 2	-1767	-1721	-1623	-1545	-1420	-1348	-1224	-1093	-955	-694	
PT-05	Push 1											
	Pull 1					Faulty Gauge						
	Push 2											
	Pull 2											
PT-06	Push 1	-2107	-2244	-2545	-2970	-3324	-3677	-3998	-4279	-4574	-4691	
	Pull 1	-1943	-1878	-1819	-1721	-1636	-1577	-1465	-1354	-1223	-1027	Slipped
	Push 2	-2120	-2244	-2715	-2957	-3298	-3644	-3959	-4220	-4462	-4534	
	Pull 2	-1943	-1891	-1793	-1727	-1596	-1524	-1433	-1308	-1158		
PT-07	Push 1	-2310	-2323	-2447	-2742	-2977	-3160	-3285	-3402	-3487	-3435	
	Pull 1	-2303	-2342	-2454	-2715	-2918	-3056	-3193	-3285	-3350	-3350	-3370
	Push 2	-2297	-2329	-2539	-2735	-2938	-3121	-3252	-3337	-3389	-3311	-3239
	Pull 2	-2303	-2342	-2441	-2715	-2846	-3010	-3121	-3232	-3291	-3213	
PT-08	Push 1											
	Pull 1					Faulty Gauge						
	Push 2											
	Pull 2											
PT-09	Push 1	-1541	-1551	-1655	-1873	-2051	-2170	-2259	-2343	-2402	-2363	
	Pull 1	-1546	-1566	-1640	-1848	-1982	-2081	-2185	-2254	-2303	-2294	-2303
	Push 2	-1536	-1556	-1724	-1843	-2016	-2140	-2219	-2294	-2328	-2269	-2219
	Pull 2	-1546	-1556	-1635	-1823	-1932	-2046	-2130	-2194	-2239	-2190	
PT-10	Push 1	-1957	-1970	-2048	-2251	-2421	-2487	-2513	-2526	-2533	-2362	
	Pull 1	-1976	-2009	-2153	-2519	-2801	-3036	-3213	-3357	-3495	-3527	-3619
	Push 2	-1950	-1970	-2133	-2245	-2317	-2389	-2415	-2415	-2382	-2205	-1937
	Pull 2	-1976	-2022	-2146	-2513	-2749	-2991	-3174	-3298	-3423	-3396	
PT-11	Push 1	-1355	-1355	-1440	-1611	-1774	-1827	-1853	-1866	-1872	-1709	
	Pull 1	-1355	-1395	-1539	-1879	-2154	-2357	-2540	-2684	-2802	-2815	-2920
	Push 2	-1342	-1362	-1506	-1597	-1670	-1728	-1761	-1755	-1728	-1558	-1329
	Pull 2	-1355	-1388	-1539	-1866	-2075	-2305	-2494	-2625	-2724	-2691	
PT-12	Push 1											
	Pull 1					Faulty Gauge						
	Push 2											
	Pull 2											

Table 4-16: PT-HL Maximum Microstrain, Post-Tensioning

Strain Gauge	Cycle	0.25%	0.50%	1%	2%	3%	4%	5%	6%	7%	8%	10%
PT-13	Push 1	-2402	-2330	-2239	-2127	-1931	-1748	-1551	-1342	-1113	-779	
	Pull 1	-2585	-2729	-3030	-3561	-3947	-4320	-4693	-5059	-5419	-5622	-6198
	Push 2	-2402	-2324	-2180	-2023	-1826	-1650	-1460	-1250	-1028	-655	-125
	Pull 2	-2585	-2729	-3037	-3508	-3868	-4274	-4647	-5013	-5314	-5478	
PT-14	Push 1	-2546	-2487	-2389	-2265	-2114	-1937	-1754	-1571	-1374	-1080	
	Pull 1	-2716	-2854	-3122	-3632	-3999	-4313	-4712	-5046	-5393	-5609	-6126
	Push 2	-2526	-2480	-2337	-2186	-2022	-1865	-1675	-1492	-1276	-942	-366
	Pull 2	-2716	-2854	-3128	-3587	-3920	-4313	-4653	-4994	-5308	-5452	
PT-15	Push 1	-2900	-2855	-2724	-2619	-2442	-2246	-2056	-1853	-1624	-1317	
	Pull 1	-3084	-3228	-3515	-4032	-4418	-4778	-5164	-5524	-5871	-6087	-6643
	Push 2	-2881	-2815	-2691	-2534	-2338	-2174	-1971	-1762	-1539	-1160	-545
	Pull 2	-3084	-3221	-3515	-3987	-4347	-4733	-5106	-5472	-5780	-5937	
PT-16	Push 1	-1709	-1637	-1552	-1427	-1296	-1159	-1015	-844	-667	-458	
	Pull 1	-1905	-2036	-2305	-2822	-3261	-3660	-4027	-4401	-4741	-4977	-5540
	Push 2	-1702	-1650	-1493	-1368	-1244	-1100	-943	-766	-602	-340	-150
	Pull 2	-1905	-2023	-2318	-2816	-3202	-3608	-3994	-4355	-4656	-4852	
PT-17	Push 1	-1446	-1394	-1296	-1171	-1008	-857	-706	-510	-346	-163	
	Pull 1	-1630	-1774	-2029	-2527	-2926	-3299	-3666	-4026	-4360	-4655	-5244
	Push 2	-1446	-1394	-1230	-1086	-936	-785	-621	-458	-300	-111	-25
	Pull 2	-1630	-1761	-2036	-2507	-2867	-3253	-3633	-3980	-4308	-4530	
PT-18	Push 1	-1932	-1866	-1775	-1650	-1480	-1375	-1186	-1009	-793	-551	
	Pull 1	-2128	-2265	-2553	-3057	-3508	-3875	-4281	-4647	-4987	-5197	-5753
	Push 2	-1912	-1873	-1703	-1559	-1421	-1271	-1120	-930	-734	-420	-211
	Pull 2	-2128	-2259	-2547	-3037	-3430	-3862	-4235	-4601	-4889	-5046	
PT-19	Push 1											
	Pull 1					Faulty Gauge						
	Push 2											
	Pull 2											
PT-20	Push 1	-1512	-1538	-1623	-1833	-2029	-2206	-2271	-2304	-2343	-2245	
	Pull 1	-1551	-1604	-1767	-2140	-2415	-2651	-2828	-2965	-3043	-3050	-3089
	Push 2	-1499	-1545	-1695	-1826	-1983	-2094	-2160	-2199	-2199	-2016	-1937
	Pull 2	-1551	-1604	-1754	-2121	-2369	-2612	-2775	-2886	-2958	-2867	
PT-21	Push 1	-2208	-2221	-2319	-2529	-2732	-2902	-2981	-3027	-3060	-2955	
	Pull 1	-2234	-2280	-2444	-2811	-3106	-3348	-3545	-3643	-3748	-3748	-3787
	Push 2	-2201	-2241	-2391	-2503	-2673	-2791	-2870	-2915	-2948	-2745	-2680
	Pull 2	-2234	-2286	-2437	-2804	-3066	-3296	-3459	-3590	-3656	-3564	
PT-22	Push 1	-2095	-2121	-2232	-2448	-2684	-2834	-2913	-2946	-2992	-2861	
	Pull 1	-2081	-2121	-2278	-2658	-2952	-3181	-3384	-3509	-3607	-3601	-3633
	Push 2	-2081	-2108	-2304	-2435	-2605	-2730	-2808	-2848	-2854	-2638	-2514
	Pull 2	-2081	-2134	-2278	-2638	-2900	-3155	-3312	-3443	-3502	-3417	
PT-23	Push 1	-1944	-1970	-2075	-2324	-2514	-2677	-2769	-2815	-2854	-2723	
	Pull 1	-1951	-1997	-2134	-2507	-2782	-3024	-3227	-3352	-3456	-3437	-3483
	Push 2	-1944	-1970	-2167	-2291	-2461	-2573	-2664	-2704	-2704	-2494	-2383
	Pull 2	-1951	-1997	-2141	-2501	-2736	-2998	-3155	-3286	-3371	-3267	
PT-24	Push 1											
	Pull 1					Faulty Gauge						
	Push 2											
	Pull 2											

Table 4-17: Residual Displacement Comparison

PT-LL, in (mm)				PT-HL, in (mm)			
Drift (%)	Positive	Negative	Average	Drift (%)	Positive	Negative	Average
0.25	0.05 (1.27)	0.03 (0.76)	0.04 (1.02)	0.25	0.04 (1.02)	0.03 (0.76)	0.04 (1.02)
0.5	0.06 (1.52)	0.06 (1.52)	0.06 (1.52)	0.5	0.06 (1.52)	0.06 (1.52)	0.06 (1.52)
1	0.08 (2.03)	0.12 (3.05)	0.10 (2.54)	1	0.11 (2.79)	0.09 (2.29)	0.10 (2.54)
2	0.20 (5.08)	0.43 (10.92)	0.32 (8.12)	2	0.30 (7.62)	0.31 (7.87)	0.30 (7.62)
3	0.37 (9.40)	1.00 (25.40)	0.69 (17.53)	3	0.75 (19.05)	0.85 (21.59)	0.80 (20.32)
4	0.66 (16.76)	1.84 (46.74)	1.25 (31.75)	4	1.42 (36.07)	1.58 (40.12)	1.50 (38.10)
5	0.98 (24.89)	2.71 (68.83)	1.85 (46.99)	5	2.17 (55.12)	2.35 (59.69)	2.26 (57.40)
6	1.51 (38.35)	3.50 (88.90)	2.50 (63.50)	6	2.94 (74.68)	3.19 (81.03)	3.07 (77.98)
7	1.84 (46.74)	4.04 (102.62)	2.94 (74.68)	7	3.80 (96.52)	4.08 (103.63)	3.94 (100.08)

Table 4-18: Post-Tensioning Forces

PT-LL Tendon Force, kips (kN)				PT-HL Tendon Force, kips (kN)			
Tendon 1	Tendon 2	Tendon 3	Tendon 4	Tendon 1	Tendon 2	Tendon 3	Tendon 4
33.2 (147.7)	39.1 (173.9)	39.3 (174.8)	45.5 (202.4)	46.4 (206.4)	48.5 (215.7)	54.3 (241.5)	44.9 (199.7)
Total Tendon Force=	157.1	kips		Total Tendon Force=	194.1	kips	
	698.8	kN			868.4	kN	
fc=	4489	psi		fc=	4489	psi	
	31.0	MPa			31.0	MPa	
%fcAg=	7.7			%fcAg=	9.6		

Table 4-19: Post-Tensioning Maximum Forces at Each Drift Level

PT-LL				PT-HL			
Drift (%)	Tendon Force, kips (kN)	Drift (%)	Tendon Force, kips (kN)	Drift (%)	Tendon Force, kips (kN)	Drift (%)	Tendon Force, kips (kN)
1	48 (212)	-4	83 (371)	1	59.6 (265.1)	-5	110.1 (489.7)
-1	53 (236)	5	92 (410)	-1	68.7 (305.4)	5	95.0 (422.6)
1	48 (212)	-5	92 (410)	1	63.6 (282.8)	-5	108.9 (484.6)
-1	53 (234)	5	91 (405)	-1	68.8 (305.9)	6	103.3 (459.3)
2	62 (278)	-5	90 (399)	2	70.3 (312.7)	-6	119.0 (529.5)
-2	66 (294)	6	101 (450)	-2	81.4 (362.1)	6	101.6 (451.8)
2	62 (275)	-6	100 (443)	2	69.9 (311.1)	-6	117.8 (524.2)
-2	65 (287)	6	105 (467)	-2	80.6 (358.6)	7	109.9 (488.9)
3	73 (323)	-6	97 (430)	3	79.6 (353.9)	-7	127.6 (567.7)
-3	76 (338)	7	112 (500)	-3	91.5 (406.9)	7	107.1 (476.2)
3	72 (319)	-7	104 (464)	3	78.7 (350.0)	-7	125.5 (558.1)
-3	74 (330)	7	105 (469)	-3	89.7 (399.1)	8	113.2 (503.4)
4	82 (365)	-7	102 (454)	4	88.2 (392.2)	-8	133.3 (593.0)
-4	85 (377)	-10	128 (569)	-4	100.6 (447.3)	8	109.3 (486.1)
4	82 (364)	10	131 (581)	4	87.3 (388.2)	-8	129.8 (577.3)
				-4	99.7 (443.5)	-10	147.2 (654.9)
				5	96.1 (427.4)	10	117.9 (524.3)

Table 5-1: PT-LL Analytical Residual Displacements

PT-LL, in (mm)			
Drift (%)	**Positive**	**Negative**	**Average**
0.25	0.01 (0.21)	0.01 (0.21)	0.01 (0.21)
0.5	0.02 (0.52)	0.01 (0.21)	0.01 (0.21)
1	0.04 (1.1)	0.01 (0.21)	0.03 (0.68)
2	0.18 (4.5)	0.11 (2.8)	0.14 (3.7)
3	0.62 (15.7)	0.77 (19.6)	0.69 (17.6)
4	1.27 (32.2)	1.48 (37.6)	1.38 (34.9)
5	1.95 (49.6)	2.28 (57.8)	2.11 (53.7)
6	2.65 (67.2)	2.93 (74.4)	2.79 (70.8)
7	3.32 (84.4)	3.51 (89.2)	3.42 (86.8)

Table 5-2: PT-HL Analytical Residual Displacements

PT-HL, in (mm)			
Drift (%)	**Positive**	**Negative**	**Average**
0.25	0.06 (1.5)	0.05 (1.3)	0.055 (1.4)
0.5	0.09 (2.3)	0.08 (2.0)	0.085 (2.2)
1	0.18 (4.6)	0.16 (4.1)	0.17 (4.35)
2	0.96 (24.4)	0.44 (11.2)	0.70 (17.8)
3	1.81 (46.0)	1.12 (28.4)	1.47 (37.2)
4	2.66 (67.6)	1.72 (43.7)	2.19 (55.7)
5	3.39 (86.1)	2.09 (53.1)	2.74 (69.6)
6	4.16 (105.7)	2.47 (62.7)	3.32 (84.2)
7	4.96 (126.0)	3.08 (78.2)	4.02 (102.1)

Table 5-3: PT-LL Tendon Forces

Drfit (%)	Force, kips (kN)	Drfit (%)	Force, kips (kN)
1	47 (209)	-4	93 (414)
-1	53 (236)	5	103 (458)
1	47 (209)	-5	106 (472)
-1	53 (236)	5	101 (449)
2	64 (285)	-5	103 (458)
-2	70 (311)	6	114 (507)
2	64 (285)	-6	115 (512)
-2	70 (311)	6	114 (507)
3	80 (356)	-6	113 (503)
-3	84 (374)	7	128 (569)
3	78 (347)	-7	126 (560)
-3	83 (369)	7	131 (583)
4	93 (414)	-7	126 (560)
-4	95 (423)	-10	160 (712)
4	91 (405)	10	180 (801)

Table 5-4: PT-HL Tendon Forces

Drfit (%)	Force, kips (kN)	Drfit (%)	Force, kips (kN)
1	60 (267)	-5	131 (584)
-1	68 (302)	5	121 (537)
1	60 (267)	-5	129 (575)
-1	68 (302)	6	135 (602)
2	76 (340)	-6	144 (641)
-2	85 (377)	6	133 (592)
2	77 (341)	-6	141 (629)
-2	85 (377)	7	146 (650)
3	93 (414)	-7	154 (684)
-3	101 (450)	7	143 (637)
3	93 (411)	-7	151 (670)
-3	101 (447)	8	152 (678)
4	109 (483)	-8	159 (708)
-4	117 (519)	8	148 (659)
4	108 (479)	-8	154 (685)
-4	116 (515)	-10	169 (751)
5	123 (547)	10	180 (799)

Table 5-5: PT-LL Average Residual Displacement Comparison

PT-LL, in (mm)			
Drift (%)	Average Calculated	Average Measured	Difference
0.25	0.01 (0.2)	0.04 (1.0)	0.03 (0.76)
0.5	0.01 (0.2)	0.06 (1.5)	0.05 (1.27)
1	0.03 (0.7)	0.10 (2.6)	0.07 (1.78)
2	0.14 (3.7)	0.32 (8.0)	0.18 (4.57)
3	0.69 (17.6)	0.69 (17.5)	0 (0)
4	1.38 (34.9)	1.25 (31.8)	0.13 (3.30)
5	2.11 (53.7)	1.85 (47.0)	0.26 (6.60)
6	2.79 (70.8)	2.50 (63.6)	0.29 (7.37)
7	3.42 (86.8)	2.94 (74.6)	0.48 (12.19)

Table 5-6: PT-LL Tendon Force Comparison

Drift (%)	Calculated Tendon Force, kips (kN)	Measured Tendon Force, kips (kN)	% Difference
1	47 (209)	48 (212)	1.3
-1	53 (236)	53 (236)	0.3
1	47 (209)	48 (212)	1.5
-1	53 (236)	53 (234)	0.8
2	64 (285)	62 (278)	2.5
-2	70 (311)	66 (294)	5.9
2	64 (285)	62 (275)	3.6
-2	70 (311)	65 (287)	8.5
3	80 (356)	73 (323)	10.3
-3	84 (374)	76 (338)	10.5
3	78 (347)	72 (319)	8.6
-3	83 (369)	74 (330)	11.8
4	93 (414)	82 (365)	13.3
-4	95 (423)	85 (377)	12.2
4	91 (405)	82 (364)	11.2
-4	93 (414)	83 (371)	11.4
5	103 (458)	92 (410)	11.9
-5	106 (472)	92 (410)	14.9
5	101 (449)	91 (405)	10.9
-5	103 (458)	90 (399)	14.8
6	114 (507)	101 (450)	12.7
-6	115 (512)	100 (443)	15.4
6	114 (507)	105 (467)	8.7
-6	113 (503)	97 (430)	16.8
7	128 (569)	112 (500)	13.9
-7	126 (560)	104 (464)	20.8
7	131 (583)	105 (469)	24.3
-7	126 (560)	102 (454)	23.5
-10	160 (712)	128 (569)	25.0
10	180 (801)	131 (581)	37.9

Table 5-7: PT-HL Average Residual Displacement Comparison

PT-HL, in (mm)			
Drift (%)	Average Calculated	Average Measured	Difference
0.25	0.06 (1.5)	0.03 (0.88)	0.03 (0.76)
0.5	0.09 (2.3)	0.06 (1.5)	0.03 (0.76)
1	0.17 (4.4)	0.10 (2.6)	0.07 (1.78)
2	0.70 (17.8)	0.30 (7.7)	0.40 (10.16)
3	1.47 (37.2)	0.80 (20.4)	0.67 (17.02)
4	2.19 (55.7)	1.50 (38.1)	0.69 (17.53)
5	2.74 (69.6)	2.26 (57.4)	0.48 (12.19)
6	3.32 (84.2)	3.07 (77.9)	0.25 (6.35)
7	4.02 (102.1)	3.94 (100.0)	0.08 (2.03)

Table 5-8: PT-HL Tendon Force Comparison

Drift (%)	Calculated Tendon Force, kips (kN)	Measured Tendon Force, kips (kN)	% Difference
1	60 (267)	60 (265)	0.8
-1	68 (302)	69 (305)	1.1
1	60 (267)	64 (283)	5.5
-1	68 (302)	69 (306)	1.3
2	76 (340)	70 (313)	8.7
-2	85 (377)	81 (362)	4.0
2	77 (341)	70 (311)	9.7
-2	85 (377)	81 (359)	5.2
3	93 (414)	80 (354)	16.9
-3	101 (450)	91 (407)	10.5
3	93 (412)	79 (350)	17.5
-3	101 (448)	90 (399)	12.1
4	109 (483)	88 (392)	23.1
-4	117 (519)	101 (447)	16.1
4	108 (479)	87 (388)	23.3
-4	116 (515)	100 (444)	16.0
5	123 (547)	96 (427)	27.9
-5	131 (585)	110 (490)	19.4
5	121 (537)	95 (423)	27.1
-5	129 (575)	109 (485)	18.7
6	135 (602)	103 (459)	31.0
-6	144 (641)	119 (530)	21.1
6	133 (592)	102 (452)	31.0
-6	141 (629)	118 (524)	19.9
7	146 (650)	110 (489)	32.9
-7	154 (684)	128 (568)	20.4
7	143 (637)	107 (476)	33.8
-7	151 (670)	125 (558)	20.0
8	152 (678)	113 (503)	34.7
-8	159 (708)	133 (593)	19.4
8	148 (659)	109 (486)	35.5
-8	154 (685)	130 (577)	18.7
-10	169 (751)	147 (655)	14.6
10	180 (799)	118 (524)	52.4

Table 6-1: PT-LL Prototype Residual Displacements

PT-LL Residual Displacements, in (mm)			
Drift (%)	Positive	Negative	Average
0.25	0 (0)	0 (0)	0 (0)
0.5	0.02 (0.51)	0 (0)	0.01 (0.25)
1	0.12 (3.05)	0.02 (0.51)	0.07 (1.78)
2	0.30 (7.62)	0.25 (6.35)	0.27 (6.89)
3	0.56 (14.22)	0.46 (11.68)	0.51 (13.11)
4	1.11 (28.19)	0.78 (19.81)	0.94 (23.88)
5	1.80 (45.72)	1.70 (43.18)	1.75 (44.45)
6	3.70 (93.98)	3.74 (95.0)	3.72 (94.49)
7	6.17 (156.72)	6.27 (159.26)	6.22 (157.99)
8	10.76 (273.30)	12.83 (325.88)	11.80 (299.72)

Table 6-2: PT-HL Prototype Residual Displacements

PT-HL Residual Displacements, in (mm)			
Drift (%)	Positive	Negative	Average
0.25	0 (0)	0 (0)	0 (0)
0.5	0.02 (0.47)	0.01 (0.13)	0.01 (0.30)
1	0.10 (2.66)	0.03 (0.67)	0.07 (1.67)
2	1.51 (38.48)	1.58 (40.11)	1.55 (39.29)
3	3.21 (81.57)	3.18 (80.83)	3.20 (81.20)
4	4.61 (117.10)	4.46 (113.23)	4.53 (115.16)
5	6.46 (164.06)	6.41 (162.82)	6.43 (163.44)
6	9.19 (233.34)	9.24 (234.61)	9.21 (233.97)
7	12.51 (317.78)	12.55 (318.66)	12.53 (318.22)
8	16.26 (412.92)	16.68 (423.58)	16.47 (418.25)

Table 6-3: PT-LL Prototype Tendon Stresses

Drift (%)	Tendon Stress, ksi (MPa)	Drift (%)	Tendon Stress, ksi (MPa)
1	75.6 (521.5)	5	154.4 (1064.6)
-1	75.9 (523.6)	-5	154.9 (1068.1)
1	75.8 (522.5)	5	151.2 (1042.7)
-1	75.8 (522.7)	-5	151.5 (1044.6)
2	97.6 (672.9)	6	165.5 (1140.8)
-2	98.1 (676.3)	-6	164.8 (1136.4)
2	97.5 (672.3)	6	161.0 (1109.9)
-2	97.7 (673.9)	-6	159.5 (1099.9)
3	118.6 (817.5)	7	170.5 (1175.6)
-3	119.1 (821.0)	-7	168.5 (1161.8)
3	117.2 (808.3)	7	163.2 (1125.4)
-3	117.8 (812.0)	-7	162.0 (1116.7)
4	137.6 (948.5)	8	170.4 (1175.1)
-4	138.7 (956.4)	-8	175.3 (1208.9)
4	135.6 (934.7)	8	167.6 (1155.7)
-4	136.3 (940.0)	-8	173.1 (1193.7)

Table 6-4: PT-HL Prototype Tendon Stresses

Drift (%)	Tendon Stress, ksi (MPa)	Drift (%)	Tendon Stress, ksi (MPa)
1	75.2 (518.2)	5	149.9 (1033.4)
-1	75.4 (519.7)	-5	150.1 (1034.8)
1	75.2 (518.7)	5	147.2 (1015.0)
-1	75.3 (519.3)	-5	147.3 (1015.6)
2	96.1 (662.9)	6	160.9 (1109.2)
-2	96.8 (667.3)	-6	160.7 (1107.9)
2	96.5 (665.5)	6	156.8 (1081.2)
-2	96.7 (666.6)	-6	156.6 (1079.9)
3	116.5 (803.4)	7	167.9 (1157.9)
-3	116.8 (805.2)	-7	167.7 (1156.1)
3	115.2 (796.4)	7	162.0 (1116.8)
-3	115.6 (797.2)	-7	164.5 (1134.2)
4	134.9 (930.2)	8	172.1 (1186.6)
-4	135.2 (932.4)	-8	180.6 (1245.3)
4	132.5 (913.8)	8	170.6 (1176.0)
-4	133.0 (917.0)	-8	164.8 (1136.1)

Table 6-5: Parametric Study

Study	Column	Initial PT, %f'cAg	Axial Dead Load, %f'cAg	Tendon Location	Concrete Strength, ksi (MPa)
I	PT-LL	10%	10%	22.5% of d	4.5 (31)
	PT-LL	10%	15%	22.5% of d	4.5 (31)
	PT-LL	10%	20%	22.5% of d	4.5 (31)
	PT-HL	10%	10%	22.5% of d	4.5 (31)
	PT-HL	10%	15%	22.5% of d	4.5 (31)
	PT-HL	10%	20%	22.5% of d	4.5 (31)
II	PT-LL	15%	6%	22.5% of d	4.5 (31)
	PT-LL	20%	6%	22.5% of d	4.5 (31)
	PT-HL	15%	6%	22.5% of d	4.5 (31)
	PT-HL	20%	6%	22.5% of d	4.5 (31)
III	PT-LL	10%	6%	22.5% of d	10 (69)
	PT-HL	10%	6%	22.5% of d	10 (69)
III'	PT-LL	10%	6%	22.5% of d	10 (69)
	PT-HL	10%	6%	22.5% of d	10 (69)
IV	PT-LL	10%	6%	30% of d	4.5 (31)
	PT-HL	10%	6%	30% of d	4.5 (31)
V	PT-EL	10%	6%	22.5% of d	4.5 (31)

Table 6-6: PT-LL 10%f'cAg Axial Load, Residual Displacements

PT-LL Residual Displacements, in (mm)			
Drift (%)	Positive	Negative	Average
0.25	0 (0)	0 (0)	0 (0)
0.5	0.02 (0.56)	0 (0)	0.01 (0.29)
1	0.11 (2.86)	0.01 (0.19)	0.06 (1.53)
2	0.34 (8.56)	0.25 (6.24)	0.29 (7.40)
3	0.59 (15.08)	0.55 (14.00)	0.57 (15.54)
4	1.15 (29.10)	1.05 (26.73)	1.10 (27.92)
5	2.23 (56.76)	2.21 (117.90)	2.22 (56.39)
6	4.82 (122.43)	4.64 (117.90)	4.73 (120.17)
7	10.19 (258.76)	13.64 (346.45)	11.91 (302.61)

Table 6-7: PT-HL 10%f'_cA_g Axial Load, Residual Displacements

	PT-HL Residual Displacements, in (mm)		
Drift (%)	**Positive**	**Negative**	**Average**
0.25	0 (0)	0 (0)	0 (0)
0.5	0.02 (0.46)	0.01 (0.15)	0.01 (0.31)
1	0.10 (2.45)	0.02 (0.46)	0.06 (1.46)
2	1.20 (30.55)	1.13 (28.66)	1.17 (29.60)
3	2.76 (70.22)	2.72 (69.09)	2.74 (69.66)
4	4.47 (113.44)	4.32 (109.70)	4.39 (111.57)
5	6.47 (164.21)	6.43 (163.39)	6.45 (163.80)
6	9.41 (239.02)	9.53 (242.16)	9.47 (240.59)
7	13.77 (349.71)	14.54 (369.25)	14.15 (359.48)

Table 6-8: PT-LL 15%f'_cA_g Axial Load, Residual Displacements

	PT-LL Residual Displacements, in (mm)		
Drift (%)	**Positive**	**Negative**	**Average**
0.25	0.00 (0.05)	0.00 (0.00)	0 (0)
0.5	0.02 (0.53)	0.00 (0.11)	0.01 (0.32)
1	0.12 (3.08)	0.02 (0.52)	0.07 (1.80)
2	0.51 (12.96)	0.35 (8.88)	0.43 (10.92)
3	0.84 (21.42)	0.74 (18.68)	0.79 (20.05)
4	1.72 (43.75)	1.45 (36.84)	1.59 (40.29)
5	3.41 (86.49)	3.42 (86.89)	3.41 (86.69)

Table 6-9: PT-HL 15%f'_cA_g Axial Load, Residual Displacements

	PT-HL Residual Displacements, in (mm)		
Drift (%)	**Positive**	**Negative**	**Average**
0.25	0.00 (0.04)	0.00 (0.02)	0.00 (0.03)
0.5	0.02 (0.58)	0.00 (0.07)	0.01 (0.33)
1	0.11 (2.84)	0.02 (0.45)	0.06 (1.65)
2	1.09 (27.67)	1.00 (25.43)	1.05 (26.55)
3	2.63 (66.71)	2.60 (66.12)	2.61 (66.42)
4	4.28 (108.76)	4.17 (105.94)	4.23 (107.35)
5	6.56 (166.63)	6.70 (170.28)	6.63 (168.45)
6	11.32 (287.41)	12.22 (310.29)	11.77 (298.85)

Table 6-10: PT-LL 20%f'cAg Axial Load, Residual Displacements

PT-LL Residual Displacements, in (mm)			
Drift (%)	Positive	Negative	Average
0.25	0.00 (0.06)	0.00 (0.00)	0.00 (0.03)
0.5	0.02 (0.55)	0.00 (0.03)	0.01 (0.29)
1	0.13 (3.21)	0.02 (0.42)	0.07 (1.82)
2	0.54 (13.77)	0.46 (11.80)	0.50 (12.78)
3	1.04 (26.42)	0.93 (23.55)	0.98 (24.98)
4	2.21 (56.15)	1.95 (49.52)	2.08 (52.84)
5	5.39 (137.02)	6.13 (155.71)	5.76 (146.36)

Table 6-11: PT-HL 20%f'cAg Axial Load, Residual Displacements

PT-HL Residual Displacements, in (mm)			
Drift (%)	Positive	Negative	Average
0.25	0.00 (0.06)	0.00 (0.00)	0.00 (0.03)
0.5	0.02 (0.58)	0.00 (0.12)	0.01 (0.35)
1	0.11 (2.67)	0.01 (0.32)	0.06 (1.49)
2	1.04 (26.43)	1.00 (25.34)	1.02 (25.89)
3	2.49 (63.33)	2.50 (63.55)	2.50 (63.44)
4	4.30 (109.17)	4.23 (107.48)	4.26 (108.32)
5	7.80 (198.07)	8.00 (203.10)	7.90 (200.59)

Table 6-12: PT-LL 10%f'_cA_g Axial Load, Tendon Stresses

Drift (%)	Tendon Stress, ksi (MPa)	Drift (%)	Tendon Stress, ksi (MPa)
1	74.9 (516.4)	-4	134.2 (925.3)
-1	75.1 (517.8)	4	130.9 (902.3)
1	74.9 (516.6)	-4	130.9 (902.5)
-1	75.0 (517.4)	5	147.7 (1018.7)
2	95.6 (659.0)	-5	147.7 (1018.6)
-2	96.1 (662.4)	5	144.0 (992.8)
2	95.4 (657.9)	-5	144.0 (992.9)
-2	95.7 (659.8)	6	154.5 (1065.5)
3	116.0 (799.7)	-6	153.1 (1055.7)
-3	116.1 (800.2)	6	147.4 (1016.5)
3	114.5 (789.5)	-6	145.1 (1008.8)
-3	114.5 (789.1)	7	149.5 (1030.8)
4	134.0 (923.9)	-7	152.4 (1051.0)

Table 6-13: PT-HL 10%f'_cA_g Axial Load, Tendon Stresses

Drift (%)	Tendon Stress, ksi (MPa)	Drift (%)	Tendon Stress, ksi (MPa)
1	74.6 (514.4)	4	128.1 (883.3)
-1	74.7 (515.4)	-4	128.6 (887.0)
1	74.7 (514.7)	5	143.9 (992.2)
-1	74.7 (515.0)	-5	144.1 (993.8)
2	94.2 (649.7)	5	141.1 (972.5)
-2	95.3 (657.3)	-5	140.5 (968.6)
2	94.7 (652.6)	6	153.4 (1057.4)
-2	95.1 (655.4)	-6	152.5 (1051.2)
3	114.0 (786.0)	6	146.7 (1011.6)
-3	114.4 (789.0)	-6	145.5 (1003.6)
3	112.6 (776.4)	7	152.3 (1050.1)
-3	112.9 (778.6)	-7	156.6 (1080.1)
4	130.3 (898.3)	7	148.6 (1024.7)
-4	130.8 (901.8)	-7	152.4 (1050.8)

Table 6-14: PT-LL 15%f'$_c$A$_g$ Axial Load, Tendon Stresses

Drift (%)	Tendon Stress, ksi (MPa)	Drift (%)	Tendon Stress, ksi (MPa)
1	74.6 (514.6)	-3	110.4 (760.9)
-1	74.8 (515.5)	4	127.4 (878.5)
1	74.7 (515.0)	-4	127.8 (881.4)
-1	74.8 (515.5)	4	124.2 (856.5)
2	93.6 (645.7)	-4	124.4 (857.5)
-2	94.1 (648.7)	5	137.8 (950.4)
2	93.3 (643.4)	-5	136.9 (943.7)
-2	93.5 (644.5)	5	131.5 (906.7)
3	112.1 (773.3)	-5	129.5 (892.9)
-3	112.2 (773.6)	6	128.9 (889.0)
3	110.3 (760.3)		

Table 6-15: PT-HL 15%f'$_c$A$_g$ Axial Load, Tendon Stresses

Drift (%)	Tendon Stress, ksi (MPa)	Drift (%)	Tendon Stress, ksi (MPa)
1	74.5 (513.6)	4	126.0 (869.1)
-1	74.6 (514.5)	-4	126.2 (870.5)
1	74.5 (514.0)	4	123.2 (849.6)
-1	74.6 (514.4)	-4	123.3 (850.4)
2	92.8 (640.2)	5	136.9 (943.7)
-2	93.6 (645.3)	-5	136.2 (939.1)
2	92.8 (639.6)	5	131.5 (907.0)
-2	93.1 (641.7)	-5	130.0 (896.7)
3	111.0 (765.4)	6	135.4 (933.4)
-3	111.1 (766.1)	-6	133.6 (921.5)
3	109.2 (753.0)	6	127.0 (875.8)
-3	109.5 (754.7)	-6	113.6 (783.2)

Table 6-16: PT-LL 20%f'cAg Axial Load, Tendon Stresses

Drift (%)	Tendon Stress, ksi (MPa)	Drift (%)	Tendon Stress, ksi (MPa)
1	74.2 (511.7)	3	106.2 (732.3)
-1	74.3 (512.3)	-3	106.2 (732.1)
1	74.2 (511.8)	4	121.7 (839.1)
-1	74.3 (512.3)	-4	121.4 (837.2)
2	92.0 (634.5)	4	116.7 (804.6)
-2	91.6 (633.7)	-4	115.9 (798.8)
2	91.3 (629.6)	5	121.4 (837.1)
-2	91.1 (628.2)	-5	112.9 (778.6)
3	108.8 (750.0)	5	93.9 (647.6)
-3	108.7 (749.2)		

Table 6-17: PT-HL 20%f'cAg Axial Load, Tendon Stresses

Drift (%)	Tendon Stress, ksi (MPa)	Drift (%)	Tendon Stress, ksi (MPa)
1	74.0 (510.4)	-3	105.5 (727.6)
-1	74.1 (510.9)	4	121.0 (834.5)
1	74.1 (510.7)	-4	120.8 (832.7)
-1	74.1 (510.9)	4	116.6 (804.3)
2	91.3 (629.4)	-4	116.2 (801.3)
-2	91.6 (631.4)	5	124.8 (860.2)
2	90.8 (626.2)	-5	121.5 (837.4)
-2	90.8 (625.8)	5	107.9 (743.8)
3	108.0 (744.8)	-5	106.7 (735.6)
-3	107.9 (743.9)	6	65.2 (449.8)
3	105.6 (728.3)		

Table 6-18: PT-LL 15%f'_cA_g Initial Post-Tensioning, Residual Displacements

PT-LL Residual Displacements, in (mm)			
Drift (%)	Positive	Negative	Average
0.25	0.00 (0.03)	0.00 (0.02)	0.00 (0.03)
0.5	0.02 (0.57)	0.00 (0.09)	0.01 (0.33)
1	0.12 (2.97)	0.01 (0.37)	0.07 (1.67)
2	0.37 (9.31)	0.38 (9.75)	0.38 (9.53)
3	0.56 (14.13)	0.67 (16.99)	0.61 (15.56)
4	1.27 (32.13)	1.14 (29.00)	1.20 (30.57)
5	2.48 (62.88)	2.44 (61.86)	2.46 (62.37)
6	5.46 (138.57)	5.42 (137.74)	5.44 (138.15)
7	10.74 (272.77)	11.35 (288.22)	11.04 (280.49)

Table 6-19: PT-HL 15%f'_cA_g Initial Post-Tensioning, Residual Displacements

PT-HL Residual Displacements, in (mm)			
Drift (%)	Positive	Negative	Average
0.25	0.00 (0.06)	0.00 (0.01)	0.00 (0.03)
0.5	0.02 (0.53)	0.00 (0.12)	0.01 (0.32)
1	0.10 (2.65)	0.02 (0.56)	0.06 (1.60)
2	1.18 (30.07)	1.14 (29.08)	1.16 (29.58)
3	2.77 (70.39)	2.78 (70.60)	2.78 (70.49)
4	4.29 (108.92)	4.30 (109.31)	4.30 (109.11)
5	6.39 (162.32)	6.34 (161.07)	6.37 (161.69)
6	9.76 (247.87)	9.87 (250.73)	9.82 (249.30)
7	14.41 (366.09)	14.82 (376.31)	14.61 (371.20)
8	19.13 (485.94)	20.77 (527.48)	19.95 (506.71)

Table 6-20: PT-LL 20%f'_cA_g Initial Post-Tensioning, Residual Displacements

PT-LL Residual Displacements, in (mm)			
Drift (%)	Positive	Negative	Average
0.25	0.00 (0.05)	0.00 (0.00)	0.00 (0.03)
0.5	0.02 (0.57)	0.00 (0.09)	0.01 (0.33)
1	0.12 (3.17)	0.02 (0.40)	0.07 (1.79)
2	0.50 (12.72)	0.39 (9.79)	0.44 (11.26)
3	0.88 (22.47)	0.77 (19.65)	0.83 (21.06)
4	1.80 (45.63)	1.57 (39.84)	1.68 (42.73)
5	3.72 (94.51)	3.61 (91.75)	3.67 (93.13)
6	9.21 (233.84)	11.06 (280.91)	10.13 (257.37)

Table 6-21: PT-HL 20%f'_cA_g Initial Post-Tensioning, Residual Displacements

PT-HL Residual Displacements, in (mm)			
Drift (%)	Positive	Negative	Average
0.25	0.00 (0.04)	0.00 (0.00)	0.00 (0.02)
0.5	0.02 (0.55)	0.00 (0.08)	0.01 (0.31)
1	0.10 (2.50)	0.01 (0.36)	0.06 (1.43)
2	1.02 (26.01)	0.96 (24.41)	0.99 (25.21)
3	2.53 (64.35)	2.52 (64.07)	2.53 (64.21)
4	4.20 (106.67)	4.11 (104.39)	4.15 (105.53)
5	6.65 (168.95)	6.65 (168.95)	6.65 (168.95)
6	11.87 (301.60)	12.30 (312.42)	12.09 (307.01)

Table 6-22: PT-LL 15% of ALI Initial Post-Tensioning, Tendon Stresses

Drift (%)	Tendon Stress, ksi (MPa)	Drift (%)	Tendon Stress, ksi (MPa)
1	104.4 (719.6)	4	158.9 (1095.8)
-1	104.6 (721.0)	-4	159.2 (1097.6)
1	104.4 (720.1)	5	175.0 (1206.8)
-1	104.5 (720.5)	-5	175.0 (1206.5)
2	124.8 (860.7)	5	170.6 (1176.3)
-2	124.8 (860.8)	-5	170.4 (1175.0)
2	124.8 (860.7)	6	179.9 (1240.3)
-2	124.4 (857.4)	-6	179.1 (1235.1)
3	144.9 (991.1)	6	171.5 (1182.8)
-3	144.4 (995.9)	-6	169.7 (1170.3)
3	143.0 (985.8)	7	168.9 (1164.5)
-3	142.9 (985.4)	-7	161.7 (1115.1)
4	161.9 (1116.2)	7	145.3 (1001.5)
-4	162.1 (1117.9)	-7	113.7 (783.9)

Table 6-23: PT-HL 15% of ALI Initial Post-Tensioning, Tendon Stresses

Drift (%)	Tendon Stress, ksi (MPa)	Drift (%)	Tendon Stress, ksi (MPa)
1	104.1 (718.1)	-4	156.8 (1081.2)
-1	104.3 (719.0)	5	172.4 (1188.5)
1	104.2 (718.4)	-5	172.5 (1189.1)
-1	104.2 (718.7)	5	168.6 (1162.8)
2	123.6 (852.4)	-5	168.6 (1162.7)
-2	124.4 (857.4)	6	179.6 (1238.2)
2	123.8 (853.7)	-6	178.8 (1232.7)
-2	123.9 (854.2)	6	172.8 (1191.5)
3	142.9 (985.5)	-6	171.4 (1181.5)
-3	142.9 (985.1)	7	174.6 (1203.6)
3	141.5 (975.5)	-7	169.1 (1166.1)
-3	141.4 (975.1)	7	156.1 (1076.1)
4	159.3 (1098.5)	-7	153.0 (1054.6)
-4	159.3 (1098.2)	8	138.5 (955.3)
4	156.8 (1081.1)		

Table 6-24: PT-LL 20% of ALI Initial Post-Tensioning, Tendon Stresses

Drift (%)	Tendon Stress, ksi (MPa)	Drift (%)	Tendon Stress, ksi (MPa)
1	133.1 (918.0)	-3	168.2 (1159.8)
-1	133.3 (919.0)	4	184.2 (1269.8)
1	133.2 (918.3)	-4	184.4 (1271.3)
-1	133.3 (918.9)	4	180.8 (1246.3)
2	152.0 (1048.0)	-4	180.8 (1246.6)
-2	152.2 (1049.6)	5	191.8 (1322.4)
2	151.5 (1044.9)	-5	190.9 (1316.5)
-2	151.6 (1045.5)	5	184.5 (1272.0)
3	170.0 (1172.5)	-5	182.2 (1256.2)
-3	170.2 (1173.2)	6	179.3 (1236.5)
3	168.2 (1159.5)	-6	165.3 (1139.9)

Table 6-25: PT-HL 20% of ALI Initial Post-Tensioning, Tendon Stresses

Drift (%)	Tendon Stress, ksi (MPa)	Drift (%)	Tendon Stress, ksi (MPa)
1	133.0 (917.1)	4	183.2 (1263.5)
-1	133.1 (917.9)	-4	183.3 (1264.0)
1	133.1 (917.5)	4	180.3 (1243.1)
-1	133.1 (917.8)	-4	180.1 (1241.7)
2	151.2 (1042.2)	5	191.7 (1321.8)
-2	151.7 (1046.3)	-5	191.3 (1318.8)
2	151.0 (1041.2)	5	185.7 (1280.5)
-2	151.2 (1042.4)	-5	184.6 (1272.6)
3	169.0 (1165.5)	6	186.9 (1288.6)
-3	169.1 (1166.0)	-6	179.6 (1238.4)
3	167.2 (1152.6)	6	165.0 (1137.9)
-3	167.4 (1153.9)	-6	146.9 (1012.8)

Table 6-26: PT-LL Study III, f'c=10 ksi (69 MPa), Residual Displacements

PT-LL Residual Displacements, in (mm)			
Drift (%)	Positive	Negative	Average
0.25	0.00 (0.01)	0.00 (0.00)	0.00 (0.01)
0.5	0.02 (0.49)	0.00 (0.10)	0.01 (0.30)
1	0.09 (2.20)	0.03 (0.81)	0.06 (1.51)
2	0.19 (4.93)	0.12 (3.08)	0.16 (4.01)
3	0.28 (7.14)	0.24 (6.18)	0.26 (6.66)
4	0.74 (18.89)	0.67 (17.04)	0.71 (17.96)
5	2.38 (60.53)	2.36 (59.94)	2.37 (60.24)
6	8.26 (209.71)	10.09 (256.22)	9.17 (232.96)

Table 6-27: PT-HL Study III, f'c=10 ksi (69 MPa), Residual Displacements

PT-HL Residual Displacements, in (mm)			
Drift (%)	Positive	Negative	Average
0.25	0.00 (0.02)	0.00 (0.01)	0.00 (0.02)
0.5	0.02 (0.48)	0.00 (0.11)	0.01 (0.29)
1	0.09 (2.33)	0.03 (0.80)	0.06 (1.56)
2	0.34 (8.62)	0.28 (7.08)	0.31 (7.85)
3	0.72 (18.29)	0.70 (17.73)	0.71 (18.01)
4	1.81 (46.04)	1.69 (42.94)	1.75 (44.49)
5	4.26 (108.23)	4.35 (110.43)	4.30 (109.33)
6	10.22 (259.70)	11.77 (299.08)	11.00 (279.39)

Table 6-28: PT-LL Study III', f'c=10 ksi (69 MPa), Residual Displacements

PT-LL Residual Displacements, in (mm)			
Drift (%)	Positive	Negative	Average
0.25	0.01 (0.16)	0.00 (0.04)	0.00 (0.10)
0.5	0.02 (0.43)	0.01 (0.24)	0.01 (0.34)
1	0.06 (1.63)	0.03 (0.66)	0.05 (1.15)
2	0.06 (1.41)	0.06 (1.51)	0.06 (1.57)
3	0.12 (2.93)	0.23 (5.83)	0.17 (4.38)
4	0.65 (16.50)	0.89 (22.61)	0.77 (19.56)
5	1.70 (43.14)	1.67 (42.43)	1.68 (42.79)
6	3.11 (79.00)	3.31 (84.16)	3.21 (81.58)
7	5.83 (147.98)	6.09 (154.65)	5.96 (151.32)
8	8.58 (217.92)	8.60 (218.39)	8.59 (218.15)

Table 6-29: PT-HL Study III', f'c=10 ksi (69 MPa), Residual Displacements

PT-HL Residual Displacements, in (mm)			
Drift (%)	Positive	Negative	Average
0.25	0.01 (0.13)	0.00 (0.06)	0.00 (0.10)
0.5	0.01 (0.31)	0.01 (0.21)	0.01 (0.26)
1	0.08 (2.14)	0.04 (0.97)	0.06 (1.56)
2	0.81 (20.66)	0.99 (25.04)	0.90 (22.85)
3	1.52 (38.49)	1.54 (39.20)	1.53 (38.84)
4	2.76 (70.20)	2.68 (68.05)	2.72 (69.13)
5	4.61 (117.18)	4.53 (114.97)	4.57 (116.08)
6	6.98 (177.18)	7.09 (179.97)	7.03 (178.58)
7	10.64 (270.38)	10.39 (264.03)	10.52 (267.20)
8	14.51 (368.57)	13.31 (338.02)	13.91 (353.30)

Table 6-30: PT-LL Study III, f'c=10 ksi (69 MPa), Tendon Stresses

Drift (%)	Tendon Stress, ksi (MPa)	Drift (%)	Tendon Stress, ksi (MPa)
1	75.9 (523.2)	-3	115.6 (797.3)
-1	76.0 (524.1)	4	131.4 (905.7)
1	76.0 (523.7)	-4	130.7 (901.4)
-1	76.0 (524.0)	4	128.1 (883.1)
2	97.4 (671.4)	-4	128.1 (883.3)
-2	97.6 (673.1)	5	137.2 (946.2)
2	97.4 (671.7)	-5	137.0 (944.7)
-2	97.4 (671.3)	5	131.4 (906.2)
3	116.8 (805.5)	-5	130.4 (898.9)
-3	116.9 (805.8)	6	126.6 (872.9)
3	115.4 (795.6)	-6	118.3 (815.7)

Table 6-31: PT-HL Study III, f'c=10 ksi (69 MPa), Tendon Stresses

Drift (%)	Tendon Stress, ksi (MPa)	Drift (%)	Tendon Stress, ksi (MPa)
1	75.5 (520.7)	4	129.4 (892.5)
-1	75.7 (521.8)	-4	129.6 (893.6)
1	75.6 (521.4)	4	127.0 (875.3)
-1	75.6 (521.5)	-4	127.0 (875.4)
2	96.4 (664.8)	5	137.7 (949.3)
-2	96.9 (668.4)	-5	136.9 (944.2)
2	96.6 (665.9)	5	132.7 (914.9)
-2	96.7 (666.6)	-5	131.2 (904.6)
3	115.4 (795.7)	6	132.5 (913.6)
-3	115.5 (796.0)	-6	130.2 (897.8)
3	114.2 (787.2)	6	107.9 (744.2)
-3	114.2 (787.7)		

Table 6-32: PT-LL Study III', f'c=10 ksi (69 MPa), Tendon Stresses

Drift (%)	Tendon Stress, ksi (MPa)	Drift (%)	Tendon Stress, ksi (MPa)
1	77.6 (535.2)	5	170.9 (1178.1)
-1	77.9 (537.0)	-5	171.2 (1180.3)
1	77.8 (536.6)	5	168.3 (1160.1)
-1	77.9 (537.1)	-5	168.8 (1163.8)
2	103.5 (713.6)	6	183.1 (1262.6)
-2	103.5 (713.9)	-6	182.9 (1261.1)
2	103.6 (714.7)	6	177.3 (1222.5)
-2	103.4 (713.3)	-6	177.3 (1222.8)
3	128.0 (882.3)	7	184.9 (1275.0)
-3	127.5 (879.4)	-7	183.6 (1265.8)
3	127.4 (878.7)	7	177.0 (1220.5)
-3	127.2 (877.1)	-7	175.5 (1210.0)
4	150.6 (1038.1)	8	180.9 (1247.1)
-4	150.9 (1040.4)	-8	188.2 (1297.4)
4	149.7 (1032.4)	8	179.8 (1240.0)
-4	149.3 (1029.6)		

Table 6-33: PT-HL Study III', f'_c=10 ksi (69 MPa), Tendon Stresses

Drift (%)	Tendon Stress, ksi (MPa)	Drift (%)	Tendon Stress, ksi (MPa)
1	76.8 (529.4)	5	166.0 (1144.6)
-1	77.1 (531.4)	-5	167.3 (1153.4)
1	77.0 (530.6)	5	163.5 (1127.3)
-1	77.1 (531.5)	-5	164.2 (1131.9)
2	102.0 (703.2)	6	179.7 (1239.1)
-2	102.0 (703.1)	-6	178.6 (1231.2)
2	102.3 (705.5)	6	175.3 (1208.9)
-2	101.8 (701.7)	-6	172.9 (1192.0)
3	125.7 (866.4)	7	182.5 (1258.5)
-3	125.5 (865.1)	-7	182.3 (1256.9)
3	125.1 (862.9)	7	177.3 (1222.3)
-3	125.0 (862.0)	-7	176.4 (1216.1)
4	147.6 (1017.7)	8	183.8 (1267.5)
-4	148.3 (1022.7)	-8	190.0 (1310.0)
4	146.5 (1010.2)	8	182.0 (1255.0)
-4	146.9 (1012.6)	-8	191.4 (1319.5)

Table 6-34: PT-LL 30% of Diameter Tendon Location, Residual Displacements

PT-LL Residual Displacements, in (mm)			
Drift (%)	Positive	Negative	Average
0.25	0.00 (0.06)	0.00 (0.04)	0.00 (0.05)
0.5	0.02 (0.55)	0.01 (0.19)	0.01 (0.37)
1	0.11 (2.77)	0.04 (1.11)	0.08 (1.94)
2	0.30 (7.58)	0.29 (7.48)	0.30 (7.53)
3	0.45 (11.56)	0.50 (12.66)	0.48 (12.11)
4	0.98 (24.81)	0.77 (19.67)	0.88 (22.24)
5	1.63 (41.29)	1.51 (38.43)	1.57 (39.86)
6	3.20 (81.31)	3.33 (84.53)	3.26 (82.92)
7	6.39 (162.18)	6.73 (170.84)	6.56 (166.51)

Table 6-35: PT-HL 30% of Diameter Tendon Location, Residual Displacements

PT-HL Residual Displacements, in (mm)			
Drift (%)	Positive	Negative	Average
0.25	0.00 (0.10)	0.00 (0.02)	0.00 (0.06)
0.5	0.02 (0.46)	0.01 (0.18)	0.01 (0.32)
1	0.11 (2.76)	0.04 (1.00)	0.07 (1.88)
2	1.53 (38.89)	1.59 (40.30)	1.56 (39.60)
3	3.12 (79.23)	3.11 (78.90)	3.11 (79.06)
4	4.37 (111.10)	4.18 (106.17)	4.28 (108.64)
5	5.74 (145.71)	5.68 (144.38)	5.71 (145.05)
6	7.81 (198.46)	7.80 (198.21)	7.81 (198.33)
7	11.09 (281.79)	11.14 (282.99)	11.12 (282.39)
8	16.94 (430.28)	17.97 (456.55)	17.46 (443.42)

Table 6-36: PT-LL 30% of Diameter Tendon Location, Tendon Stresses

Drift (%)	Tendon Stress, ksi (MPa)	Drift (%)	Tendon Stress, ksi (MPa)
1	80.4 (554.3)	4	151.1 (1041.8)
-1	80.6 (555.8)	-4	151.7 (1045.8)
1	80.5 (555.0)	5	174.0 (1199.7)
-1	80.5 (555.2)	-5	174.6 (1204.1)
2	106.0 (730.6)	5	170.7 (1177.0)
-2	106.1 (731.4)	-5	171.2 (1180.3)
2	106.0 (731.1)	6	187.6 (1293.3)
-2	105.7 (728.6)	-6	187.8 (1295.0)
3	130.7 (901.4)	6	189.4 (1306.0)
-3	130.5 (899.5)	-6	191.8 (1322.3)
3	129.5 (892.7)	7	200.9 (1385.1)
-3	129.3 (891.3)	-7	208.8 (1440.0)
4	153.1 (1055.9)	7	208.0 (1434.4)
-4	153.8 (1060.6)	-7	209.6 (1445.5)

Table 6-37: PT-HL 30% of Diameter Tendon Location, Tendon Stresses

Drift	Tendon Stress, ksi (MPa)	Drift	Tendon Stress, ksi (MPa)
1	79.9 (550.7)	-4	148.9 (1026.8)
-1	80.1 (552.1)	5	169.5 (1168.5)
1	80.0 (551.6)	-5	169.9 (1171.3)
-1	80.0 (551.9)	5	167.2 (1152.9)
2	104.5 (720.8)	-5	167.1 (1152.0)
-2	105.1 (724.8)	6	184.0 (1268.8)
2	104.8 (722.8)	-6	187.7 (1294.4)
-2	105.0 (723.9)	6	188.1 (1296.9)
3	128.6 (886.8)	-6	193.0 (1331.0)
-3	128.7 (887.5)	7	202.0 (1393.0)
3	127.5 (879.0)	-7	210.2 (1449.0)
-3	127.6 (880.1)	7	208.9 (1440.5)
4	150.1 (1035.2)	-7	210.2 (1449.2)
-4	150.7 (1039.1)	8	210.7 (1452.5)
4	148.4 (1023.4)	-8	213.7 (1473.2)

Table 6-38: PT-EL 0.34% Longitudinal Reinforcement Residual Displacements

PT-EL Residual Displacements, in (mm)			
Drift (%)	Positive	Negative	Average
0.25	0 (0)	0 (0)	0 (0)
0.5	0.02 (0.51)	0 (0)	0.01 (0.25)
1	0.11 (2.71)	0.03 (0.69)	0.07 (1.78)
2	0.15 (3.90)	0.10 (2.59)	0.13 (3.18)
3	0.25 (6.40)	0.15 (3.70)	0.20 (5.08)
4	0.46 (11.67)	0.30 (7.69)	0.38 (9.65)
5	0.88 (22.33)	0.73 (18.57)	0.81 (20.45)
6	2.20 (55.96)	2.10 (53.32)	2.15 (54.61)
7	5.08 (129.11)	5.13 (130.42)	5.11 (129.67)
8	12.32 (312.95)		

Table 6-39: PT-EL 0.34% Longitudinal Reinforcement Tendon Stresses

Drift (%)	Tendon Stress, ksi (MPa)	Drift (%)	Tendon Stress, ksi (MPa)
1	76.2 (525.4)	-4	136.4 (940.8)
-1	76.4 (526.9)	5	154.1 (1062.5)
1	76.3 (526.3)	-5	154.9 (1067.7)
-1	76.4 (526.6)	5	150.3 (1036.2)
2	98.6 (680.0)	-5	150.6 (1038.1)
-2	98.8 (681.2)	6	161.7 (1114.9)
2	98.3 (677.9)	-6	160.4 (1106.3)
-2	98.5 (678.8)	6	155.2 (1070.4)
3	119.5 (824.1)	-6	154.2 (1062.9)
-3	119.8 (826.1)	7	162.5 (1120.7)
3	118.2 (815.3)	-7	160.9 (1109.2)
-3	118.5 (816.7)	7	153.5 (1058.6)
4	138.4 (954.4)	-7	156.9 (1082.1)
-4	138.7 (956.7)	8	151.9 (1047.7)
4	136.1 (938.2)	-8	148.0 (1020.5)
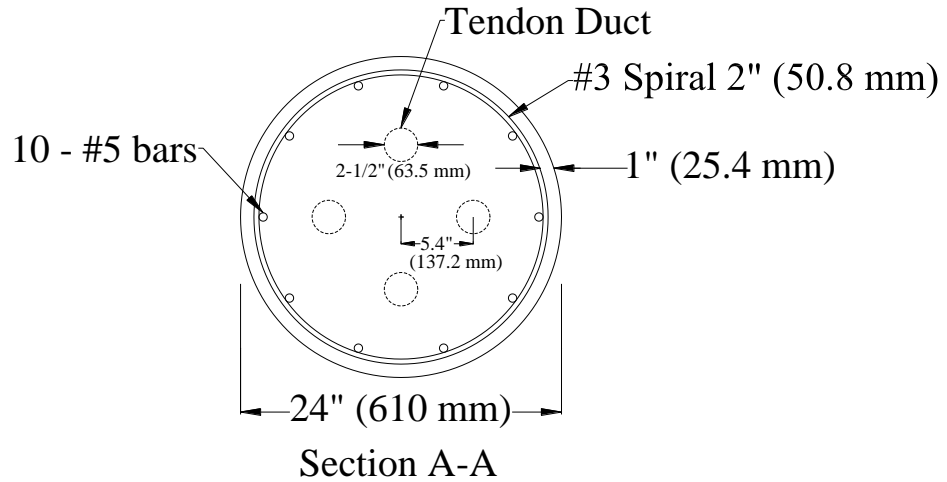
Section A-A

Figure 2-1: PT-LL Cross Section
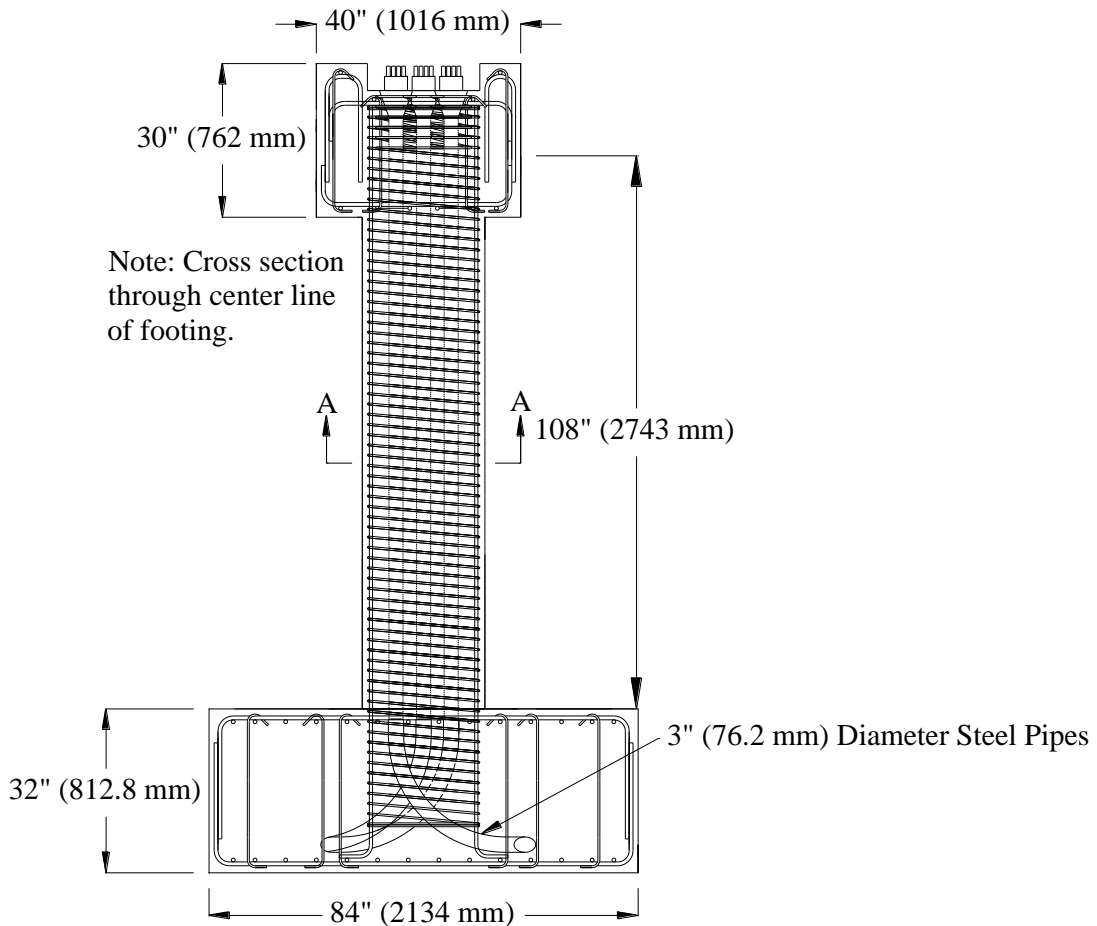
Figure 2-2: PT-LL Elevation

98

Tendon Duct

#3 Spiral 2" (50.8 mm) Pitch

10 - #7 bars

2-1/2" (63.5 mm)

1" (25.4 mm)

5.4"
(137.2 mm)

24" (610 mm)
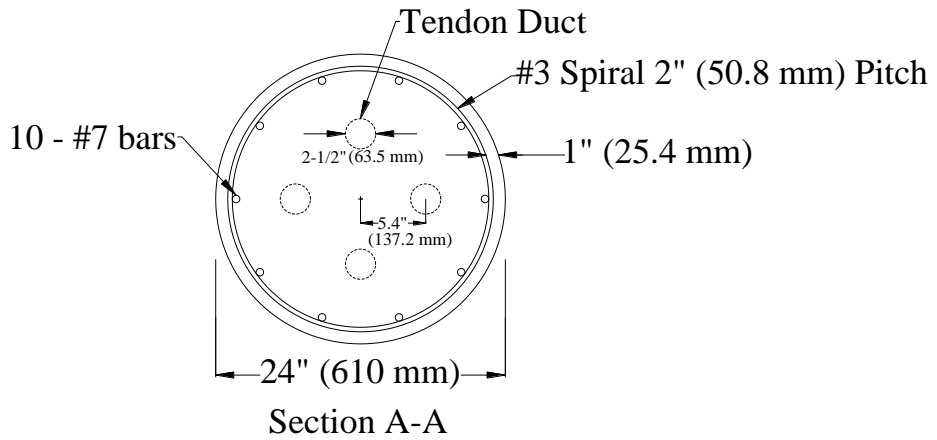
Section A-A

Figure 2-3: PT-HL Cross Section

40" (1016 mm)

30" (762 mm)

Note: Cross section through center line of footing.

A   A

108" (2743 mm)

3" (76.2 mm) Diameter Steel Pipes

32" (812.8 mm)

84" (2134 mm)
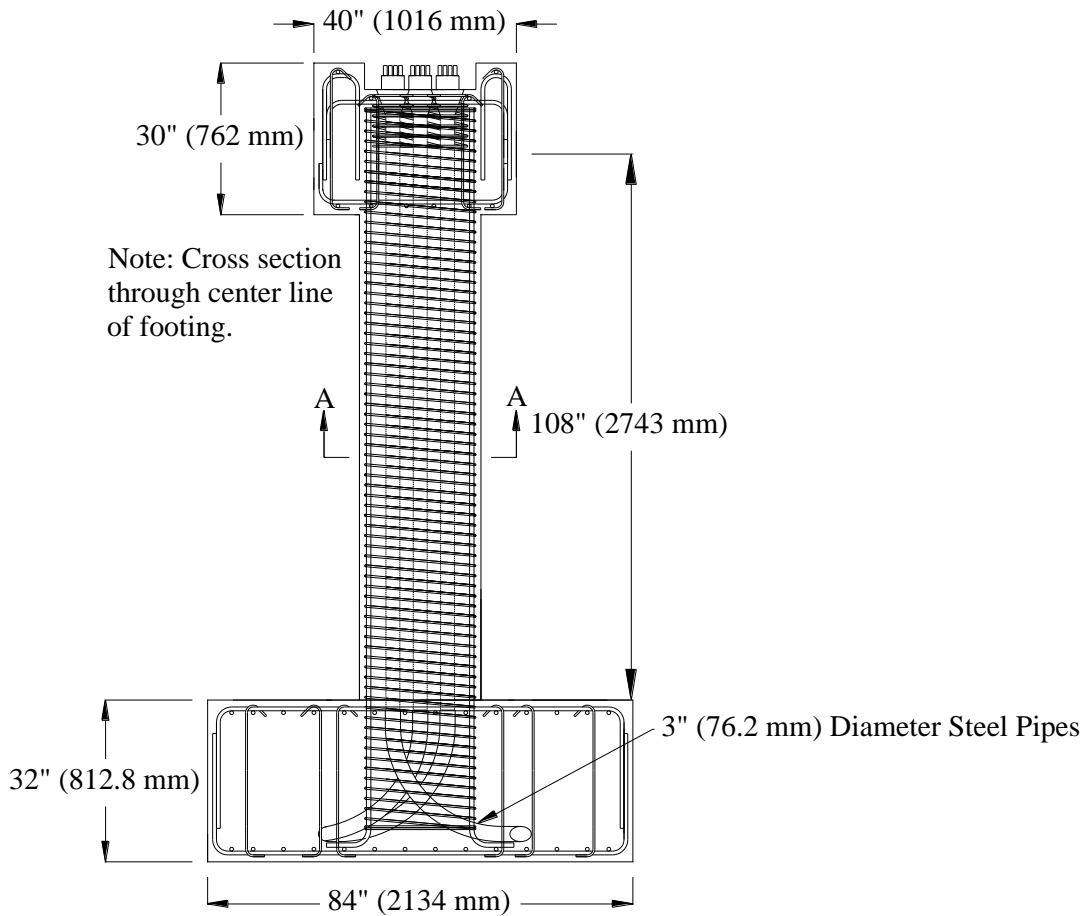
Figure 2-4: PT-HL Elevation

1" (25.4 mm)

32" (812.8 mm)

84" (2134 mm)

4" (101.6 mm)
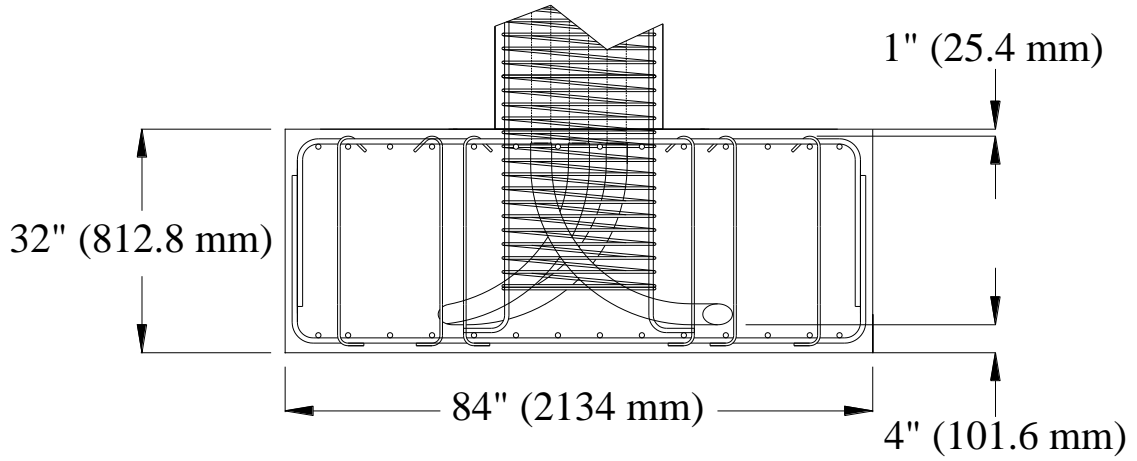
Figure 2-5: Footing Elevation

$5\frac{7}{8}$" (149 mm)

Axial Dead Load Tie Down

Footing Tie Down

North

Tendon Duct

84" (2134 mm)

Steel Pipe

Anchorage

84" (2134 mm)
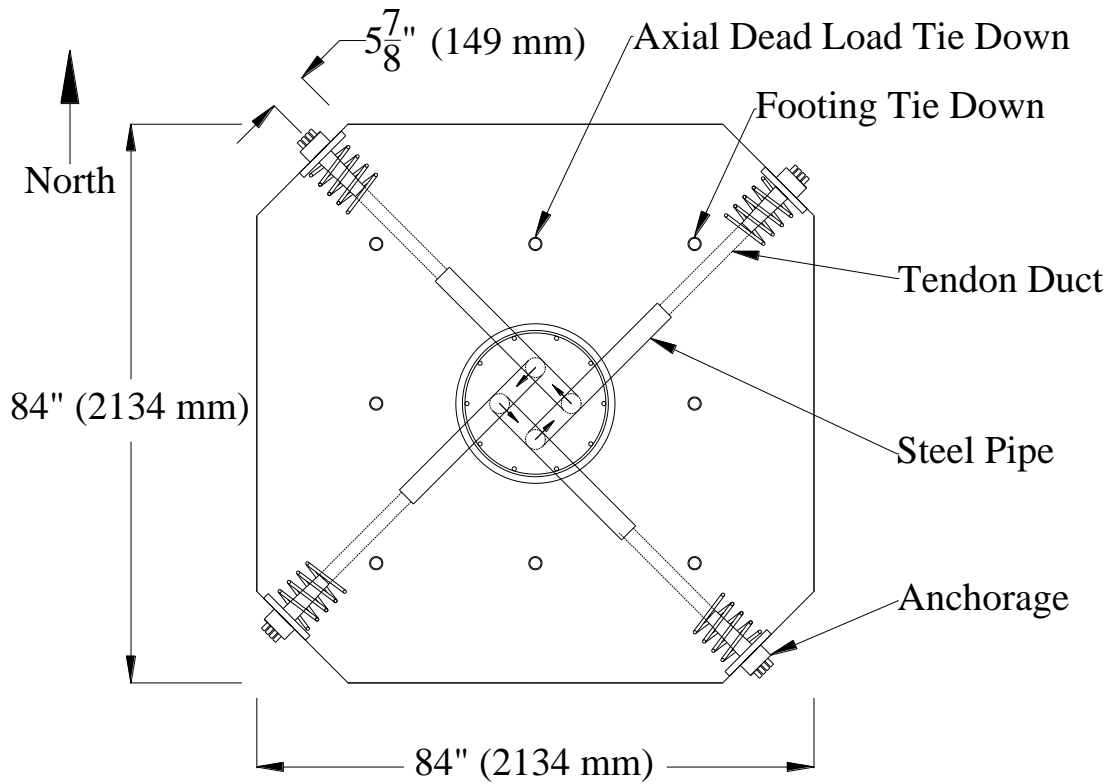
Figure 2-6: Footing Plan View

#3 J Hook

84" (2134 mm)

North

6" (152 mm)
Spacing (Typ.)

#6 bars

2-1/2" (63.5 mm) Dia Schedule 40 PVC Pipe
(Typ.)

84" (2134 mm)
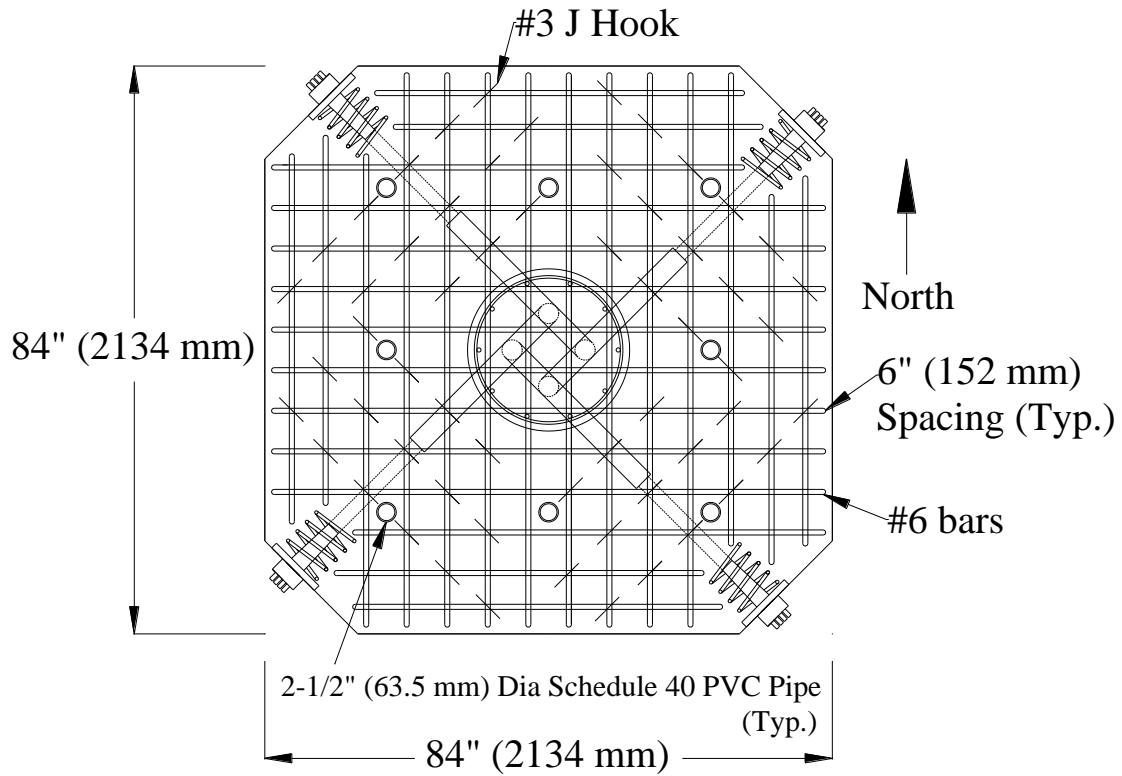
Figure 2-7: Footing Reinforcement Plan View

#3 J-Hook   Anchorage

36" (914 mm)

#7 bars

40" (1016 mm)
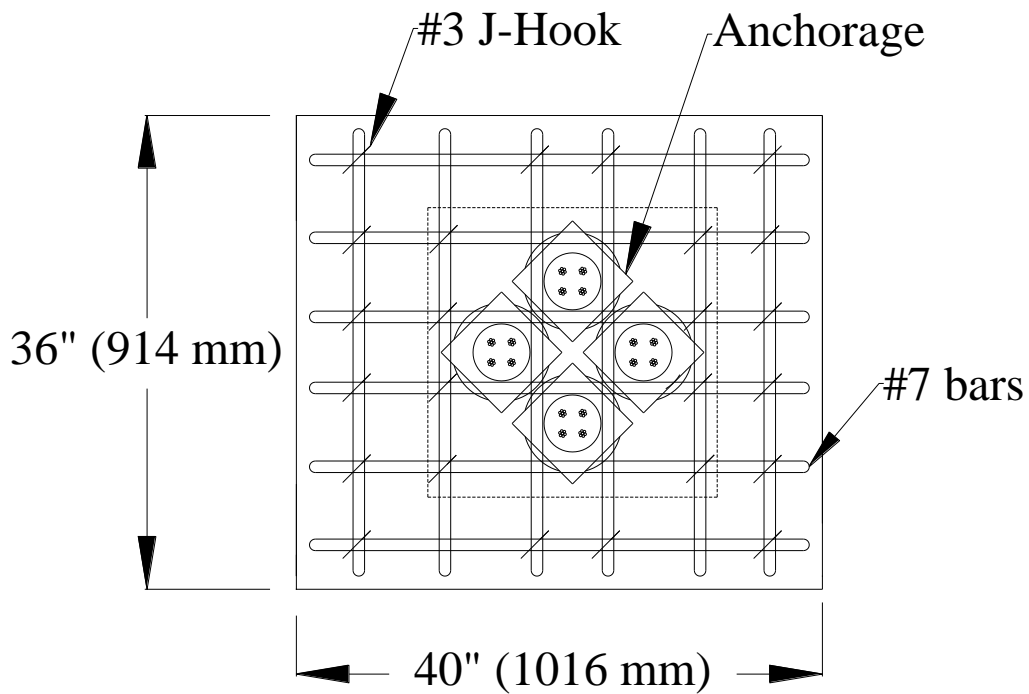
Figure 2-8: Loading Head Plan View

101
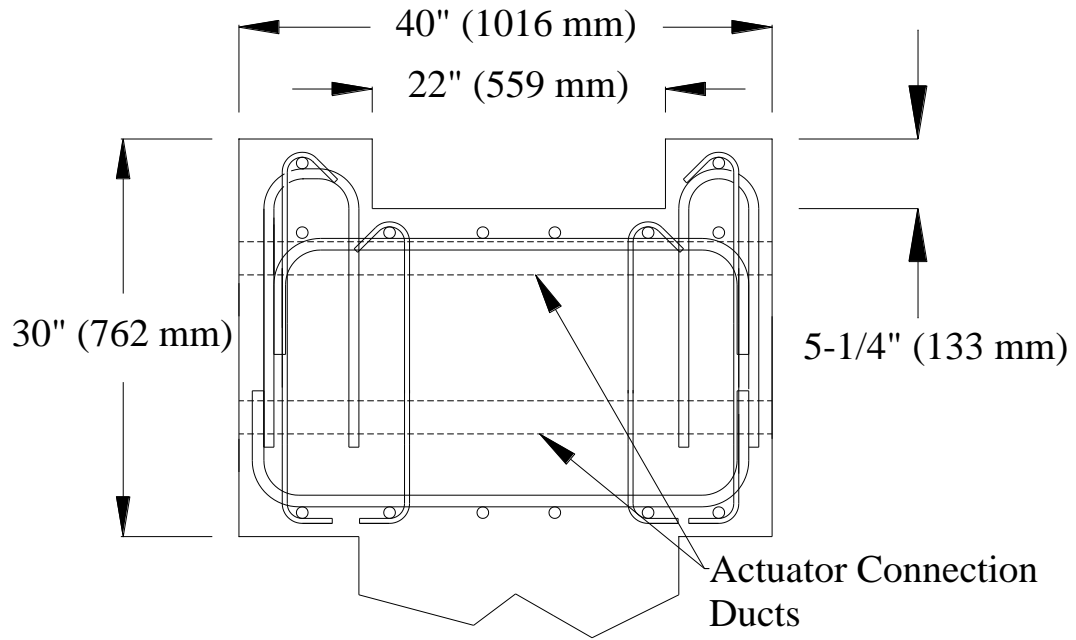
Figure 2-9: Loading Head Elevation
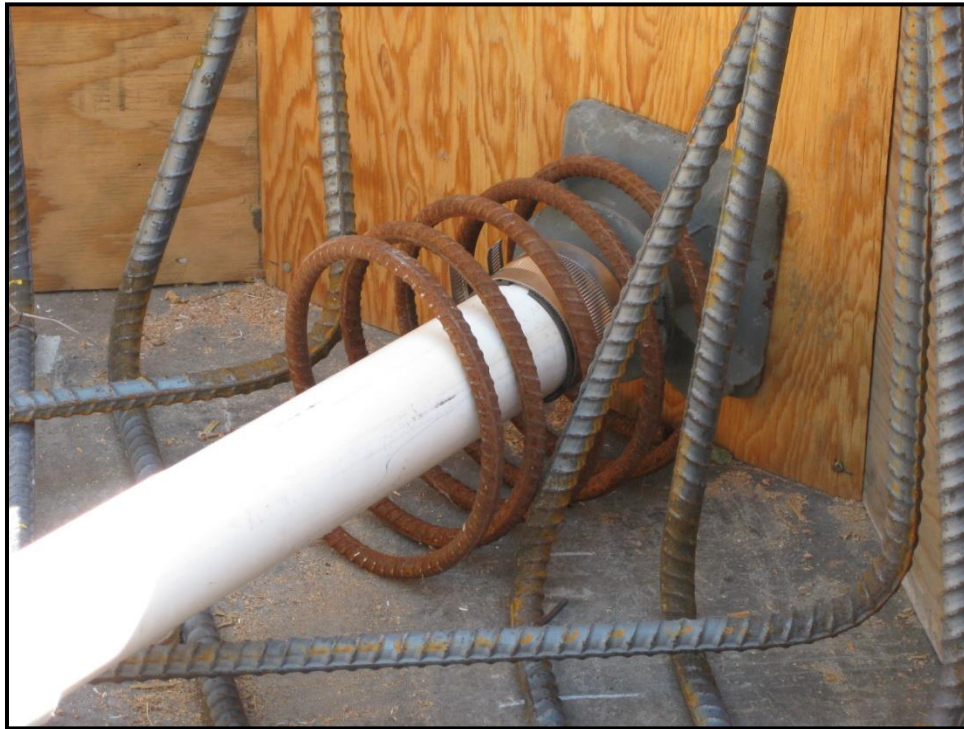
Figure 2-10: Anchor Head with Local Spiral Reinforcement

Figure 2-11: Steel Pipes in Footing

Figure 2-12: Hairpin Reinforcement

Figure 2-13: Top Mat of Footing Reinforcement

Figure 2-14: Poured Footing

Figure 2-15: Sonotube and Deck

Figure 2-16: Cable Gripper

Figure 2-17: Pushing Bullet

Figure 2-18: Complete Construction

Figure 2-19: Anchor Head on Shim Stack, Prior to Stressing

Figure 2-20: Initial Stressing with Monostrand Jack
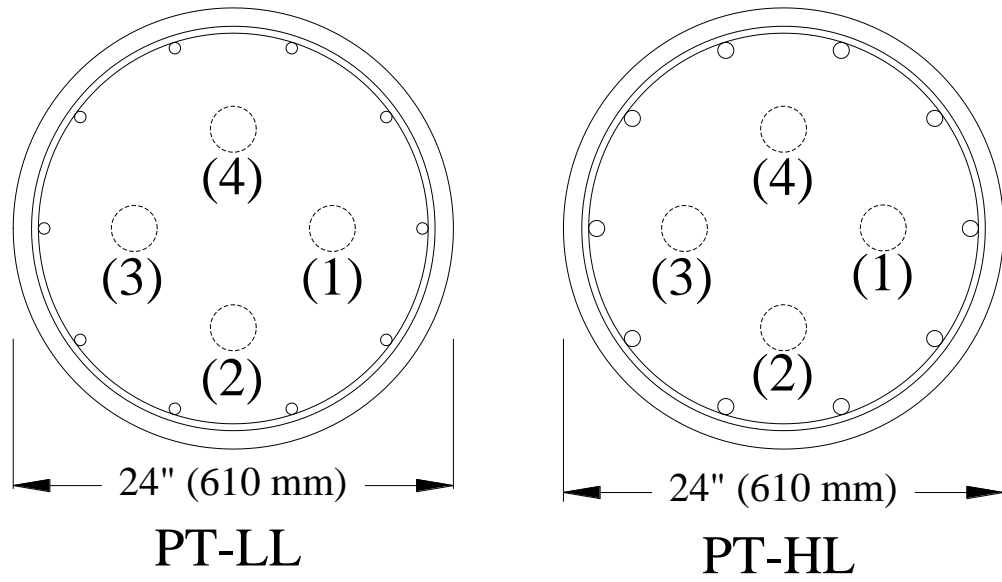
Figure 2-21: Numbered Tendons

Figure 2-22: Jack Chair with Multistrand Jack Performing Liftoff
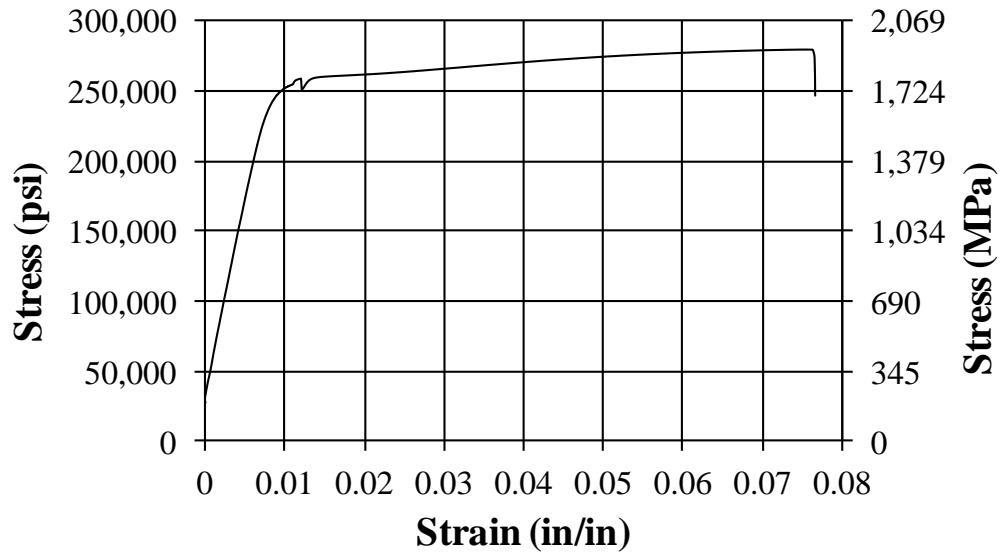
Figure 2-23: 0.6" 7-Wire Grade 270 Stress Strain Curve

Longitudinal Strain Gage □
Transverse Strain Gage ×

E ⟵   ⟶ W
Loading Direction

SG3
SG4
SG1
SG2
Section 1-1

SG25
SG28
SG26
SG23
SG21
SG24
SG22
SG27
Section 4-4

SG9
SG12
SG10
SG7
SG5
SG8
SG6
SG11
Section 2-2

SG33
SG36
SG34
SG31
SG29
SG32
SG30
SG35
Section 5-5

SG17
SG20
SG18
SG15
SG13
SG16
SG14
SG19
Section 3-3

SG41
SG44
SG42
SG39
SG37
SG40
SG38
SG43
Section 6-6

6-6
5-5
4-4
3-3
2-2
1-1

6" (152.4 mm)
6" (152.4 mm)
6" (152.4 mm)
6" (152.4 mm)
1/2"
(12.7 mm)

4" (101.6 mm)

Figure 3-1: Column Strain Gauge Plan

110

Figure 3-2: Strain Gauges on Column Rebar Cage
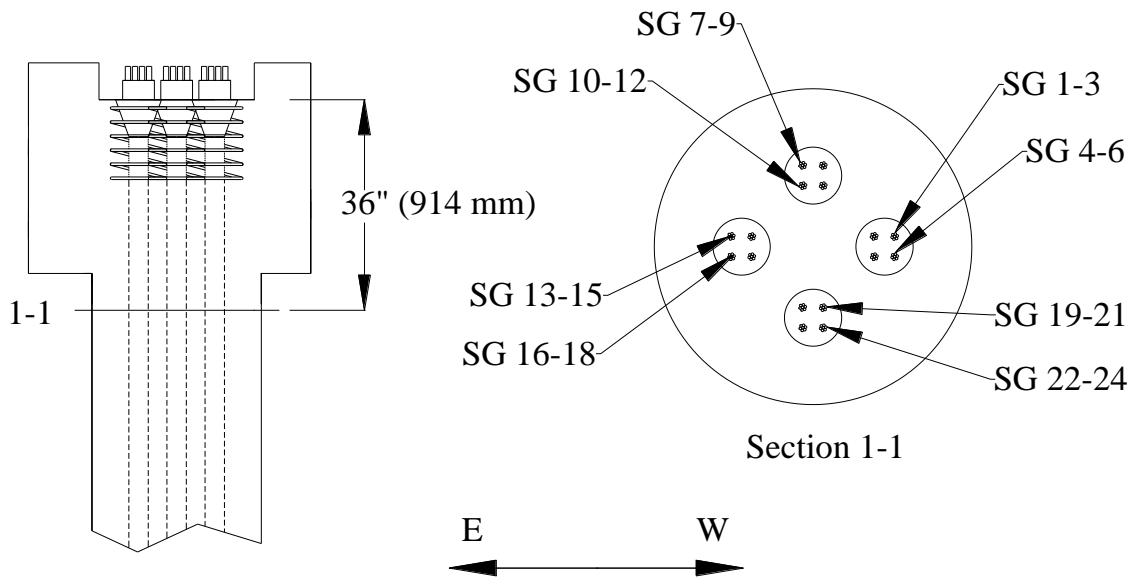
Figure 3-3: Tendon Strain Gauge Plan
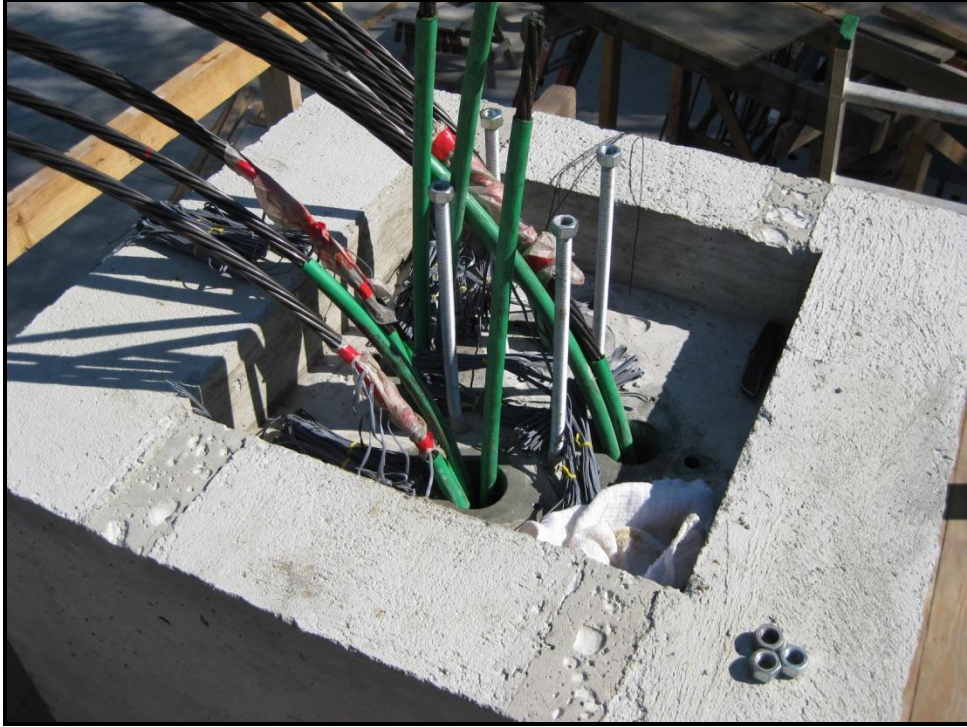
Figure 3-4: Tendon Strain Gauges Installed

Figure 3-5: Strain Gauge Wires Exiting Anchor Plate

String POTs @ Three Corners
D01-D03

D01   D02

D03

Loading Head, East Elevation

S ← → N

Novotechniks

C05 → ← C10
C04 → ← C09
C03 → ← C08
C02 → ← C07
C01 → ← C06

E ← → W
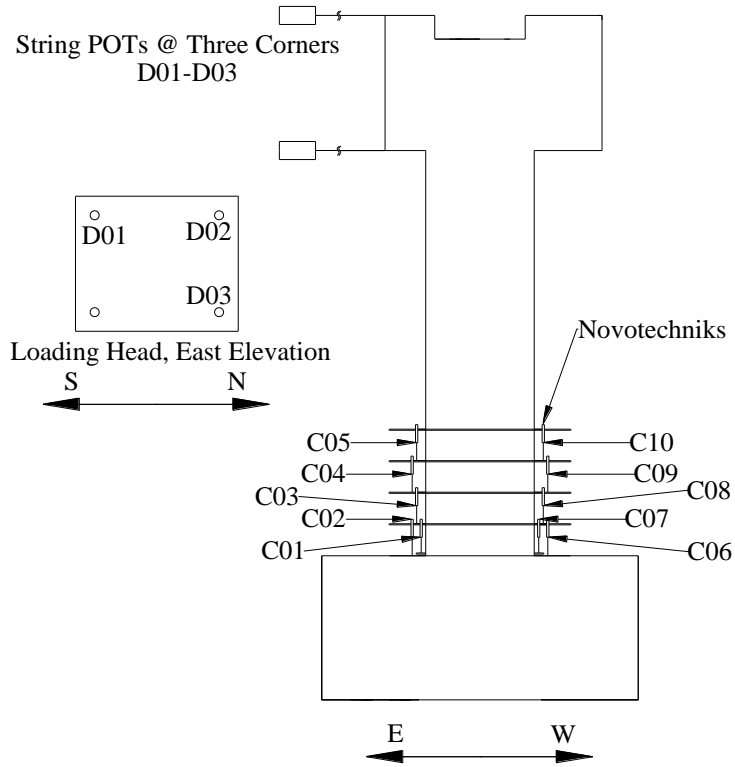
Figure 3-6: Novotechnik & String POT Plan

Figure 3-7: Reaction Wall
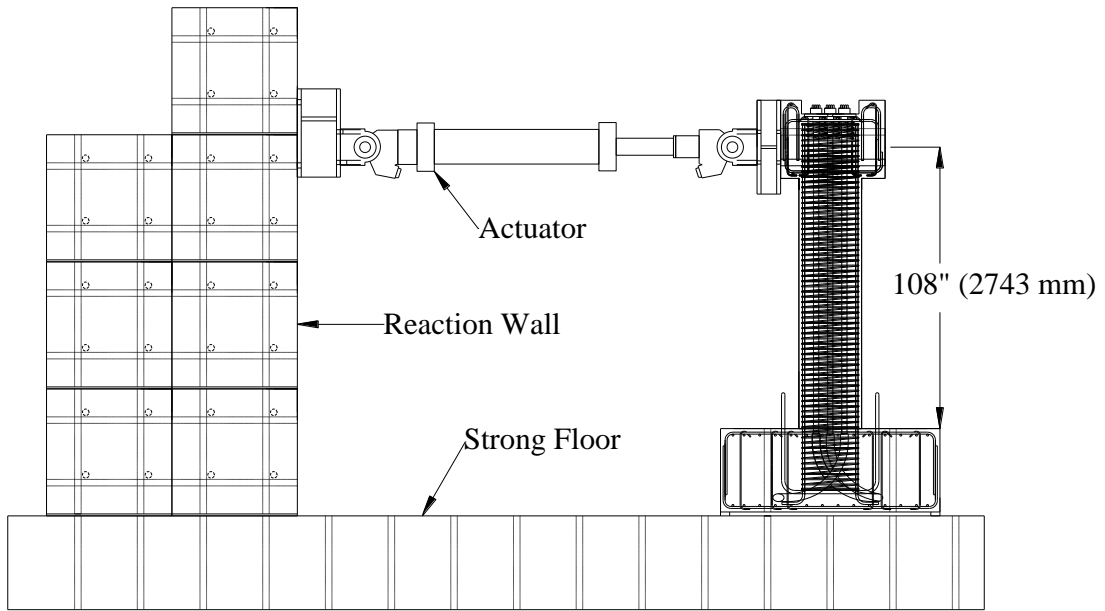
Figure 3-8: Test Setup

Figure 3-9: Outdoor Test Setup
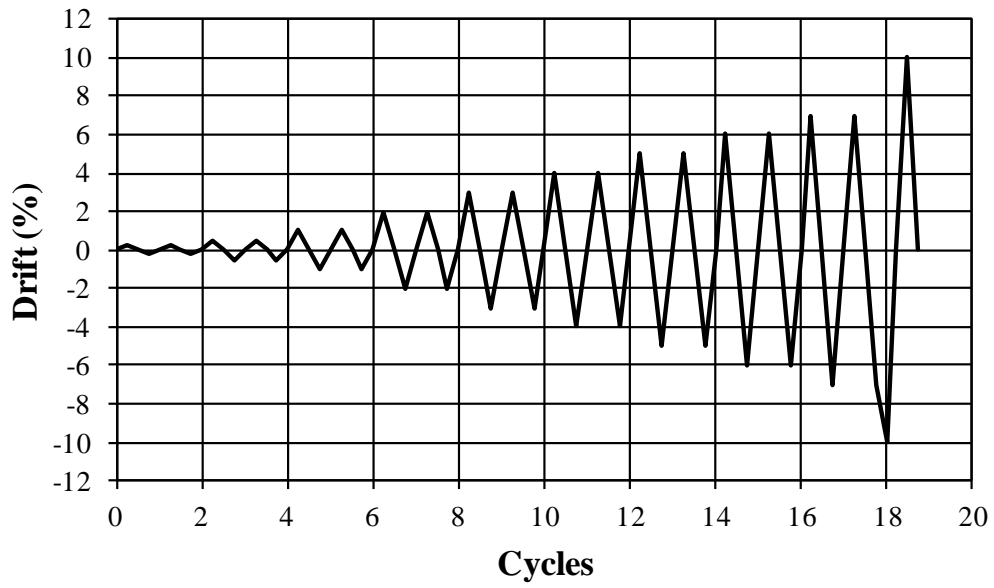
Figure 3-10:Cyclic Loading Protocol, PT-LL
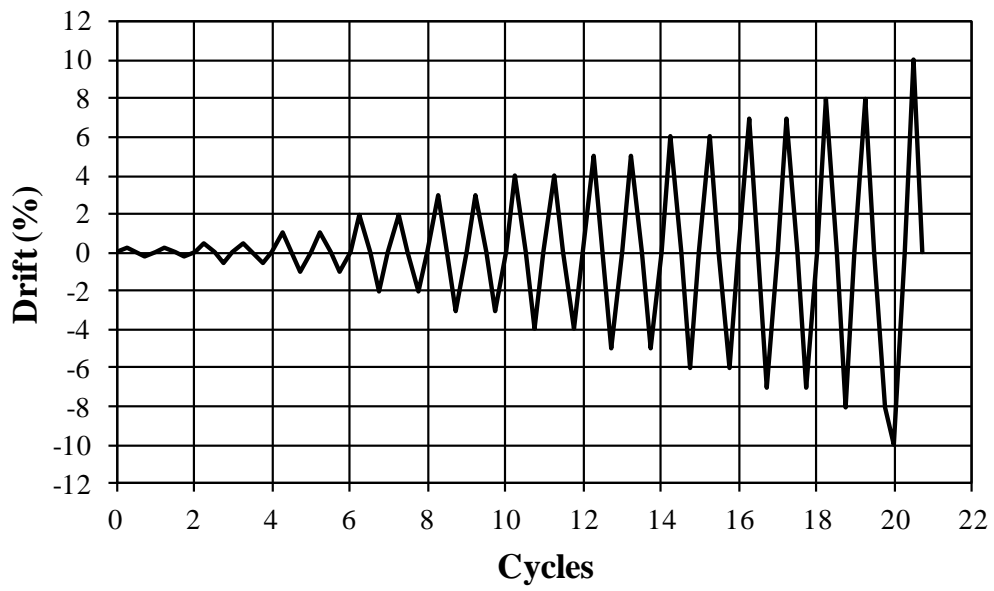
Figure 3-11: Cyclic Loading Protocol, PT-HL
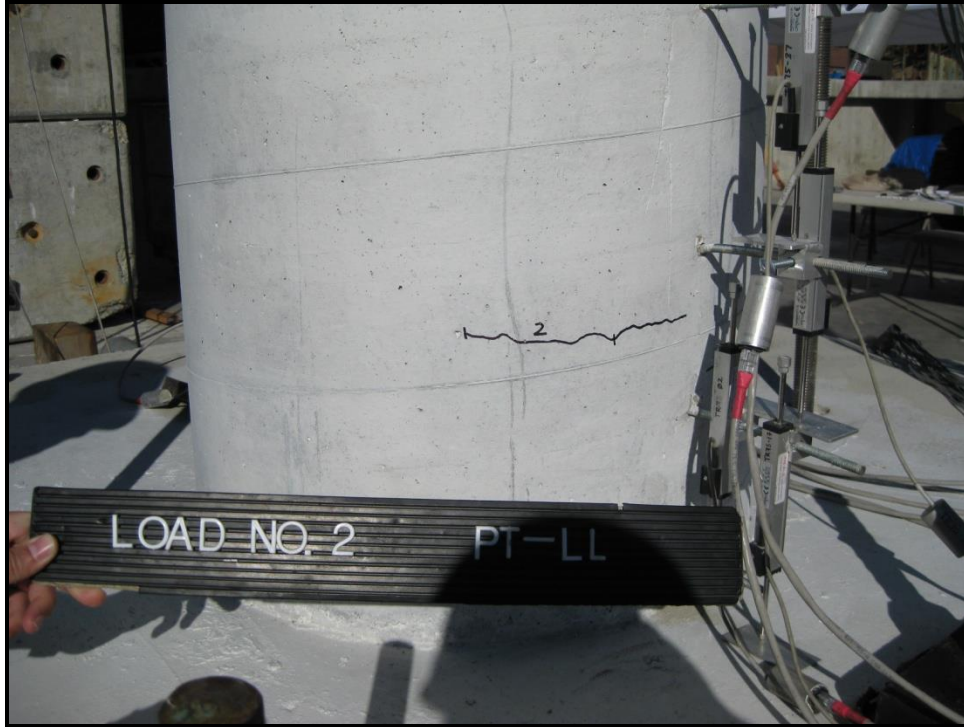
Figure 4-1: PT-LL First Crack

Figure 4-2: PT-LL Initial Spalling on West

Figure 4-3: PT-LL Initial Spalling on East, Visible Spiral
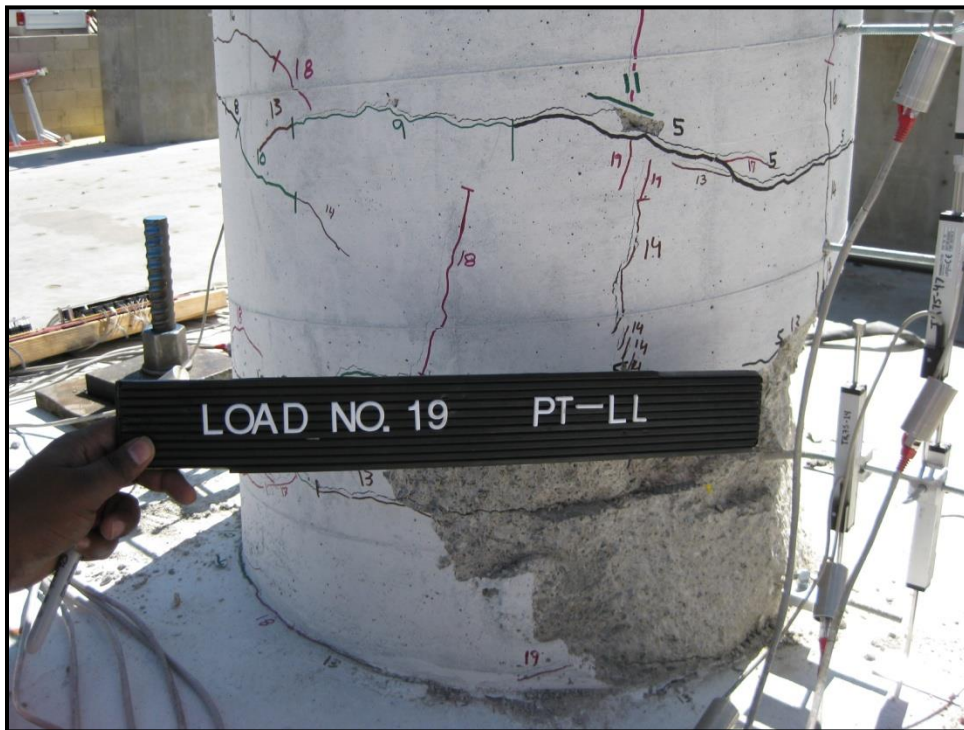
Figure 4-4: PT-LL Visible Spiral on West

Figure 4-5: PT-LL Buckling Longitudinal Reinforcing Bar, East
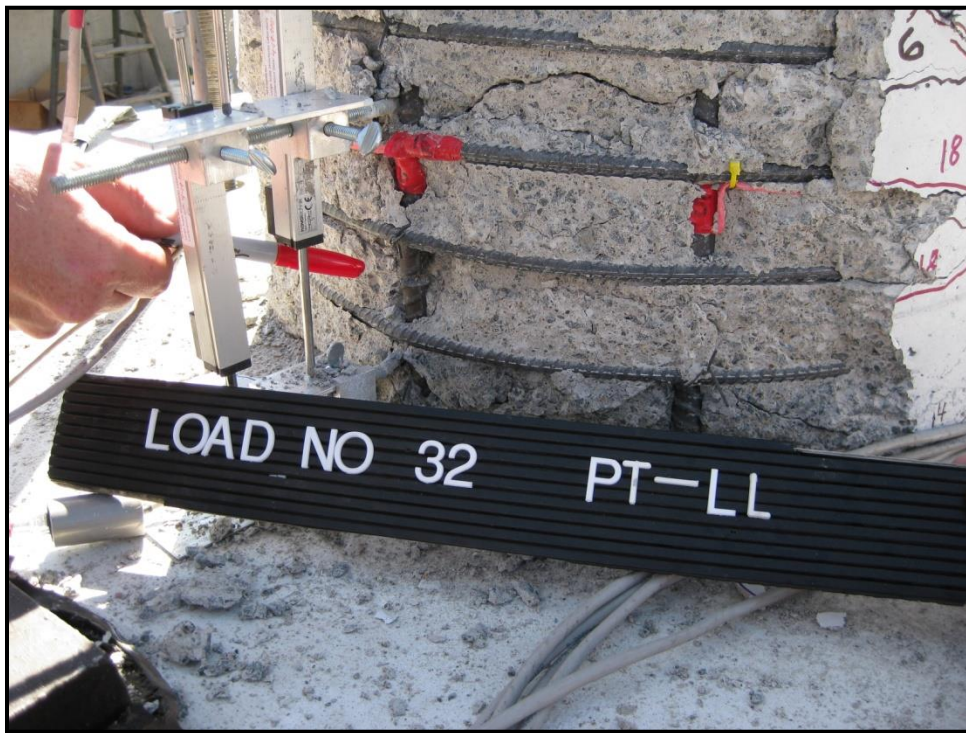
Figure 4-6: PT-LL Fractured Longitudinal Reinforcing Bar, East
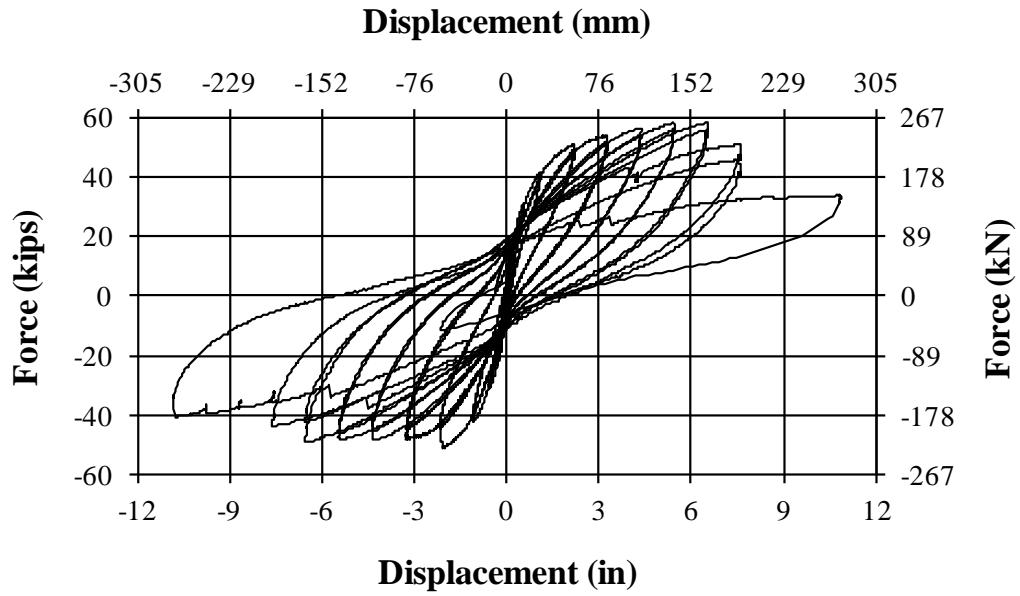
Figure 4-7: PT-LL Hysteresis
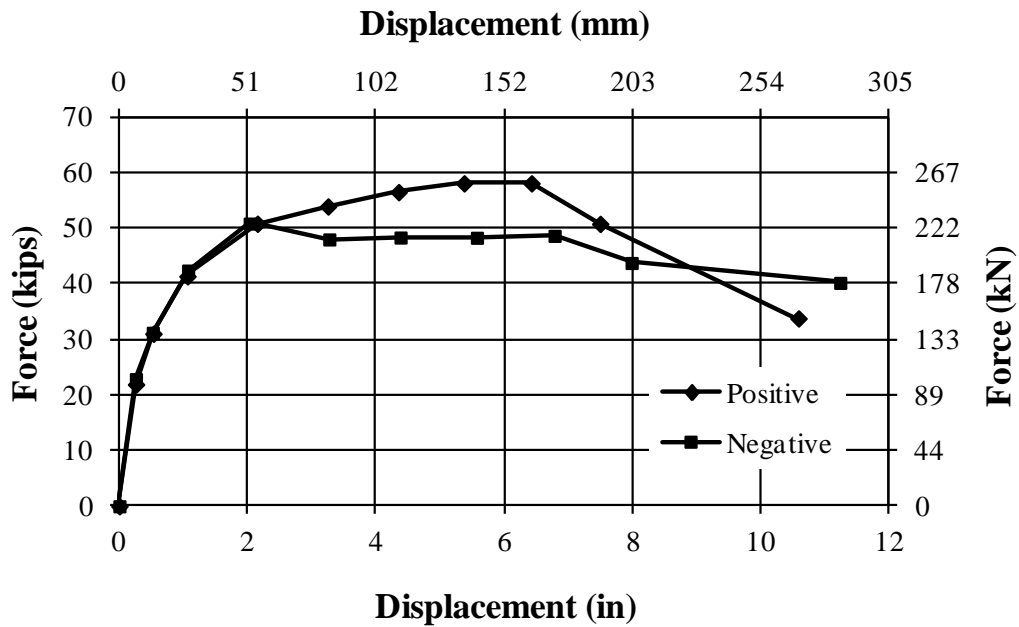
Figure 4-8: PT-LL Positive and Negative Hysteretic Envelope
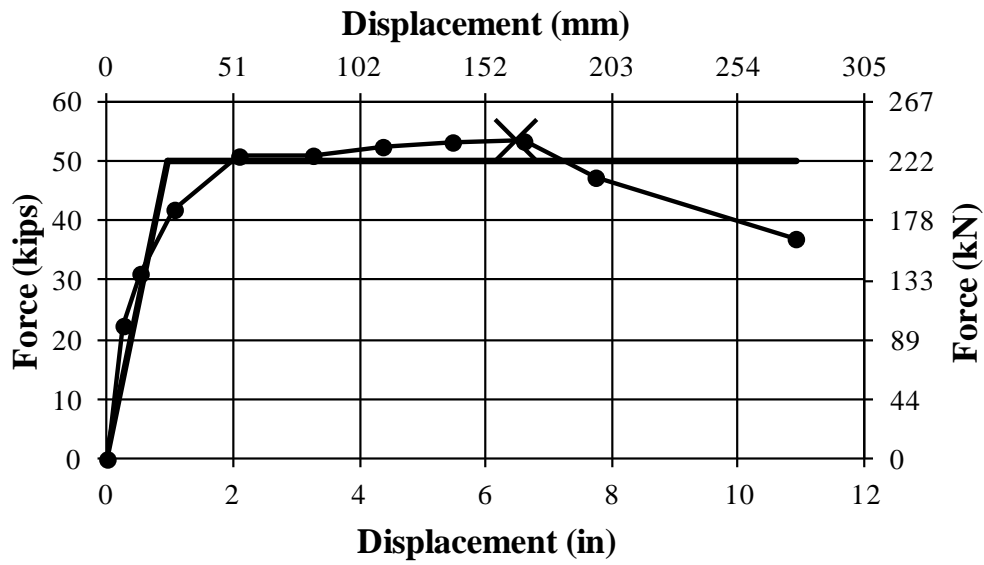
Figure 4-9: PT-LL Average Pushover Curve
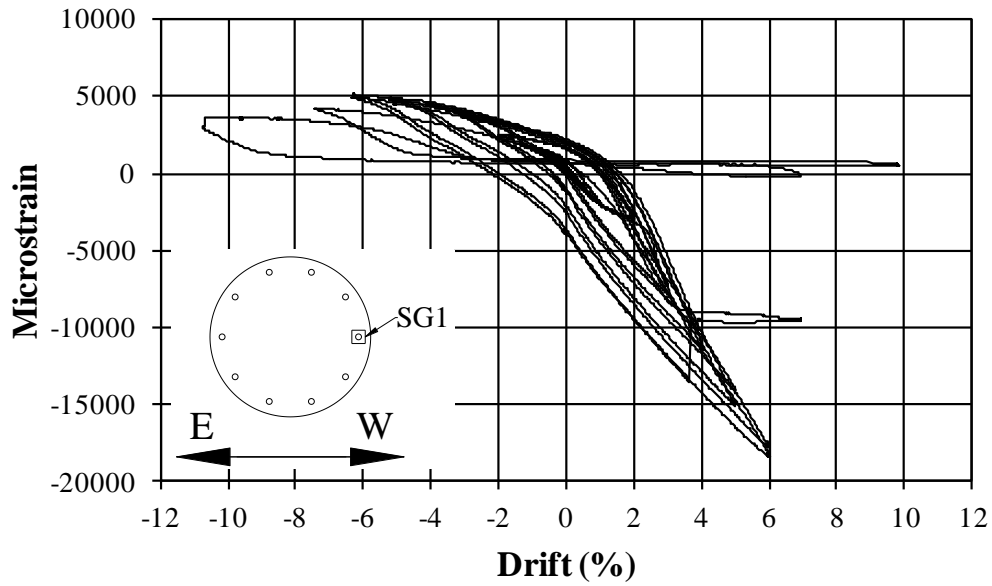
Figure 4-10: PT-LL Strain vs. Drift, Strain Gauge 1
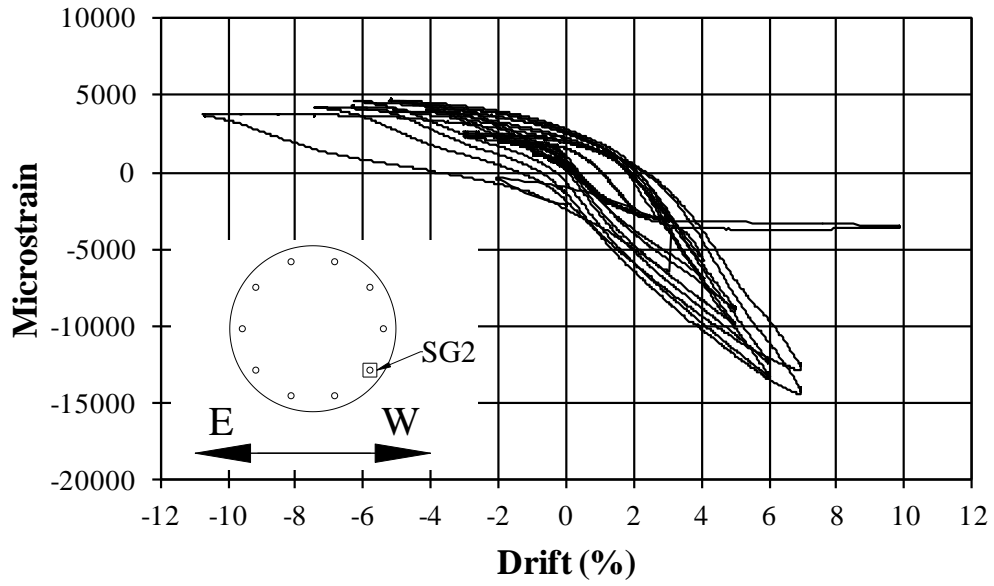
Figure 4-11: PT-LL Strain vs. Drift, Strain Gauge 2
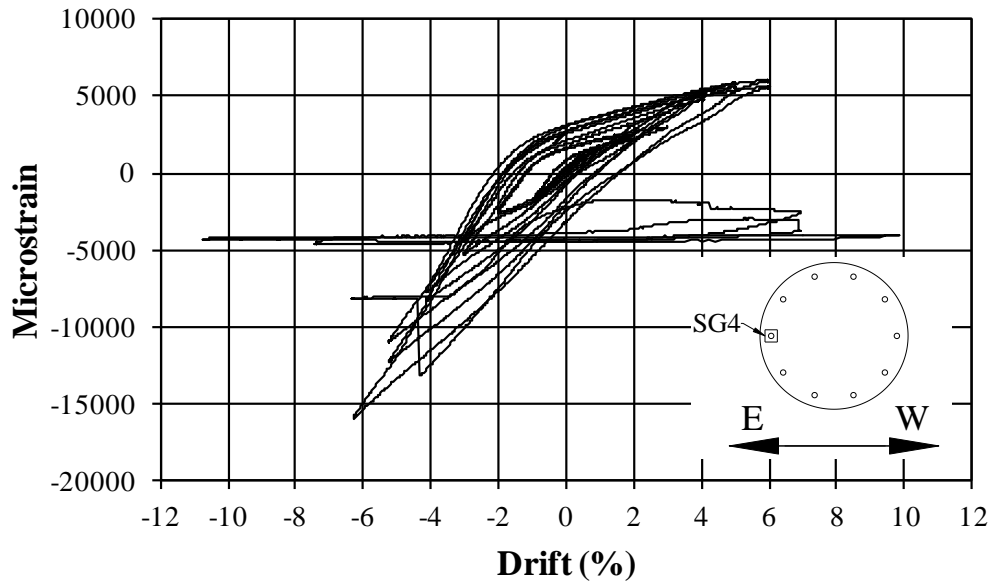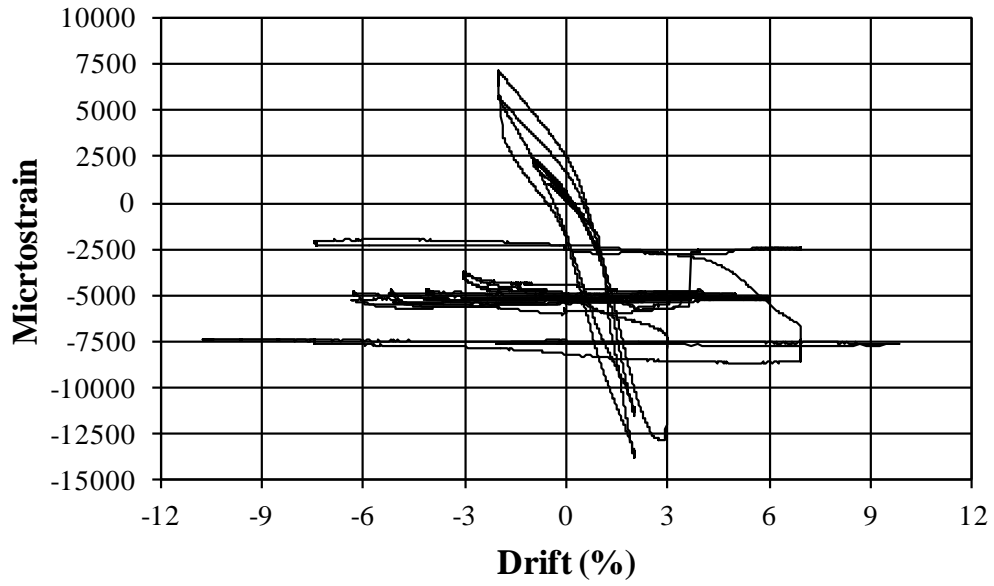

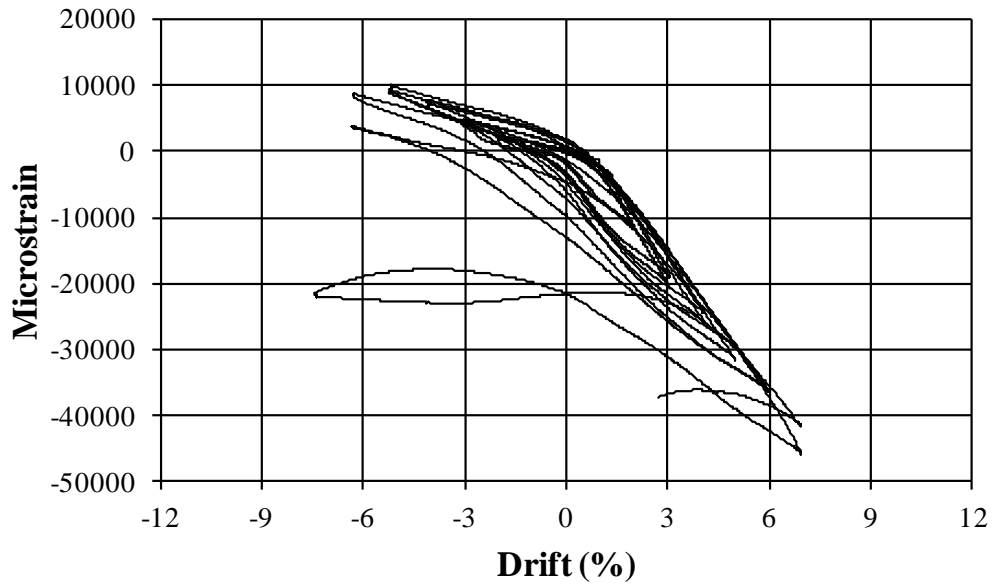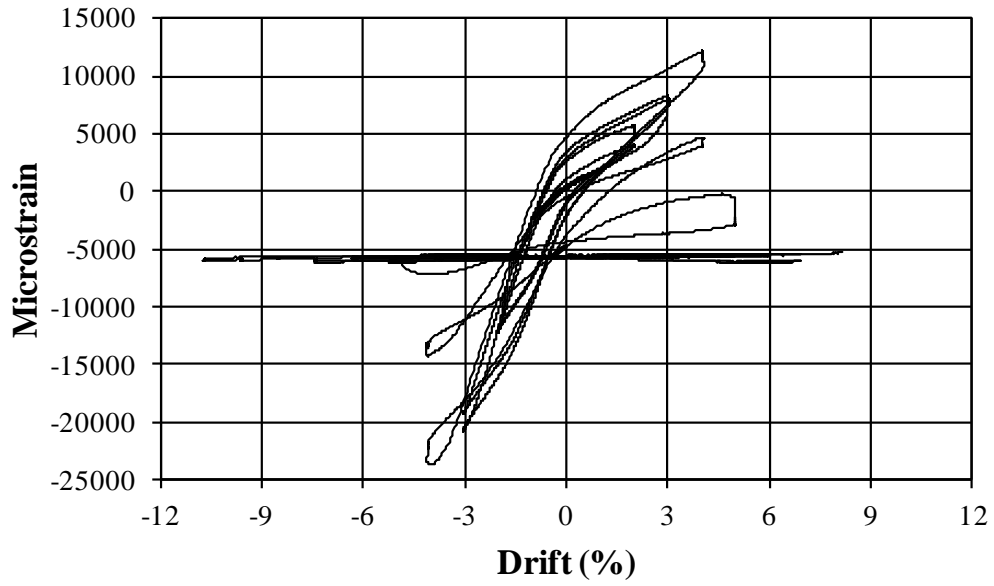**Figure 4-12: PT-LL Strain vs. Drift, Strain Gauge 4**
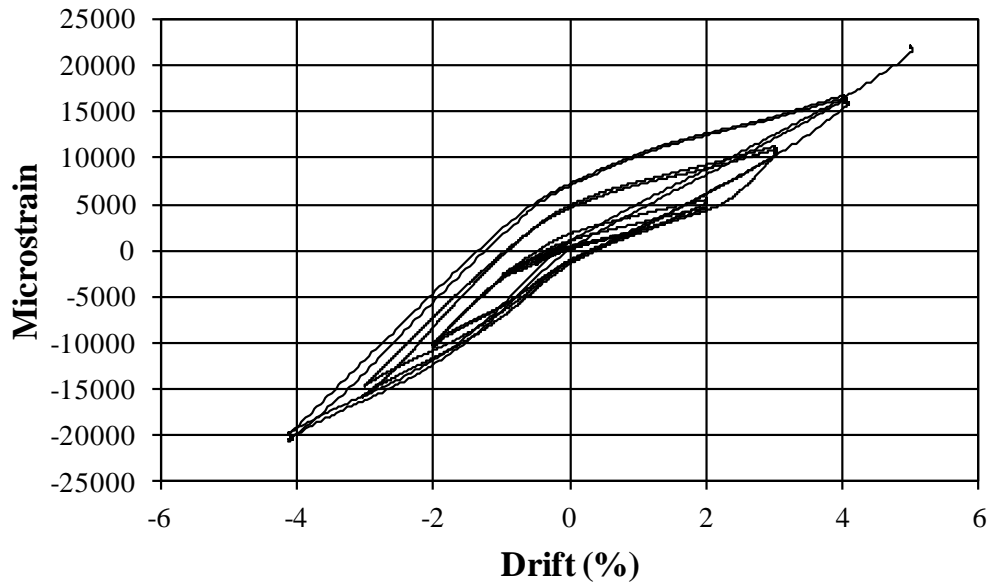
121
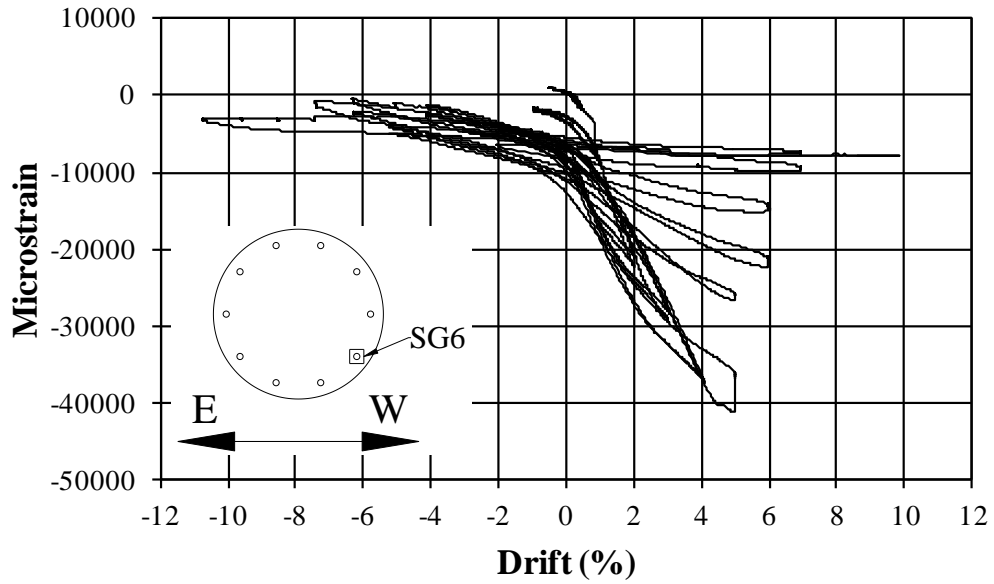
Figure 4-13: PT-LL Strain vs. Drift, Strain Gauge 6
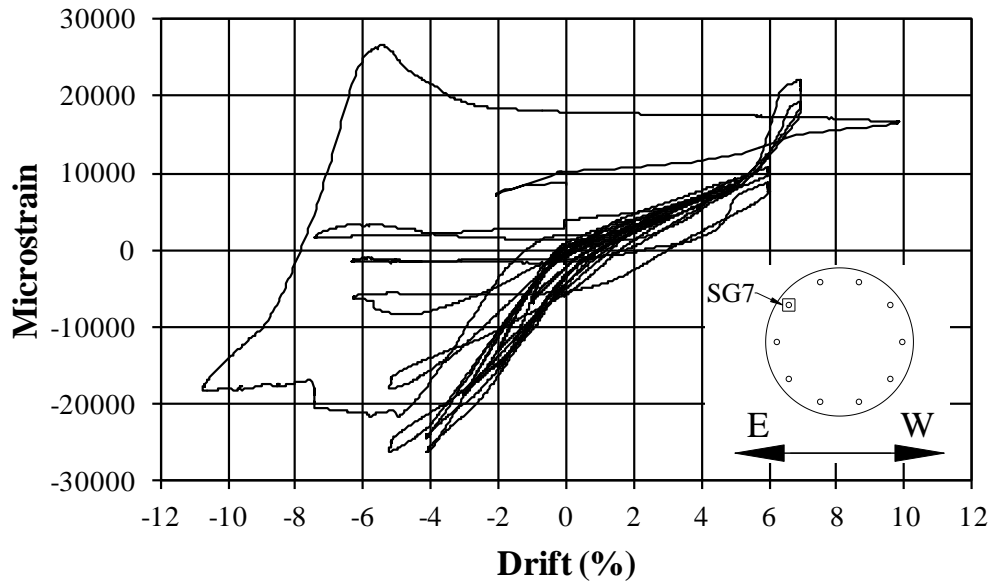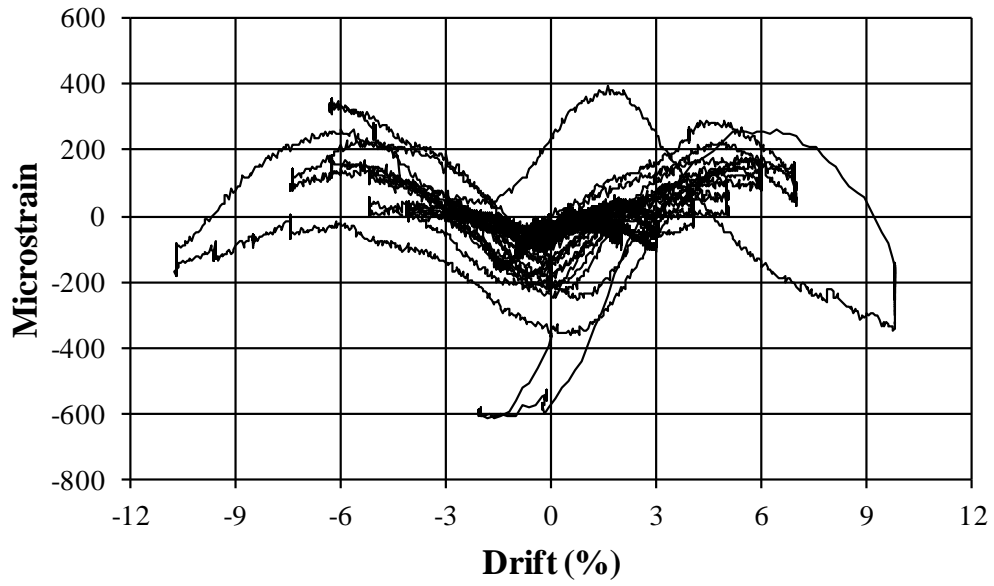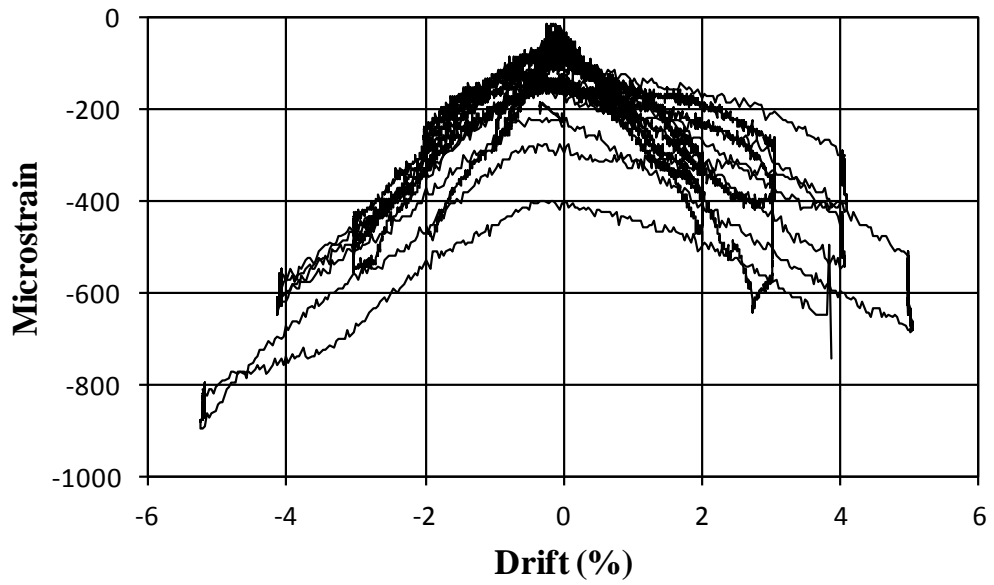

Figure 4-14: PT-LL Strain vs. Drift, Strain Gauge 7

122
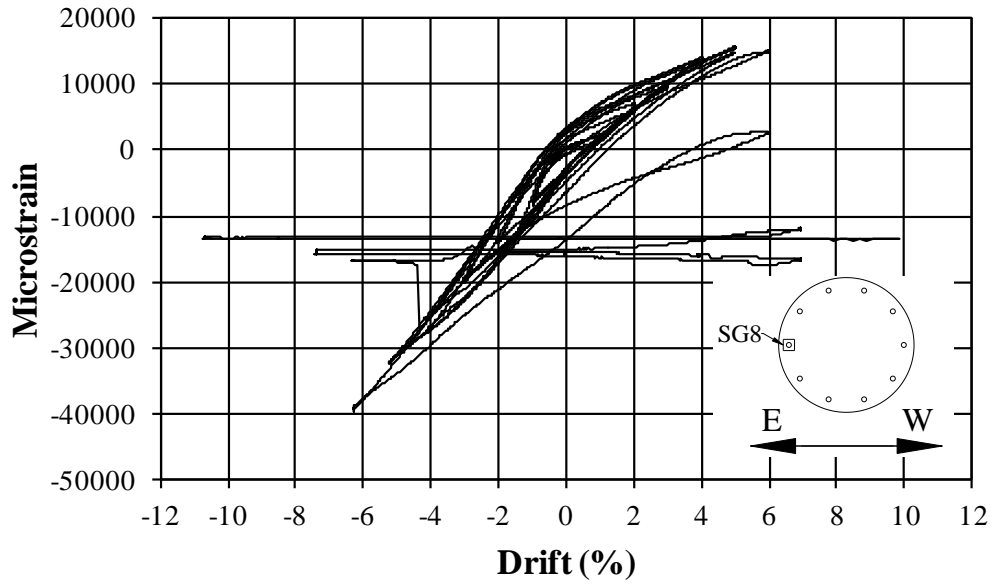
Figure 4-15: PT-LL Strain vs. Drift, Strain Gauge 8
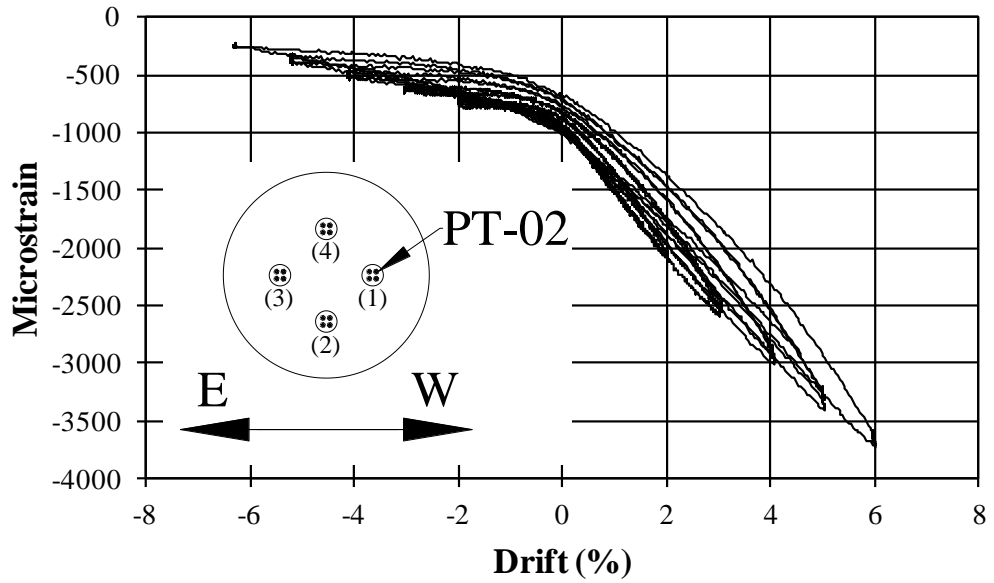
Figure 4-16: PT-LL Strain vs. Drift, Strain Gauge PT-02, Tendon 1

123
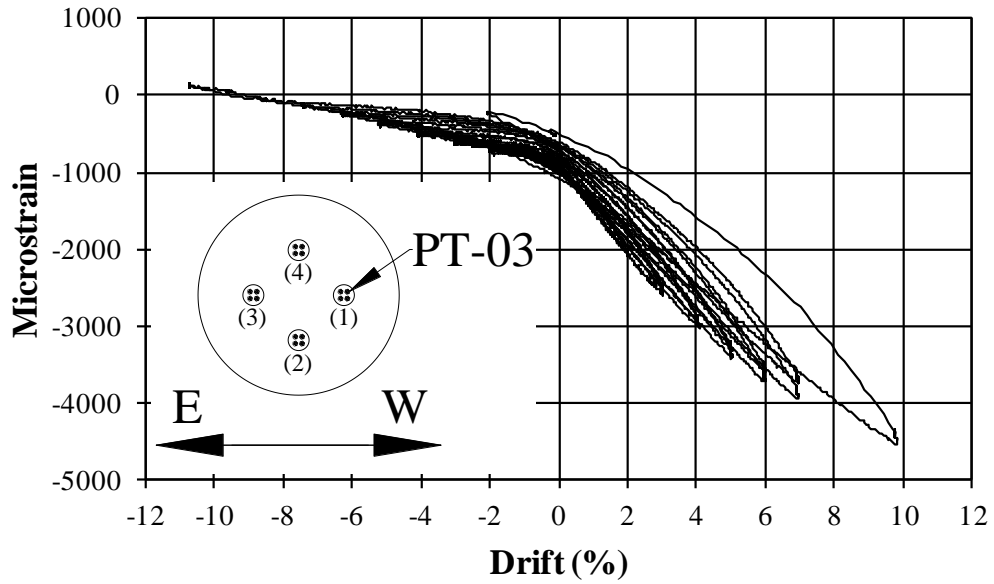
Figure 4-17: PT-LL Strain vs. Drift, Strain Gauge PT-03, Tendon 1
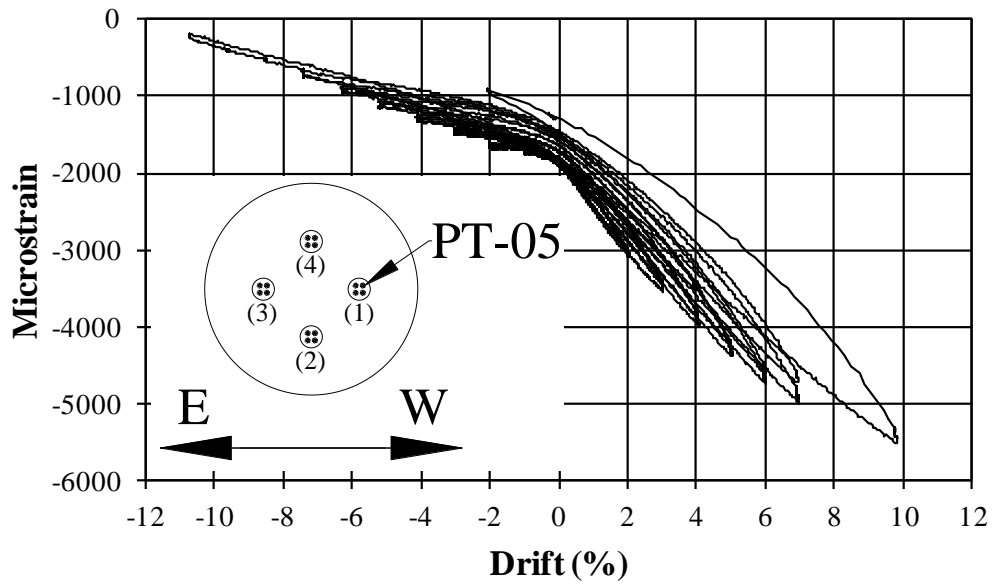
Figure 4-18: PT-LL Strain vs. Drift, Strain Gauge PT-05, Tendon 1
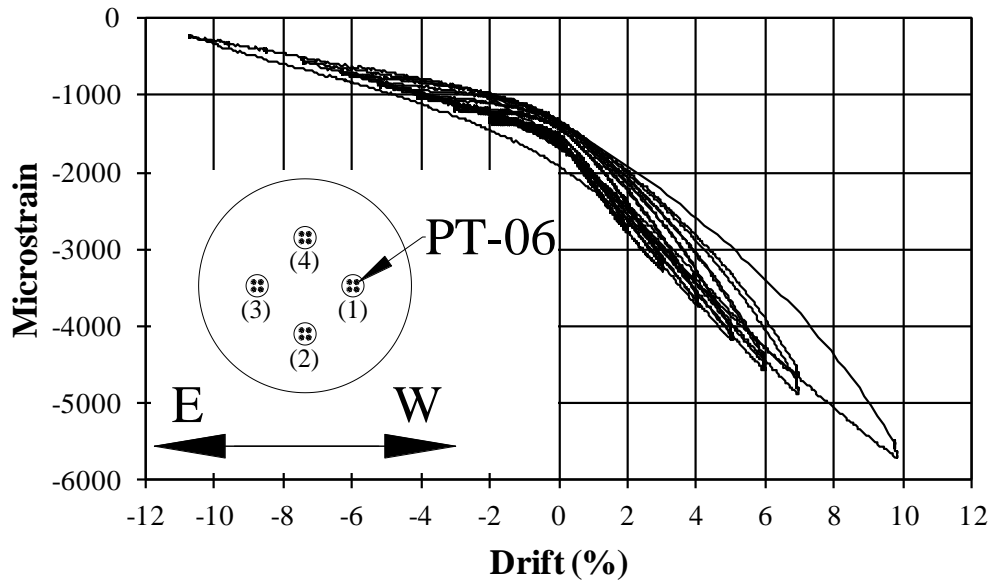
Figure 4-19: PT-LL Strain vs. Drift, Strain Gauge PT-06, Tendon 1
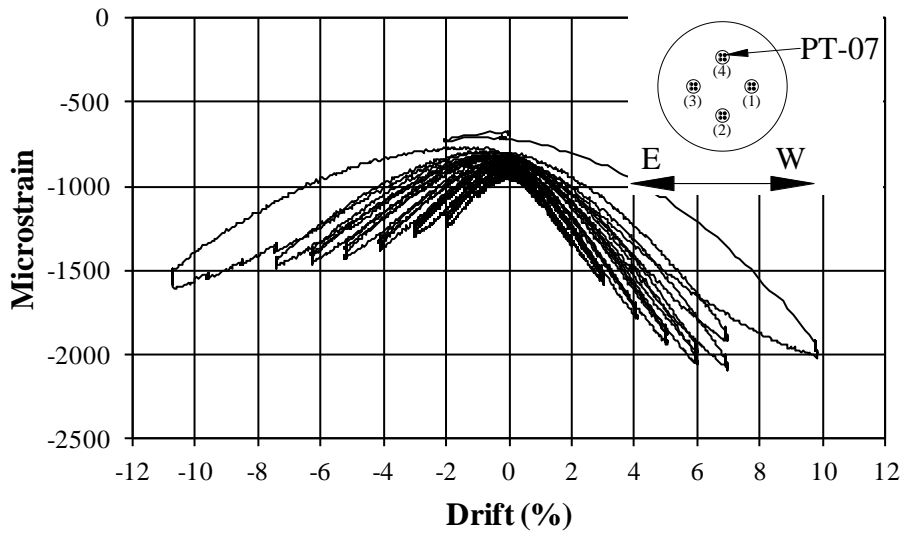
Figure 4-20: PT-LL Strain vs. Drift, Strain Gauge PT-07, Tendon 4
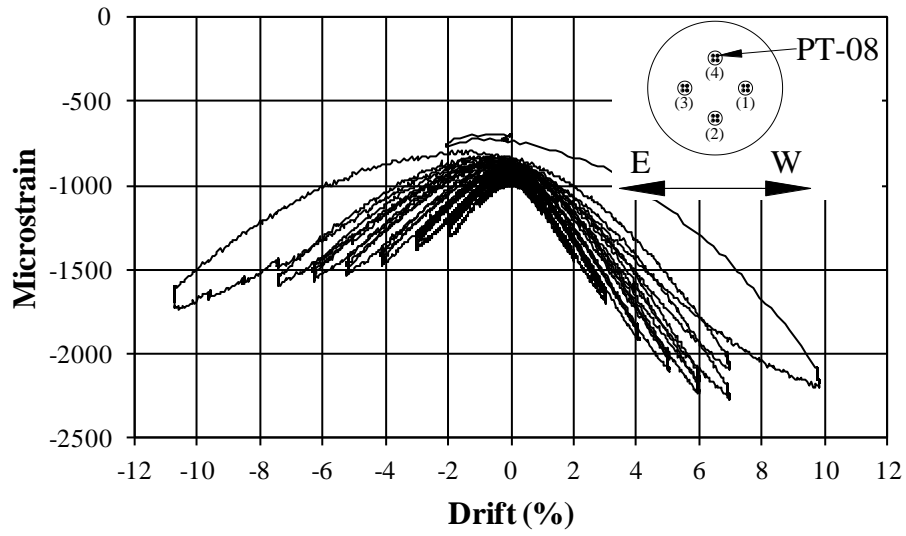
Figure 4-21: PT-LL Strain vs. Drift, Strain Gauge PT-08, Tendon 4
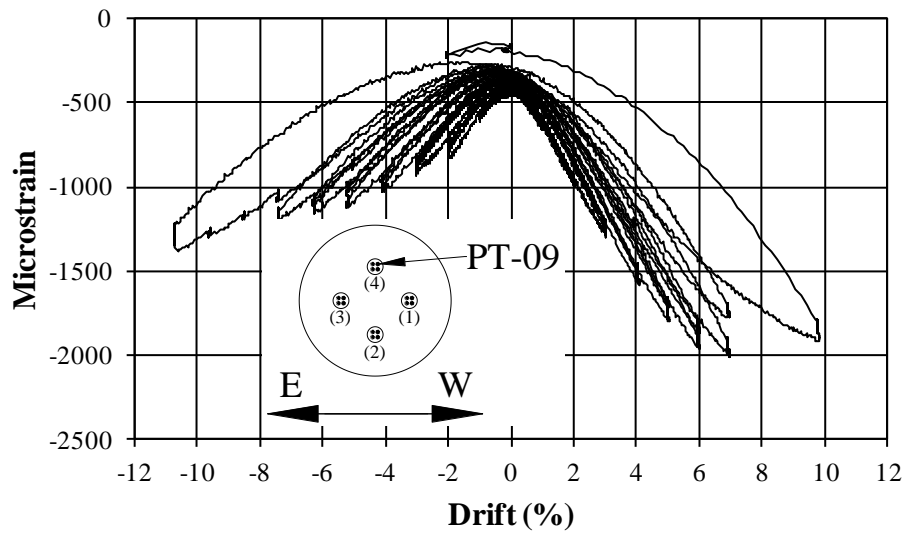
Figure 4-22: PT-LL Strain vs. Drift, Strain Gauge PT-09, Tendon 4
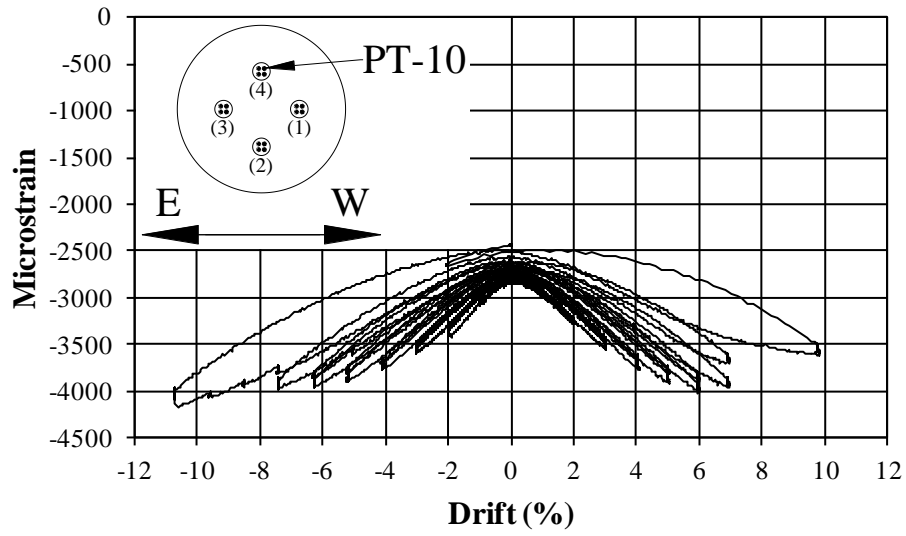
Figure 4-23: PT-LL Strain vs. Drift, Strain Gauge PT-10, Tendon 4
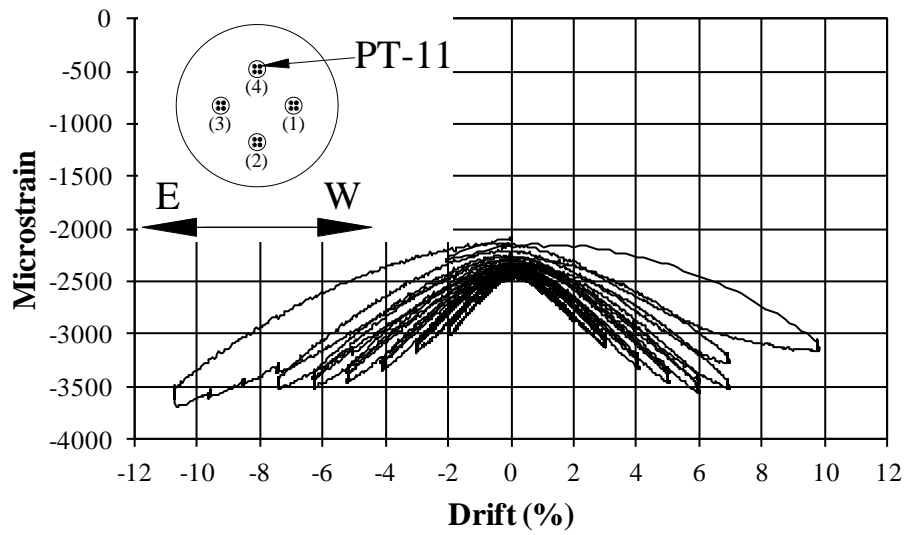
Figure 4-24: PT-LL Strain vs. Drift, Strain Gauge PT-11, Tendon 4

127
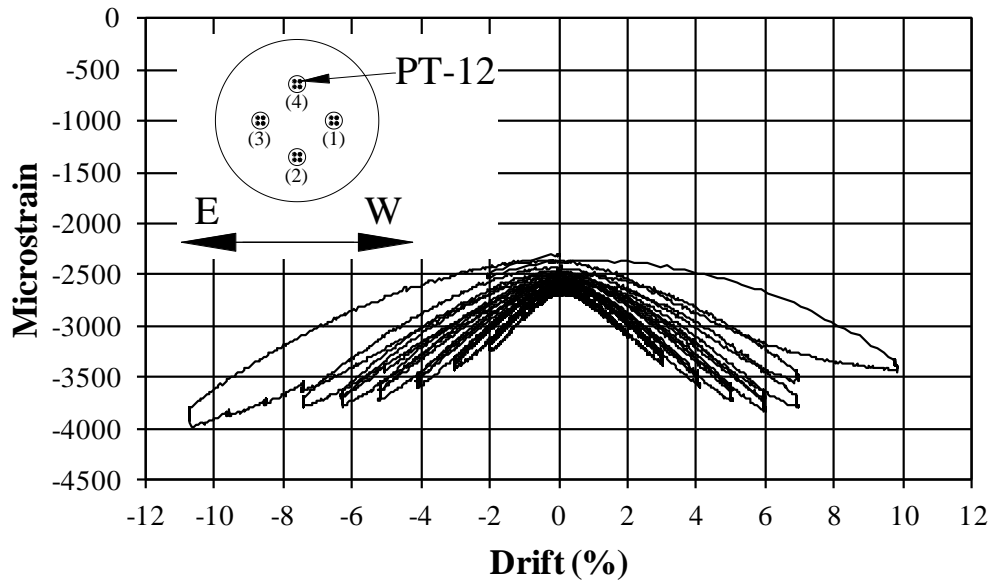
Figure 4-25: PT-LL Strain vs. Drift, Strain Gauge PT-12, Tendon 4
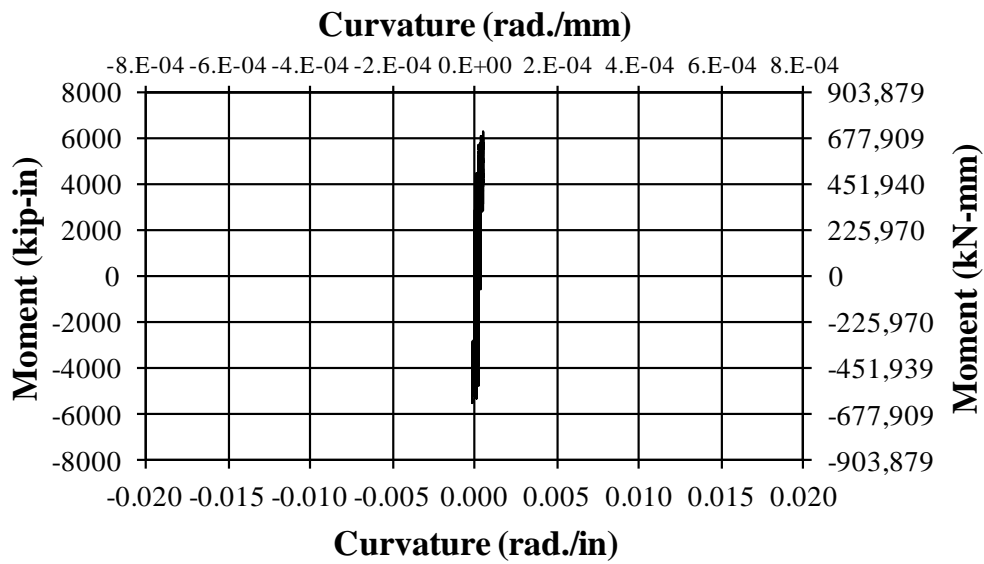
Figure 4-26: PT-LL Moment Curvature, Layer 4

128
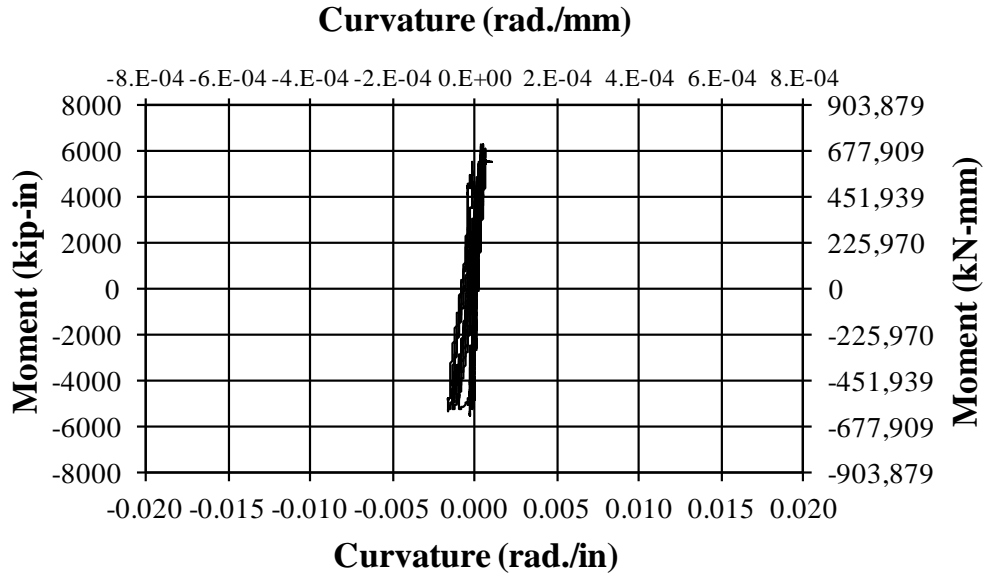
Figure 4-27: PT-LL Moment Curvature, Layer 3
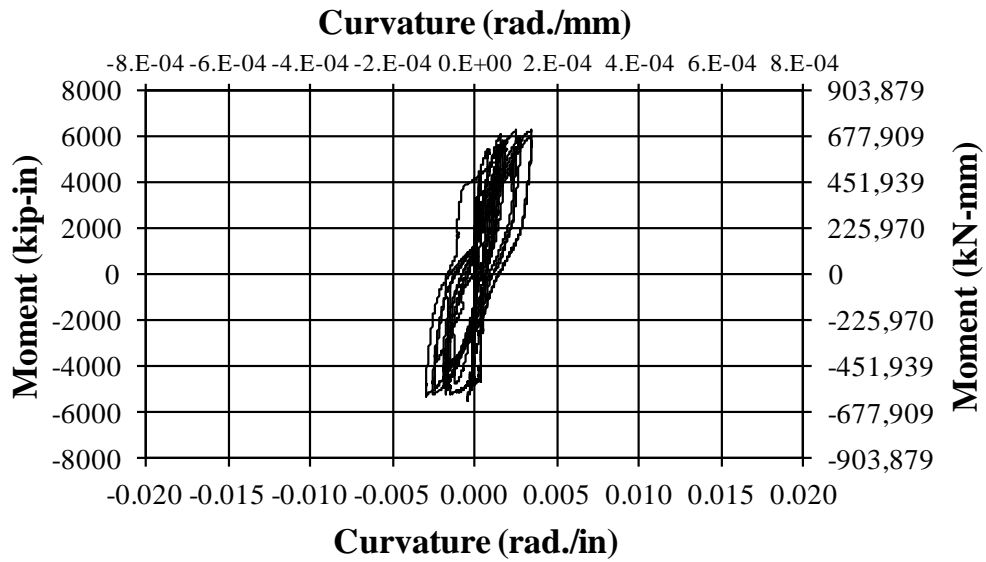
Figure 4-28: PT-LL Moment Curvature, Layer 2

129
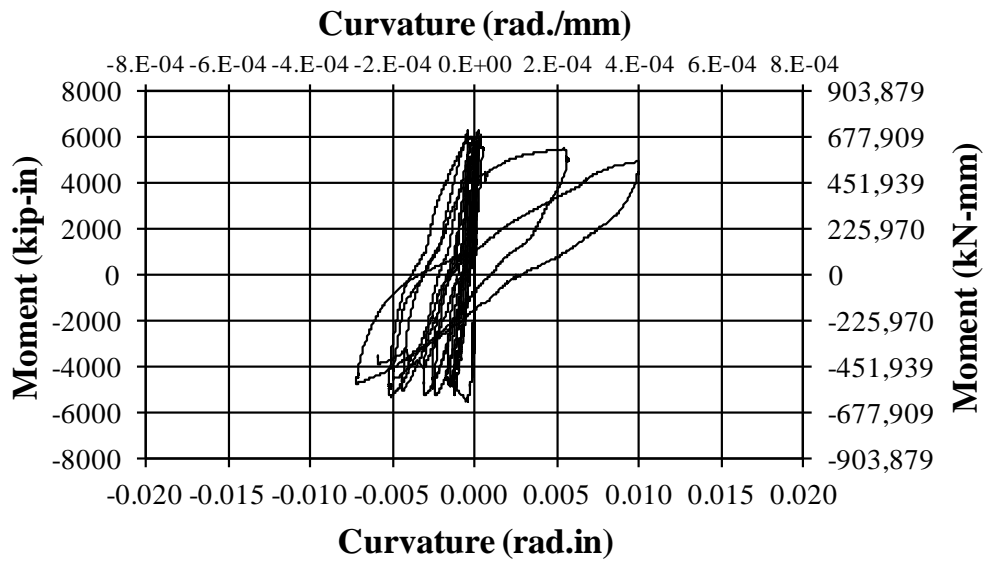
Figure 4-29: PT-LL Moment Curvature, Layer 1
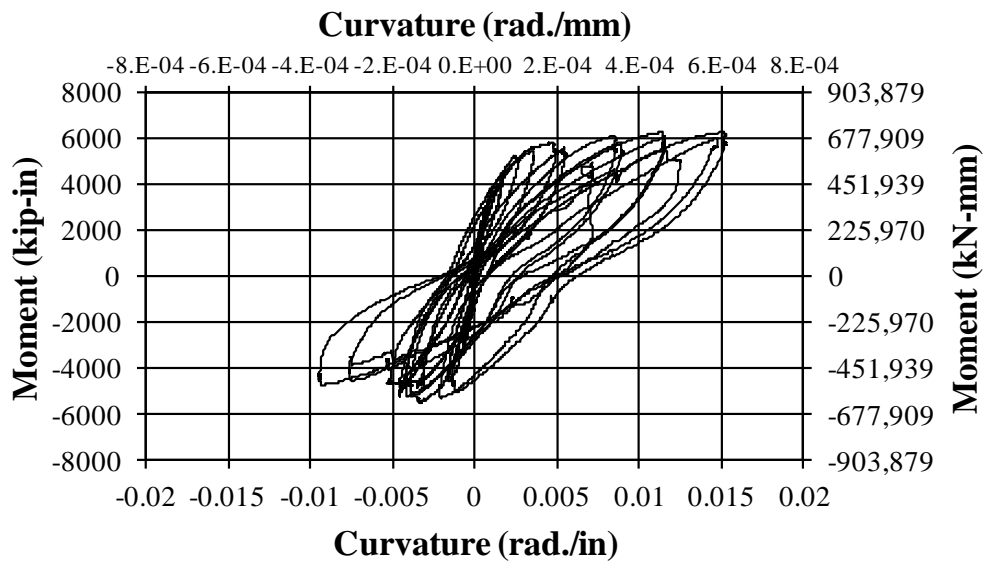
Figure 4-30: PT-LL Moment Curvature, Layer 4

130
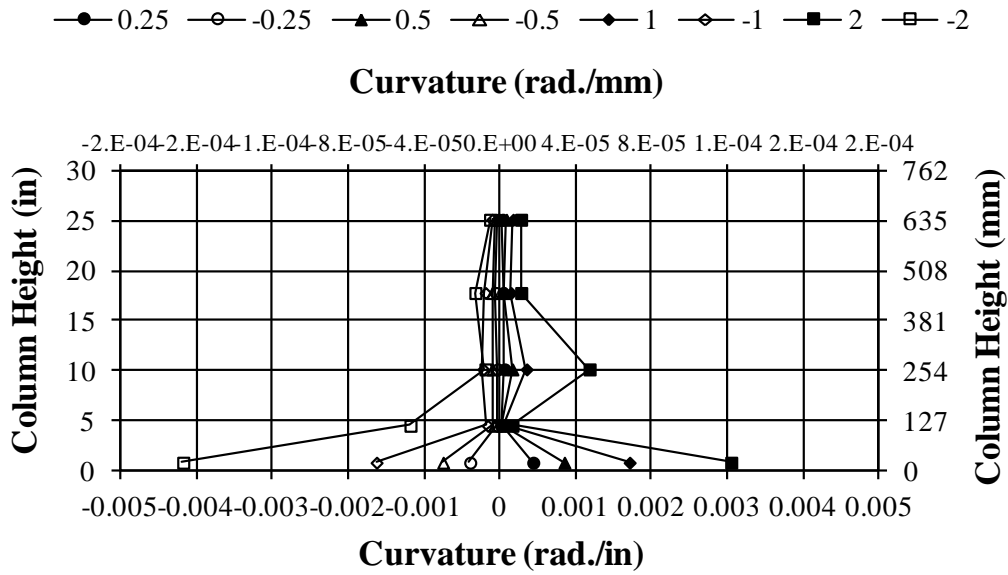
Figure 4-31: PT-LL, Column Height vs. Curvature, 0.25% to 2% Drift
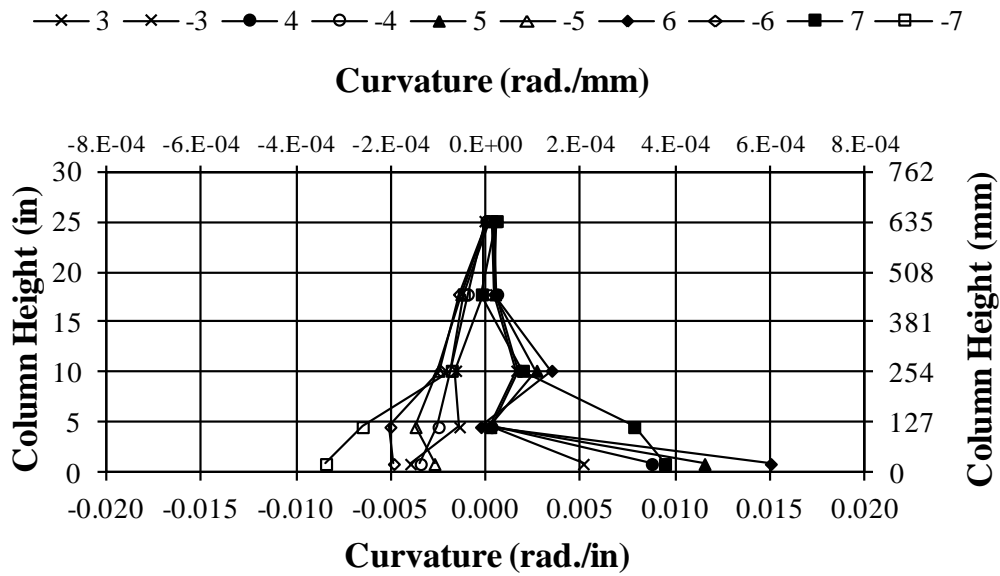
Figure 4-32: PT-LL, Column Height vs. Curvature, 3% to 7% Drift

131

Figure 4-33: PT-HL, First Crack
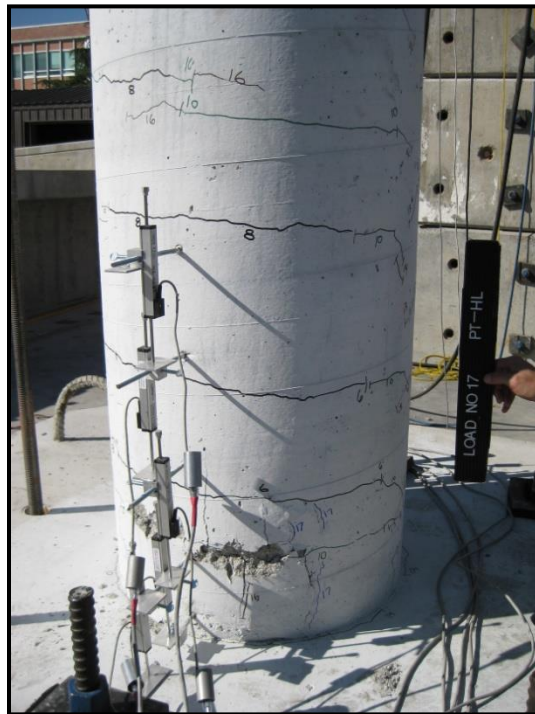
Figure 4-34: PT-HL, First Spalling, East Side

Figure 4-35: PT-HL, First Spalling, West Side

Figure 4-36: PT-HL, Visible Spiral, East Side
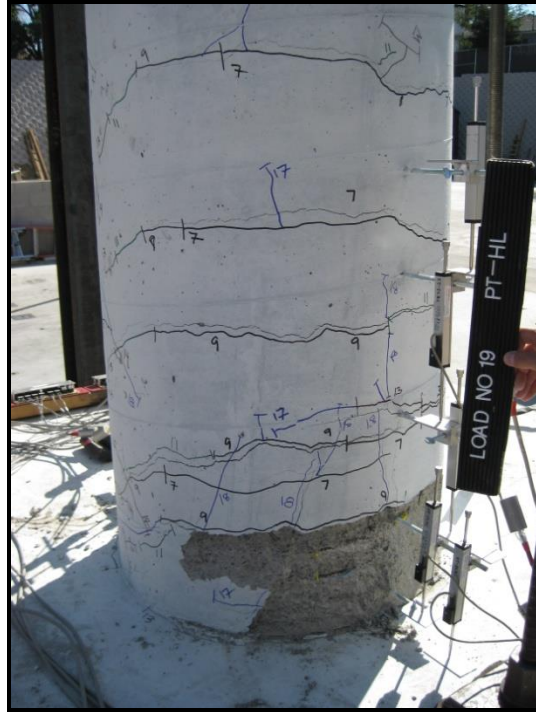
Figure 4-37: PT-HL, Visible Spiral, West Side

Figure 4-38: PT-HL, Visible Longitudinal Reinforcement, West Side

Figure 4-39: PT-HL, Visible Longitudinal Reinforcement, East Side
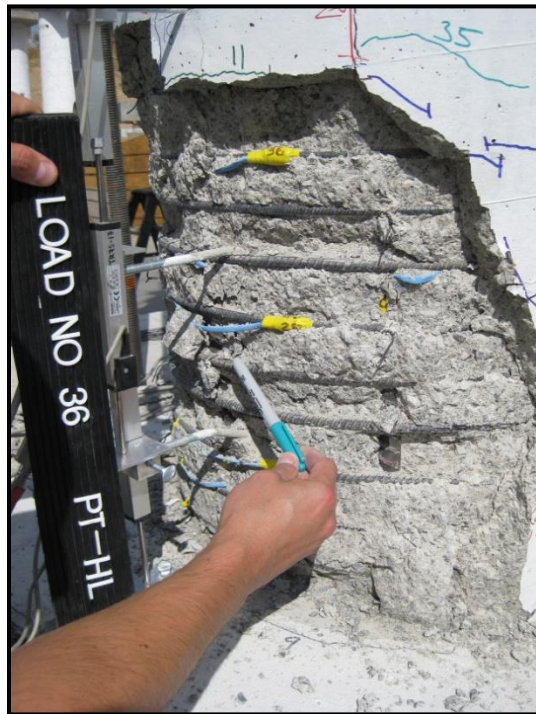
Figure 4-40: PT-HL, Longitudinal Reinforcing Bar Buckling, West Side

Figure 4-41: PT-HL, First Transverse Reinforcing Bar Fracture
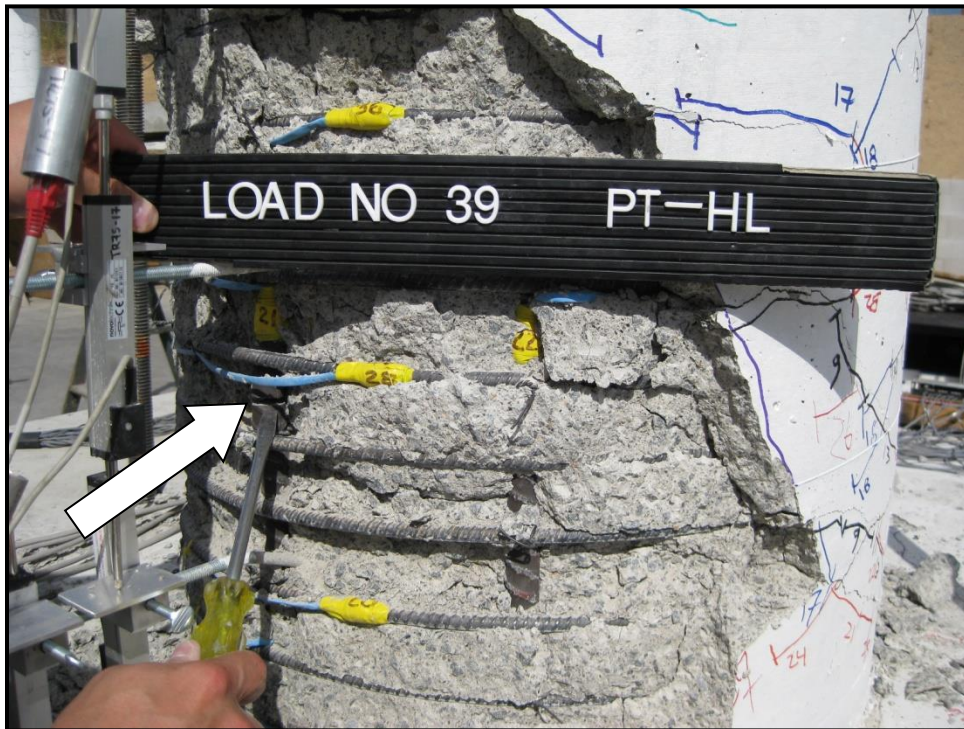
Figure 4-42: PT-HL, First Longitudinal Reinforcing Bar Fracture
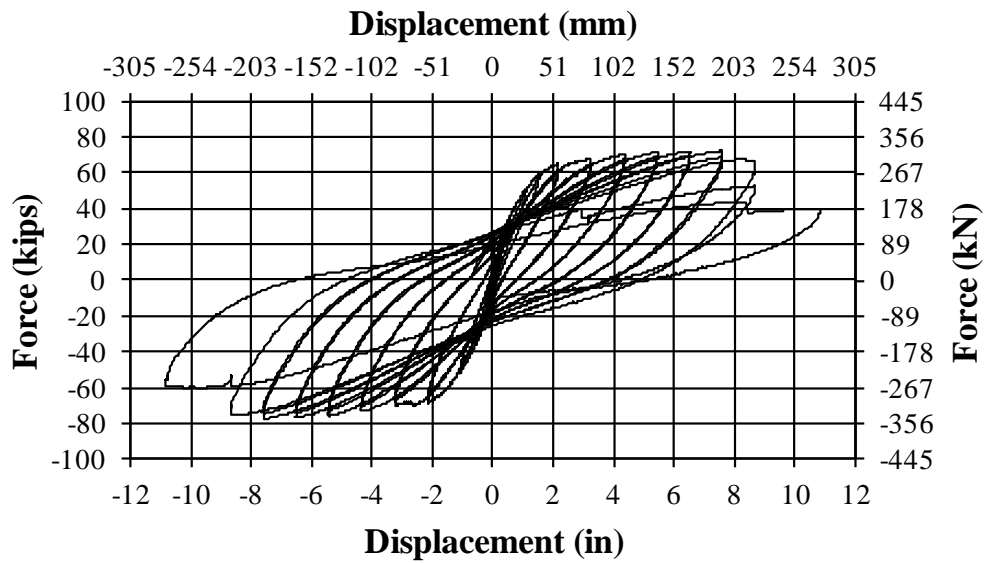
Figure 4-43: PT-HL Hysteresis
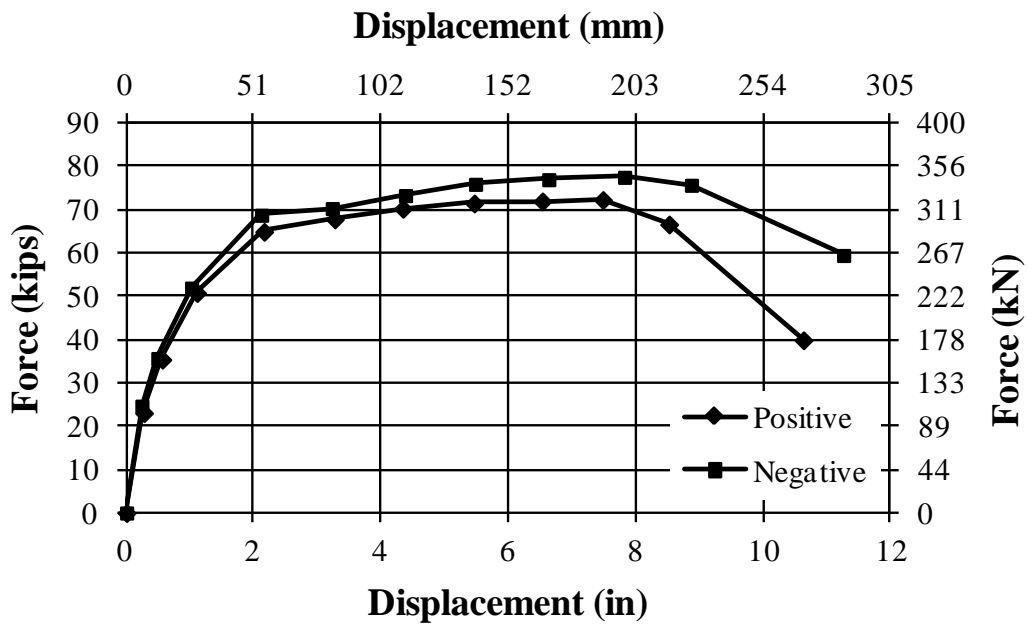
Figure 4-44: PT-HL Positive and Negative Hysteretic Envelope

137
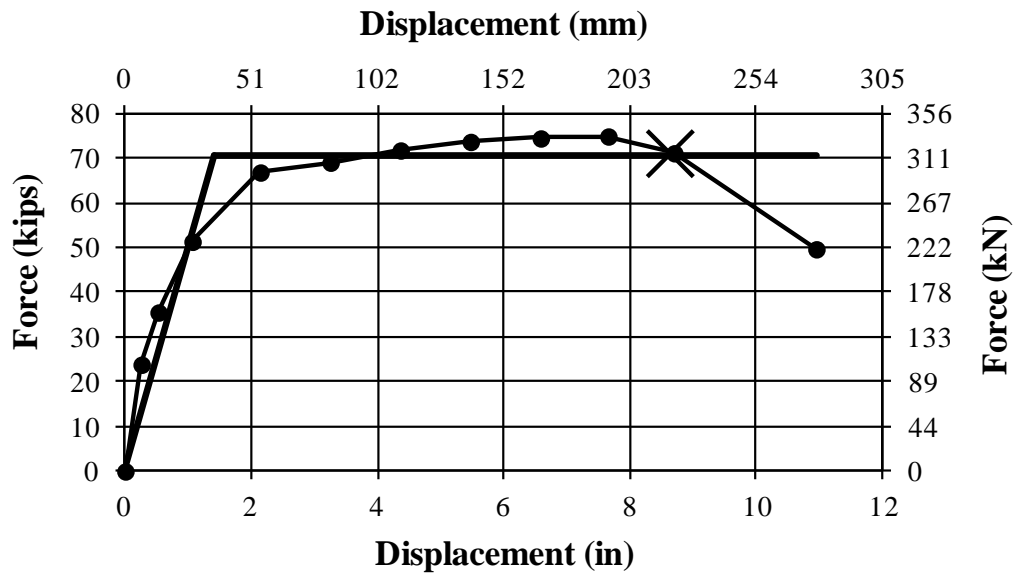
Figure 4-45: PT-HL Average Pushover Curve
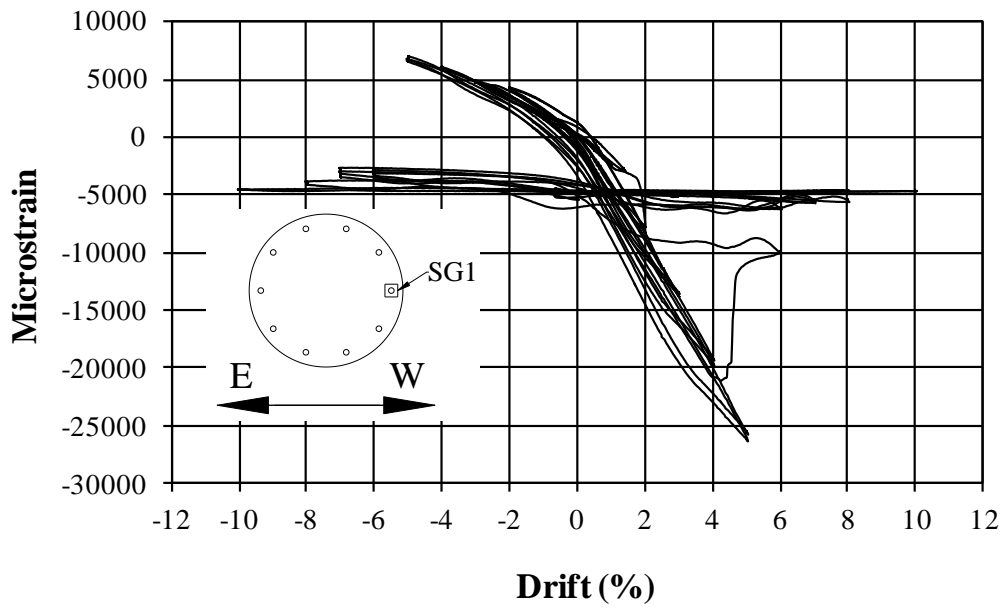
Figure 4-46: PT-HL Strain vs. Drift, Strain Gauge 1
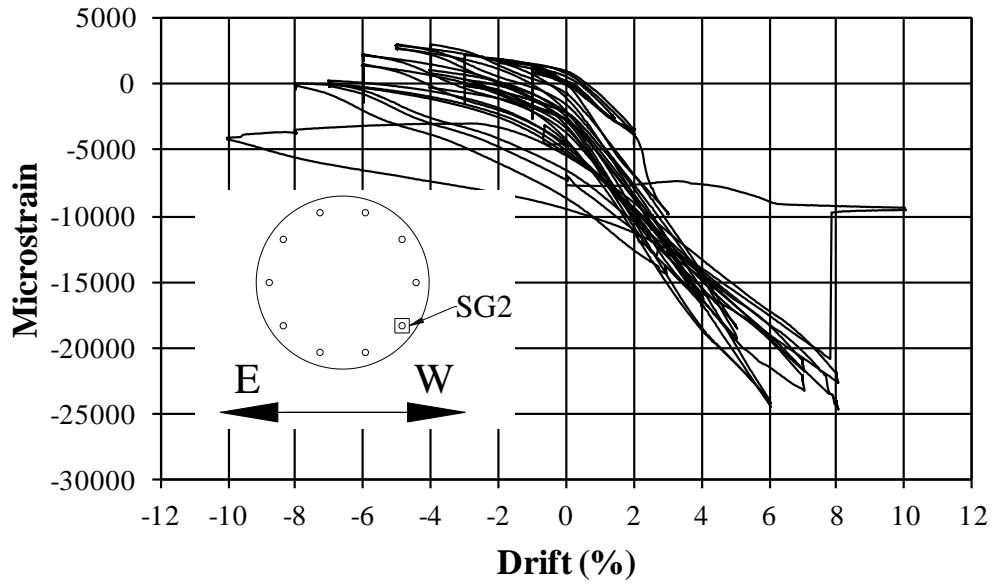
Figure 4-47: PT-HL Strain vs. Drift, Strain Gauge 2
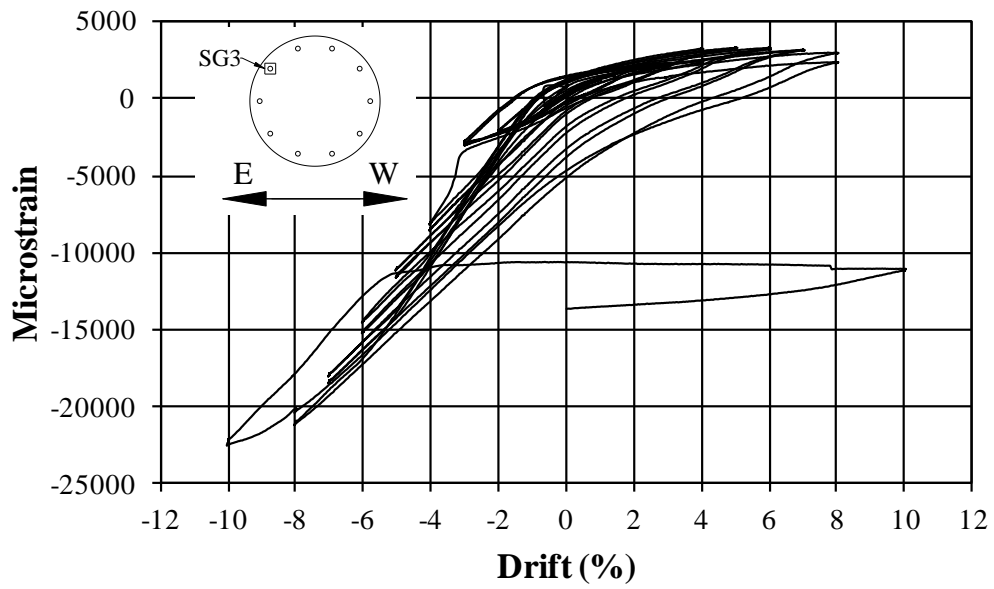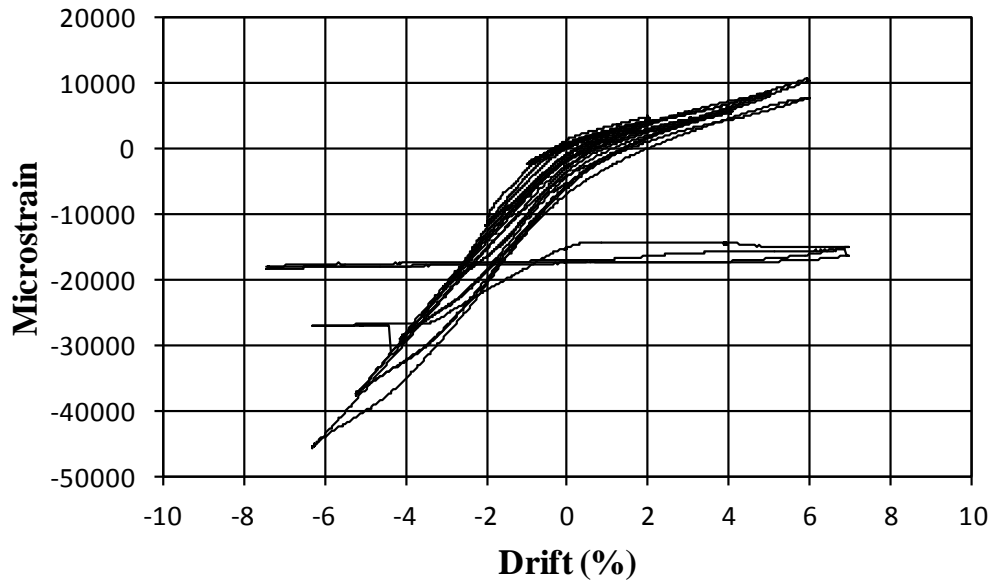

Figure 4-48: PT-HL Strain vs. Drift, Strain Gauge 3
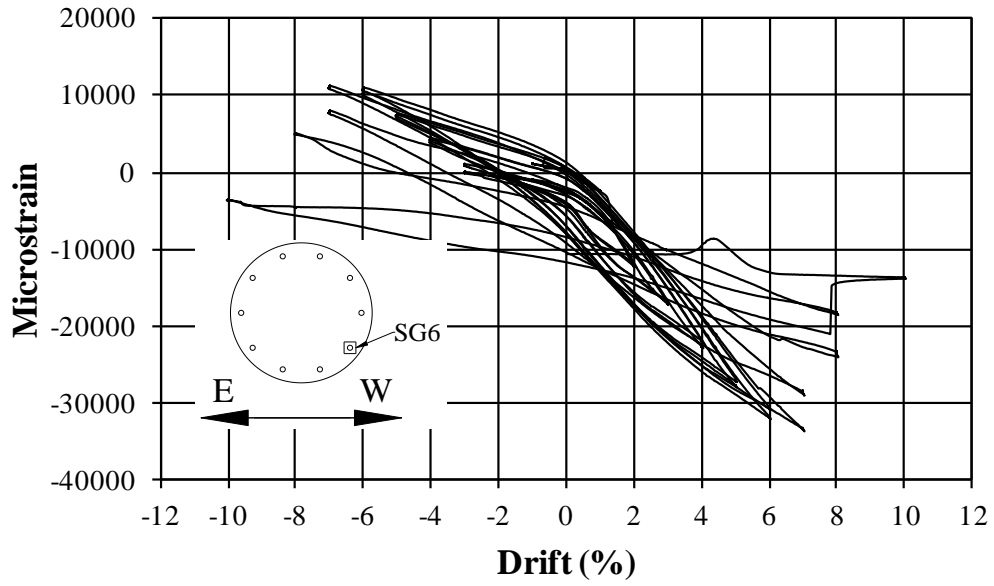
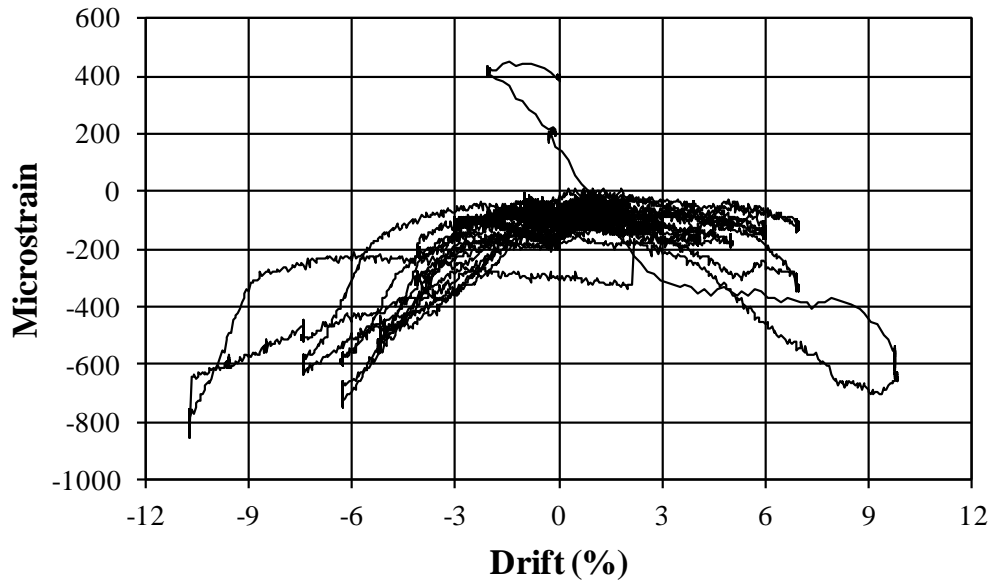**Figure 4-49: PT-HL Strain vs. Drift, Strain Gauge 6**
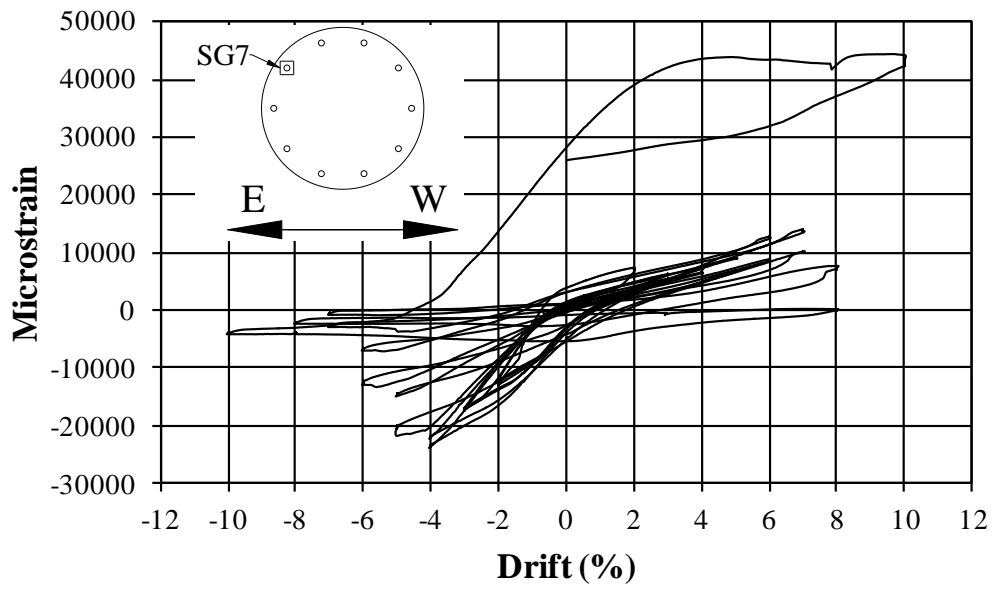
Figure 4-50: PT-HL Strain vs. Drift, Strain Gauge 7
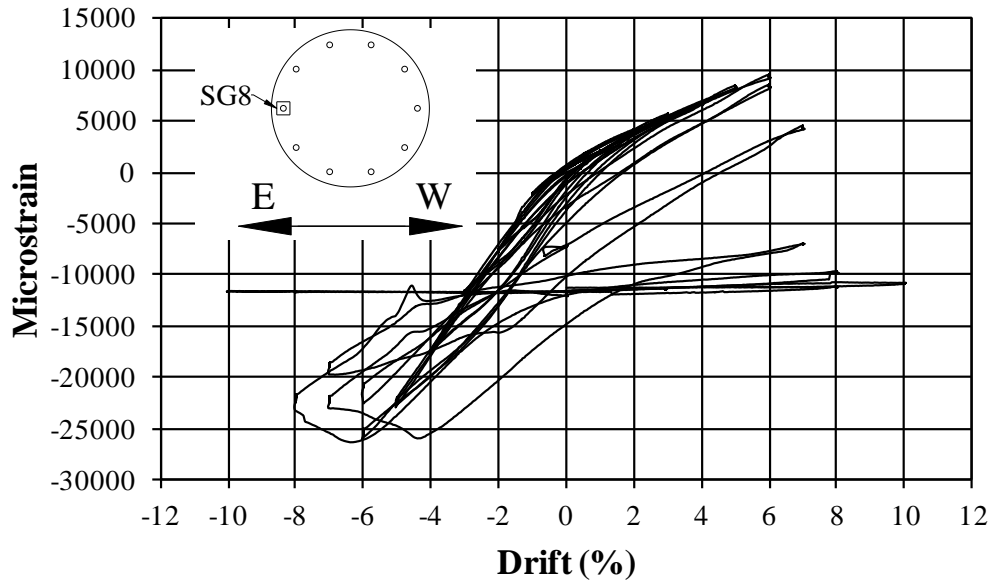
Figure 4-51: PT-HL Strain vs. Drift, Strain Gauge 8
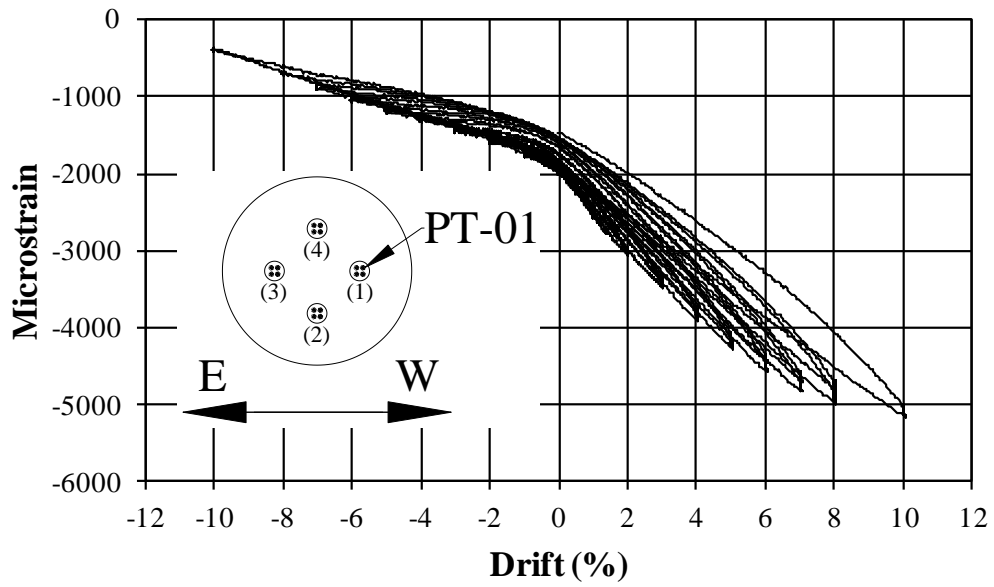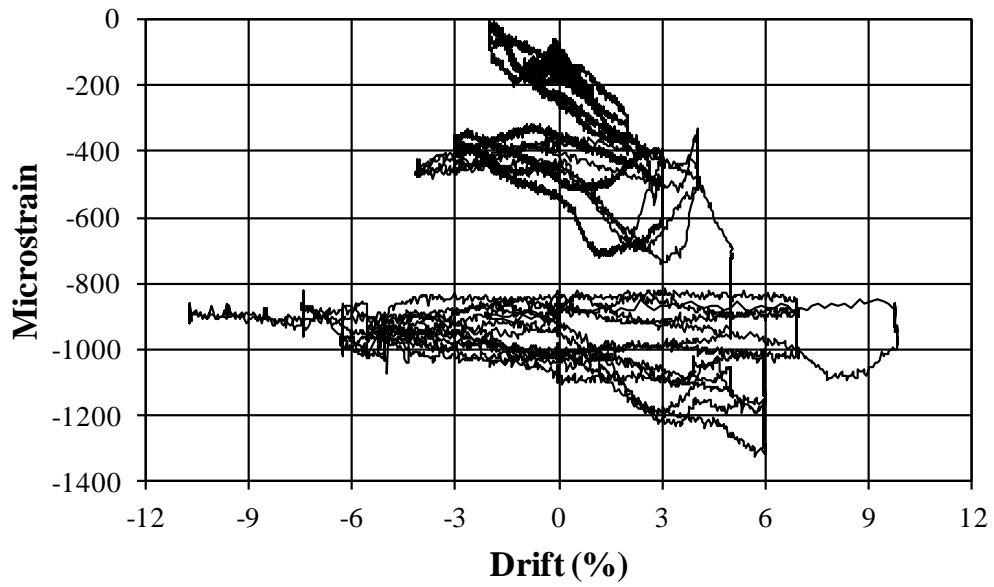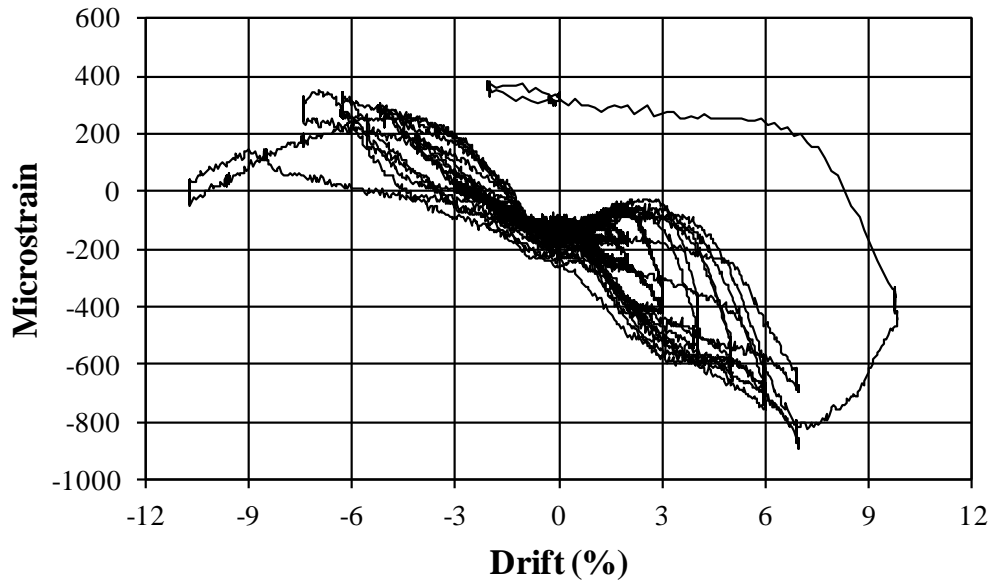

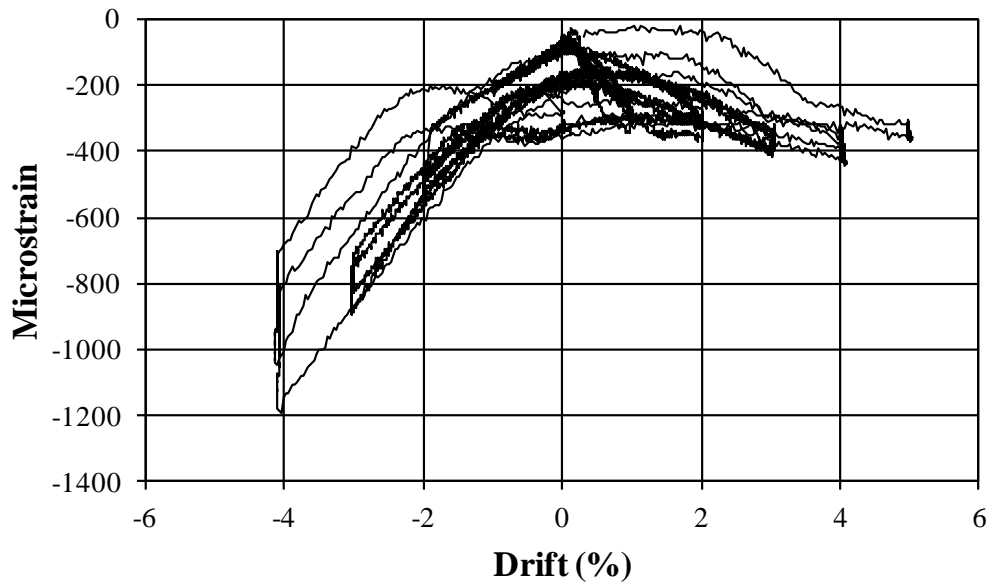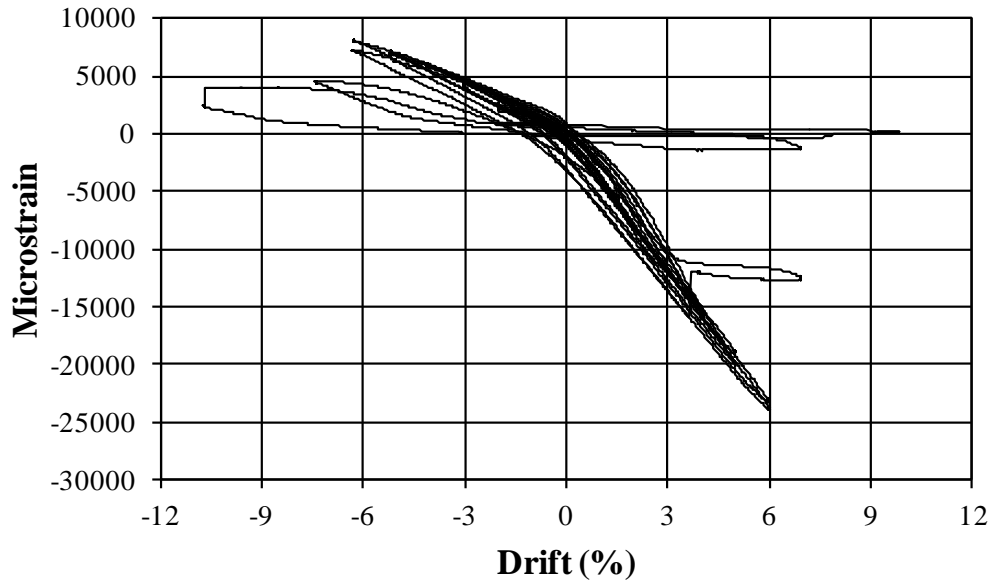**Figure 4-52: PT-HL Strain vs. Drift, Strain Gauge PT-01, Tendon 1**
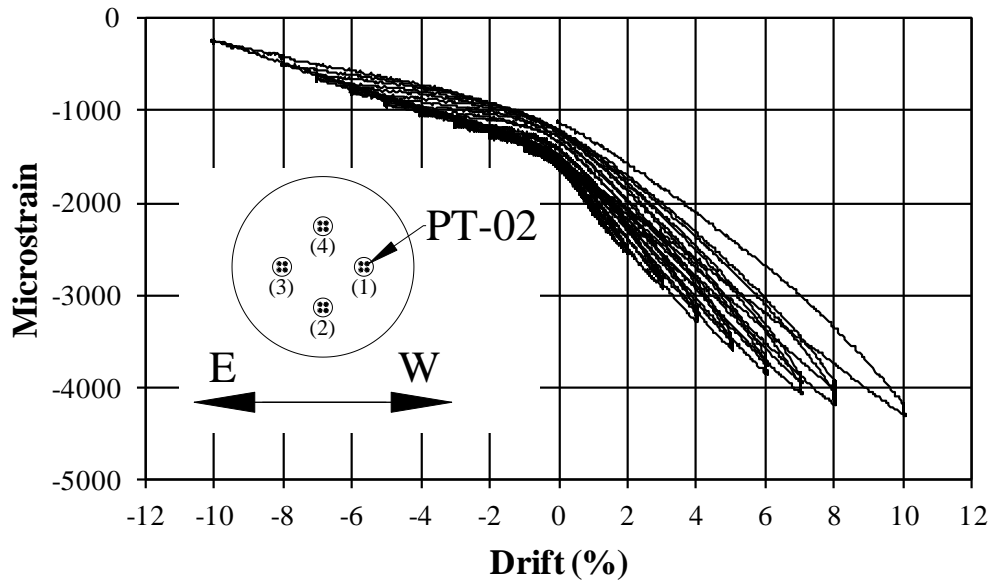
Figure 4-53: PT-HL Strain vs. Drift, Strain Gauge PT-02, Tendon 1
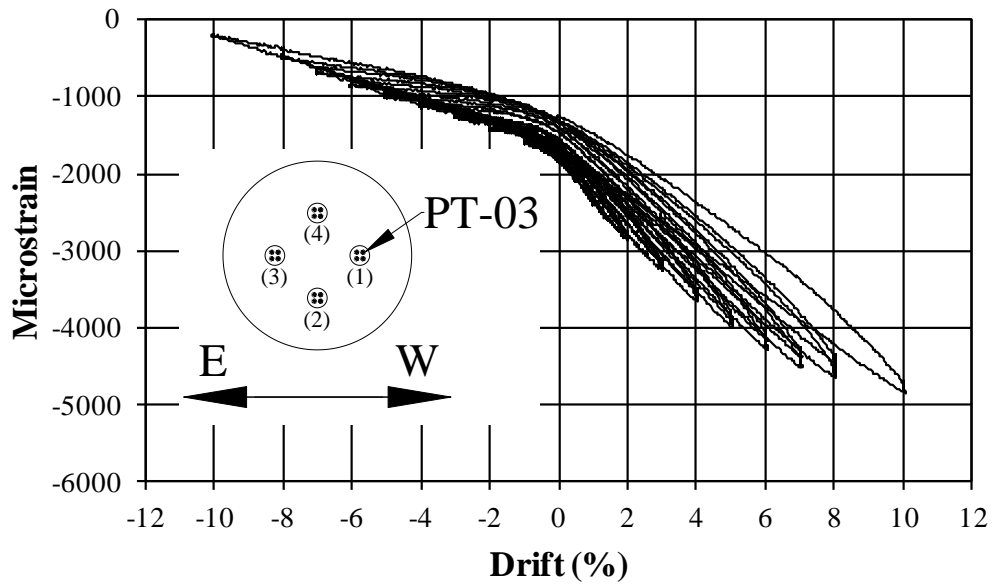
Figure 4-54: PT-HL Strain vs. Drift, Strain Gauge PT-03, Tendon 1
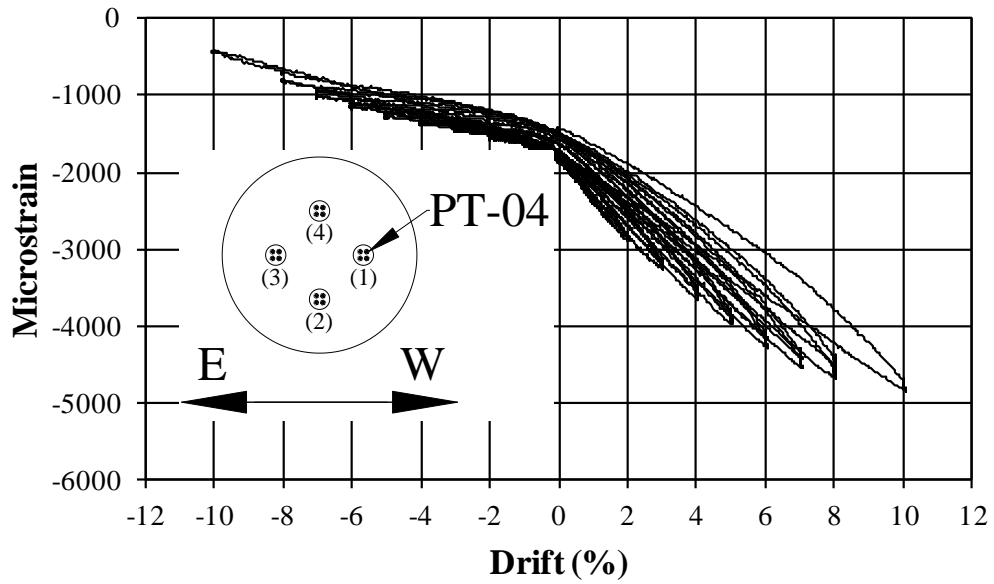
Figure 4-55: PT-HL Strain vs. Drift, Strain Gauge PT-04, Tendon 1
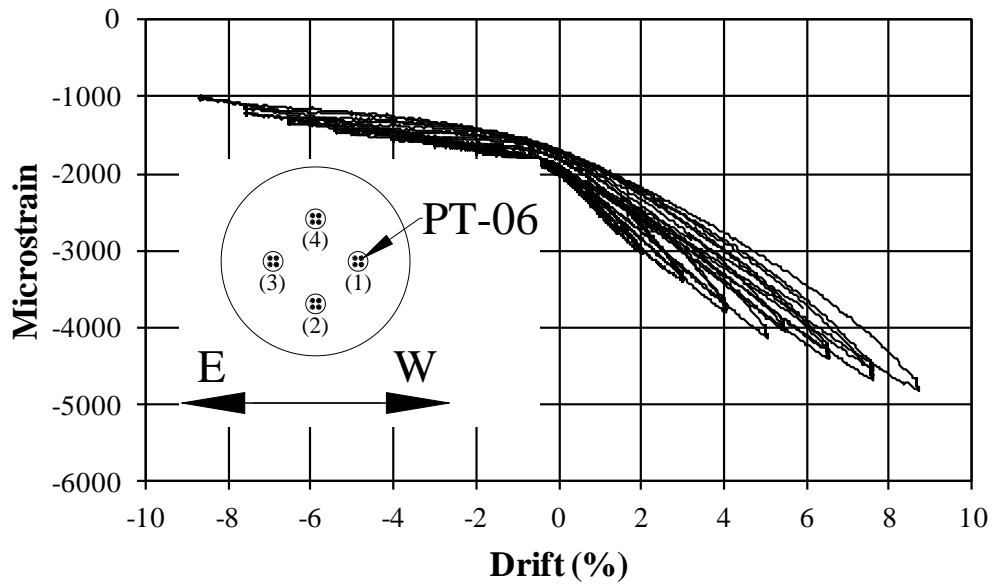
Figure 4-56: PT-HL Strain vs. Drift, Strain Gauge PT-06, Tendon 1
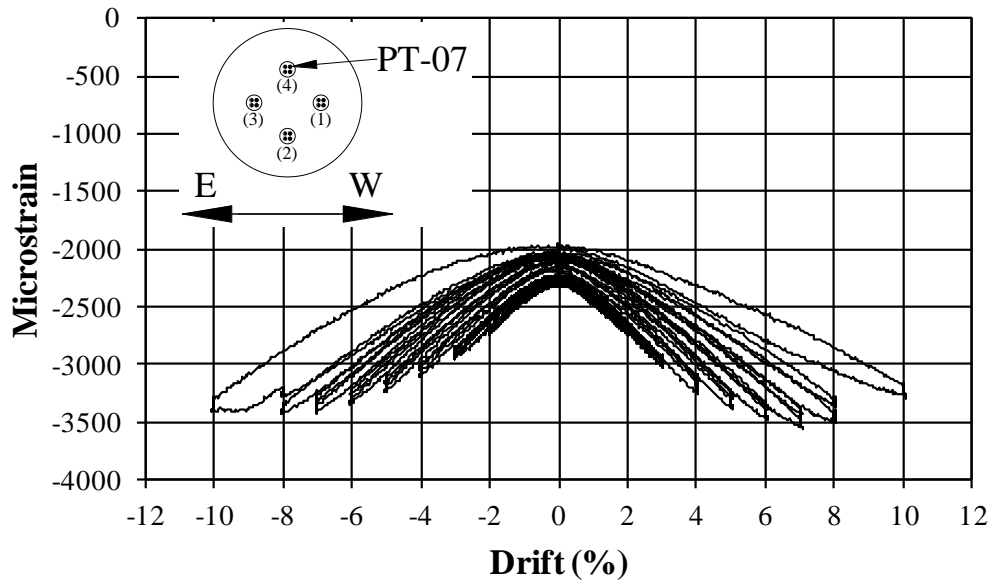
Figure 4-57: PT-HL Strain vs. Drift, Strain Gauge PT-07, Tendon 4
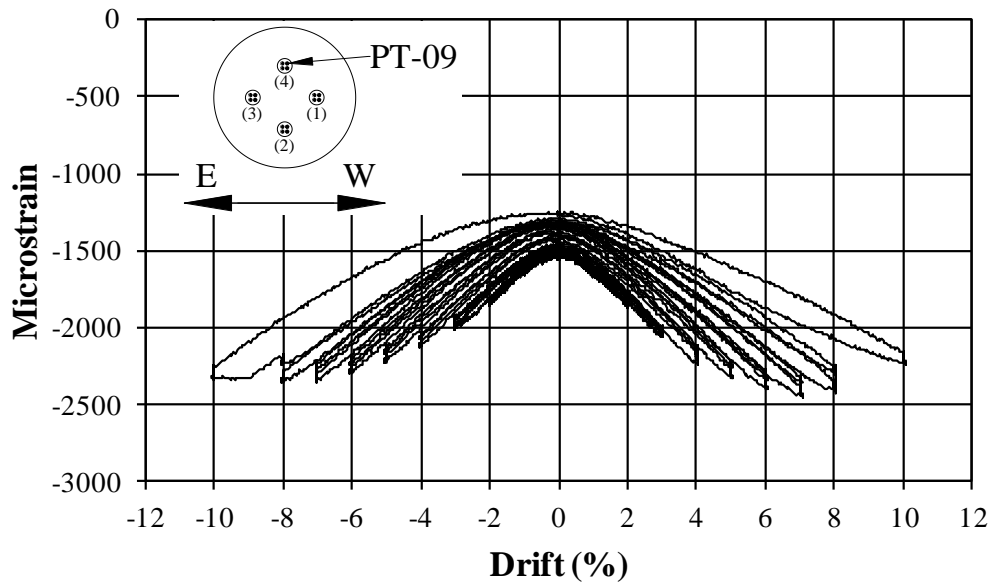
Figure 4-58: PT-HL Strain vs. Drift, Strain Gauge PT-09, Tendon 4

144
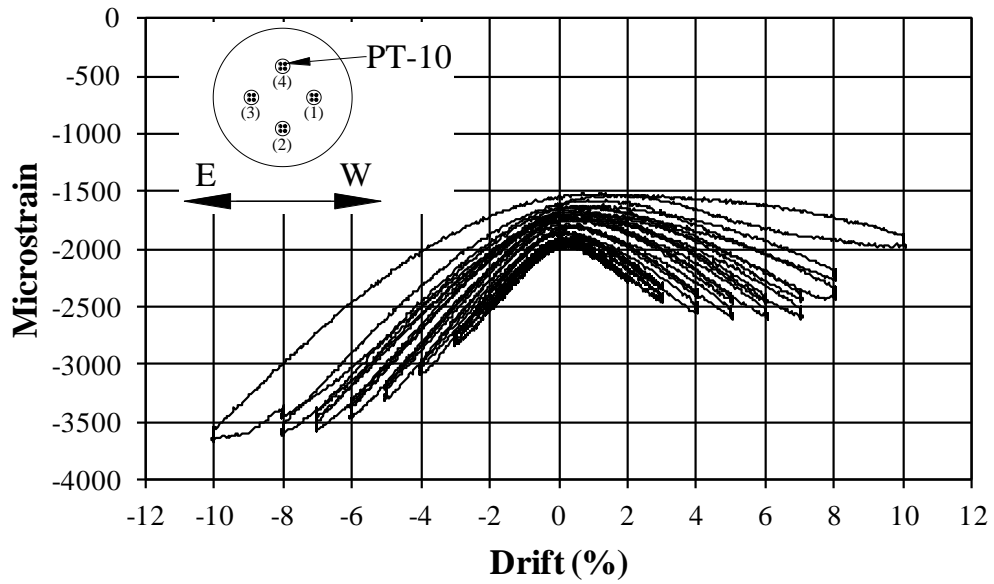
Figure 4-59: PT-HL Strain vs. Drift, Strain Gauge PT-10, Tendon 4
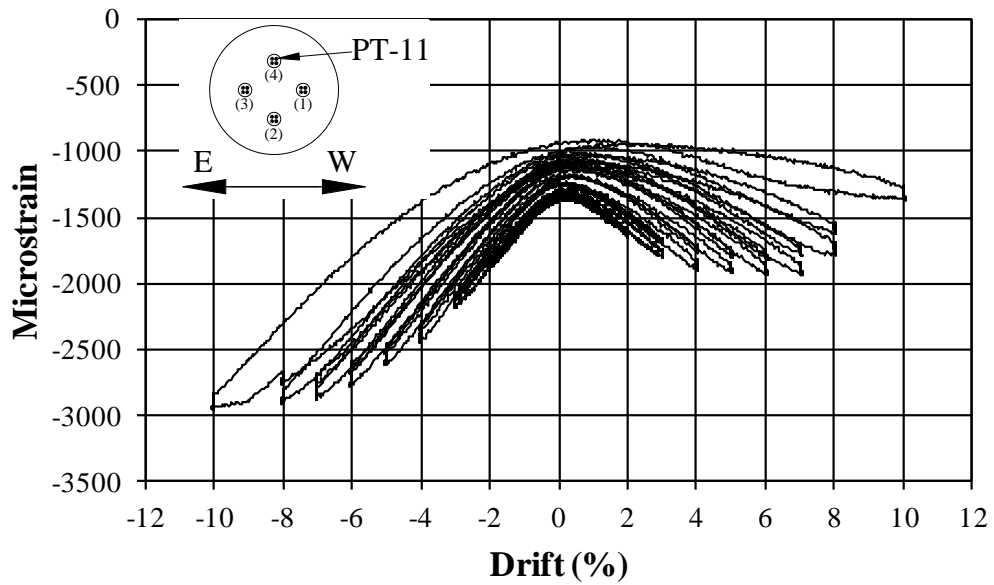
Figure 4-60: PT-HL Strain vs. Drift, Strain Gauge PT-11, Tendon 4
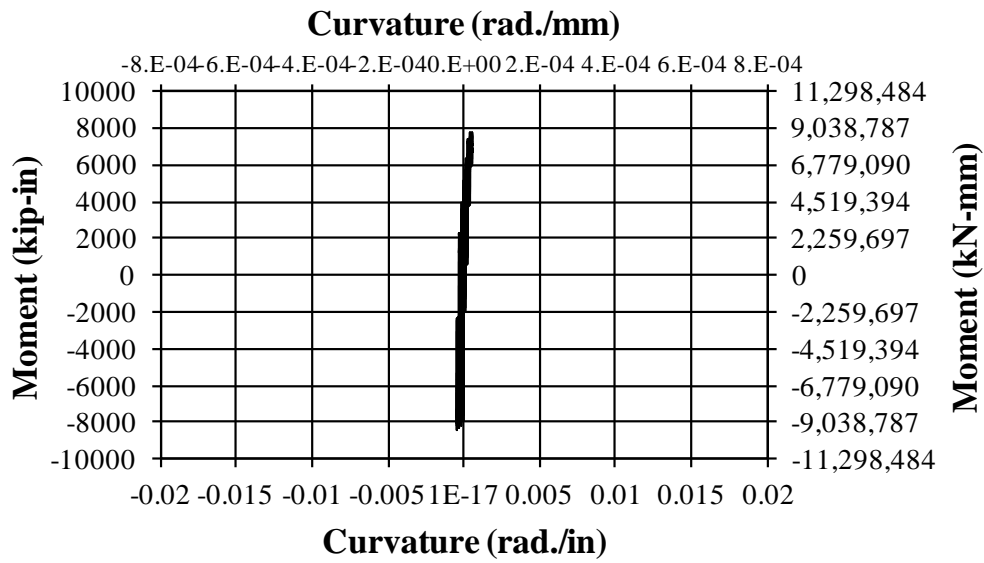
Figure 4-61: PT-HL Moment Curvature, Layer 4
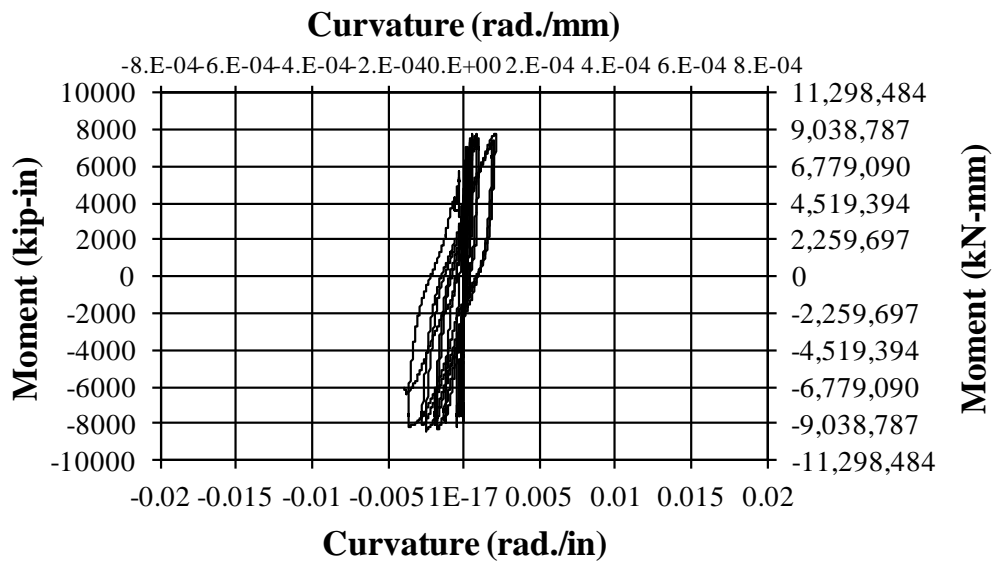
Figure 4-62: PT-HL Moment Curvature, Layer 3

146
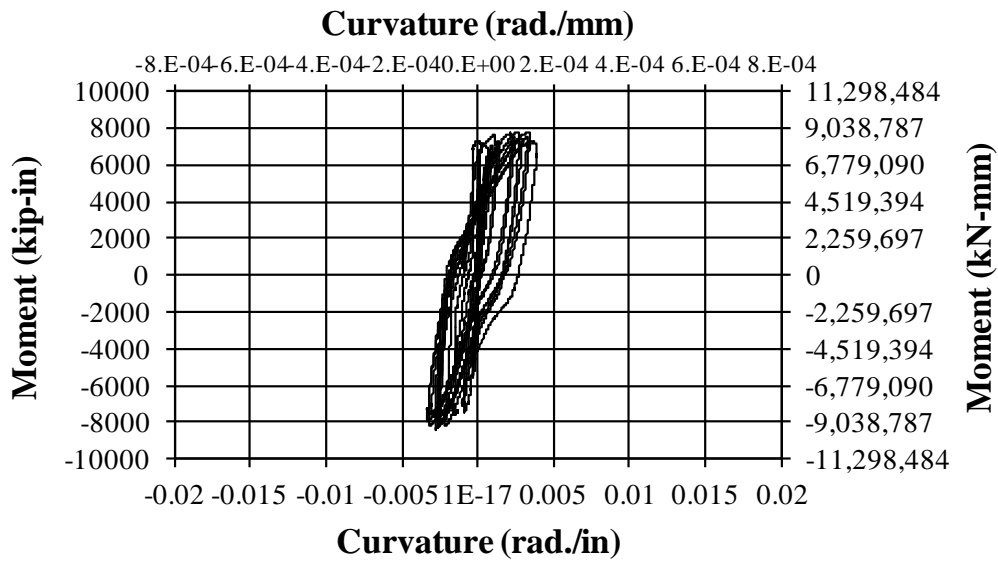
Figure 4-63: PT-HL Moment Curvature, Layer 2
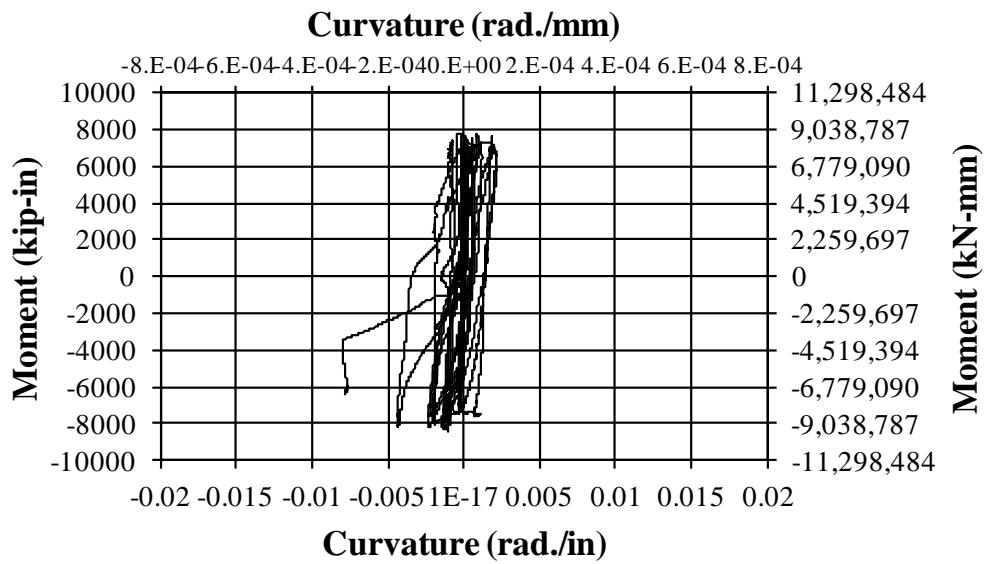
Figure 4-64: PT-HL Moment Curvature, Layer 1

147
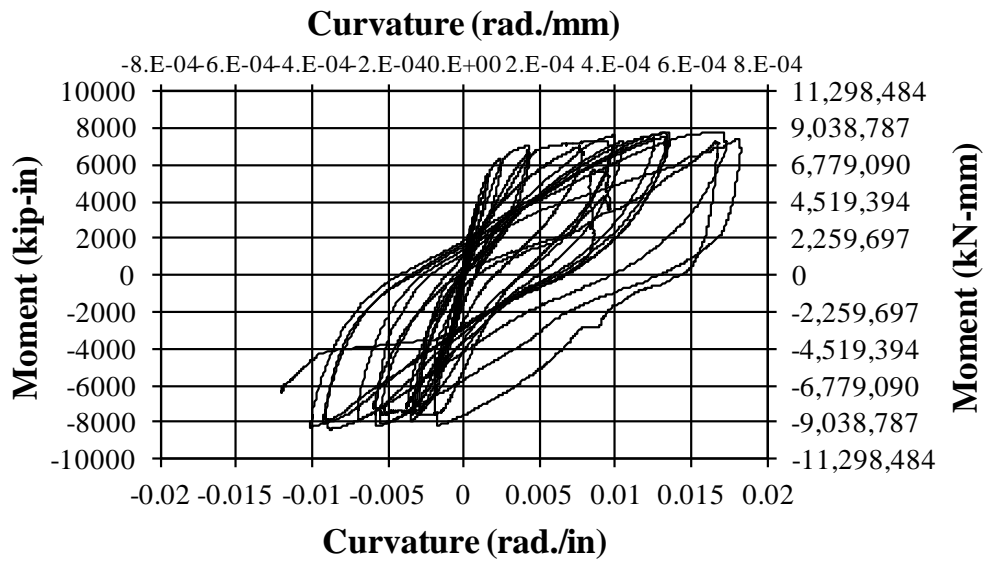
Figure 4-65: PT-HL Moment Curvature, Bond Slip
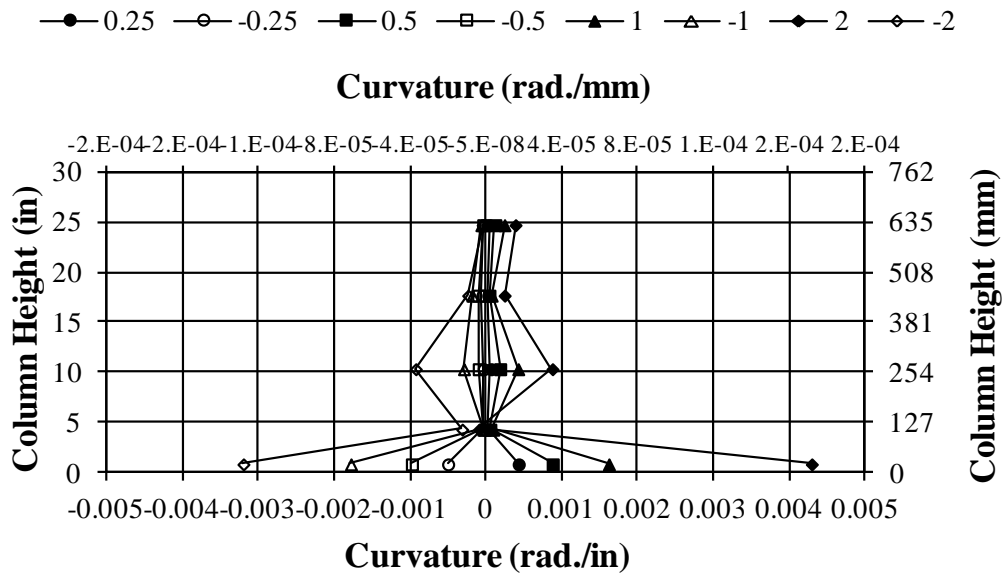
Figure 4-66: PT-HL Column Height vs. Curvature, 0.25% to 2% Drift
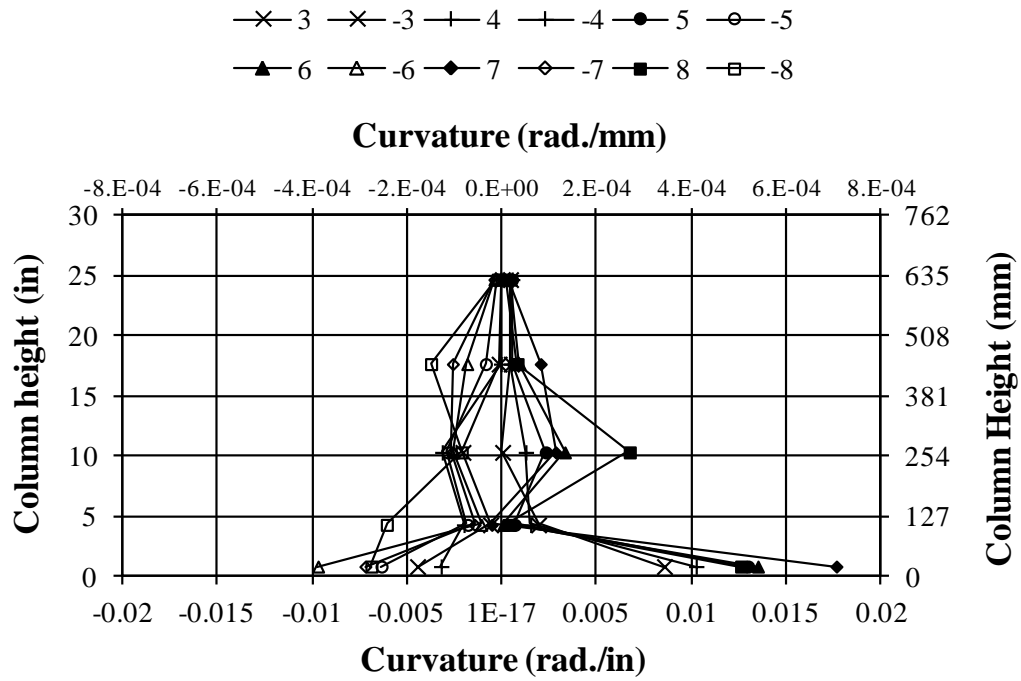
Figure 4-67: PT-HL Column Height vs. Curvature, 3% to 8% Drift
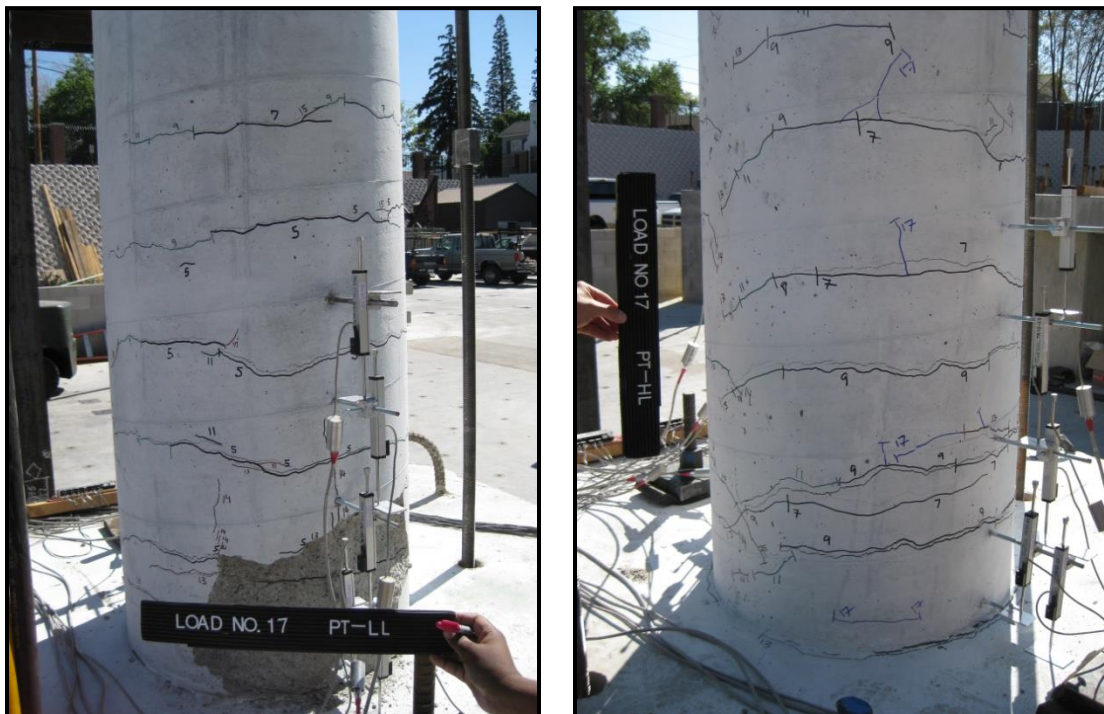
Figure 4-68: 3% Drift Damage Comparison

149

Figure 4-69: 4% Drift Damage Comparison
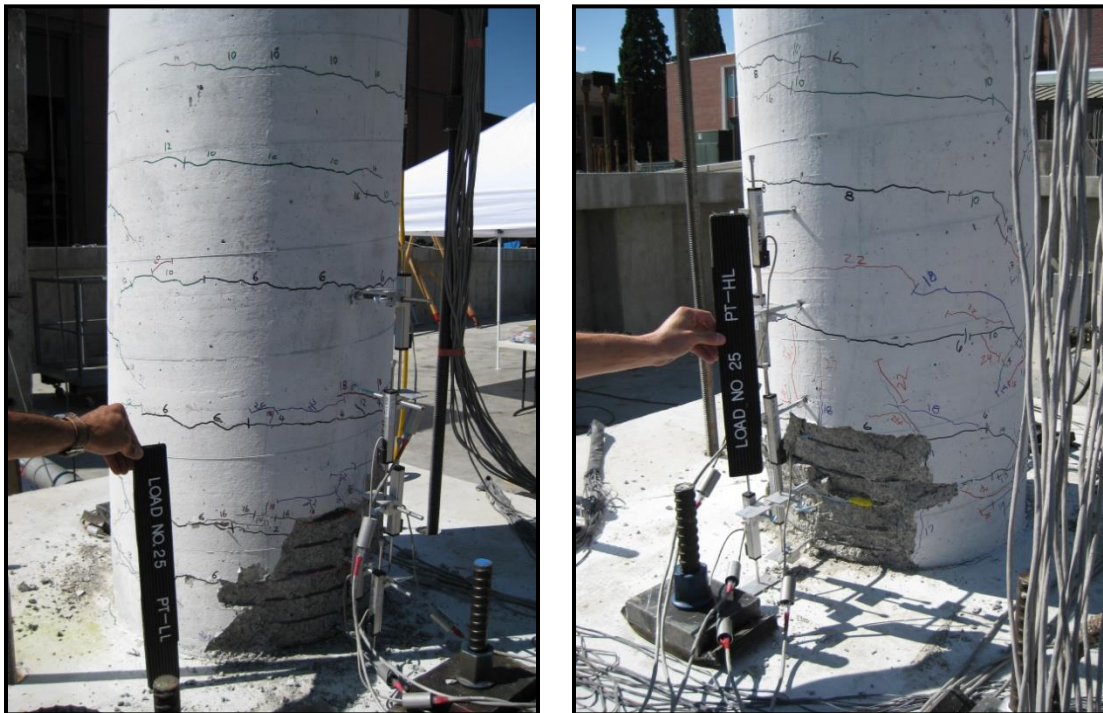
Figure 4-70: 5% Drift Damage Comparison
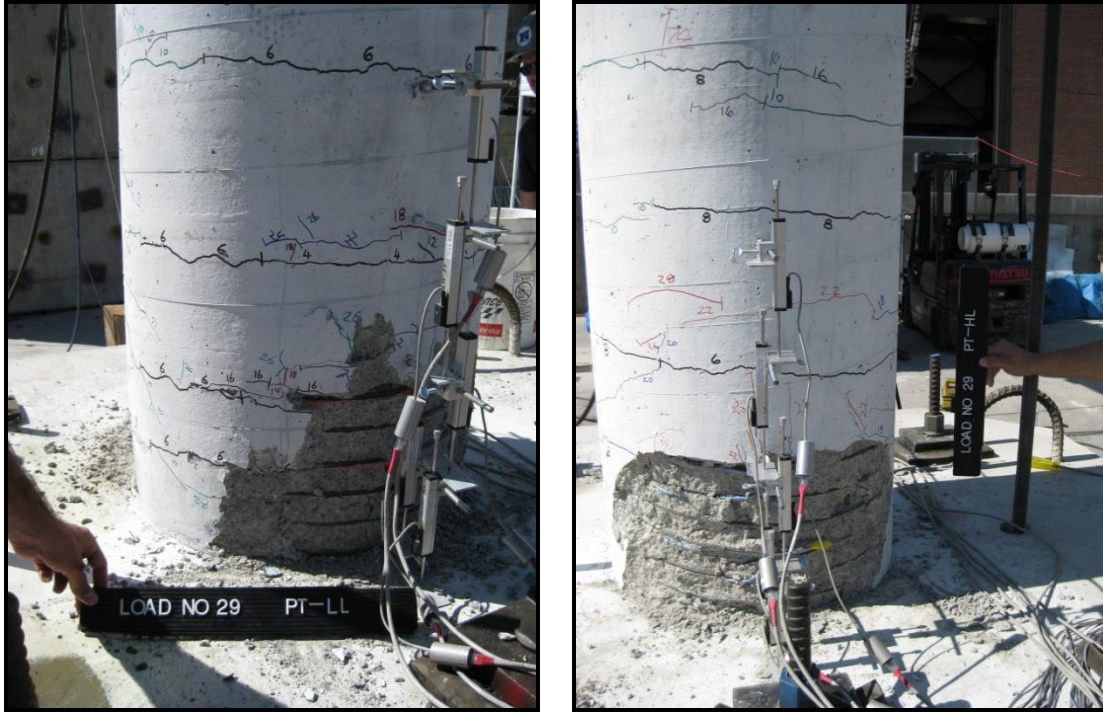
Figure 4-71: 6% Drift Damage Comparison

Figure 4-72: 7% Drift Damage Comparison

151

Figure 4-73: Removed Tendon

Figure 4-74: Strand Damage
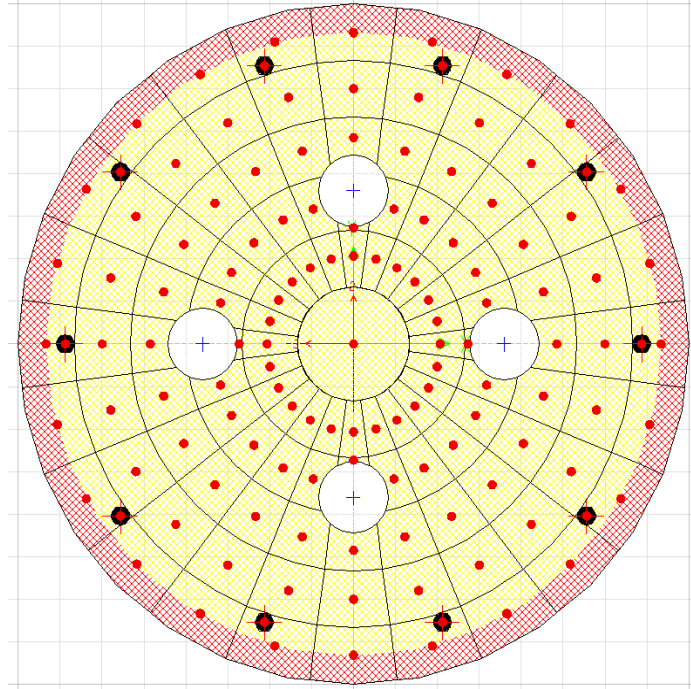
Figure 5-1: PT-LL Fiber Section
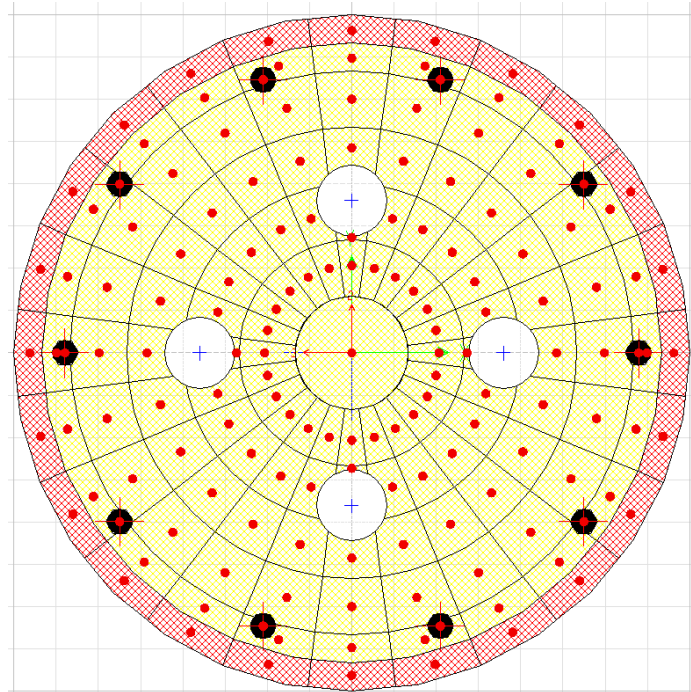
Figure 5-2: PT-HL Fiber Section

153
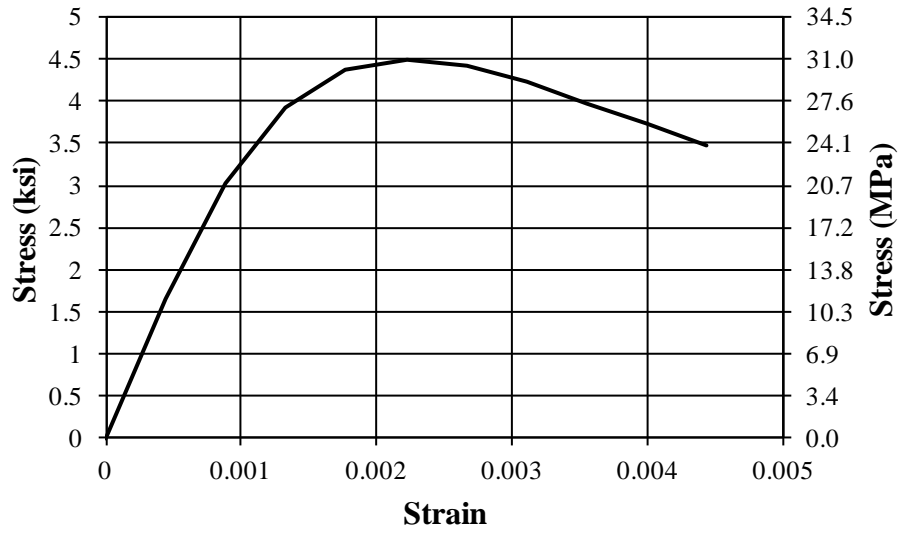
Figure 5-3: Unconfined Concrete Model
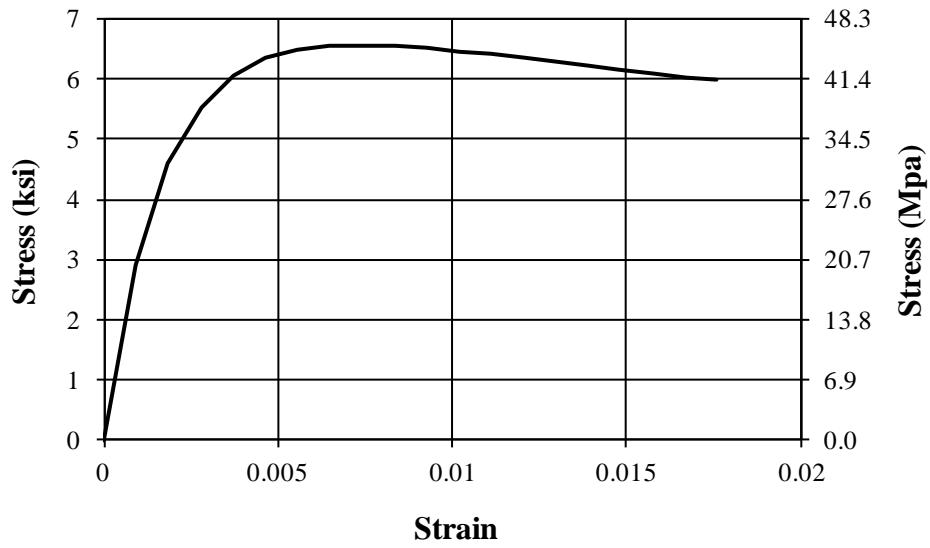
Figure 5-4: Confined Concrete Model
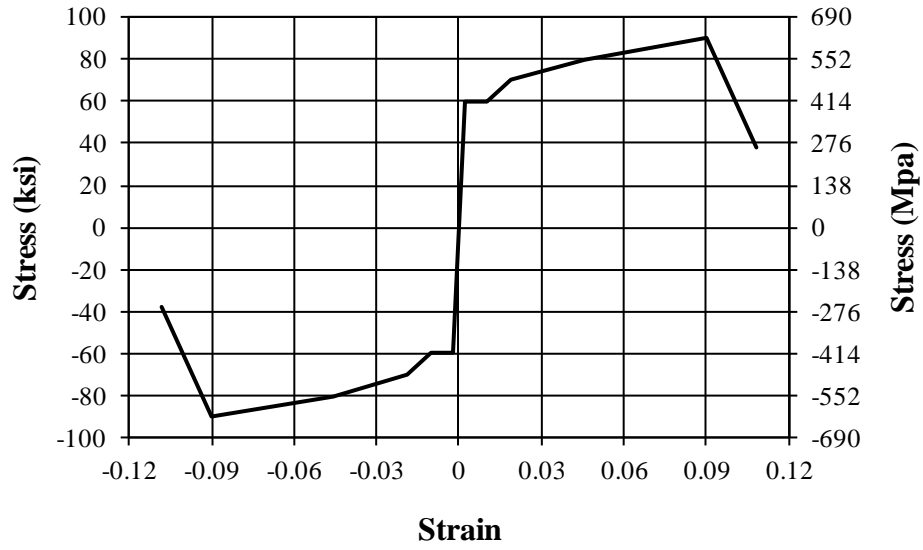
Figure 5-5: Reinforcing Steel Model
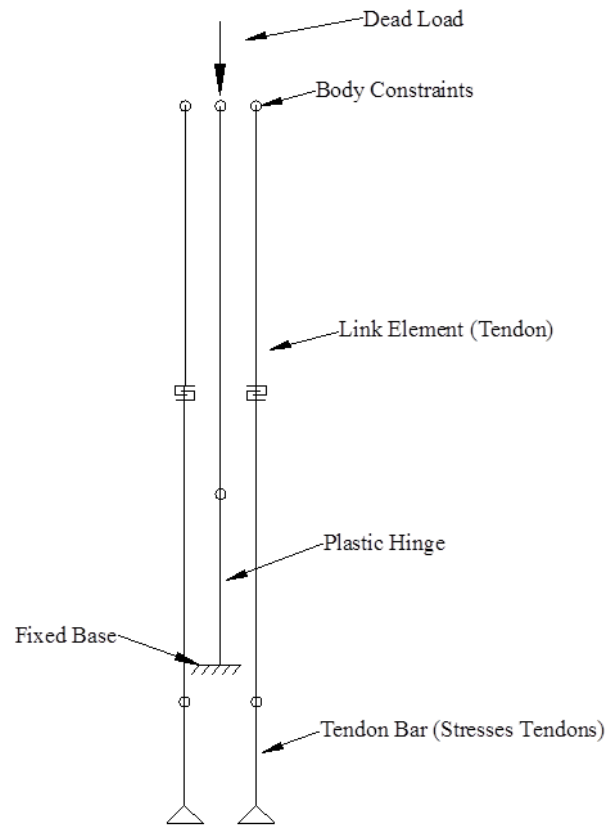
Figure 5-6: Analytical Model Elevation
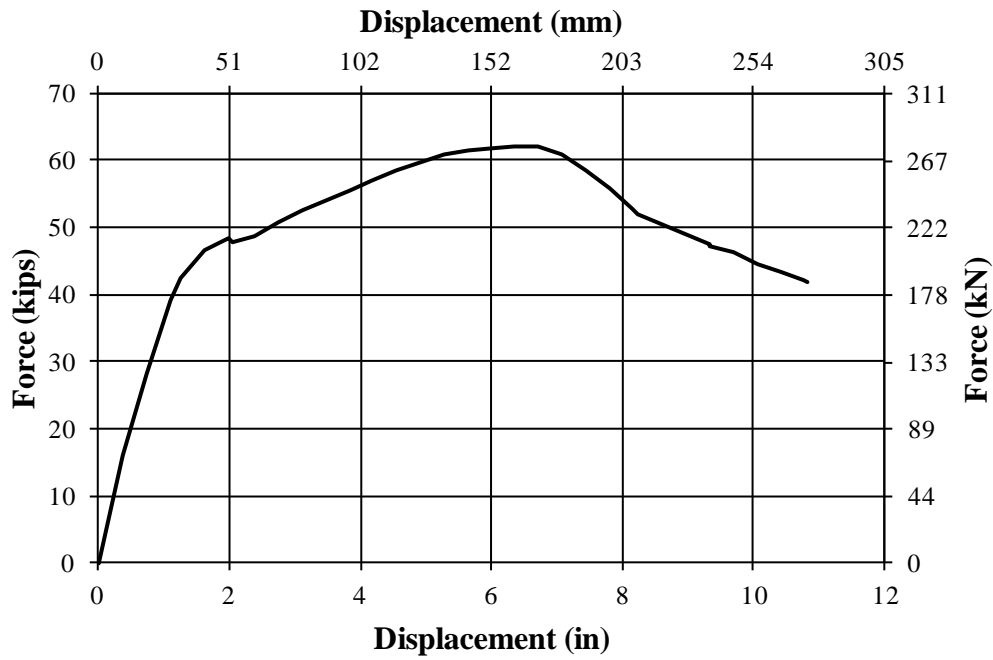
Figure 5-7: PT-LL Predicted Pushover
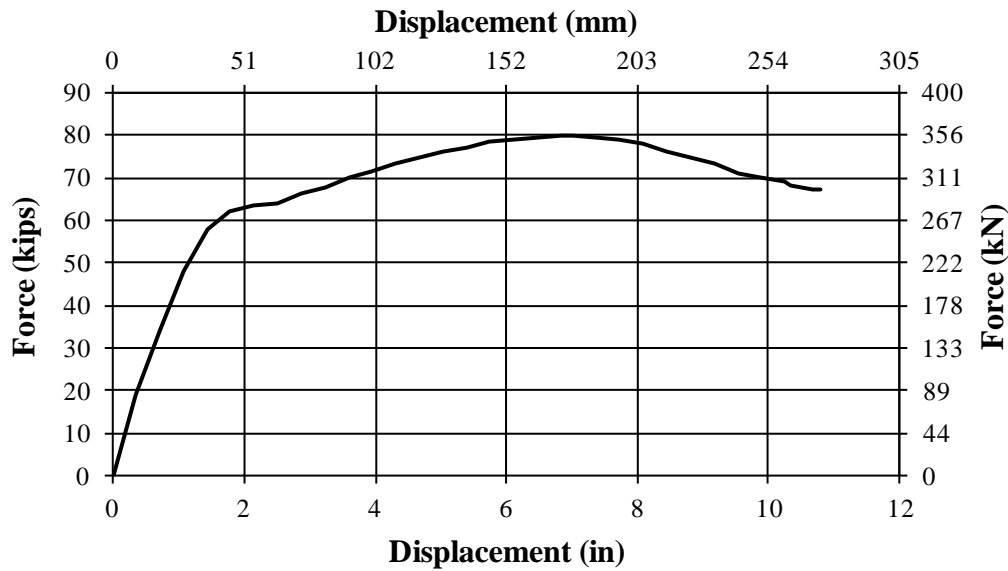
Figure 5-8: PT-HL Predicted Pushover

156
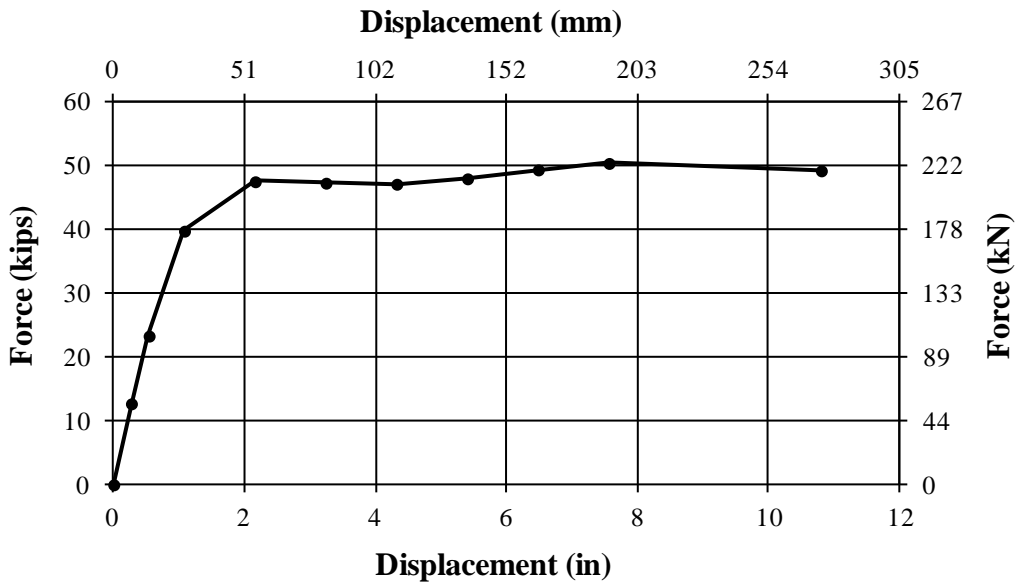
Figure 5-9: PT-LL Modified Pushover
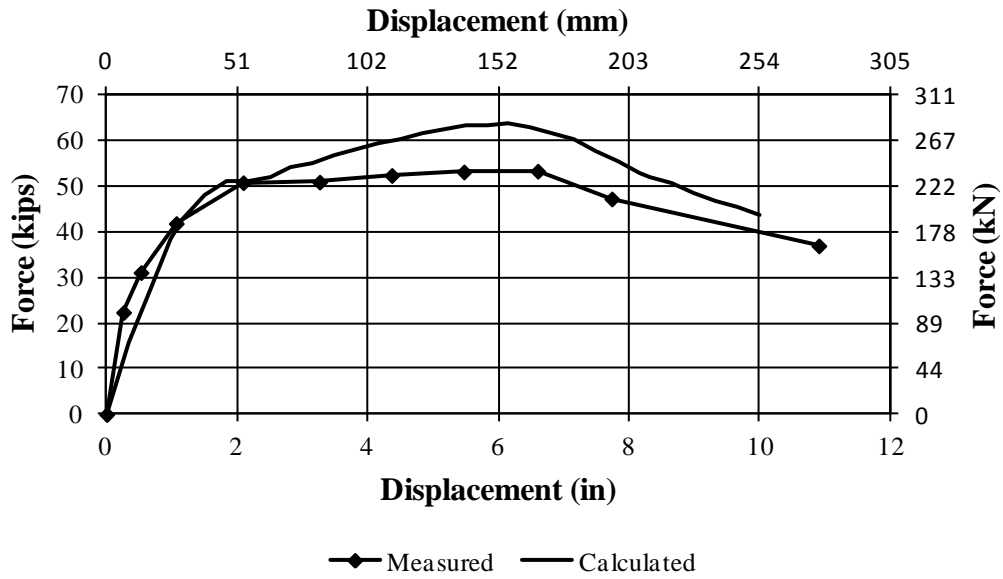
Figure 5-10: PT-LL Pushover Comparison
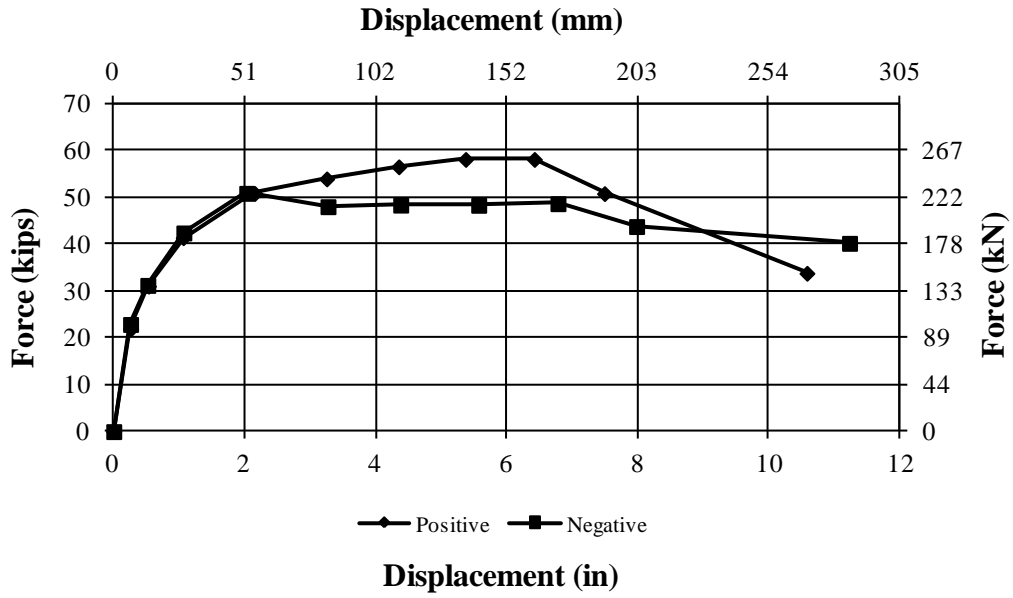
Figure 5-11: PT-LL Measured Envelopes
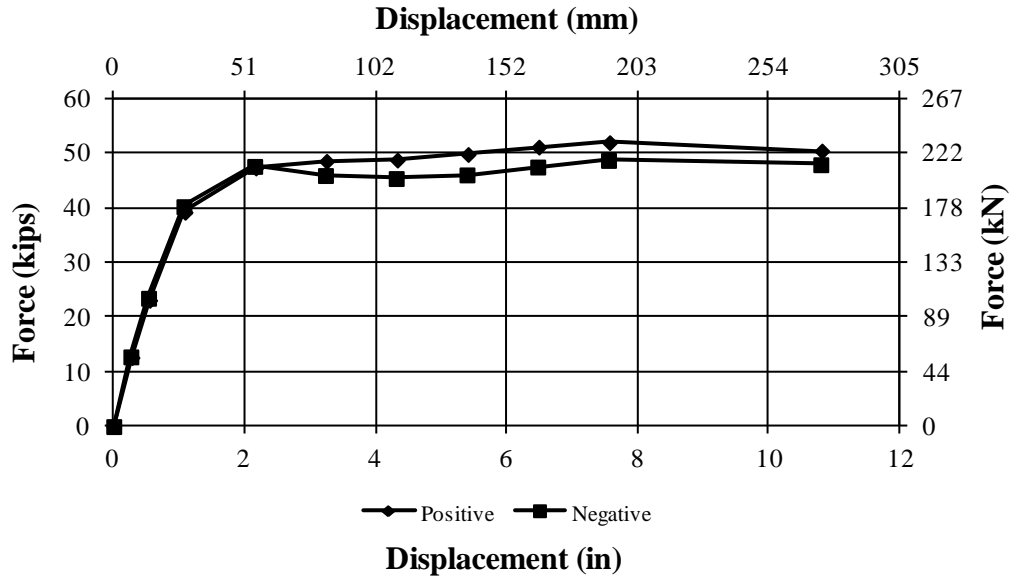
Figure 5-12: PT-LL Modified Calculated Envelopes

158
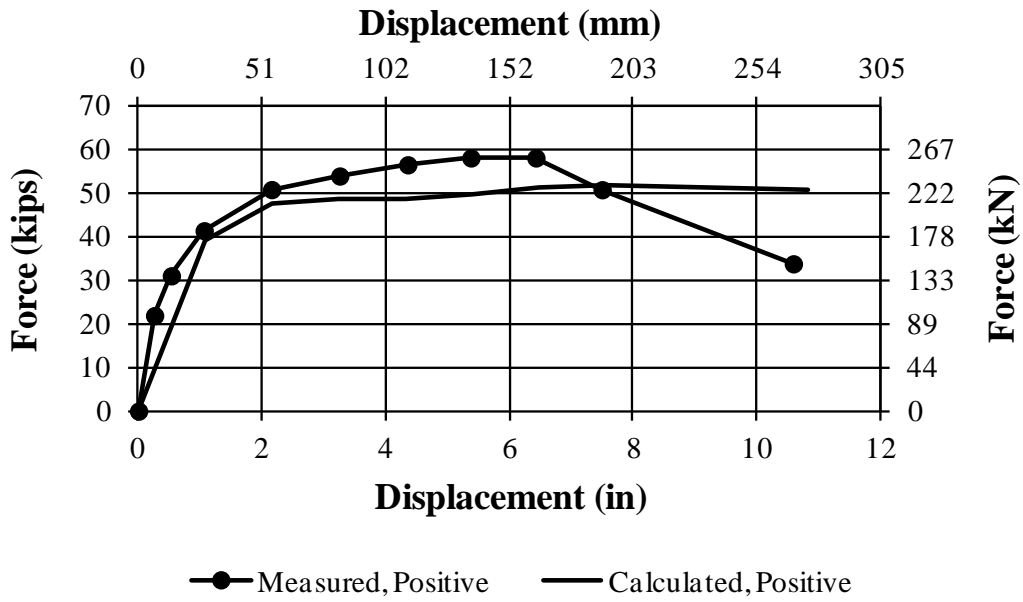
Figure 5-13: PT-LL Measured and Calculated Positive Pushover
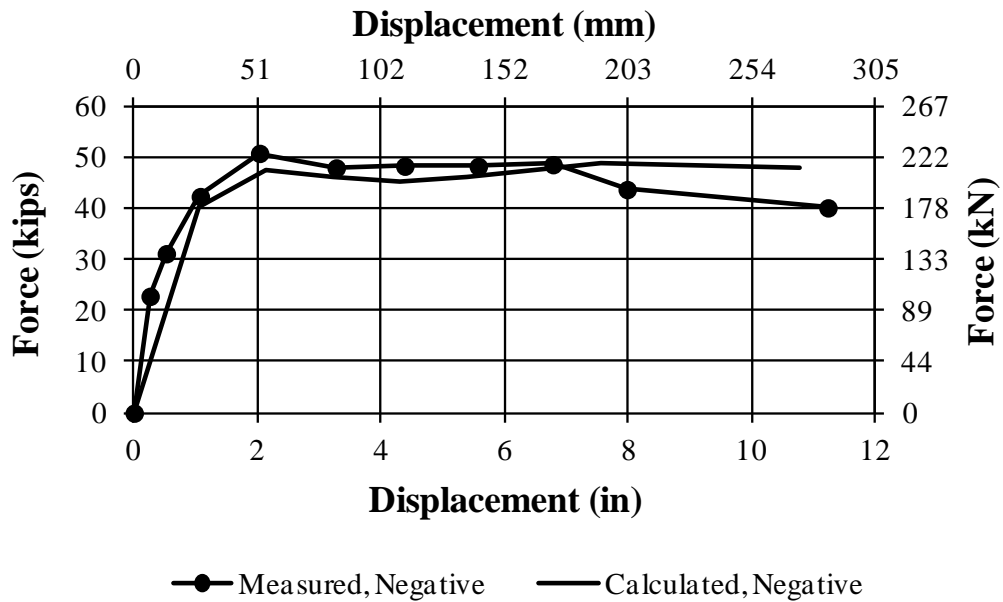
Figure 5-14: PT-LL Measured and Calculated Negative Pushover

Displacement (mm)
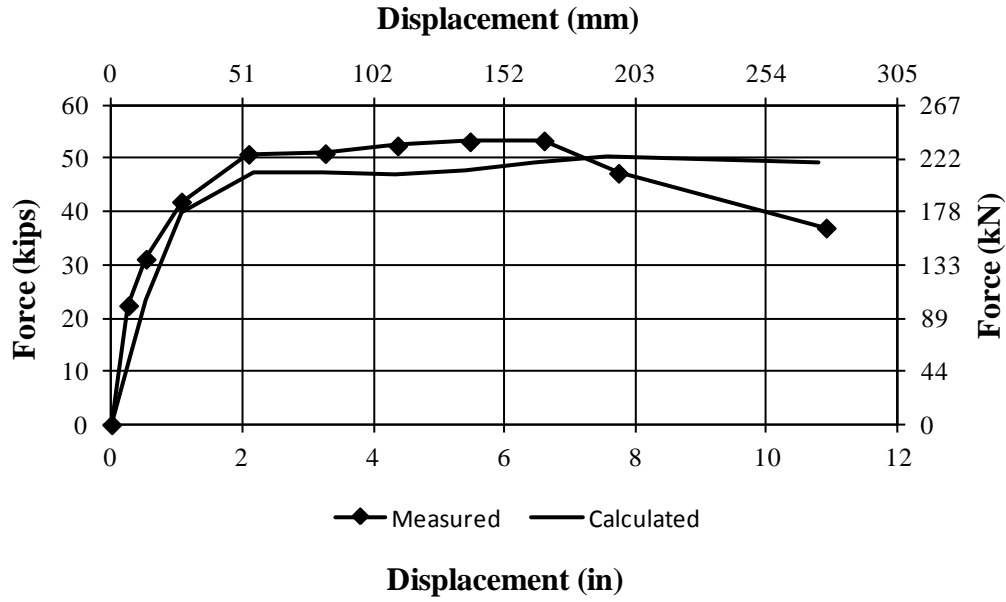
Figure 5-15: PT-LL Modified Average Pushover Comparison

Displacement (mm)
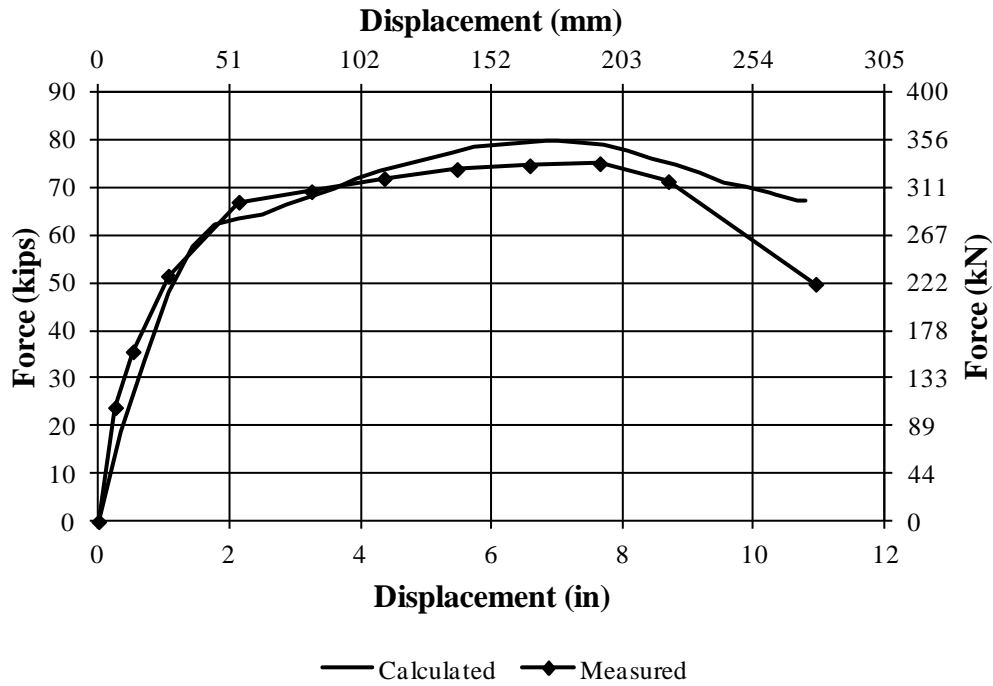
Figure 5-16: PT-HL Pushover Comparison

160
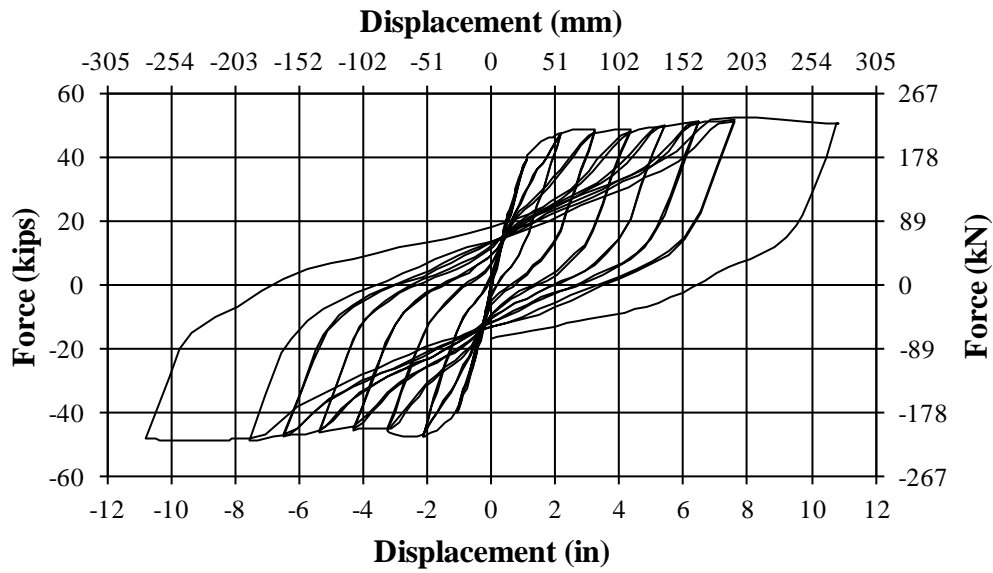
Figure 5-17: PT-LL Analytical Hysteresis
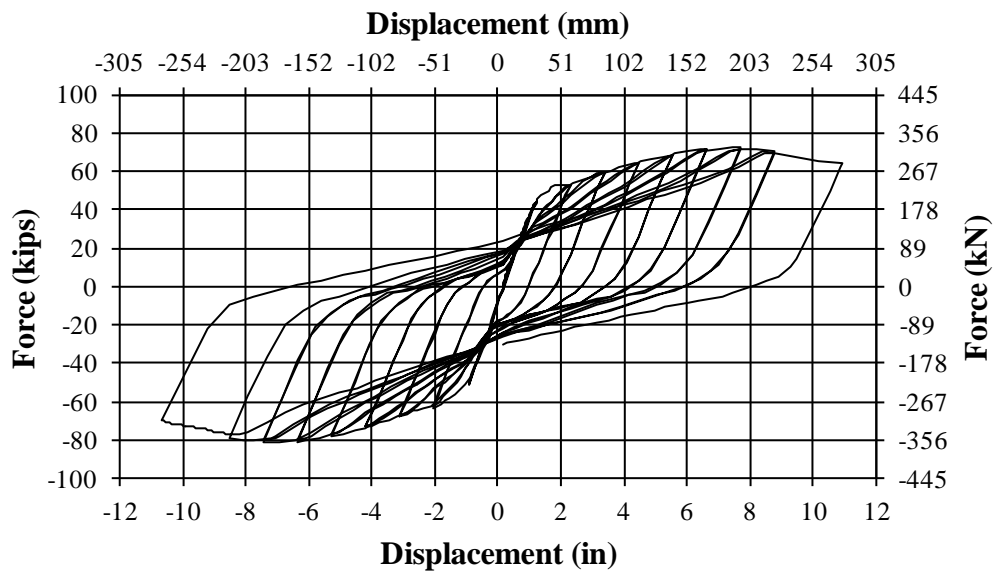
Figure 5-18: PT-HL Analytical Hysteresis

161
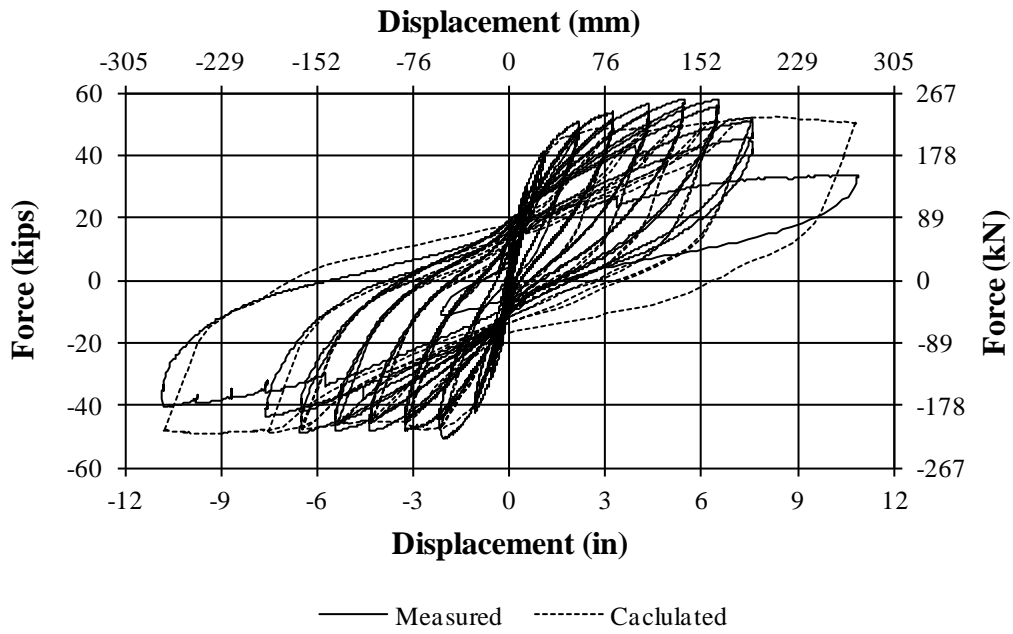
Figure 5-19: PT-LL Hysteresis Comparison
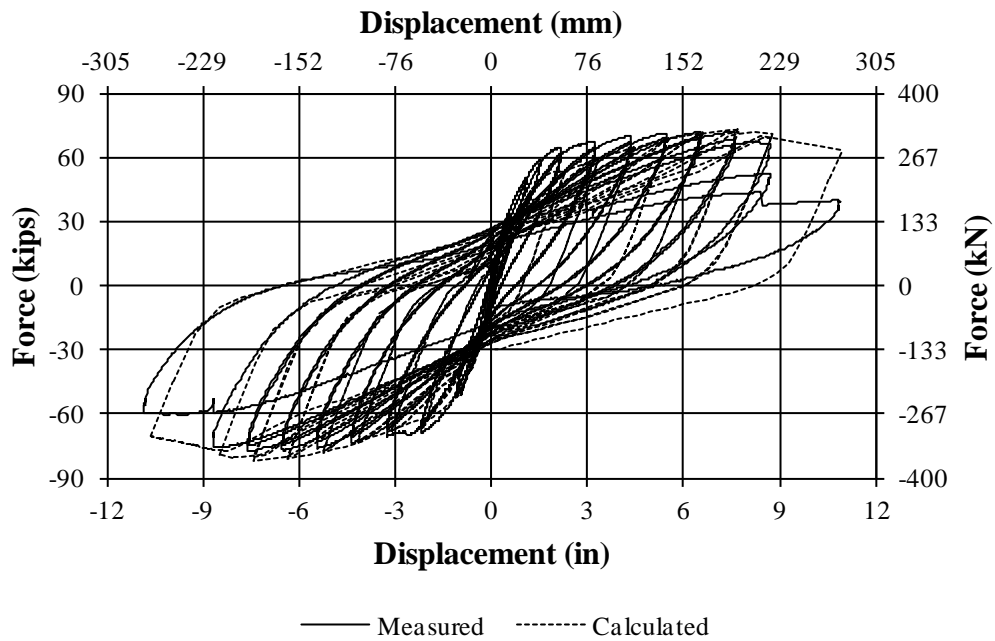
Figure 5-20: PT-HL Hysteresis Comparison

162
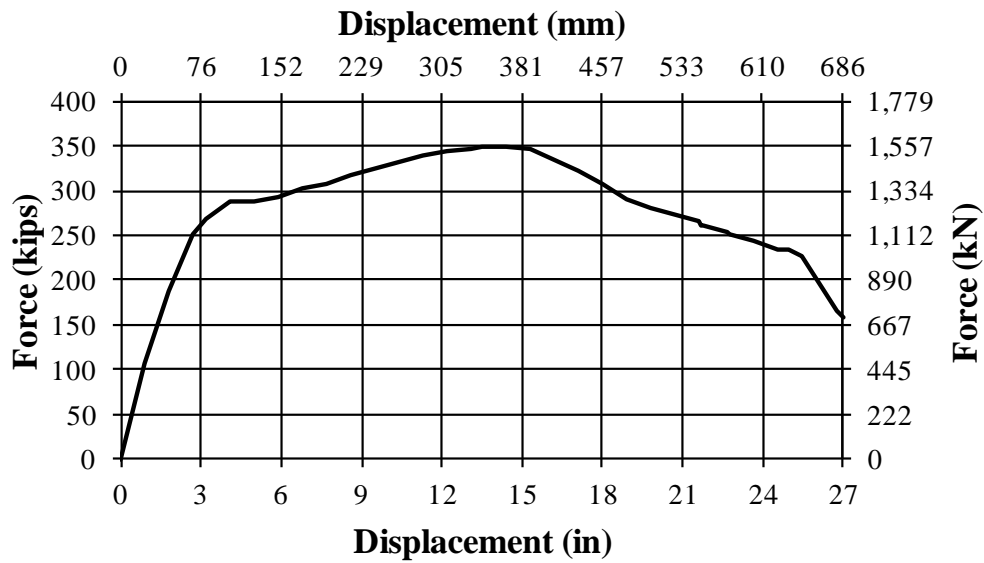
Figure 6-1: PT-LL Prototype Pushover Response
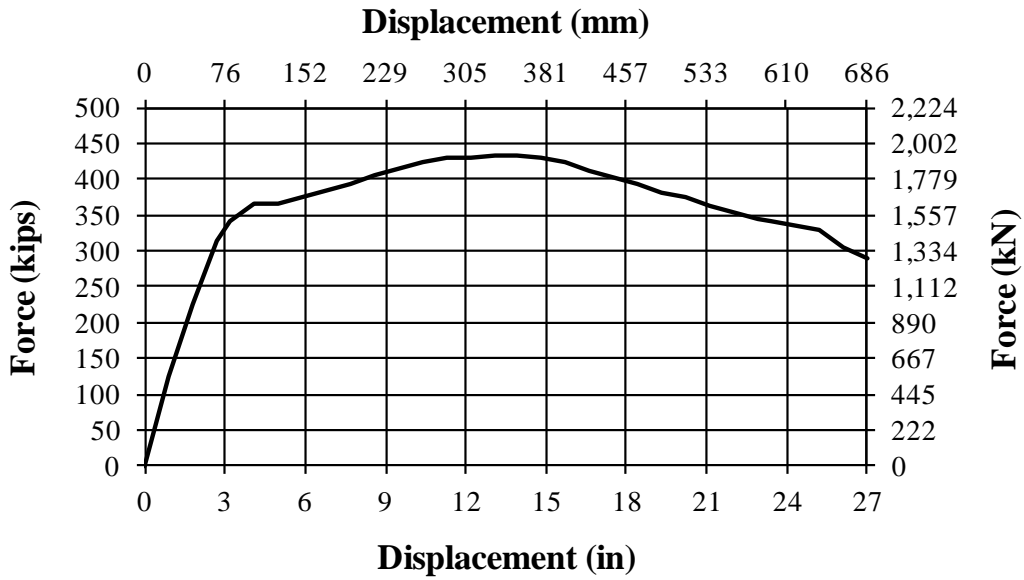
Figure 6-2: PT-HL Prototype Pushover Response

163
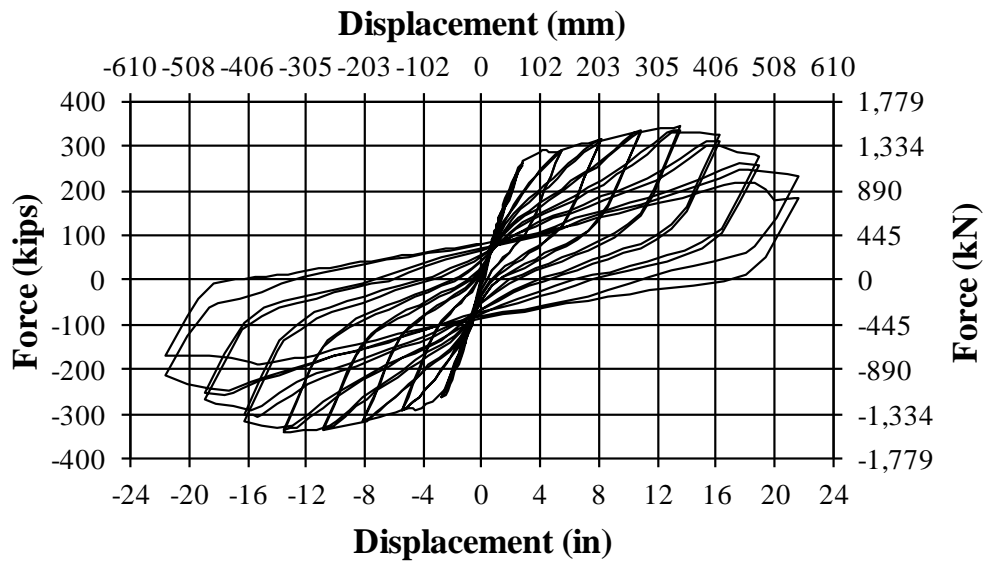
Figure 6-3: PT-LL Prototype Hysteretic Response
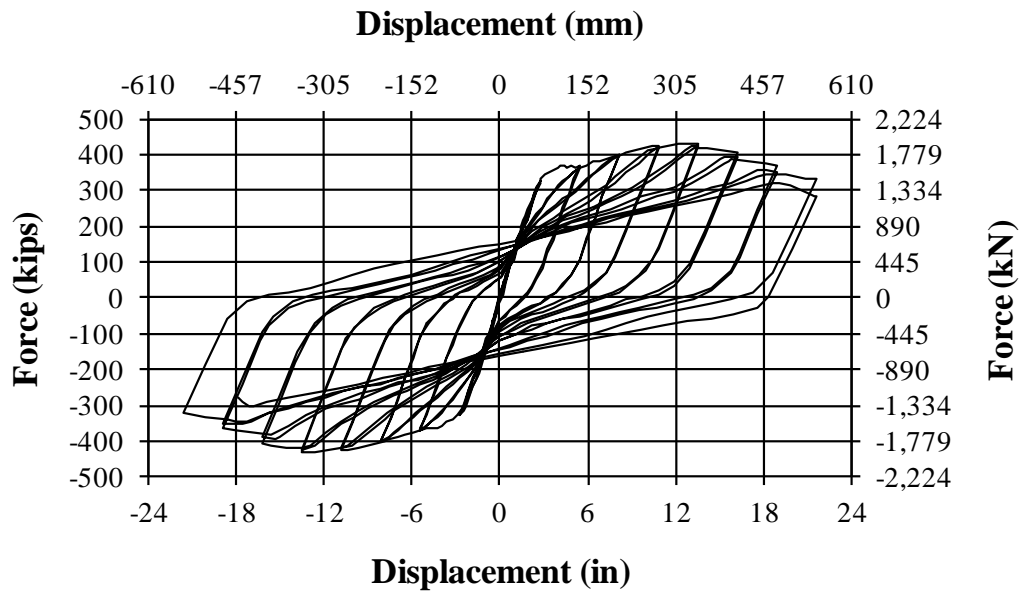
Figure 6-4: PT-HL Prototype Hysteretic Response

164
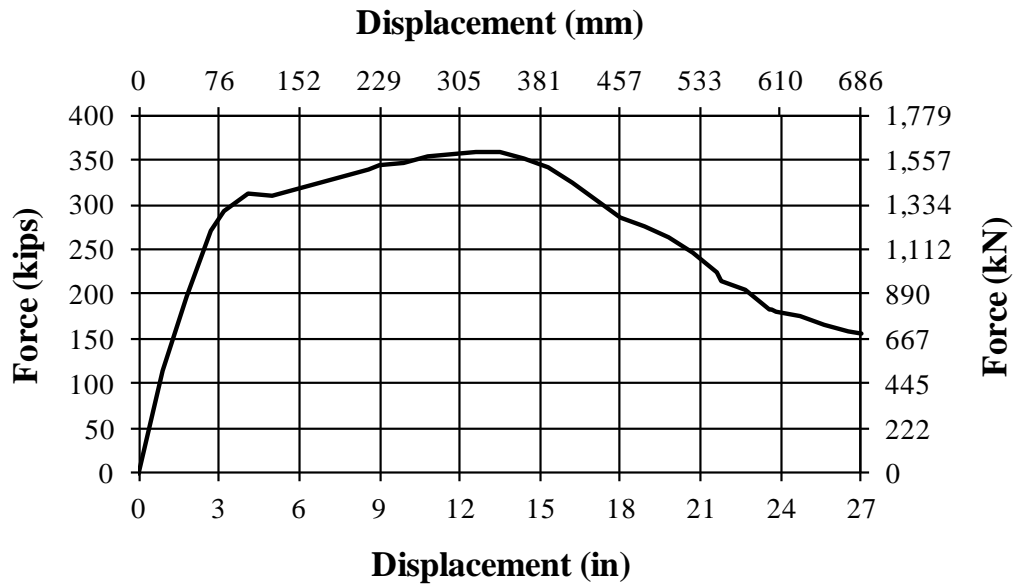
Figure 6-5: PT-LL 10%f'$_c$A$_g$ Axial Load, Pushover
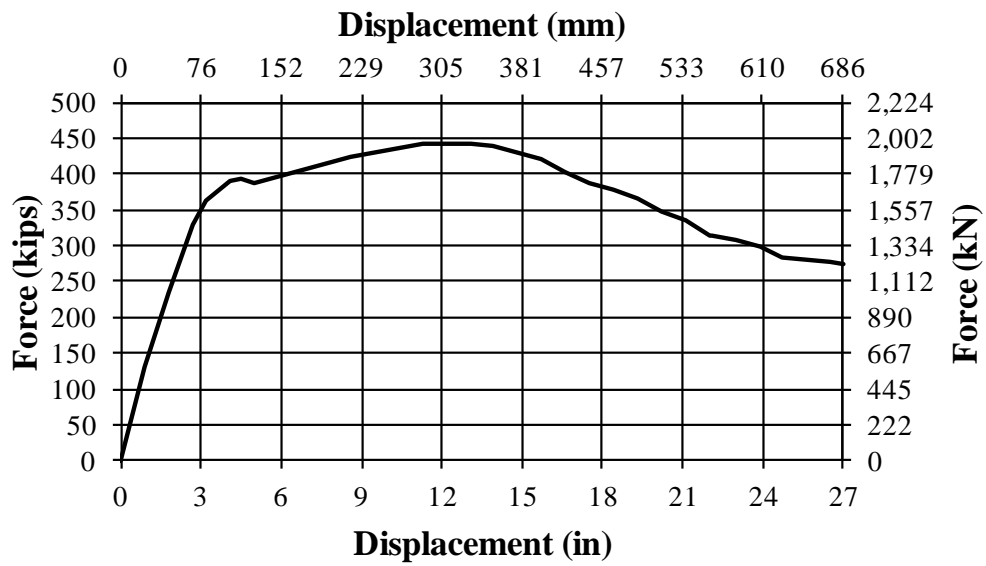
Figure 6-6: PT-HL 10%f'$_c$A$_g$ Axial Load, Pushover

165
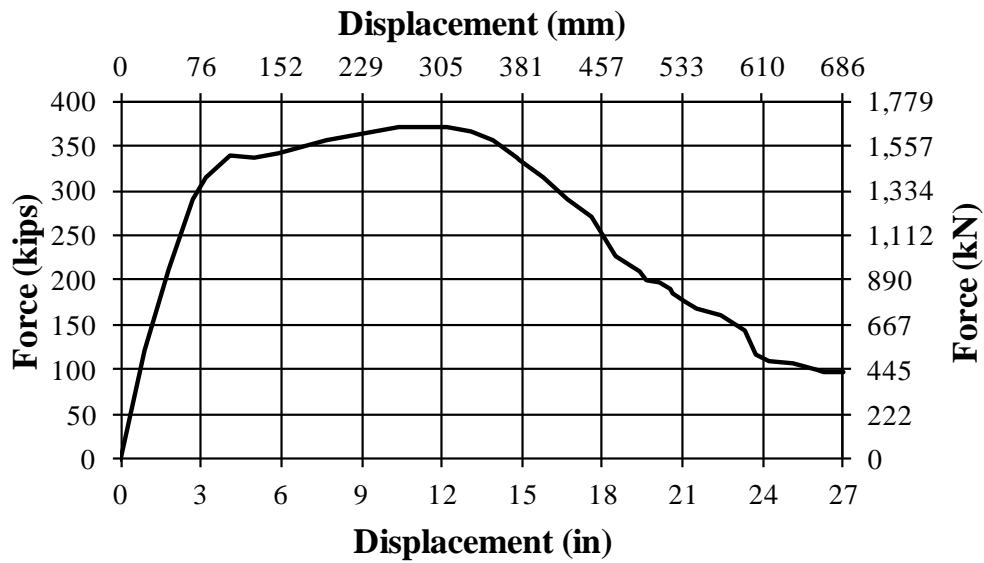
Figure 6-7: PT-LL 15%f'$_c$A$_g$ Axial Load, Pushover
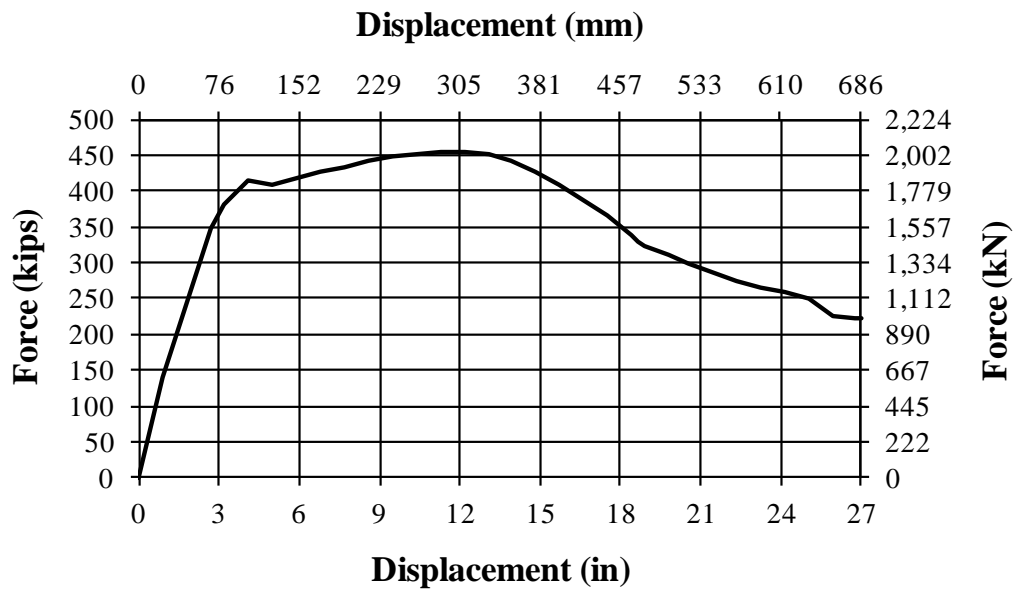
Figure 6-8: PT-HL 15%f'$_c$A$_g$ Axial Load, Pushover

166
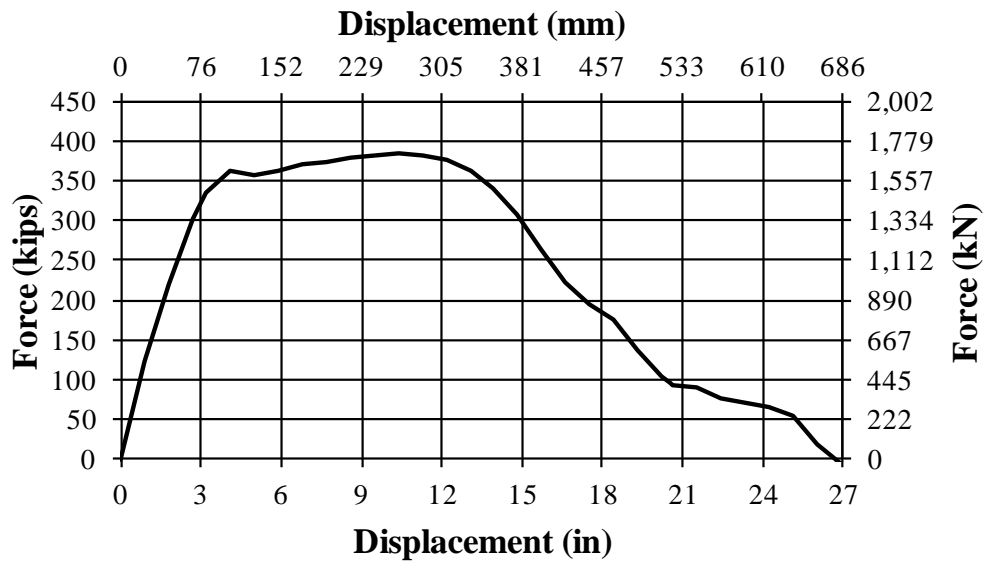
Figure 6-9: PT-LL 20%f'$_c$A$_g$ Axial Load, Pushover
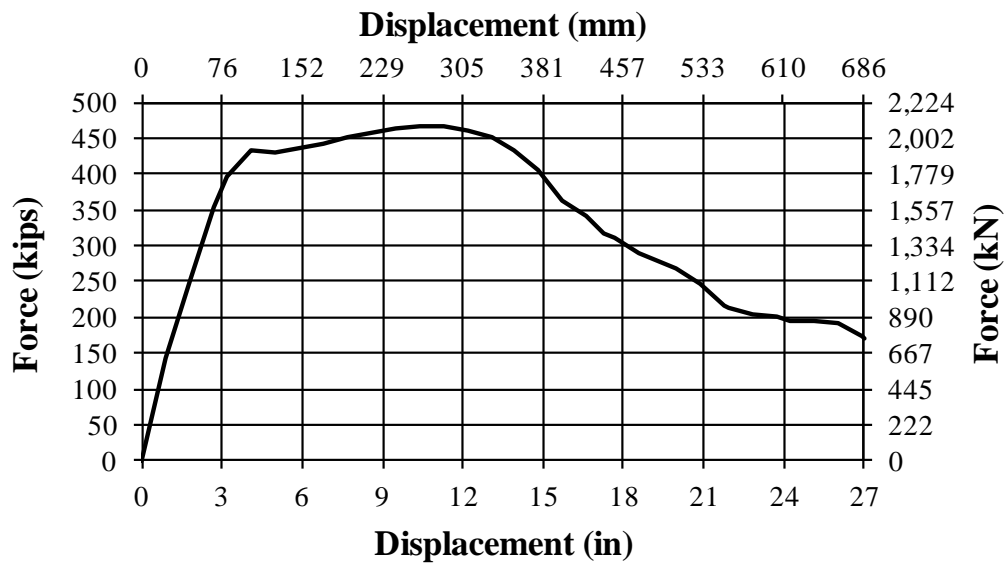
Figure 6-10: PT-HL 20%f'$_c$A$_g$ Axial Load, Pushover

167
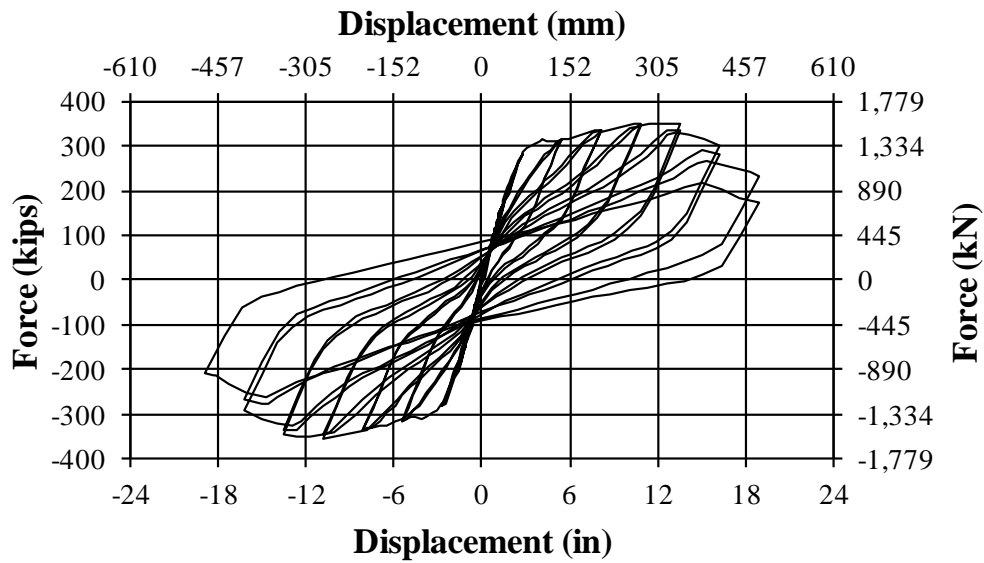
Figure 6-11: PT-LL 10%f'cAg Axial Load, Hysteresis
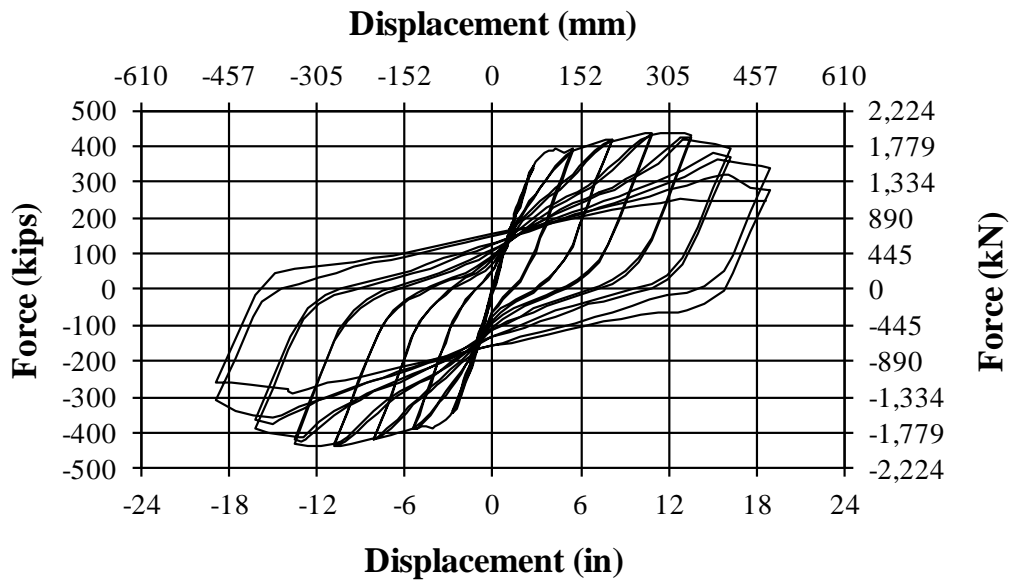
Figure 6-12: PT-HL 10%f'cAg Axial Load, Hysteresis
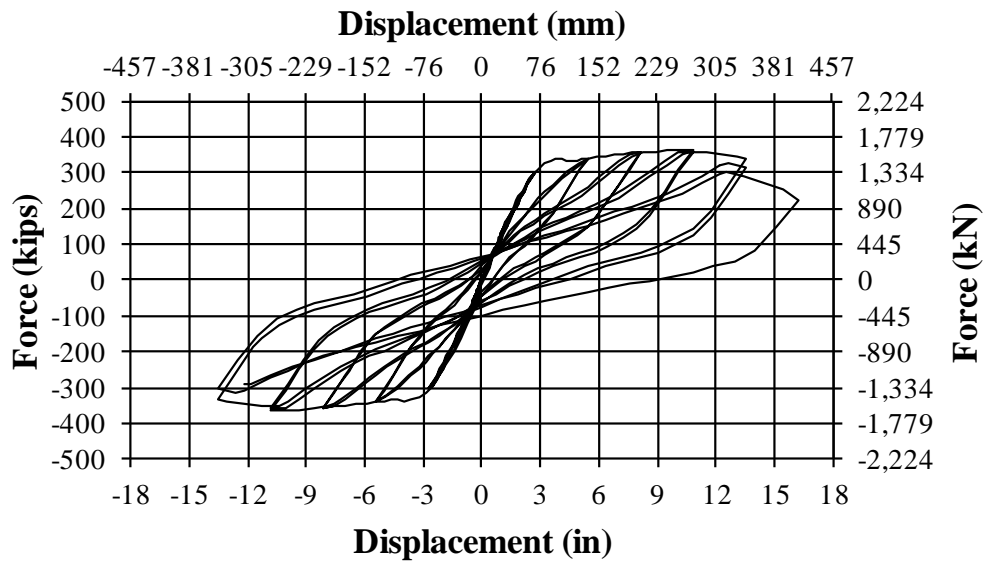
Figure 6-13: PT-LL 15%f'$_c$A$_g$ Axial Load, Hysteresis
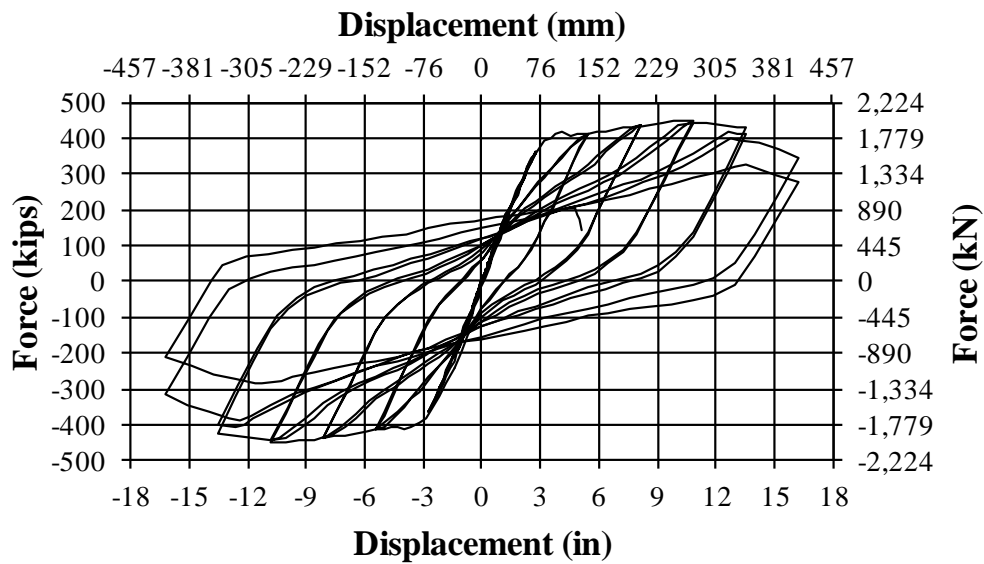
Figure 6-14: PT-HL 15%f'$_c$A$_g$ Axial Load, Hysteresis

169
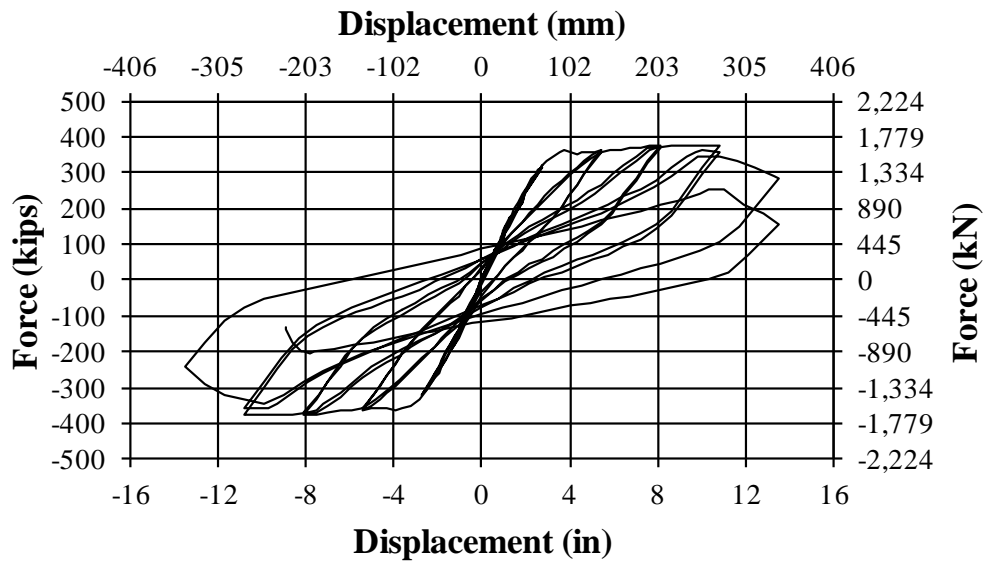
Figure 6-15: PT-LL 20%f'$_c$A$_g$ Axial Load, Hysteresis
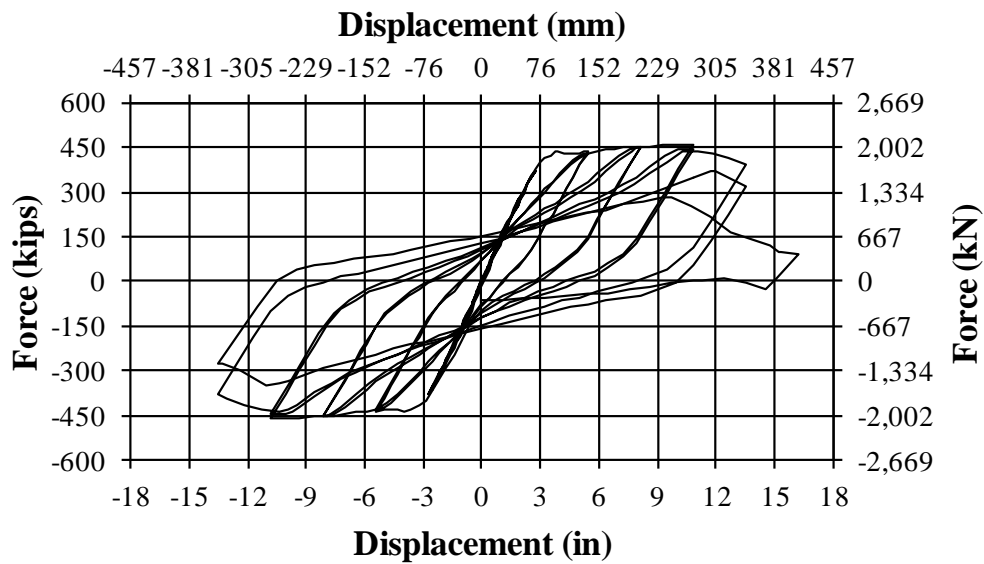
Figure 6-16: PT-HL 20%f'$_c$A$_g$ Axial Load, Hysteresis

170
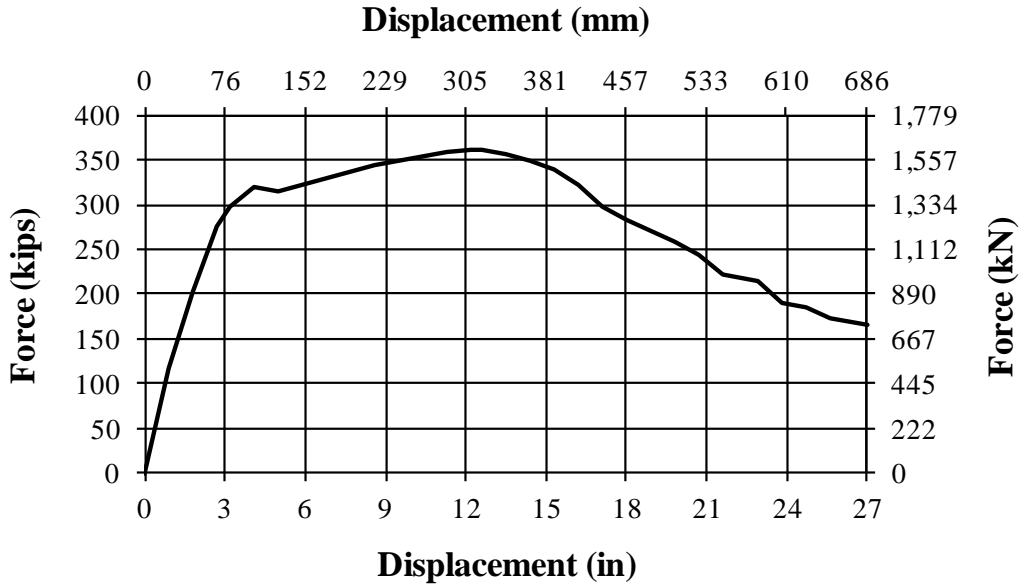
Figure 6-17: PT-LL 15%f'$_c$A$_g$ Initial Post-Tensioning, Pushover
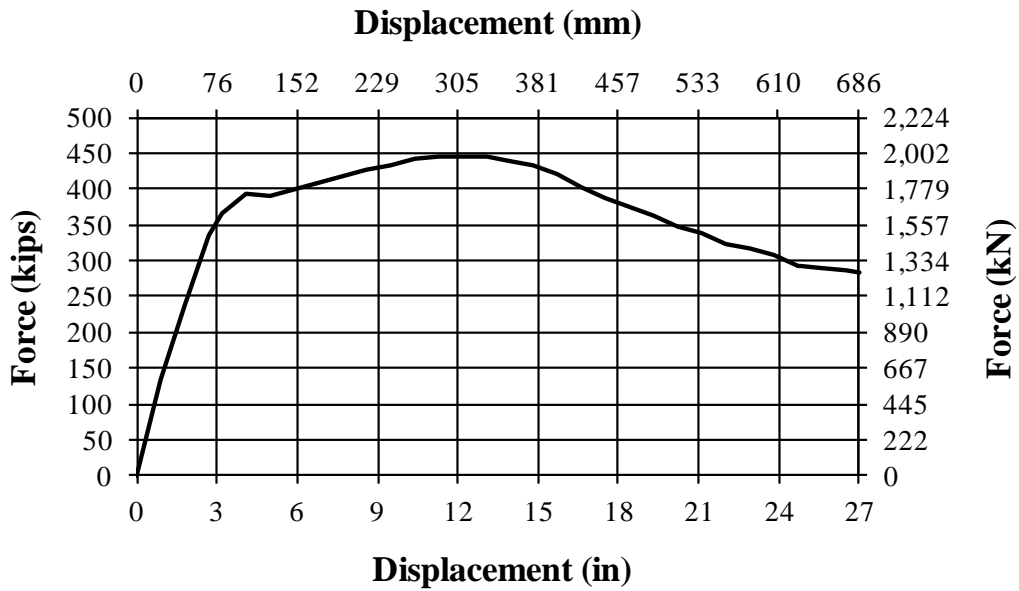
Figure 6-18: PT-HL 15%f'$_c$A$_g$ Initial Post-Tensioning, Pushover

171
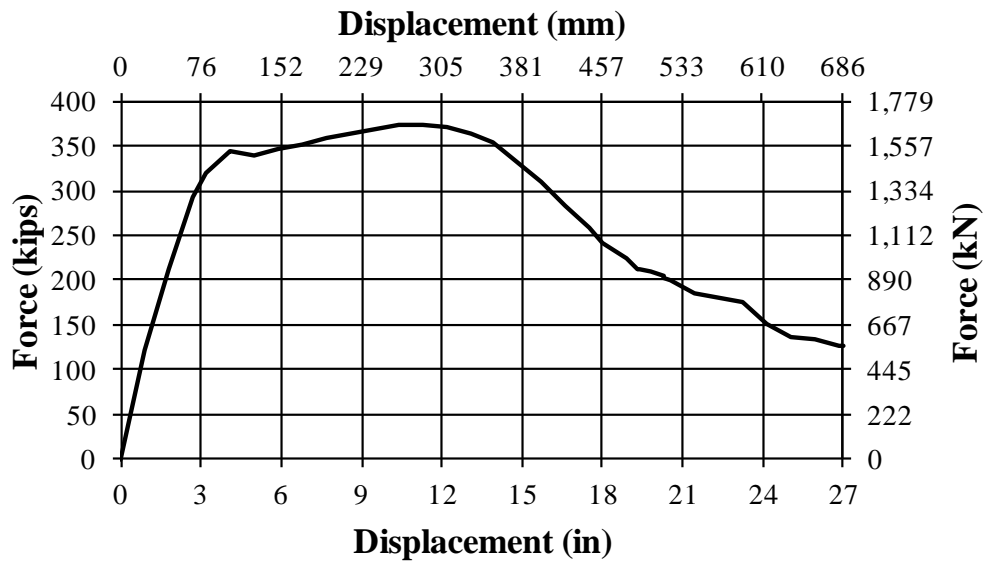
Figure 6-19: PT-LL 20%f'$_c$A$_g$ Initial Post-Tensioning, Pushover
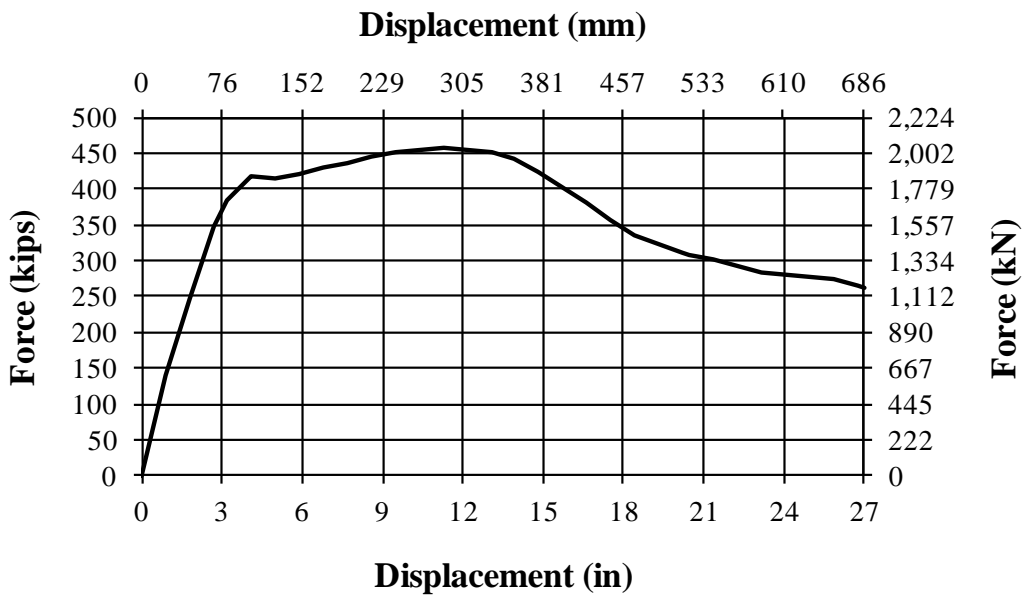
Figure 6-20: PT-HL 20%f'$_c$A$_g$ Initial Post-Tensioning, Pushover

172
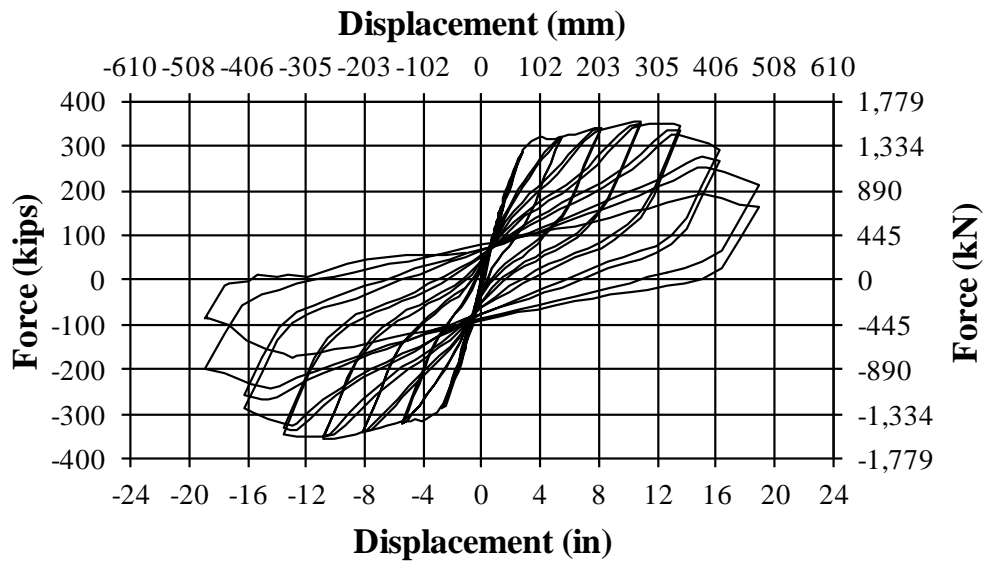
Figure 6-21: PT-LL 15%f'$_c$A$_g$ Initial Post-Tensioning, Hysteresis
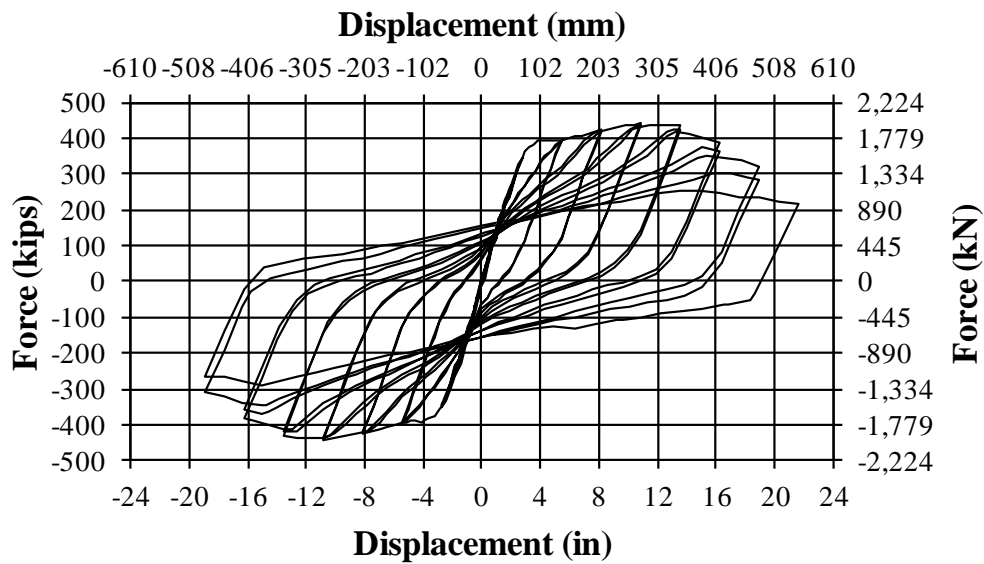
Figure 6-22: PT-HL 15%f'$_c$A$_g$ Initial Post-Tensioning, Hysteresis

173
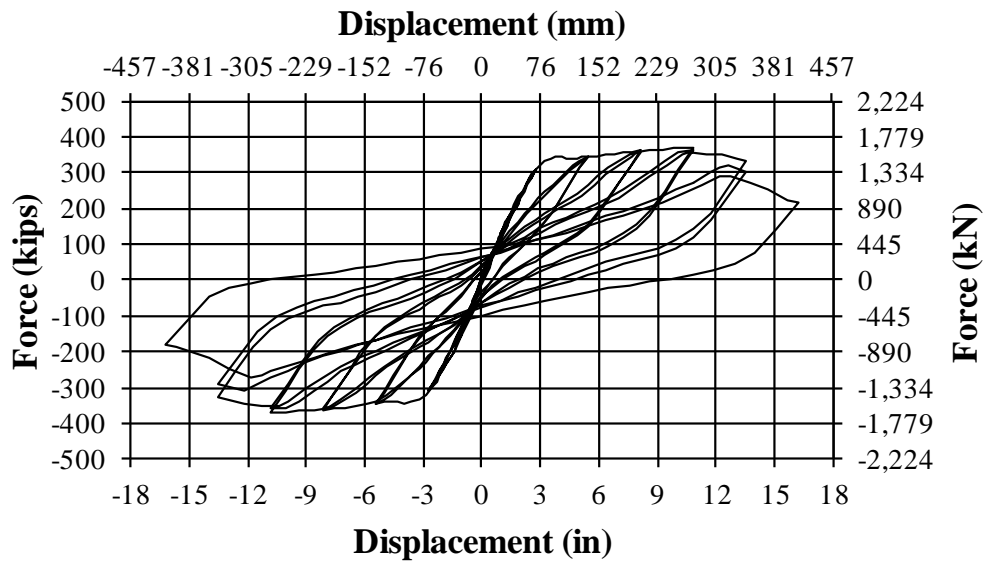
Figure 6-23: PT-LL 20%f'cAg Initial Post-Tensioning, Hysteresis
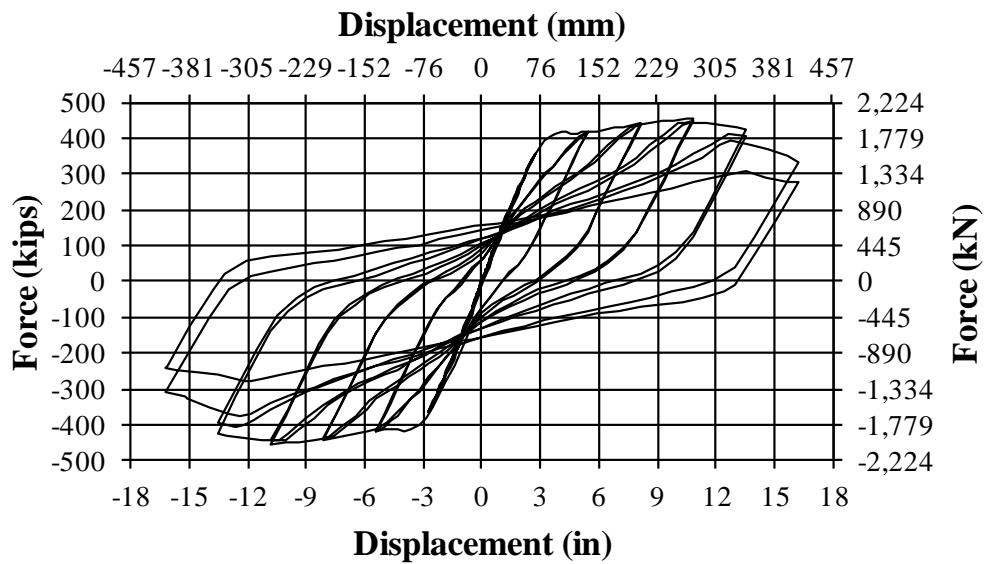
Figure 6-24: PT-HL 20%f'cAg Initial Post-Tensioning, Hysteresis

174
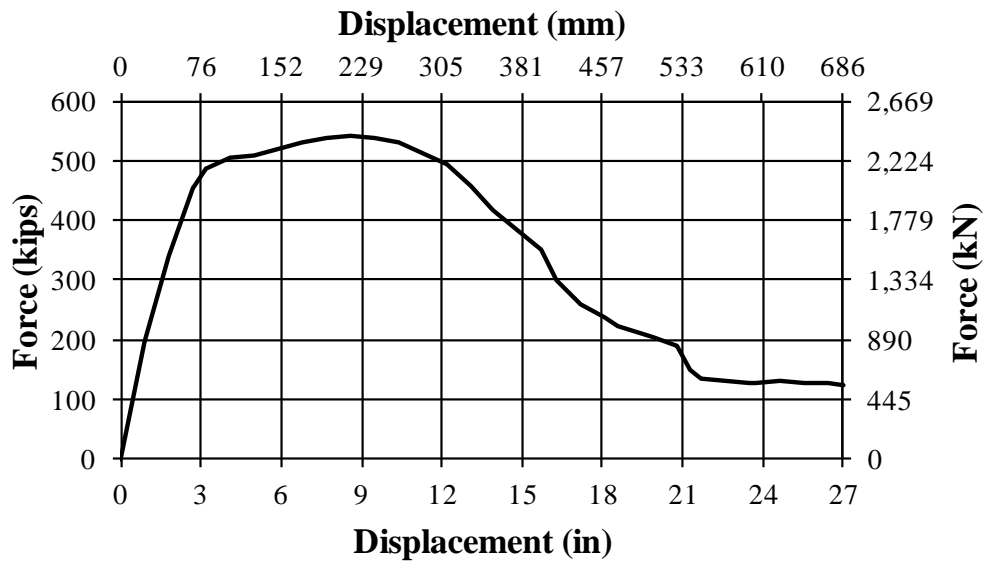
Figure 6-25: PT-LL Study III, f'c=10 ksi (69 MPa), Pushover
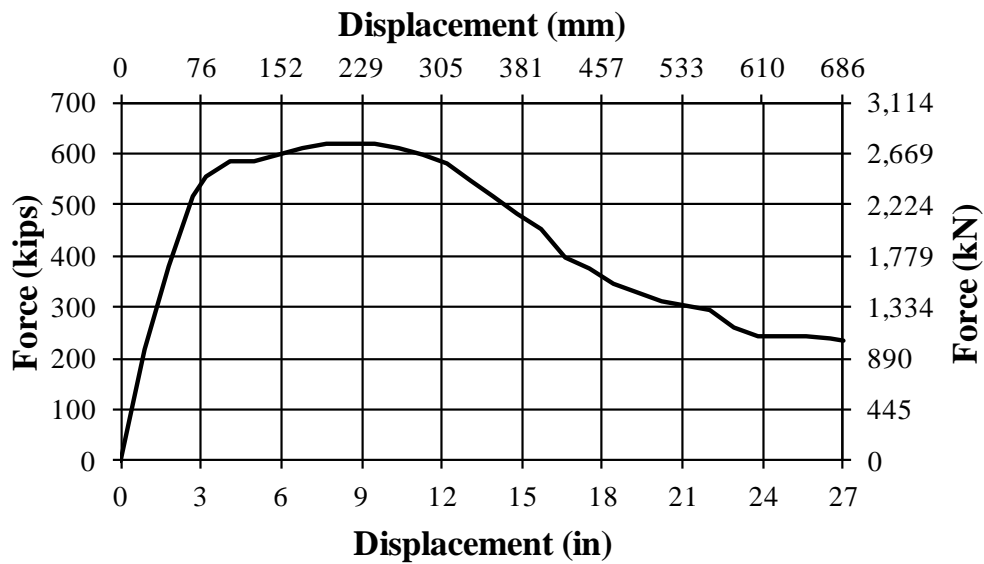
Figure 6-26: PT-HL Study III, f'c=10 ksi (69 MPa), Pushover

175
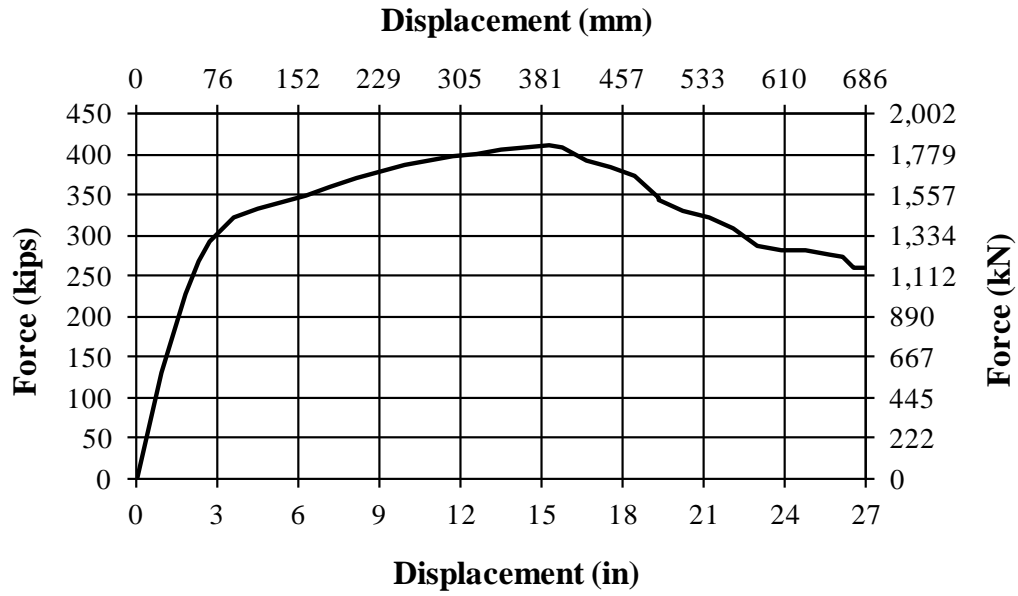
Figure 6-27: PT-LL Study III', f'c=10 ksi (69 MPa), Pushover
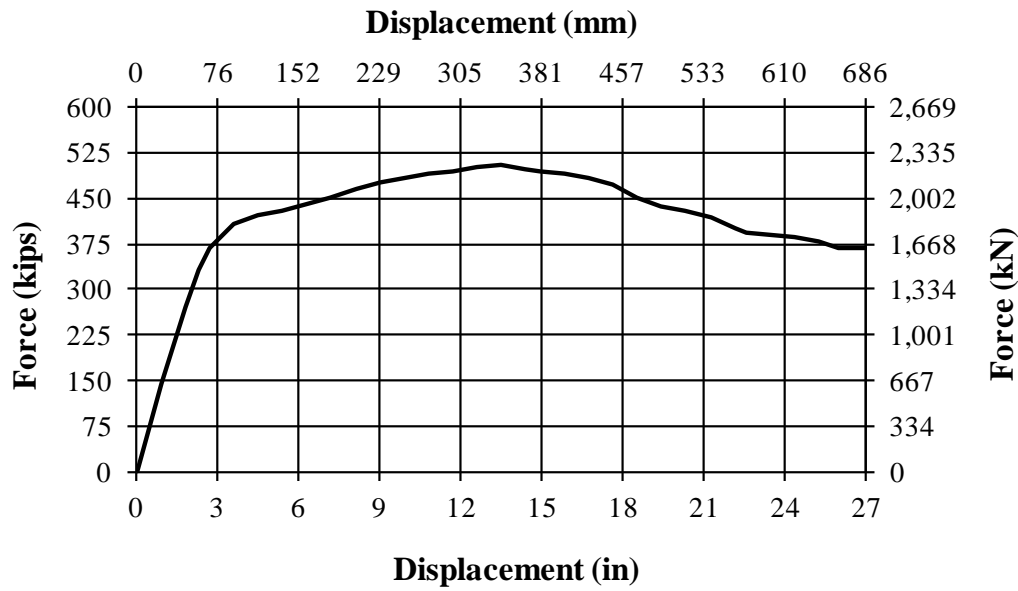
Figure 6-28: PT-HL Study III', f'c=10 ksi (69 MPa), Pushover

176
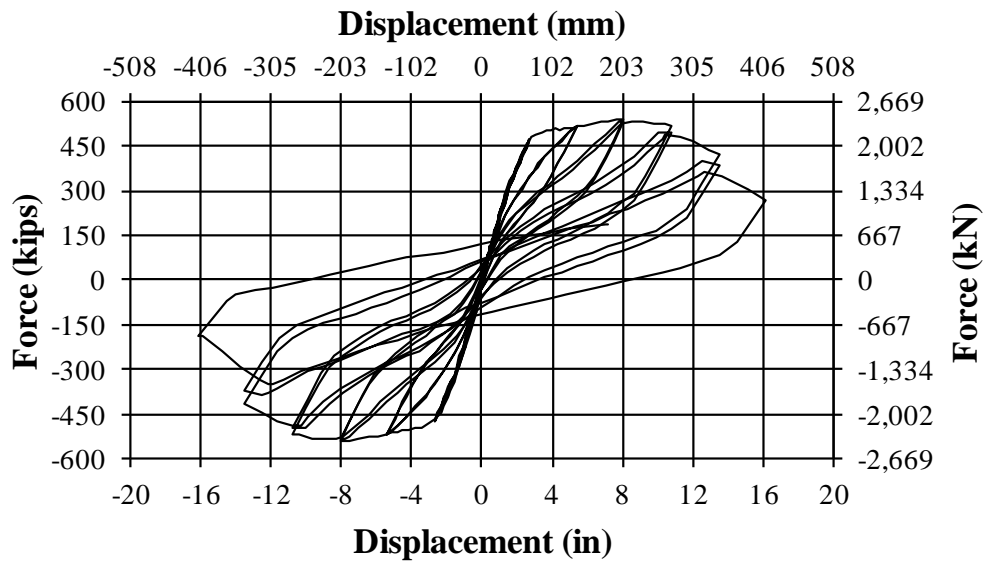
Figure 6-29: PT-LL Study III, f'c=10 ksi (69 MPa), Hysteresis
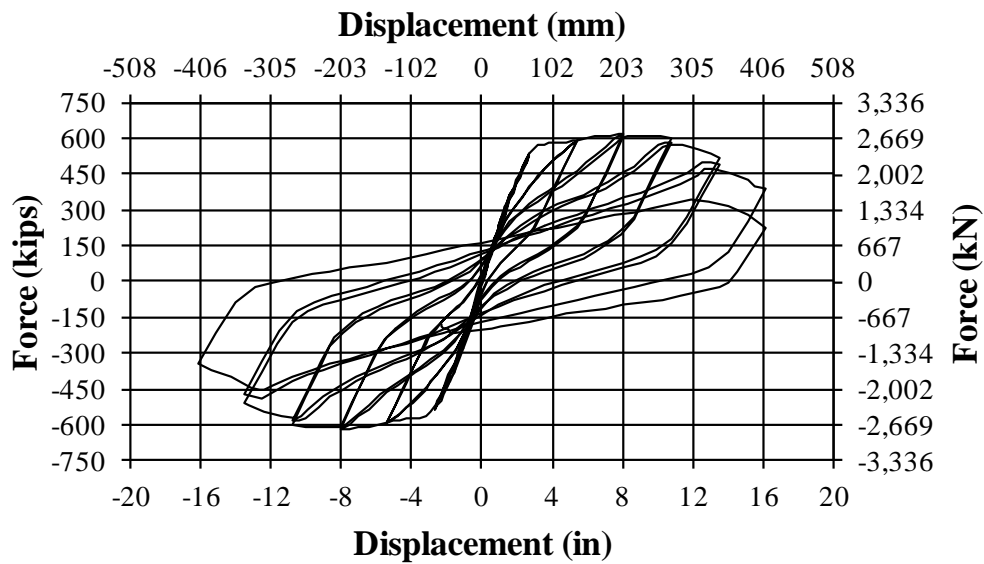
Figure 6-30: PT-HL Study III, f'c=10 ksi (69 MPa), Hysteresis
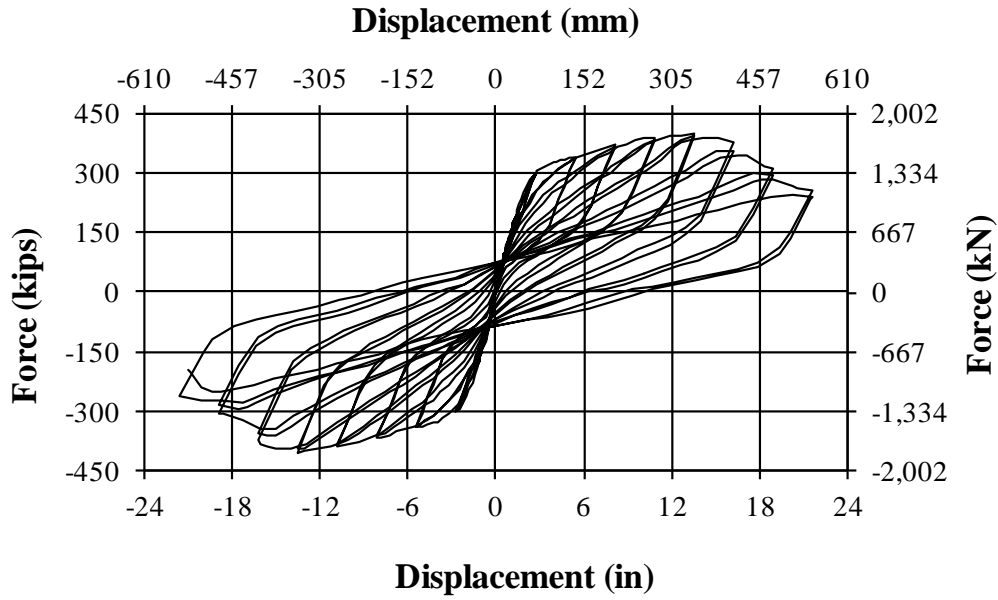
Figure 6-31: PT-LL Study III', f'c=10 ksi (69 MPa), Hysteresis
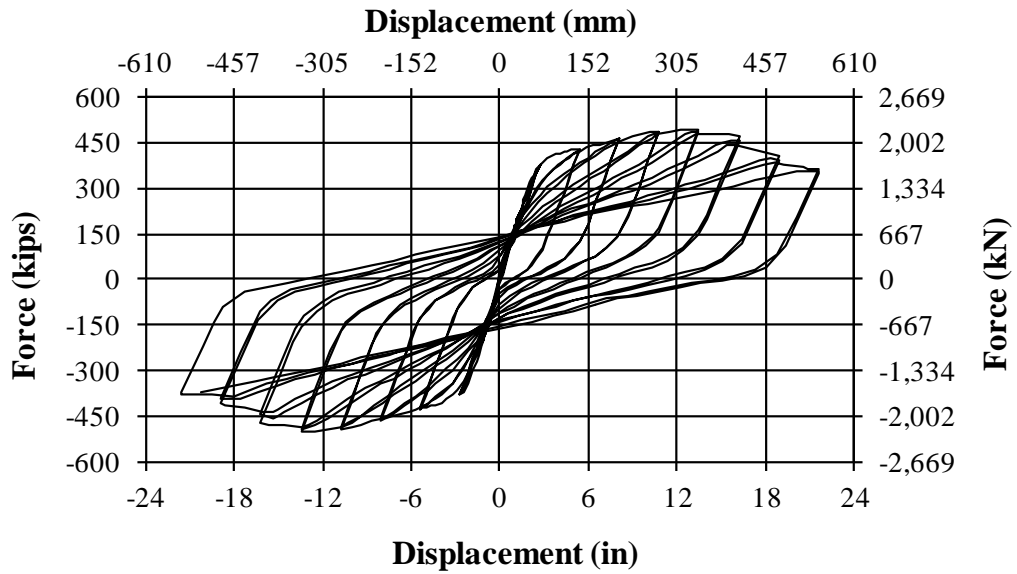
Figure 6-32: PT-HL Study III', f'c=10 ksi (69 MPa), Hysteresis
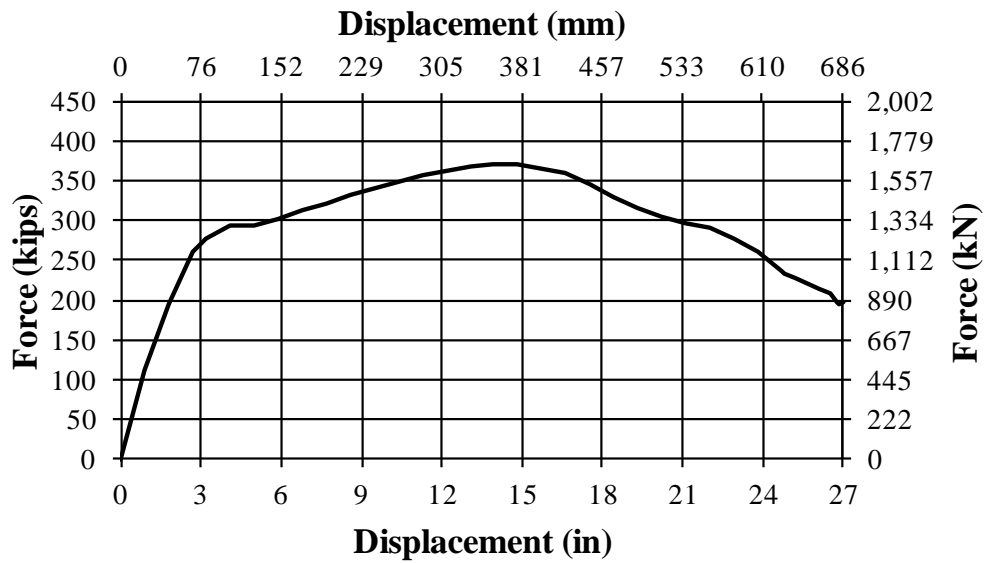
Figure 6-33: PT-LL 30% of Diameter Tendon Location, Pushover
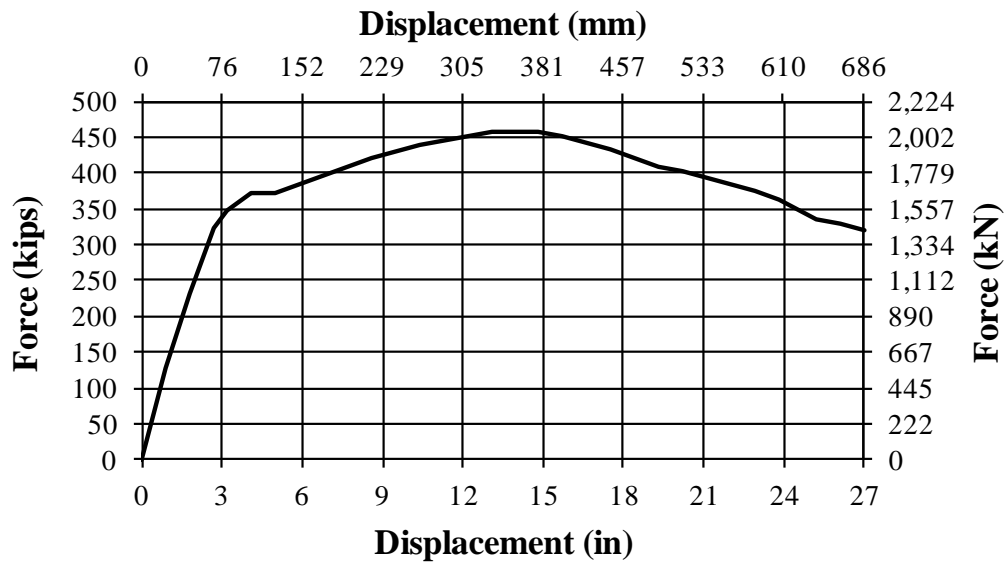
Figure 6-34: PT-HL 30% of Diameter Tendon Location, Pushover

179
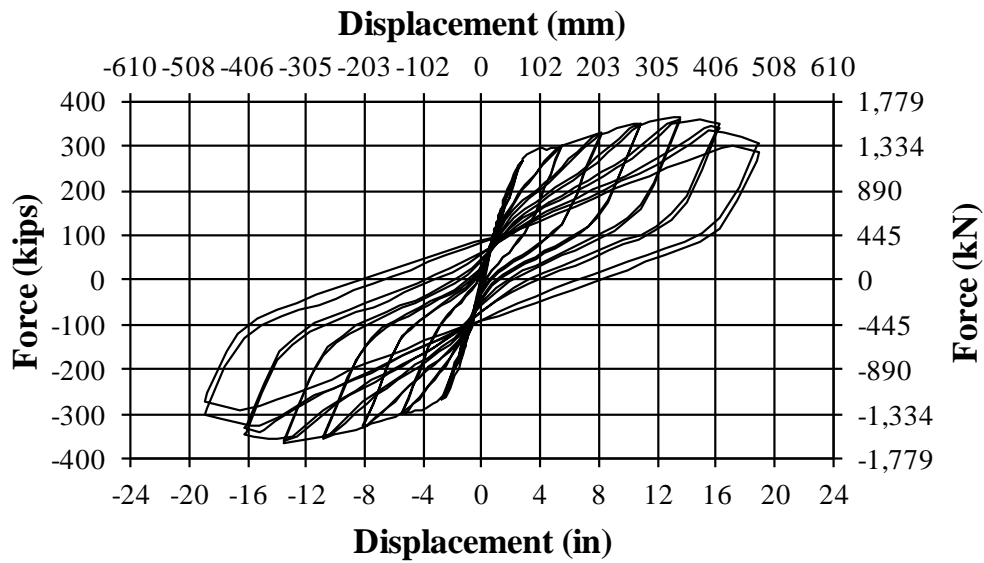
Figure 6-35: PT-LL 30% of Diameter Tendon Location, Hysteresis
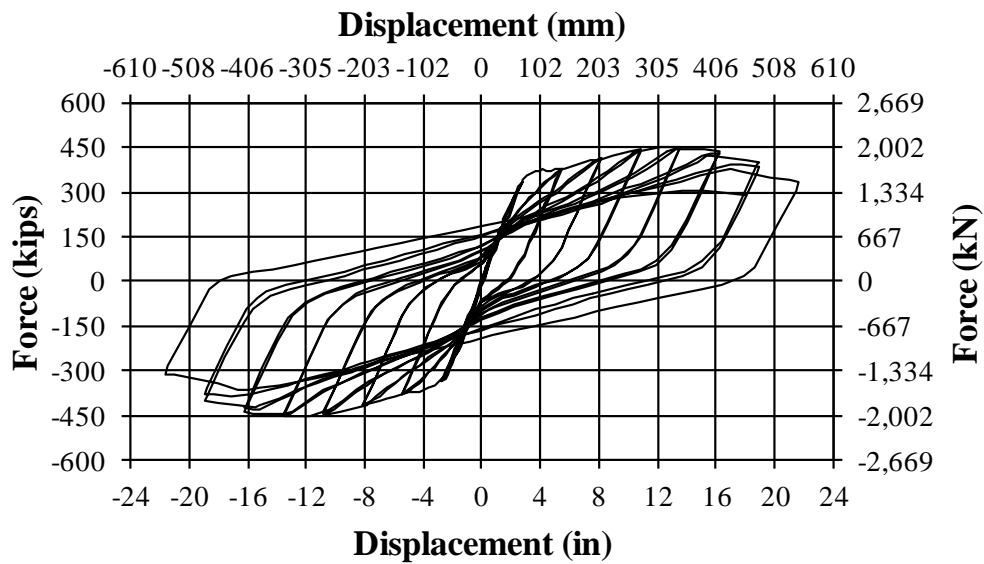
Figure 6-36: PT-HL 30% of Diameter Tendon Location, Hysteresis
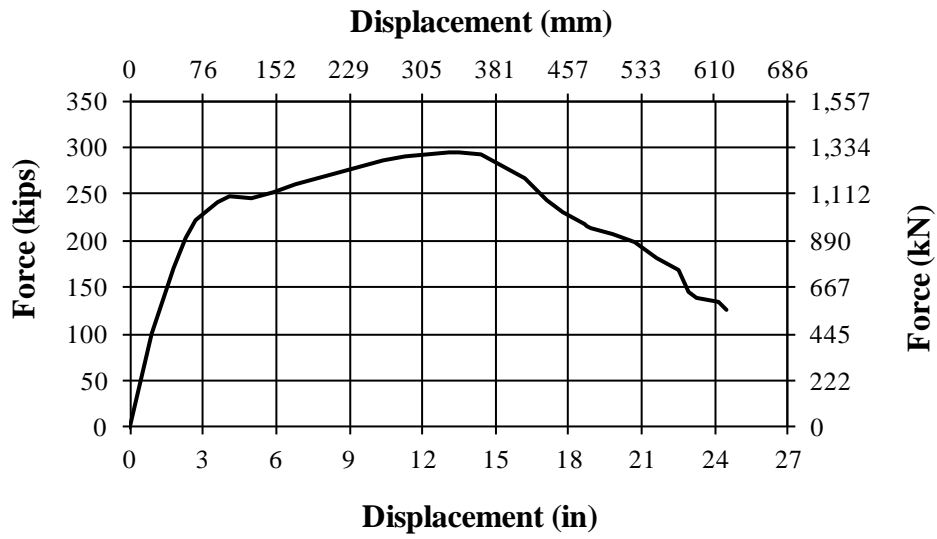
Figure 6-37: PT-EL 0.34% Longitudinal Reinforcement Pushover
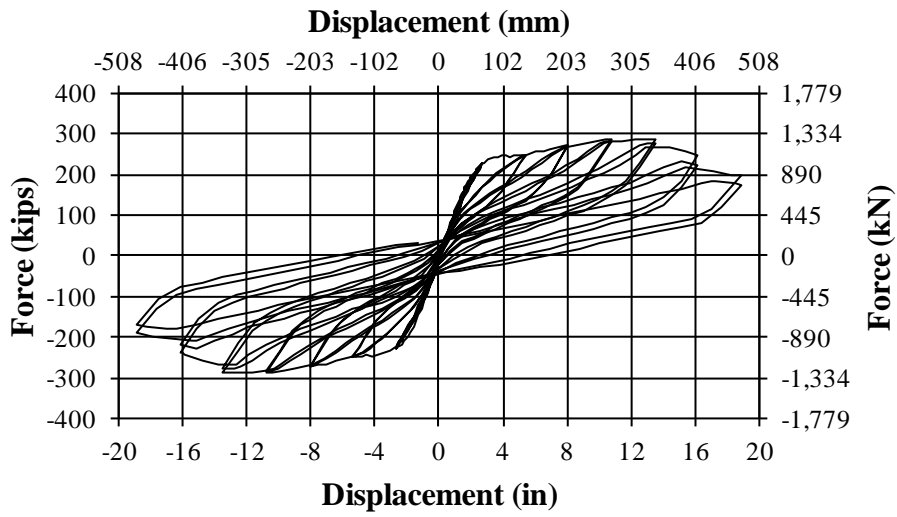
Figure 6-38: PT-EL 0.34% Longitudinal Reinforcement Hysteresis

APPENDIX A

(strain-drift hysteresis of conventional reinforcement and tendons)
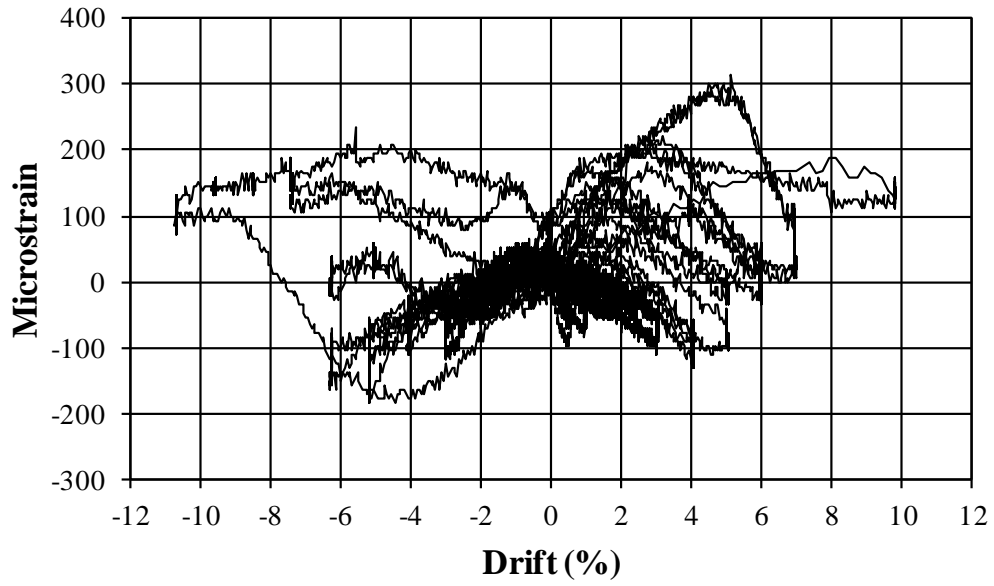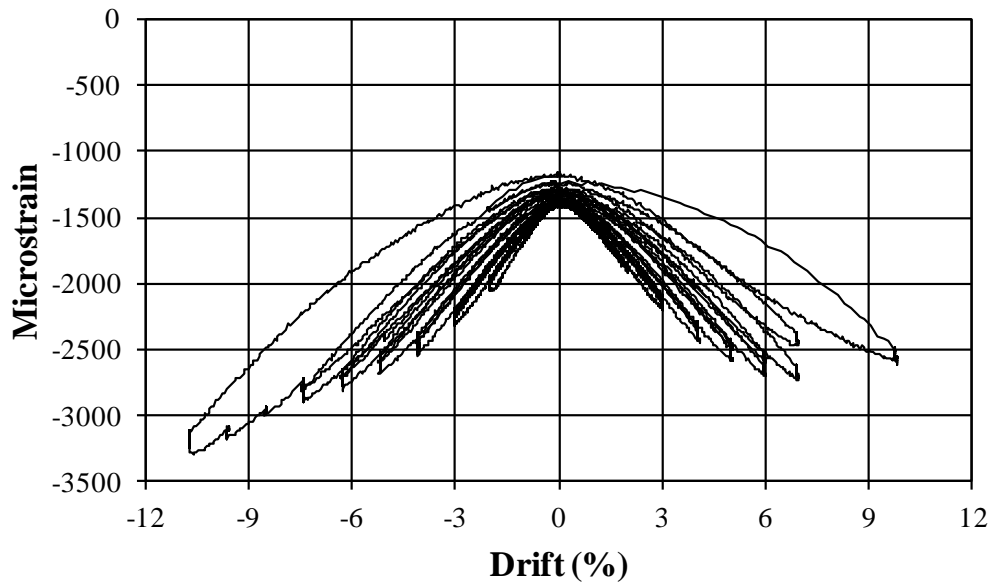
Figure A-1: PT-LL Strain vs. Drift, Strain Gauge 9
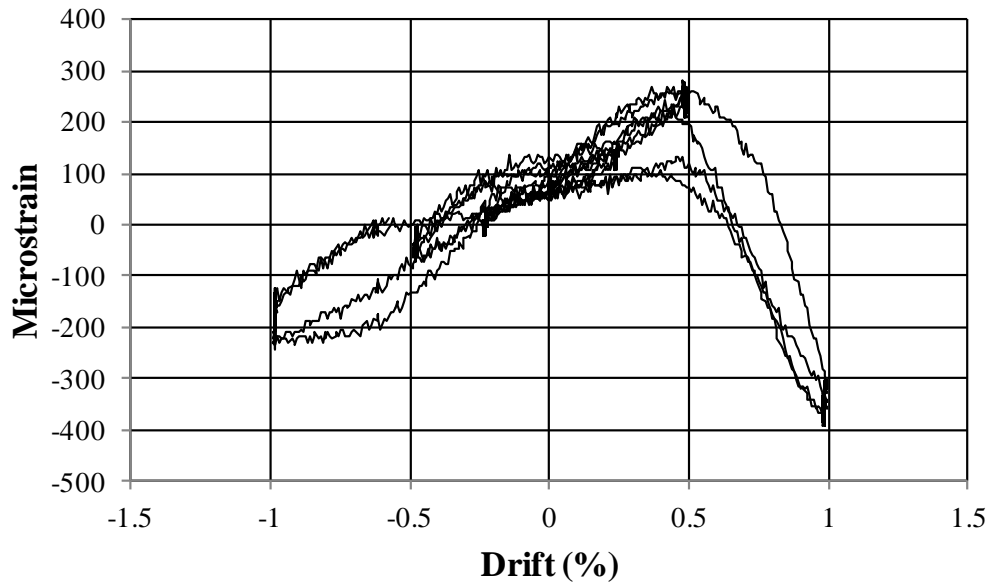
Figure A-2: PT-LL Strain vs. Drift, Strain Gauge 10
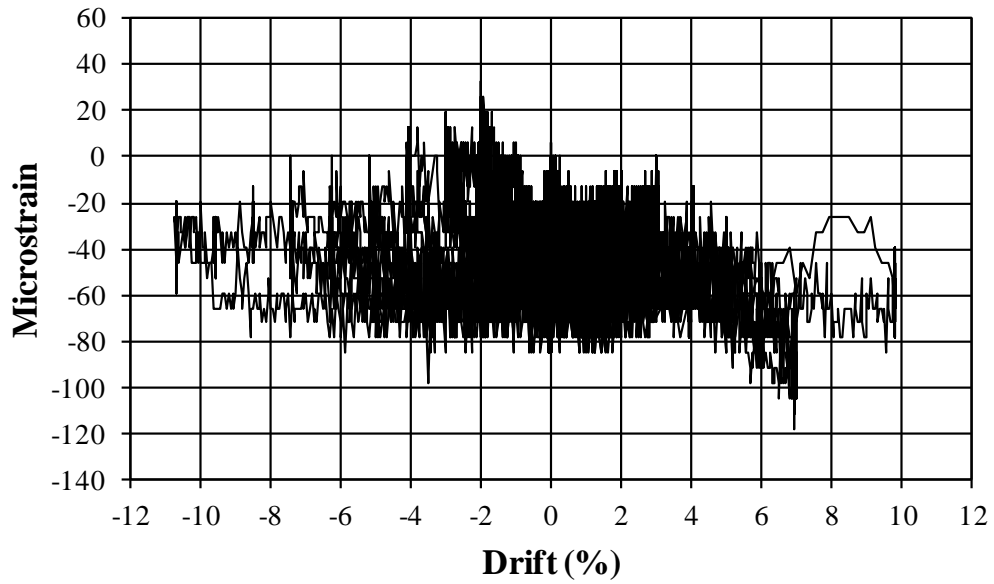
Figure A-3: PT-LL Strain vs. Drift, Strain Gauge 11
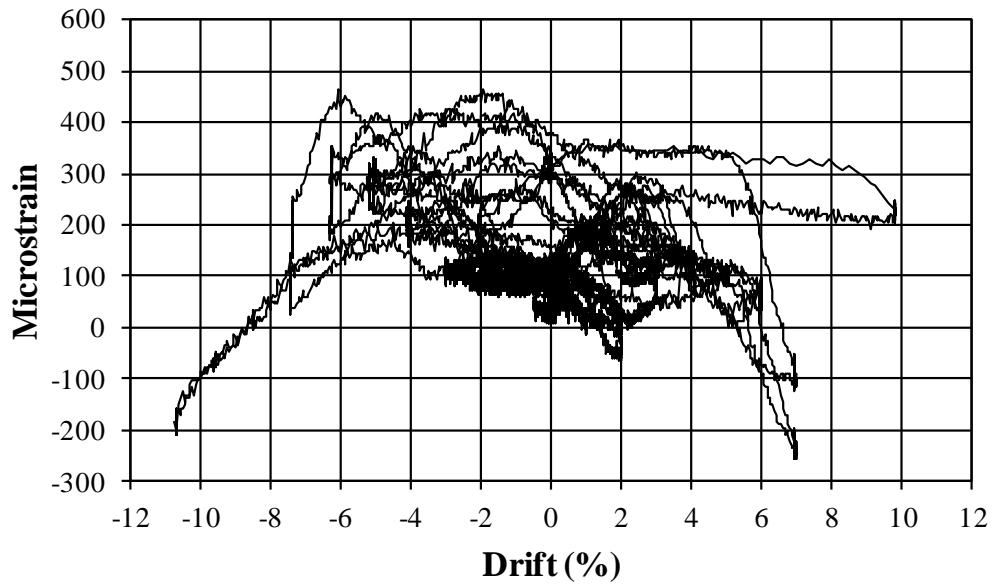
Figure A-4: PT-LL Strain vs. Drift, Strain Gauge 12

184

Figure A-5: PT-LL Strain vs. Drift, Strain Gauge 13

Figure A-6: PT-LL Strain vs. Drift, Strain Gauge 14

185

Figure A-7: PT-LL Strain vs. Drift, Strain Gauge 15

Figure A-8: PT-LL Strain vs. Drift, Strain Gauge 16

186

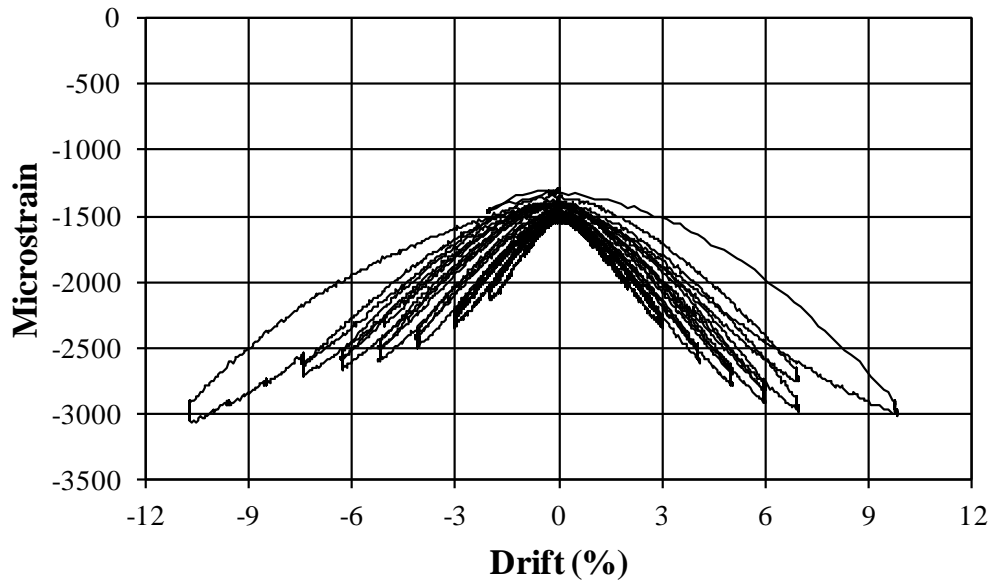**Figure A-9: PT-LL Strain vs. Drift, Strain Gauge 17**

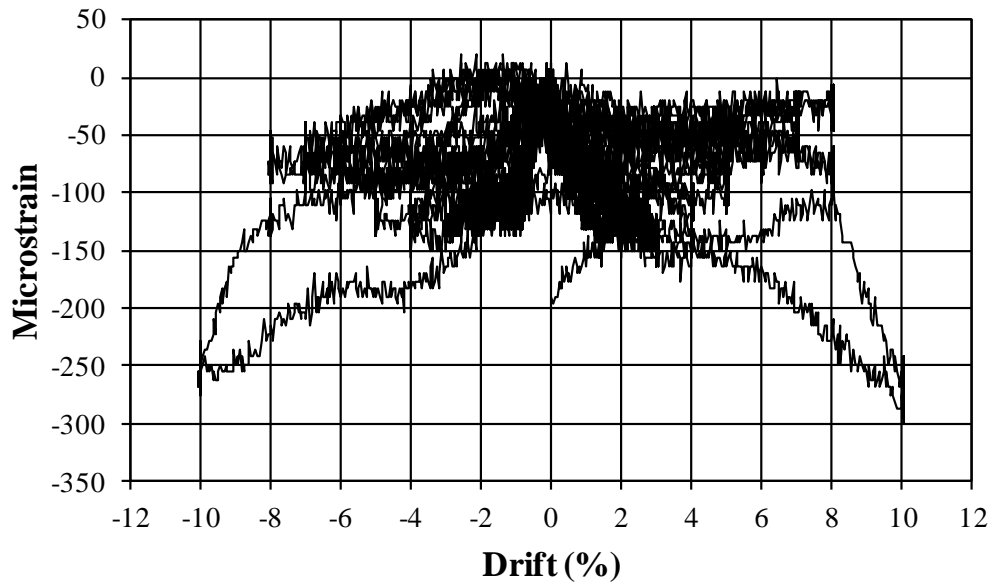**Figure A-10: PT-LL Strain vs. Drift, Strain Gauge 18**

187
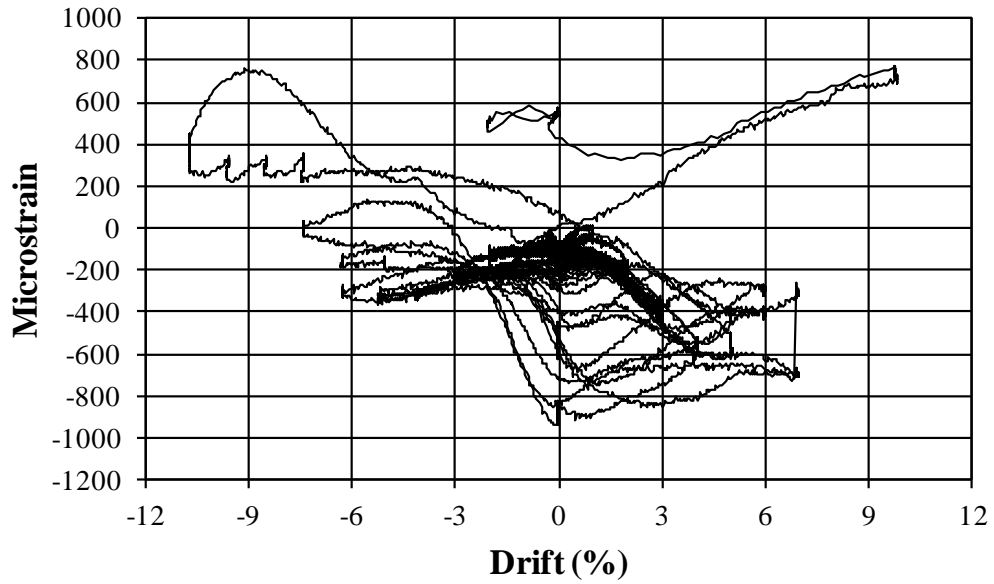
Figure A-11: PT-LL Strain vs. Drift, Strain Gauge 19
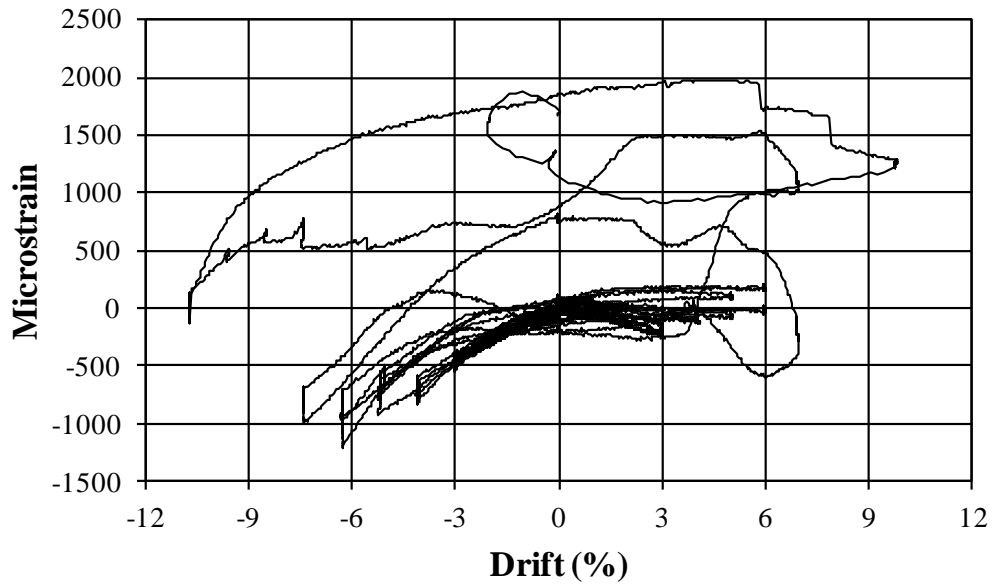
Figure A-12: PT-LL Strain vs. Drift, Strain Gauge 20
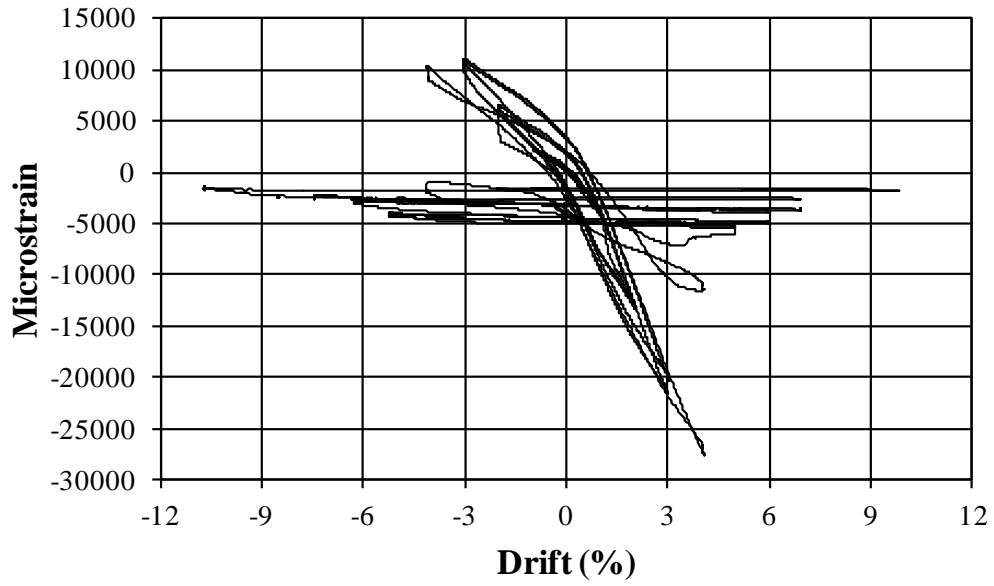
Figure A-13: PT-LL Strain vs. Drift, Strain Gauge 21
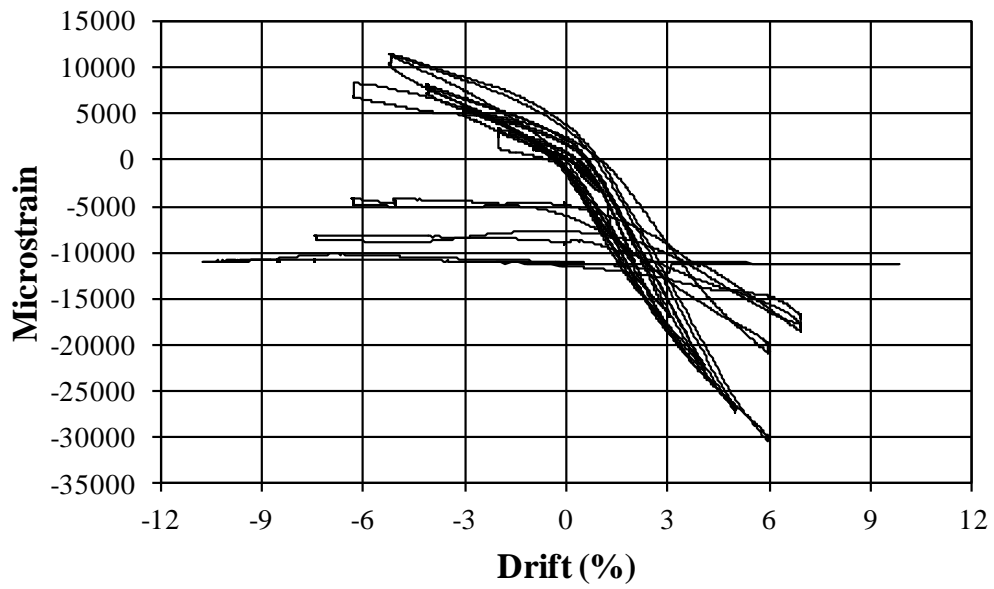
Figure A-14: PT-LL Strain vs. Drift, Strain Gauge 22
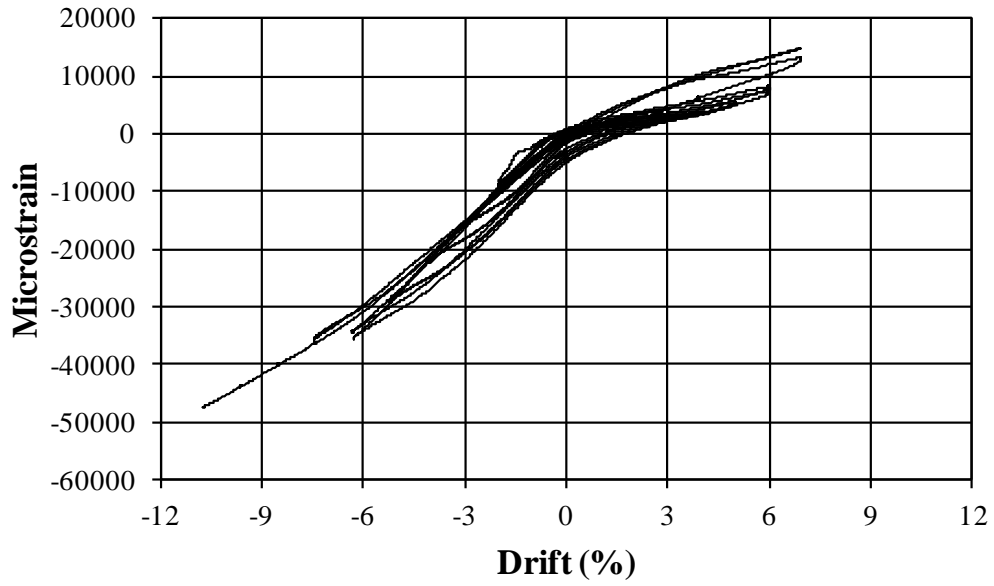
Figure A-15: PT-LL Strain vs. Drift, Strain Gauge 23

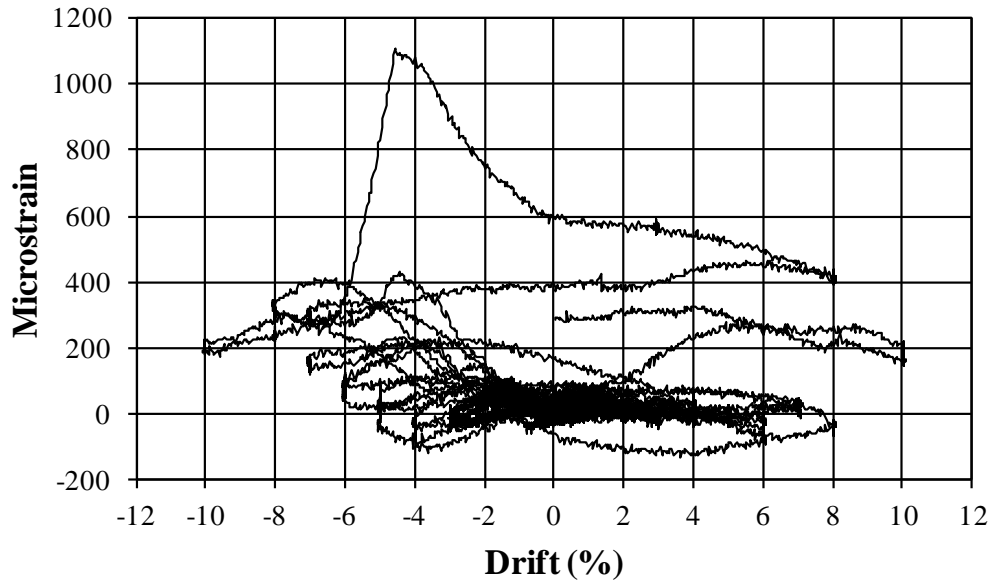**Figure A-16: PT-LL Strain vs. Drift, Strain Gauge 24**

190

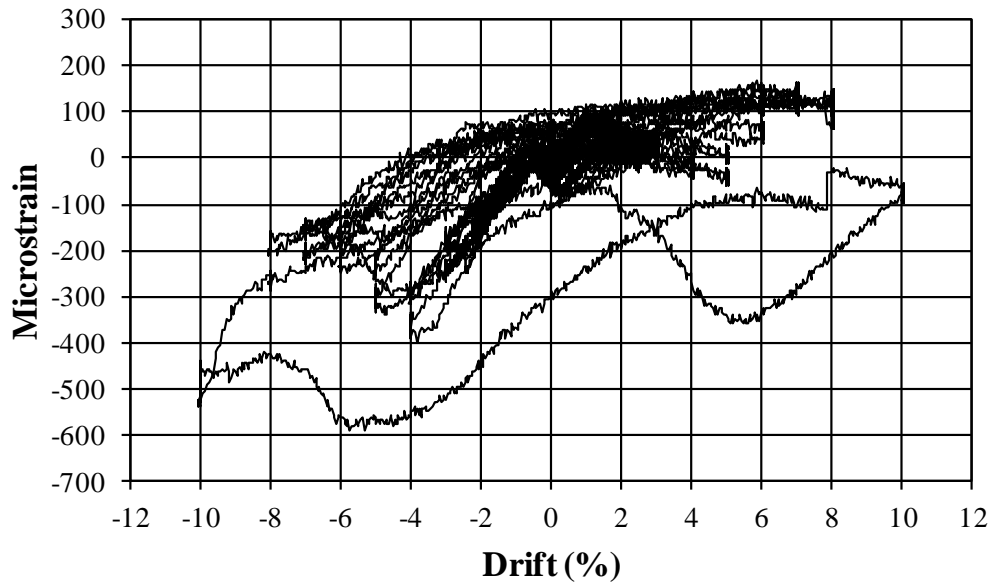**Figure A-17: PT-LL Strain vs. Drift, Strain Gauge 25**

Figure A-18: PT-LL Strain vs. Drift, Strain Gauge 26

Figure A-19: PT-LL Strain vs. Drift, Strain Gauge 27

Figure A-20: PT-LL Strain vs. Drift, Strain Gauge 28

Figure A-21: PT-LL Strain vs. Drift, Strain Gauge 29
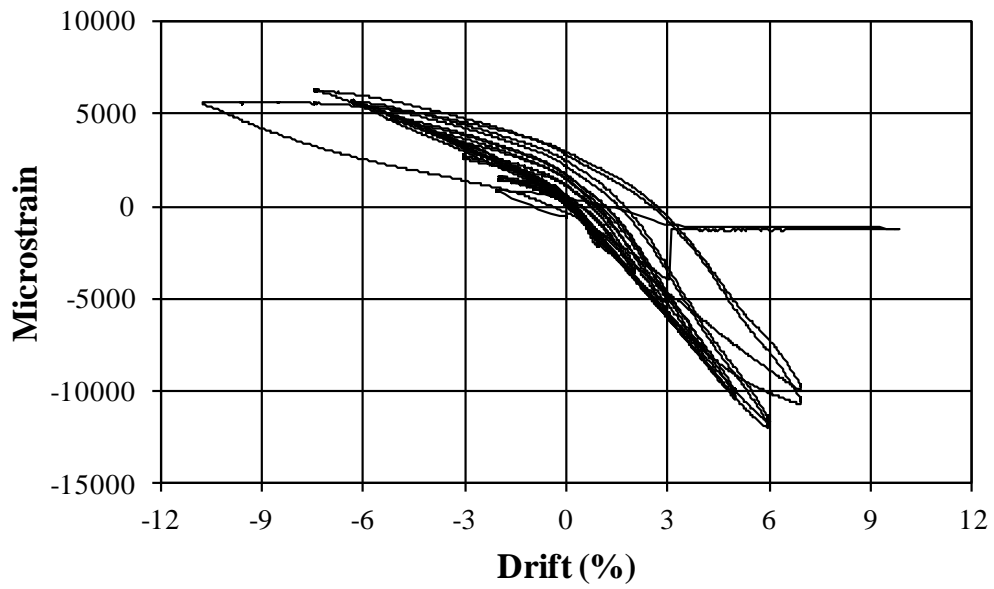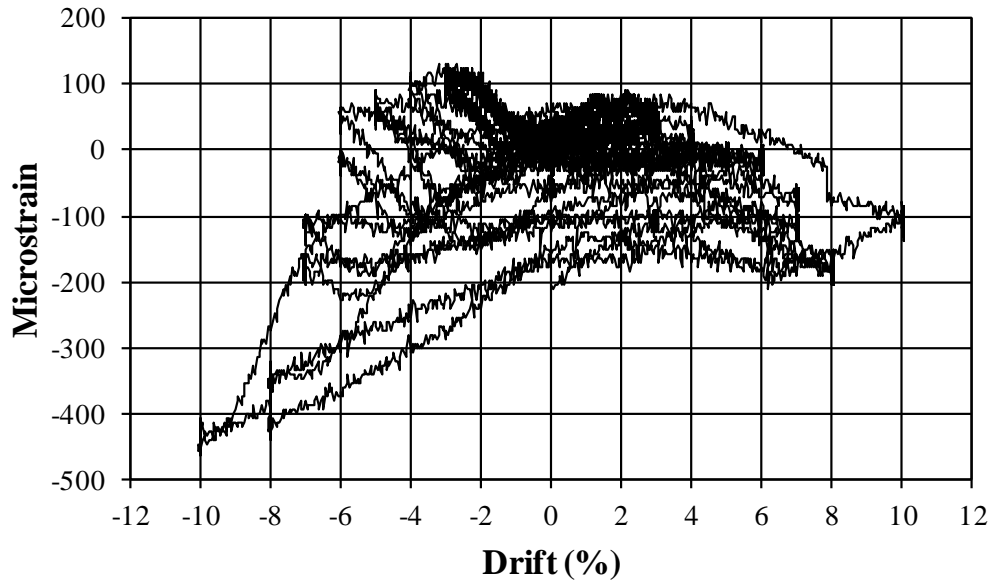

Figure A-22: PT-LL Strain vs. Drift, Strain Gauge 30

193
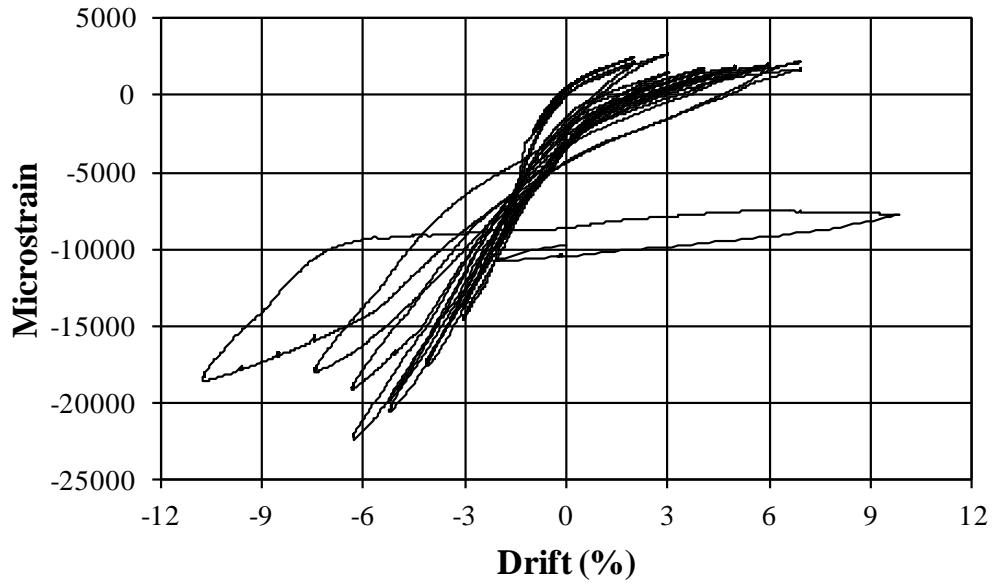
Figure A-23: PT-LL Strain vs. Drift, Strain Gauge 31
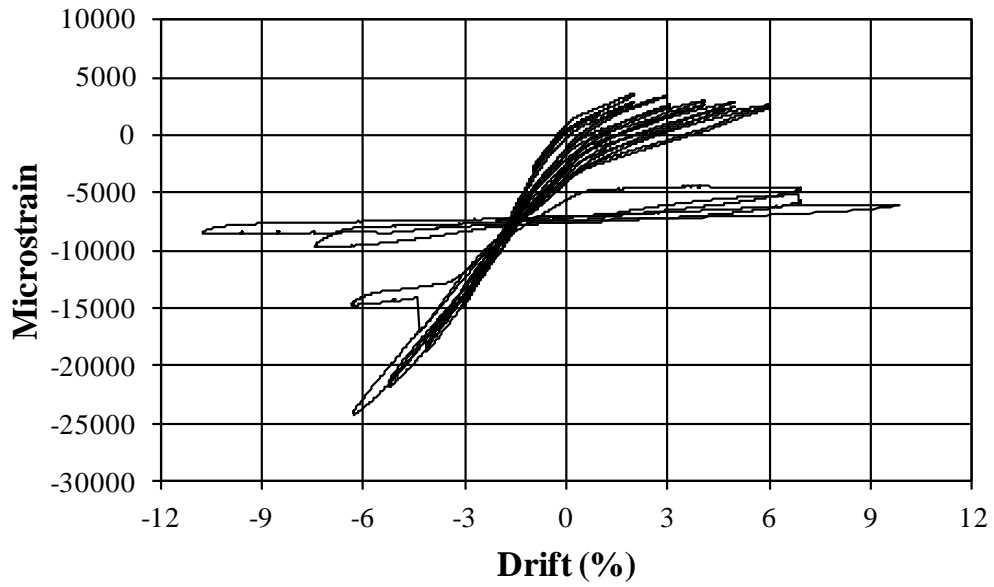
Figure A-24: PT-LL Strain vs. Drift, Strain Gauge 32

194
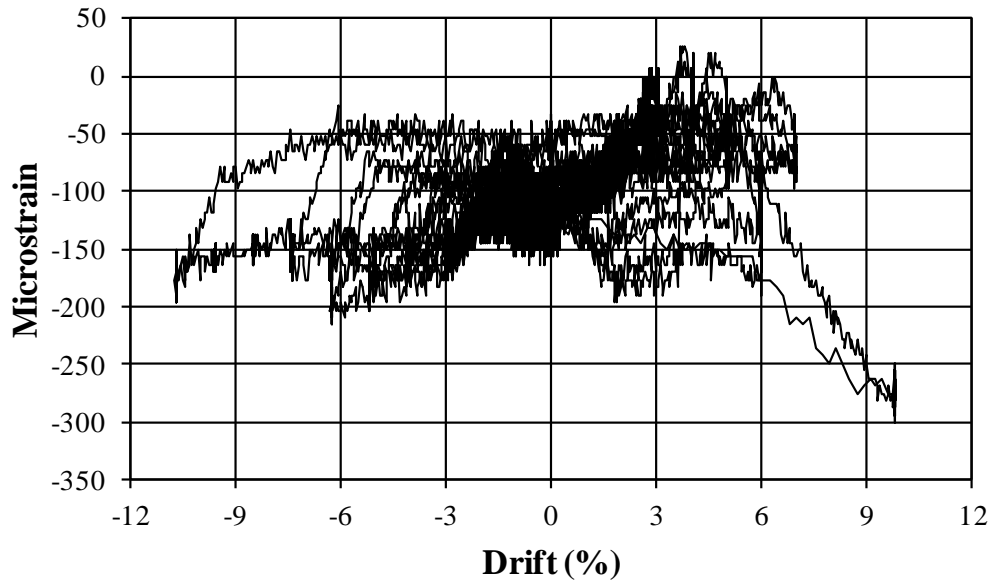
Figure A-25: PT-LL Strain vs. Drift, Strain Gauge 33
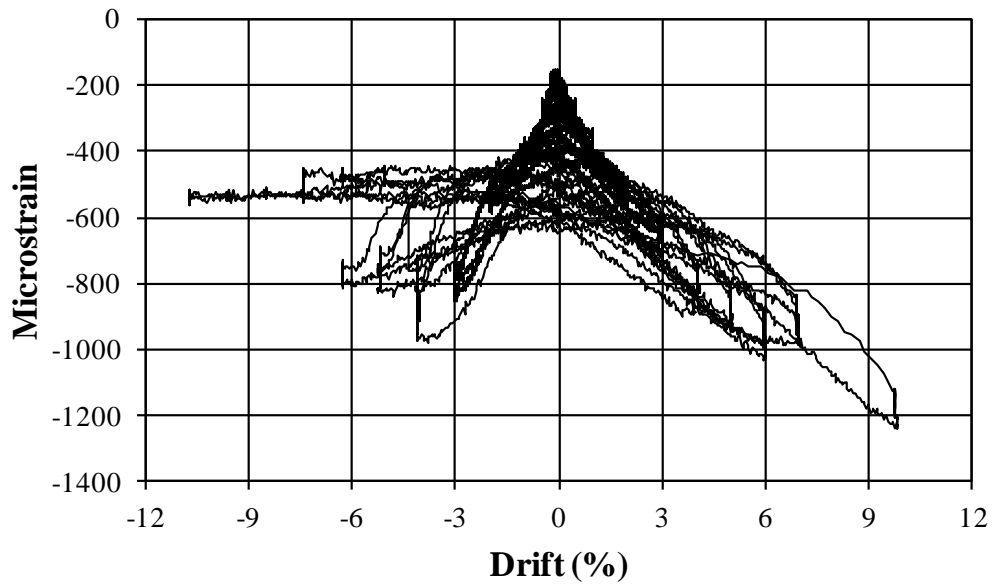
Figure A-26: PT-LL Strain vs. Drift, Strain Gauge 34
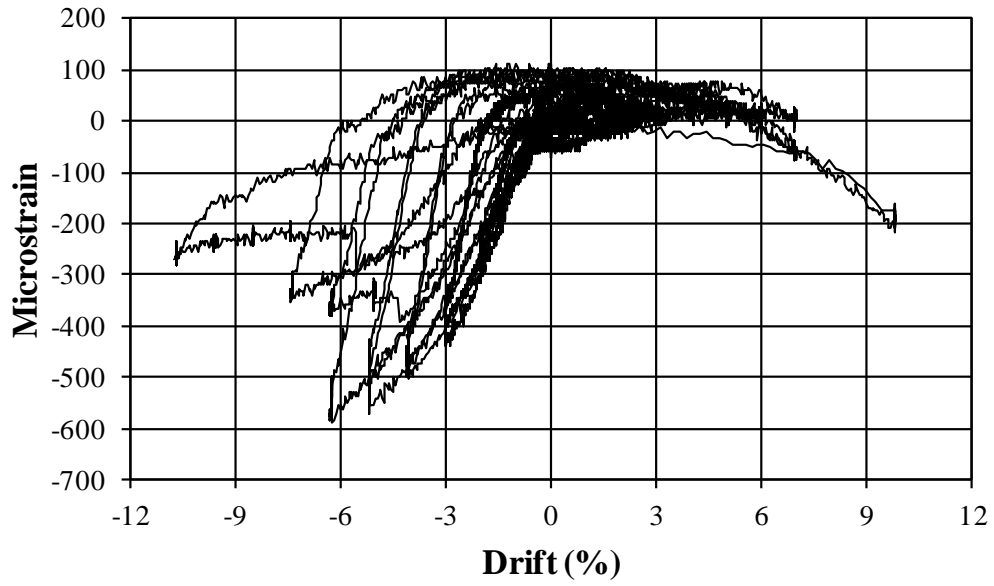
Figure A-27: PT-LL Strain vs. Drift, Strain Gauge 35
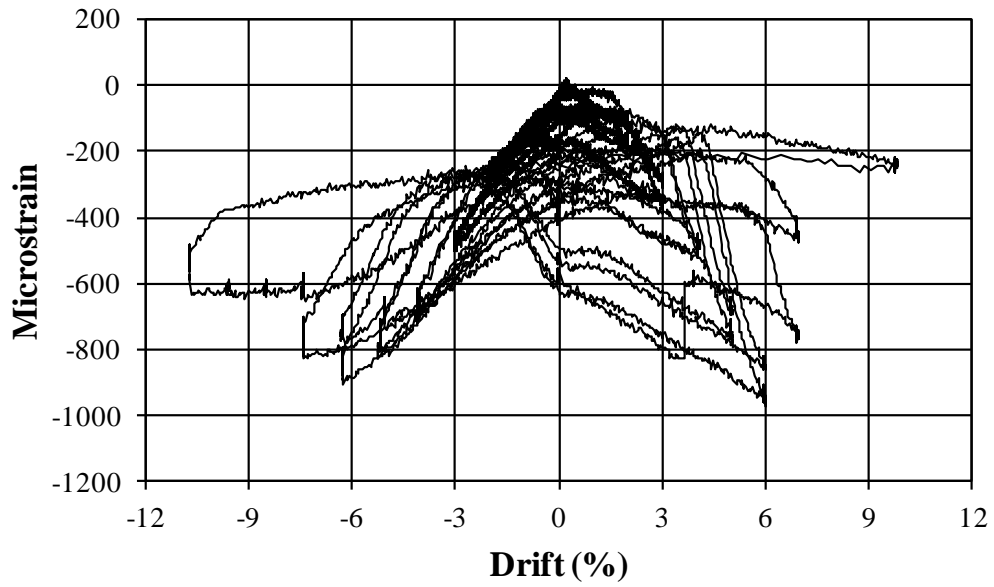
Figure A-28: PT-LL Strain vs. Drift, Strain Gauge 36
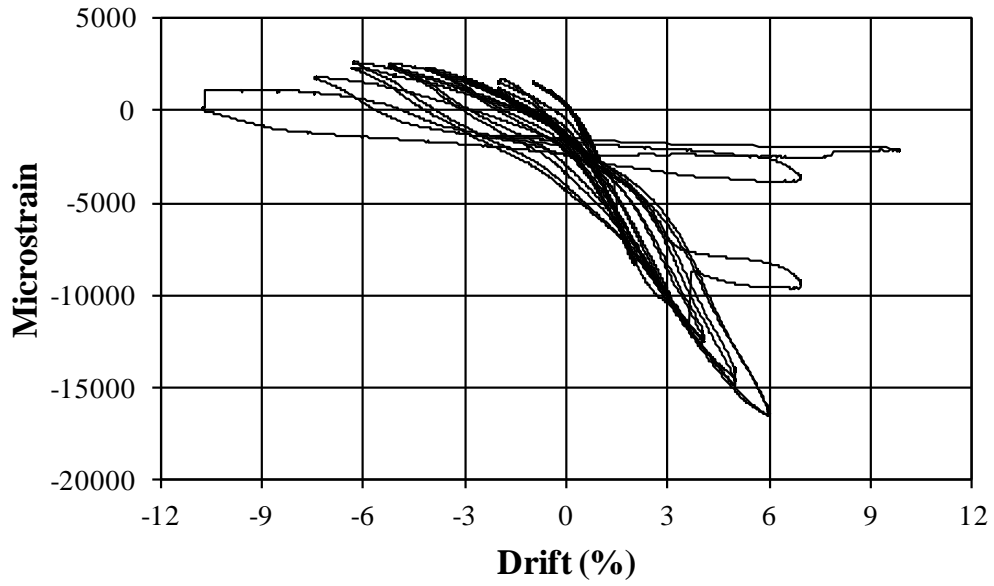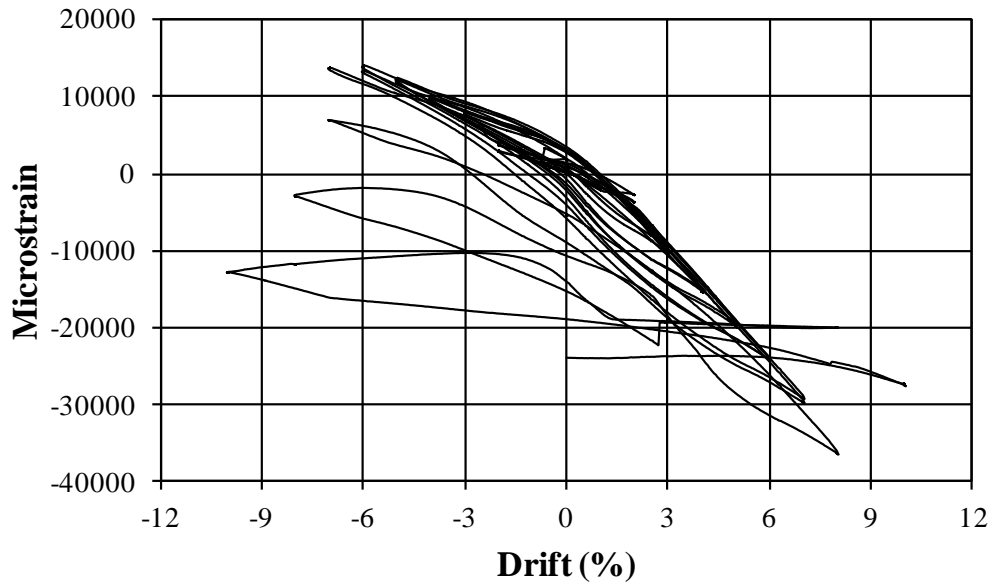
Figure A-29: PT-LL Strain vs. Drift, Strain Gauge 37
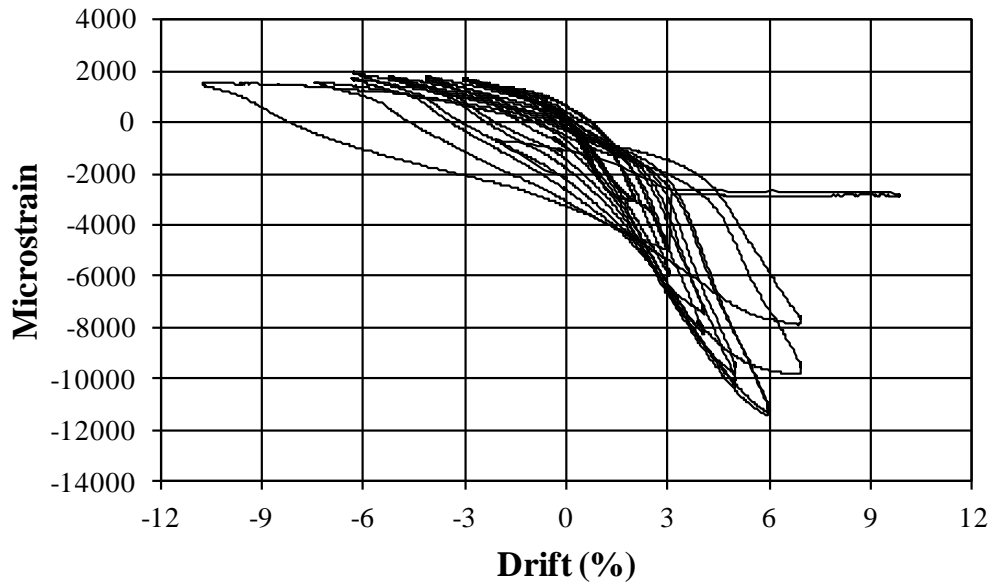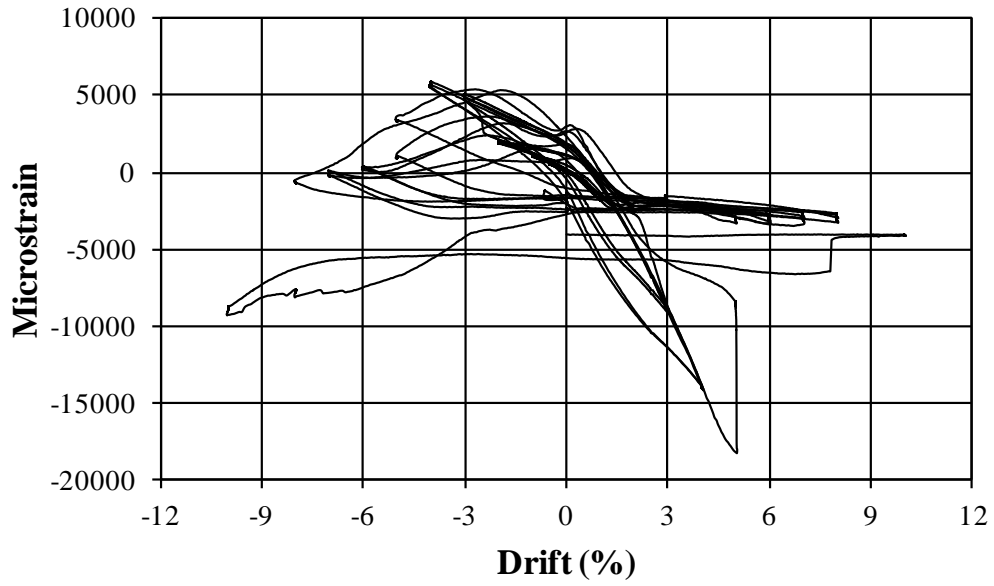

Figure A-30: PT-LL Strain vs. Drift, Strain Gauge 38
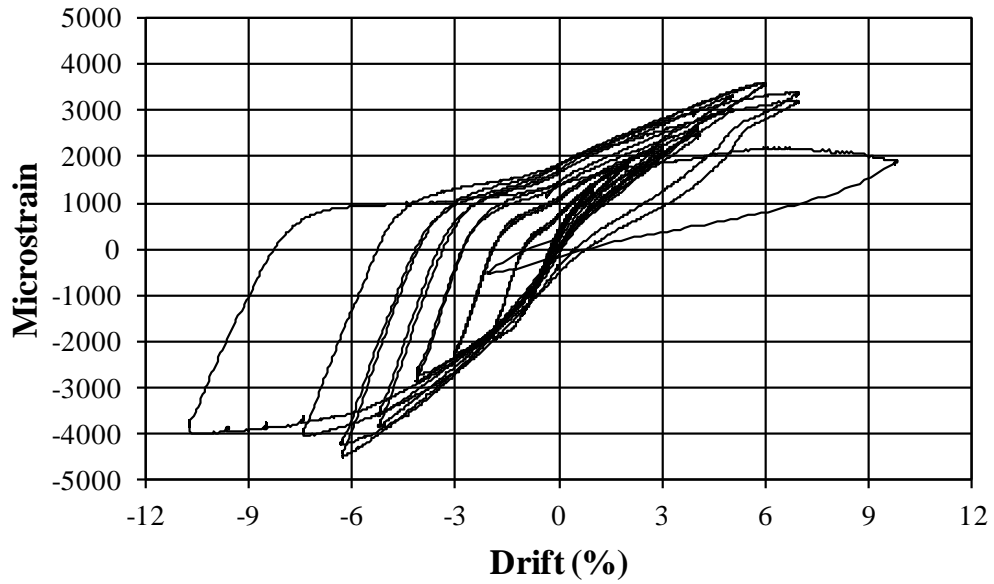
Figure A-31: PT-LL Strain vs. Drift, Strain Gauge 39
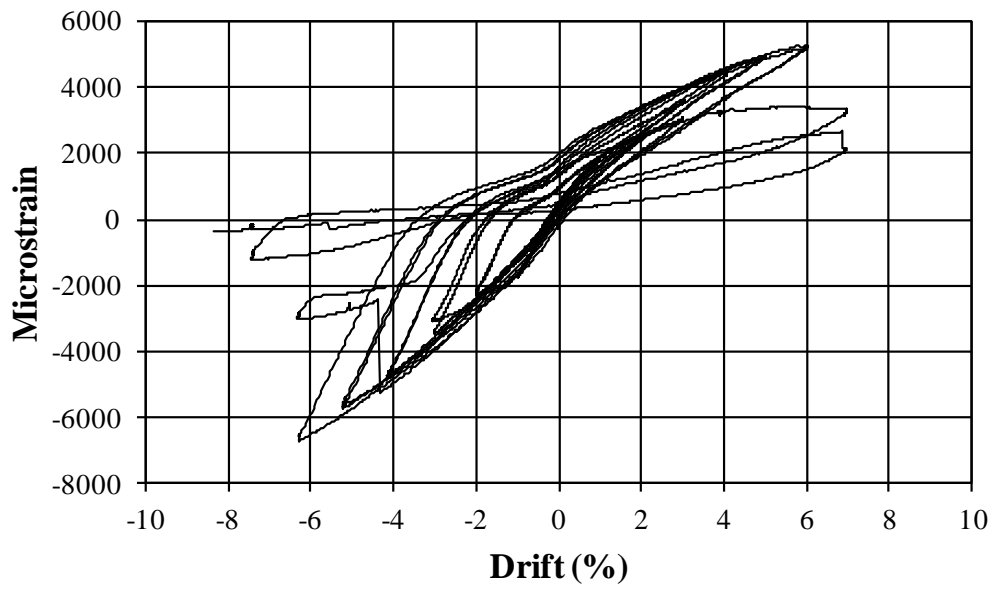
Figure A-32: PT-LL Strain vs. Drift, Strain Gauge 40

198
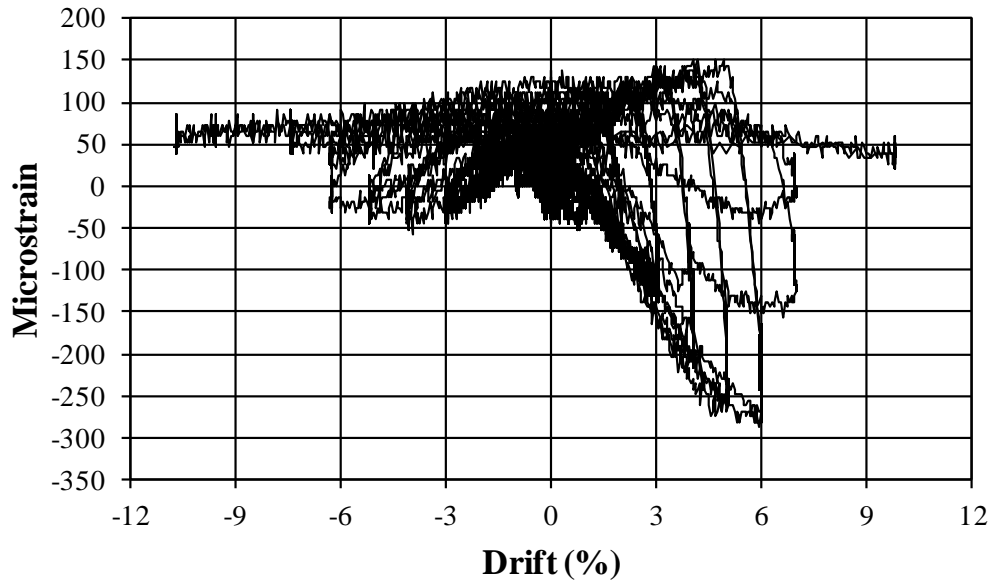
Figure A-33: PT-LL Strain vs. Drift, Strain Gauge 41
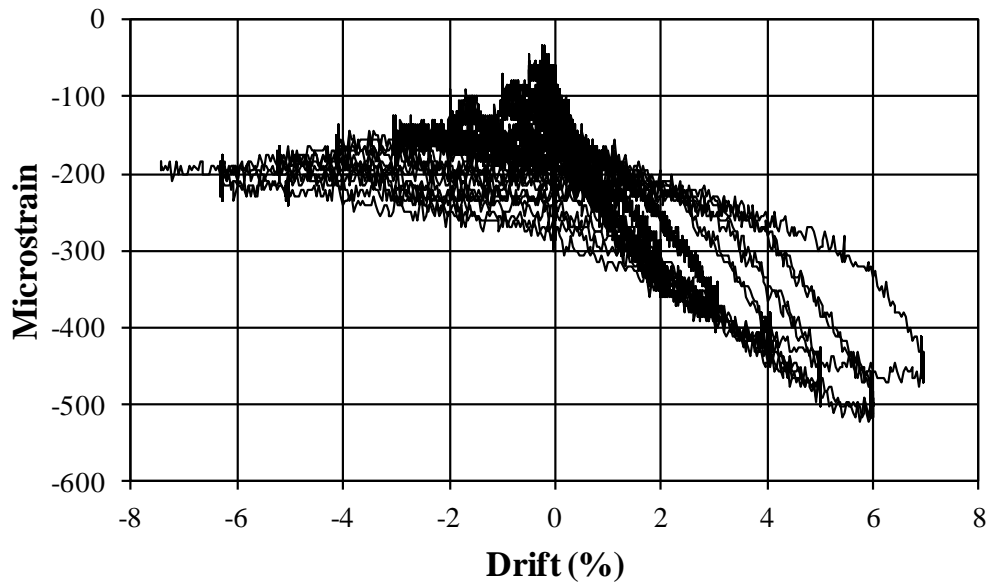
Figure A-34: PT-LL Strain vs. Drift, Strain Gauge 42

199
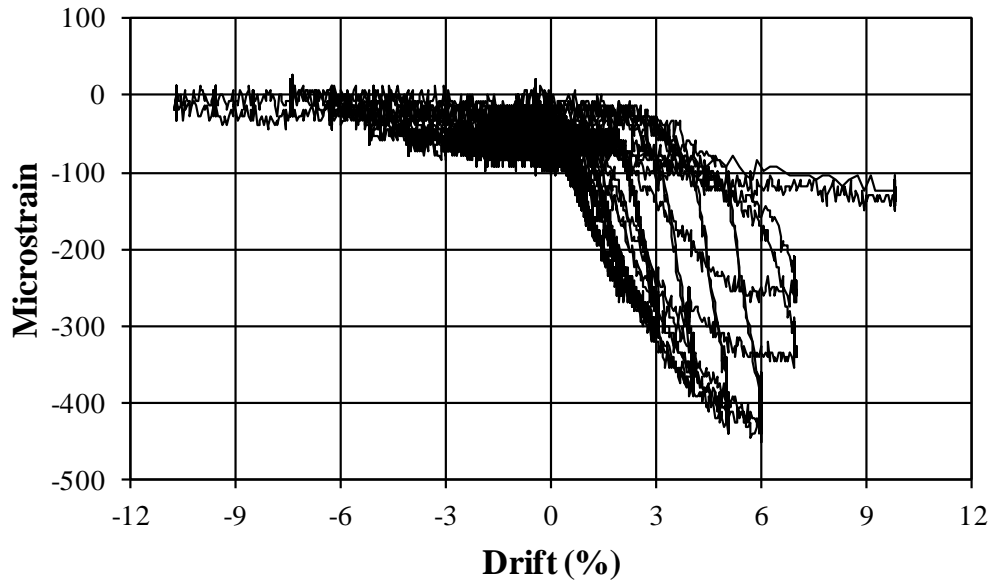
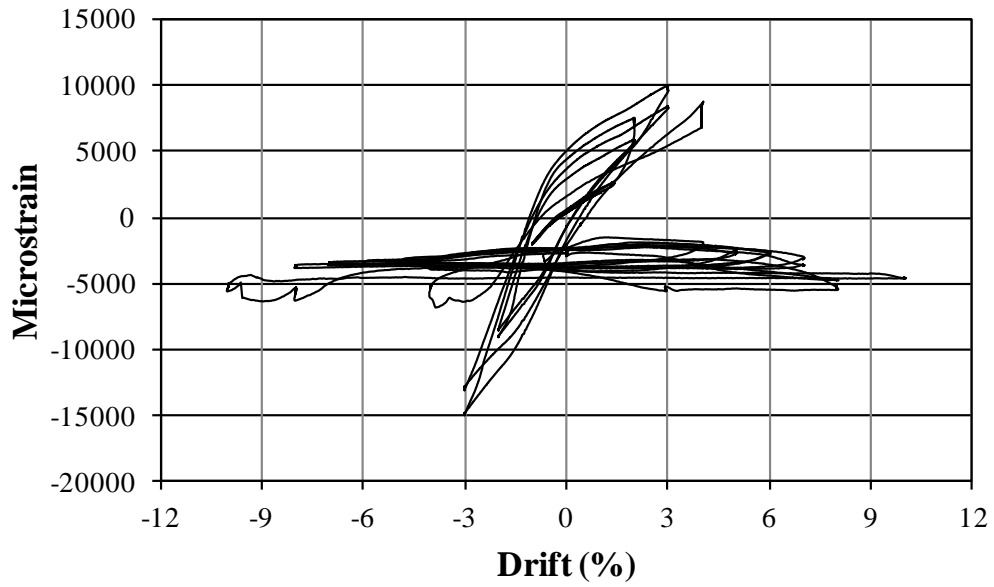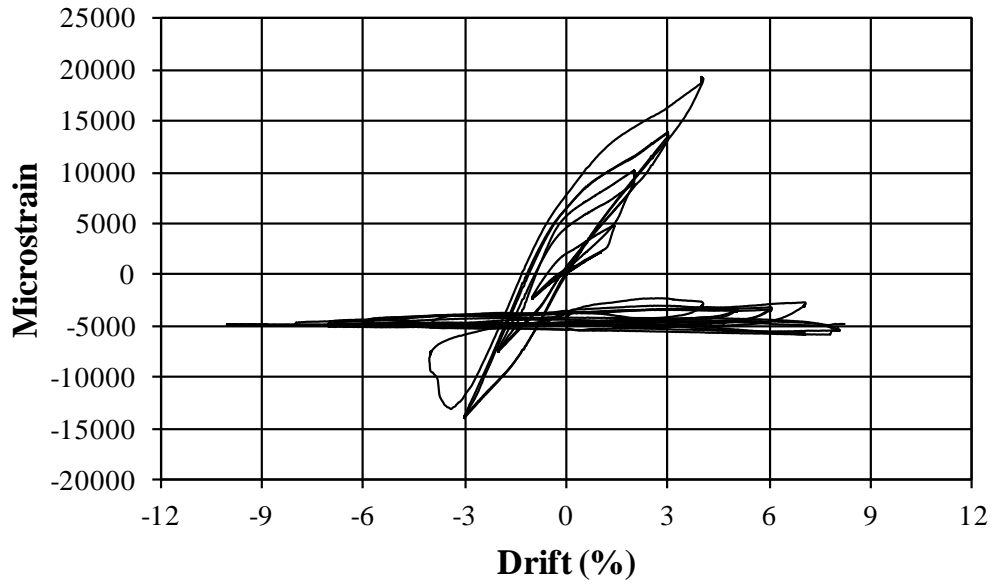**Figure A-35: PT-LL Strain vs. Drift, Strain Gauge 43**
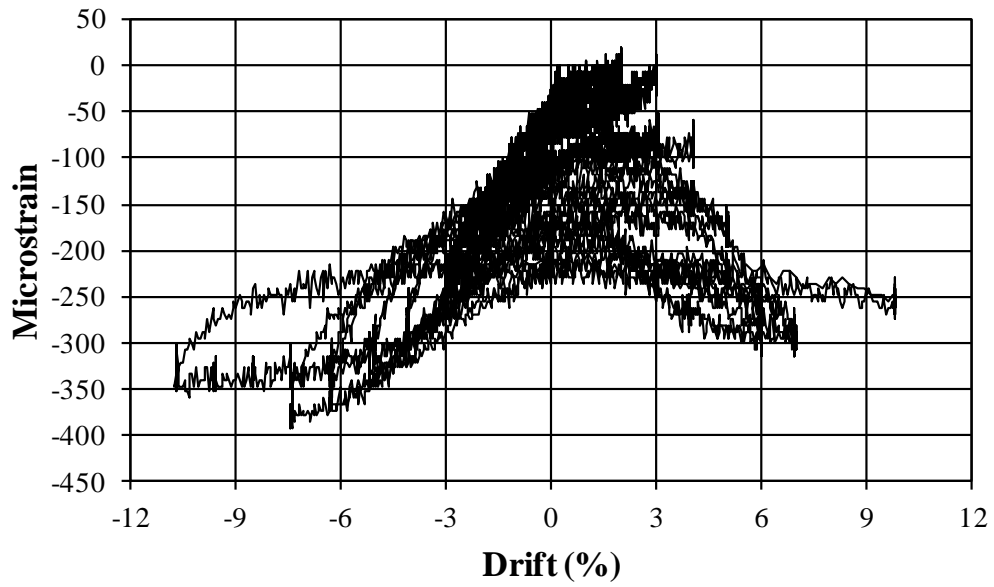
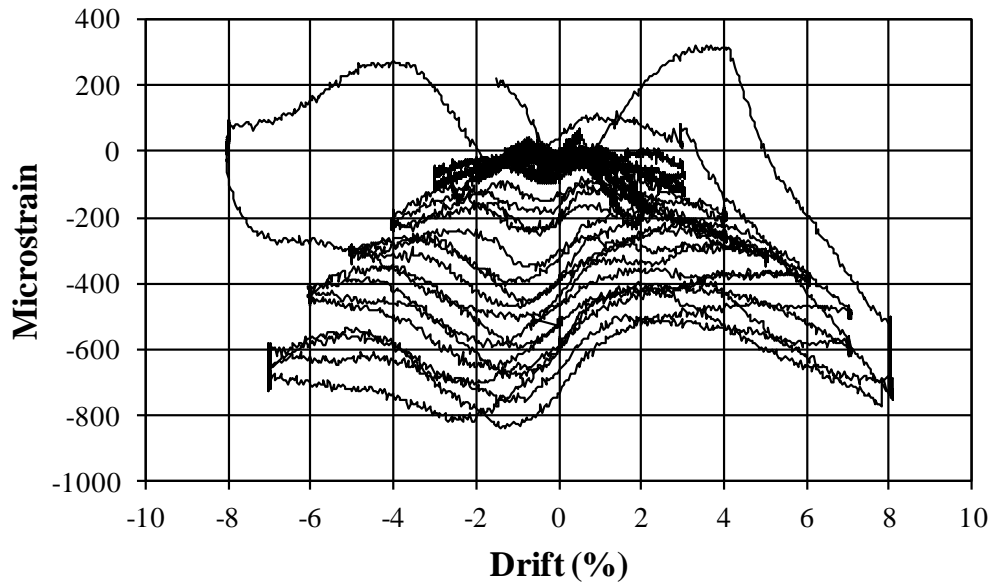**Figure A-36: PT-LL Strain vs. Drift, Strain Gauge 44**

200
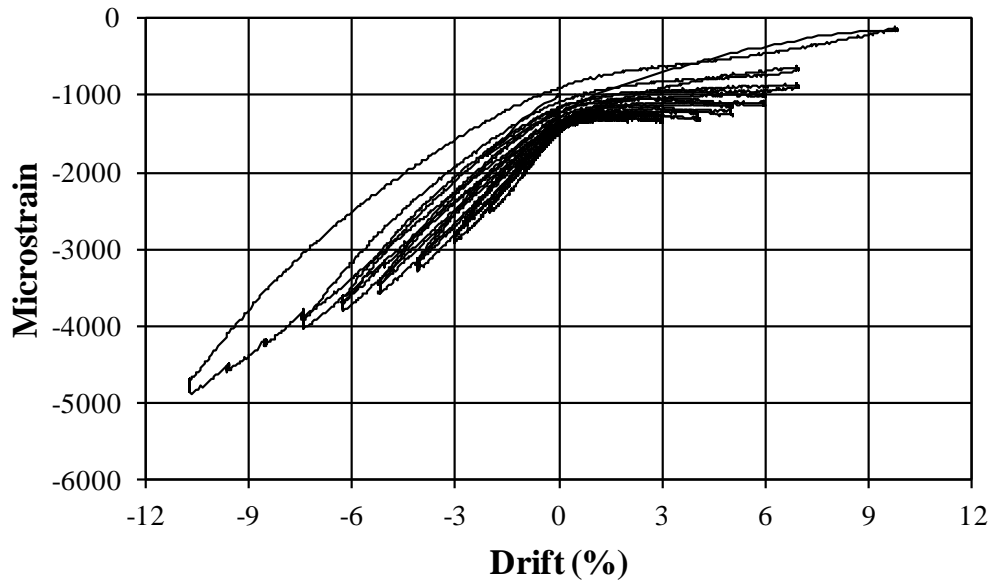
Figure A-37: PT-LL Strain vs. Drift, Strain Gauge PT-14, Tendon 3
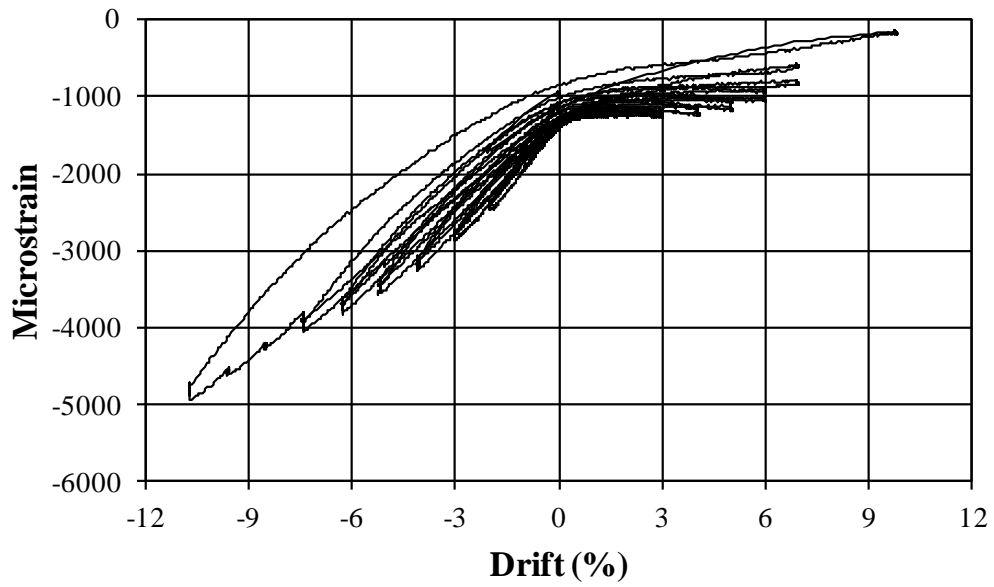
Figure A-38: PT-LL Strain vs. Drift, Strain Gauge PT-15, Tendon 3
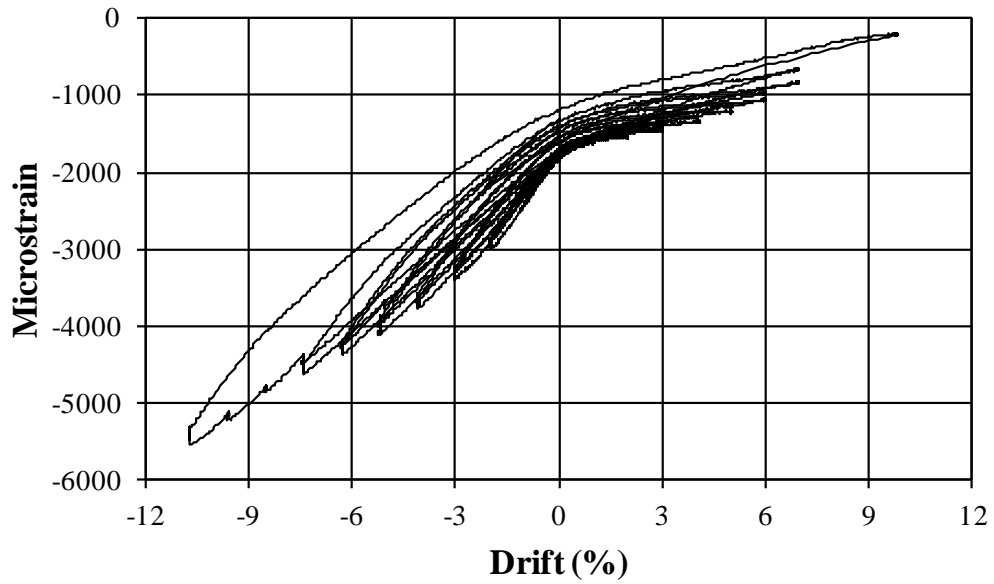
Figure A-39: PT-LL Strain vs. Drift, Strain Gauge PT-16, Tendon 3
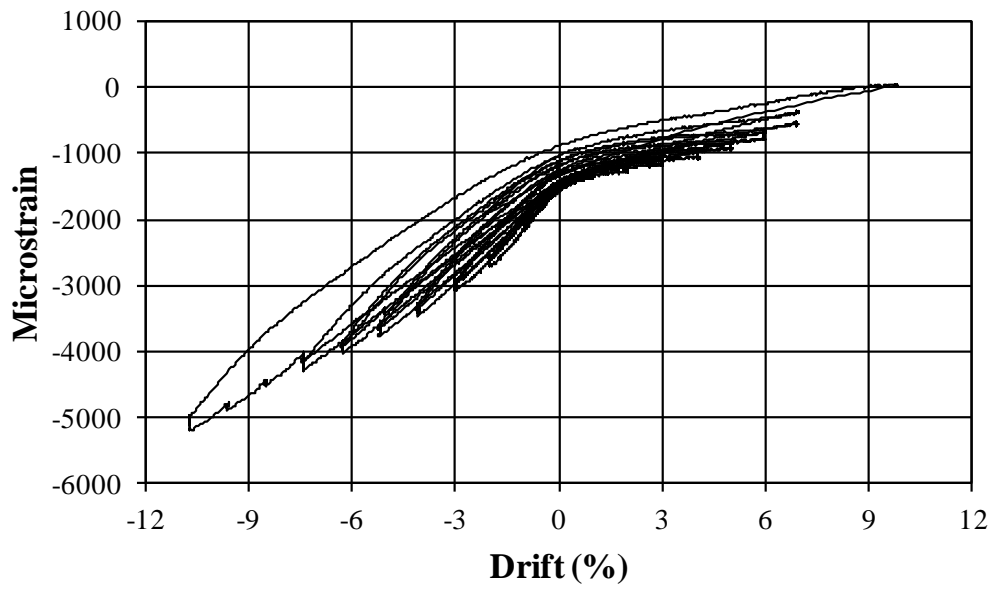
Figure A-40: PT-LL Strain vs. Drift, Strain Gauge PT-18, Tendon 3
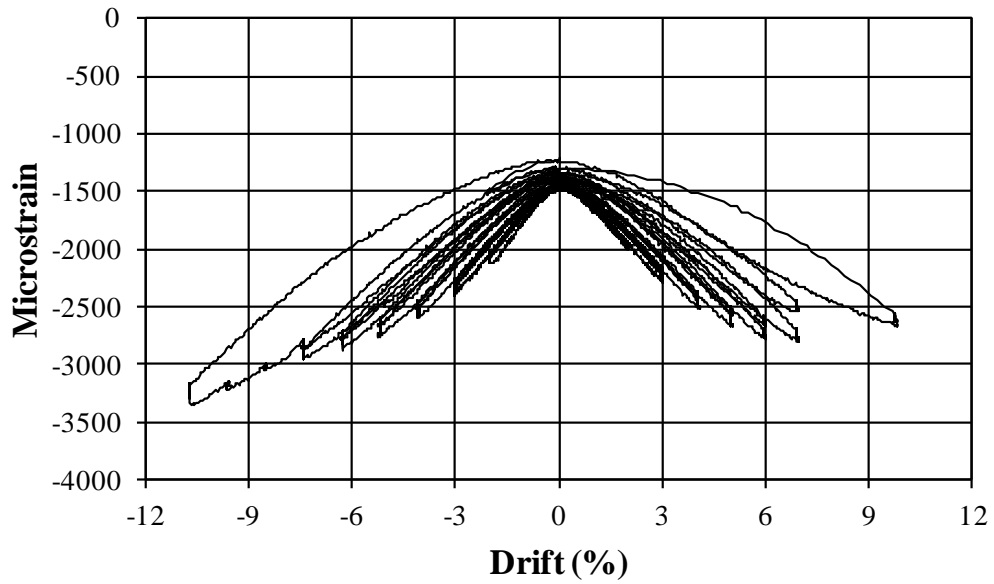
Figure A-41: PT-LL Strain vs. Drift, Strain Gauge PT-19, Tendon 2

Figure A-42: PT-LL Strain vs. Drift, Strain Gauge PT-20, Tendon 2
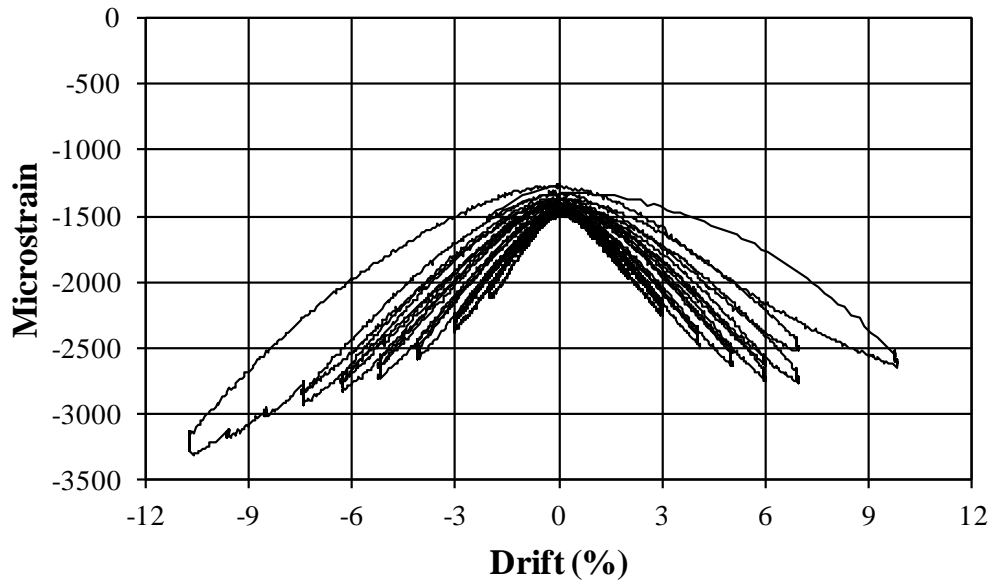
Figure A-43: PT-LL Strain vs. Drift, Strain Gauge PT-21, Tendon 2
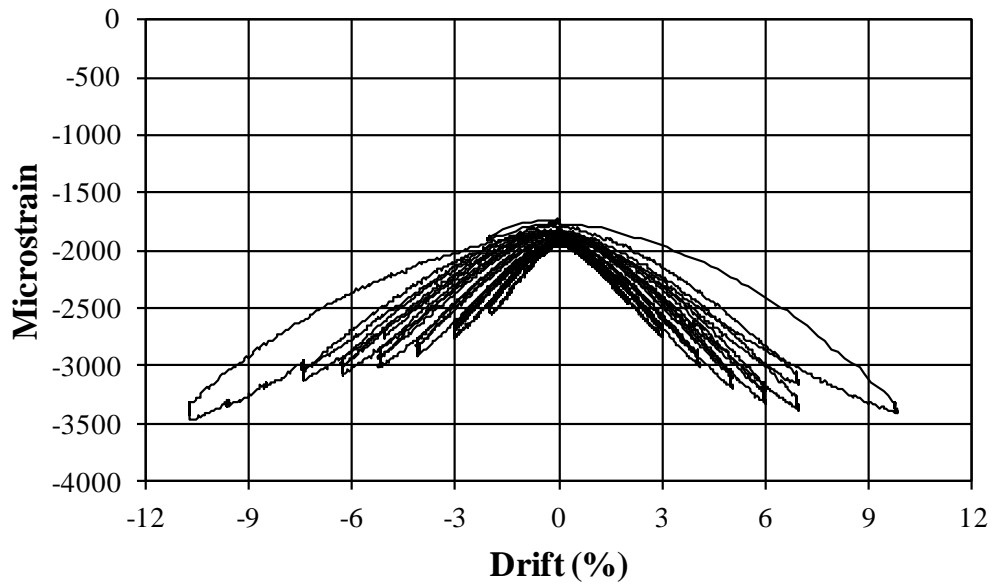
Figure A-44: PT-LL Strain vs. Drift, Strain Gauge PT-22, Tendon 2

Figure A-45: PT-LL Strain vs. Drift, Strain Gauge PT-24, Tendon 2

Figure A-46: PT-HL Strain vs. Drift, Strain Gauge 9

205

Figure A-47: PT-HL Strain vs. Drift, Strain Gauge 10

Figure A-48: PT-HL Strain vs. Drift, Strain Gauge 11
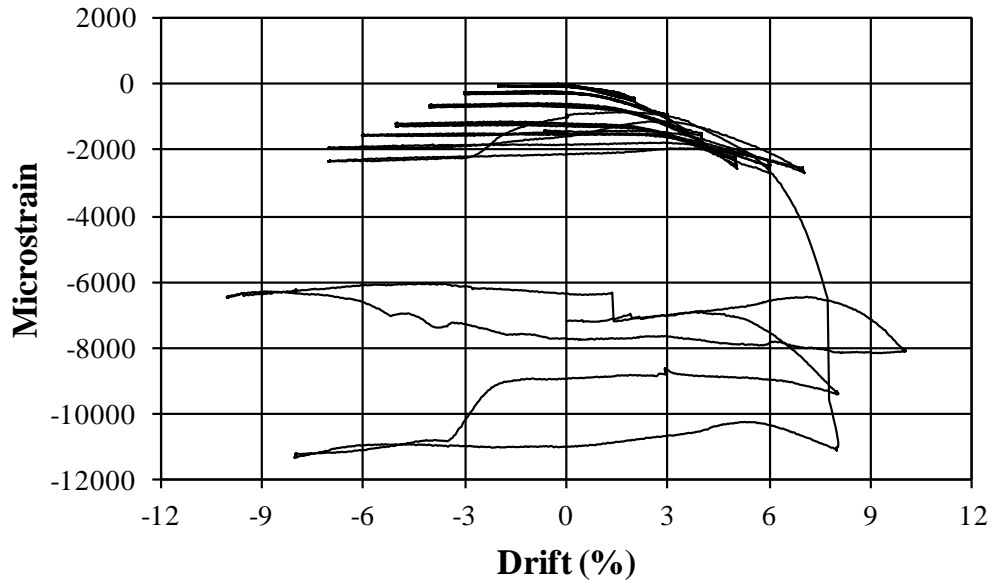
Figure A-49: PT-HL Strain vs. Drift, Strain Gauge 12

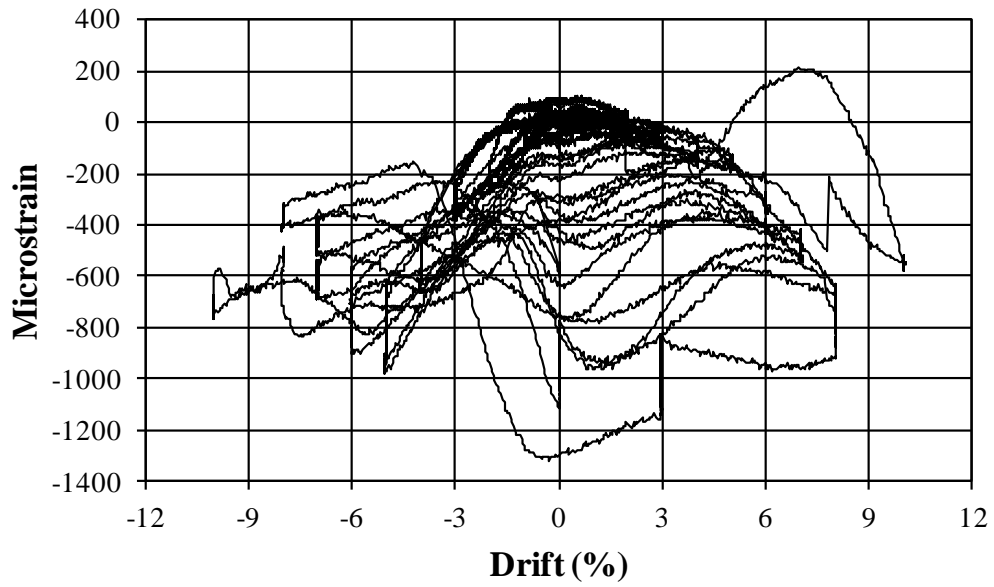**Figure A-50: PT-HL Strain vs. Drift, Strain Gauge 13**
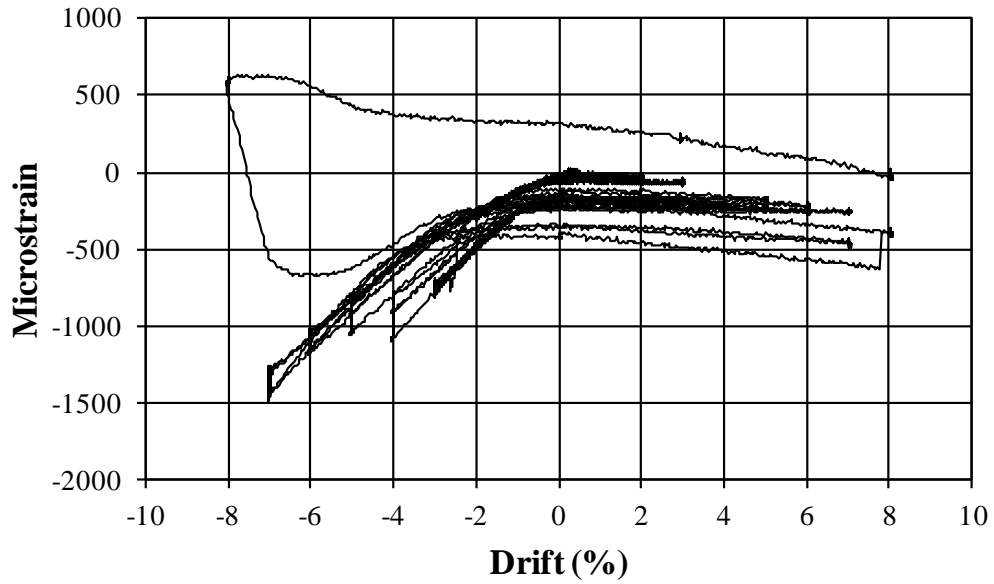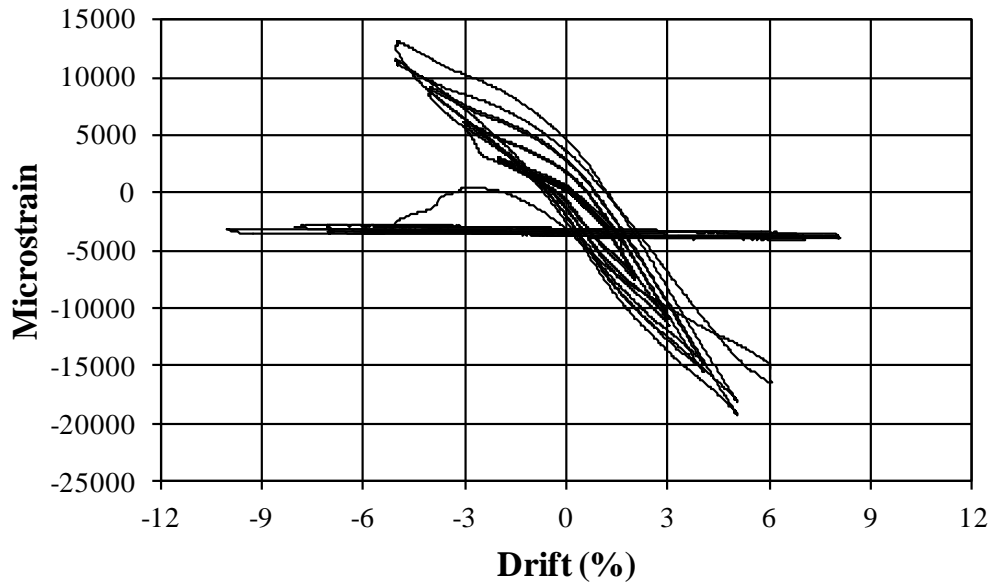
Figure A-51: PT-HL Strain vs. Drift, Strain Gauge 14

Figure A-52: PT-HL Strain vs. Drift, Strain Gauge 15

Figure A-53: PT-HL Strain vs. Drift, Strain Gauge 16

Figure A-54: PT-HL Strain vs. Drift, Strain Gauge 17

Figure A-55: PT-HL Strain vs. Drift, Strain Gauge 18

Figure A-56: PT-HL Strain vs. Drift, Strain Gauge 19

Figure A-57: PT-HL Strain vs. Drift, Strain Gauge 20
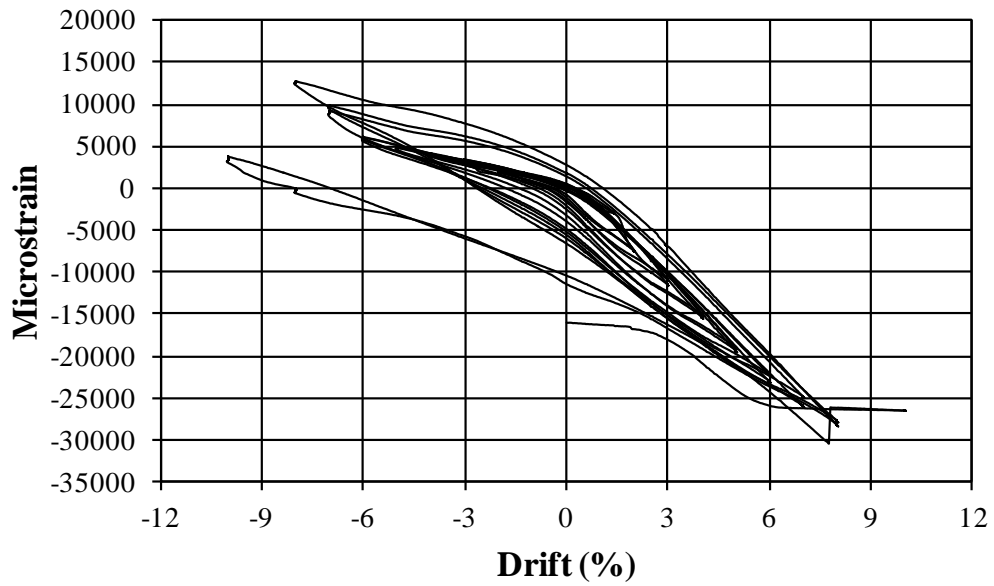

Figure A-58: PT-HL Strain vs. Drift, Strain Gauge 21

211

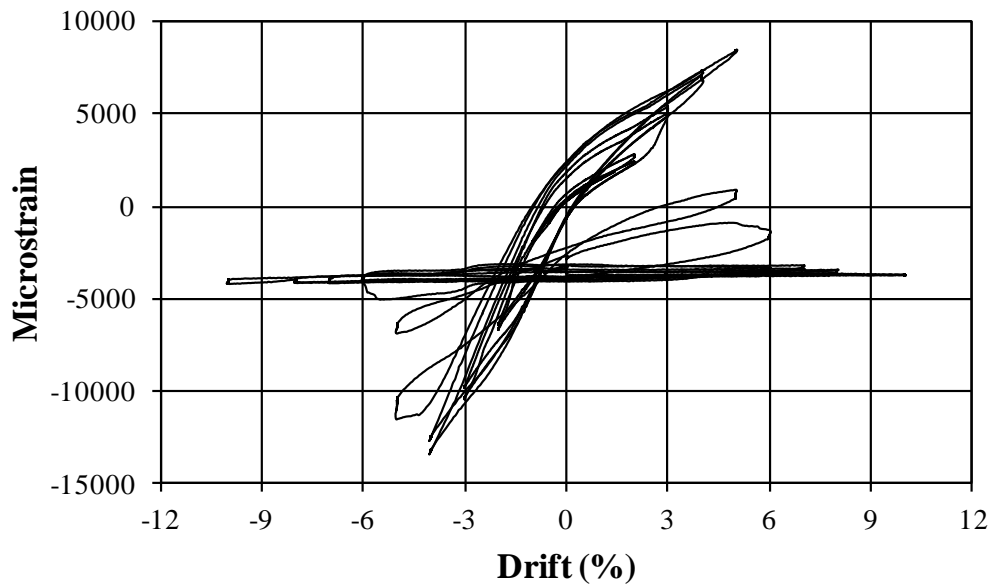**Figure A-59: PT-HL Strain vs. Drift, Strain Gauge 22**

Figure A-60: PT-HL Strain vs. Drift, Strain Gauge 23

Figure A-61: PT-HL Strain vs. Drift, Strain Gauge 25

Figure A-62: PT-HL Strain vs. Drift, Strain Gauge 26

213

Figure A-63: PT-HL Strain vs. Drift, Strain Gauge 27

Figure A-64: PT-HL Strain vs. Drift, Strain Gauge 28

Figure A-65: PT-HL Strain vs. Drift, Strain Gauge 29
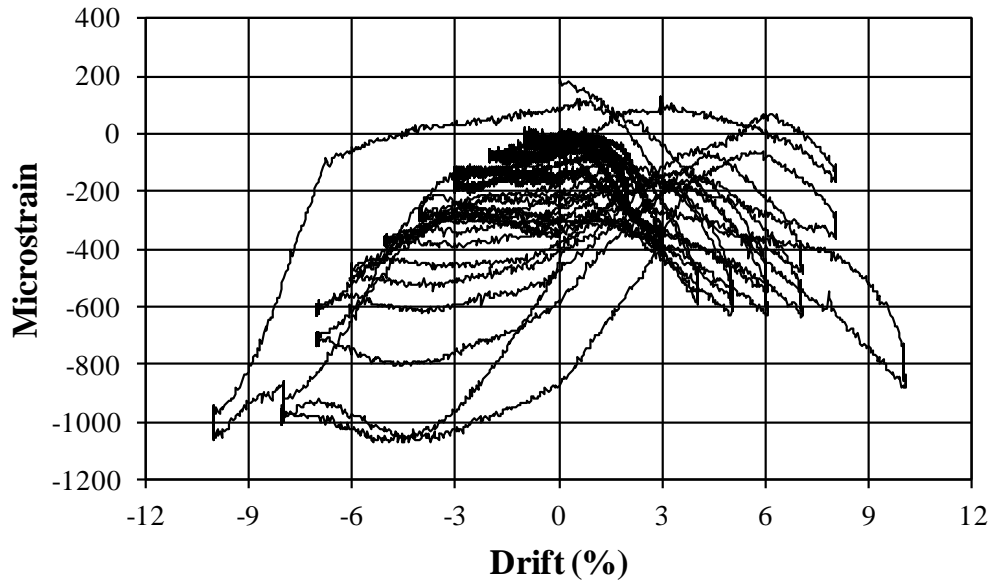

Figure A-66: PT-HL Strain vs. Drift, Strain Gauge 30

215

Figure A-67: PT-HL Strain vs. Drift, Strain Gauge 31

Figure A-68: PT-HL Strain vs. Drift, Strain Gauge 32
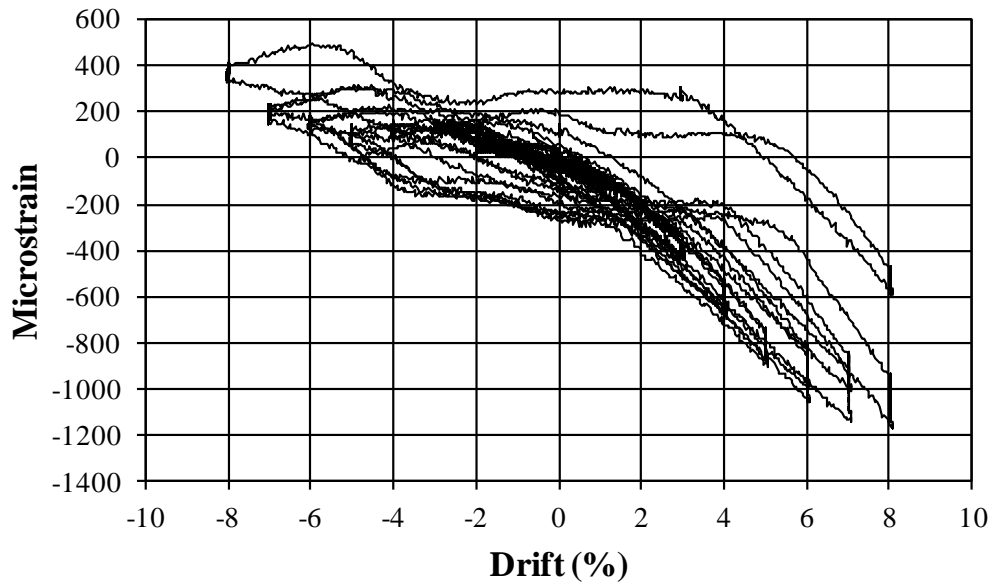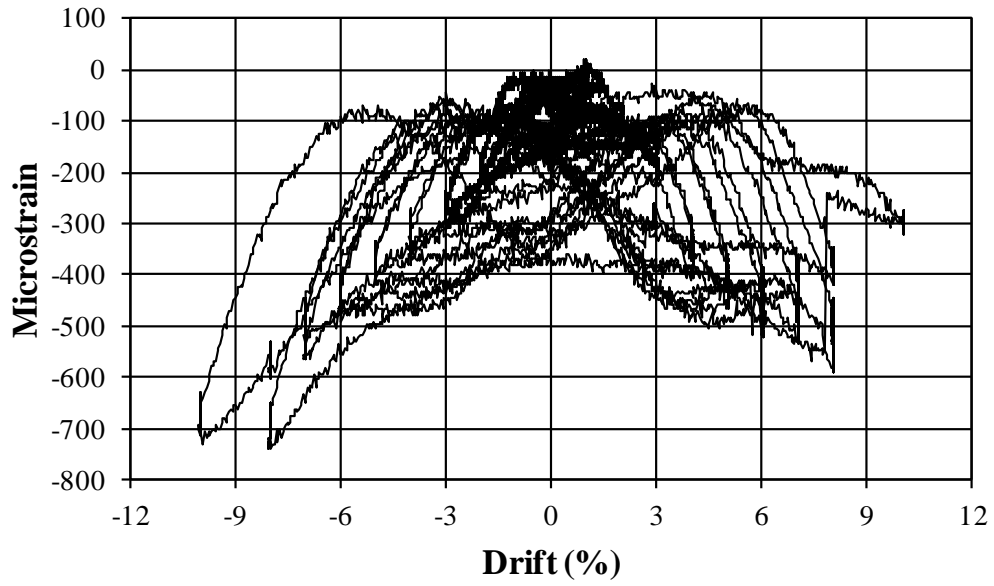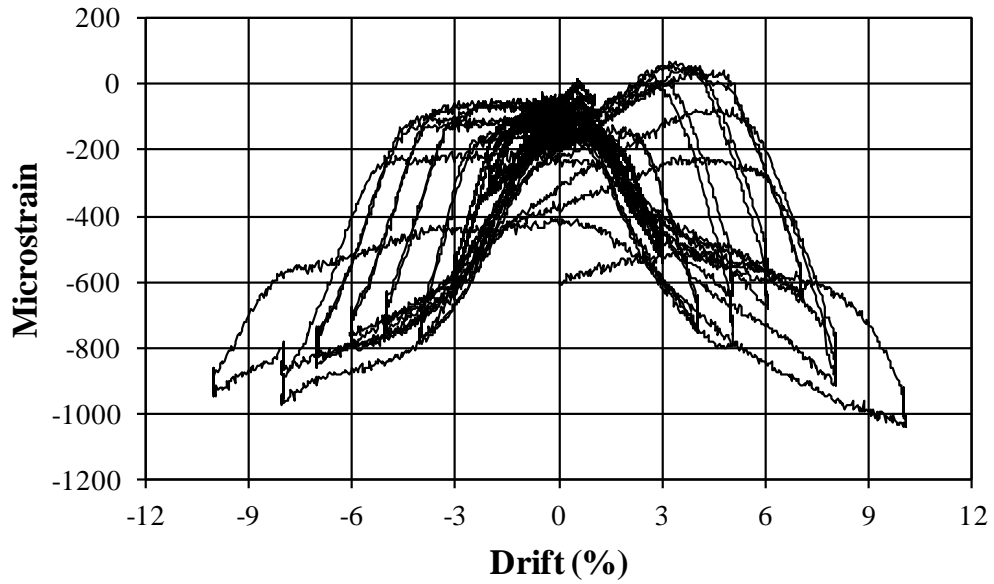
Figure A-69: PT-HL Strain vs. Drift, Strain Gauge 33
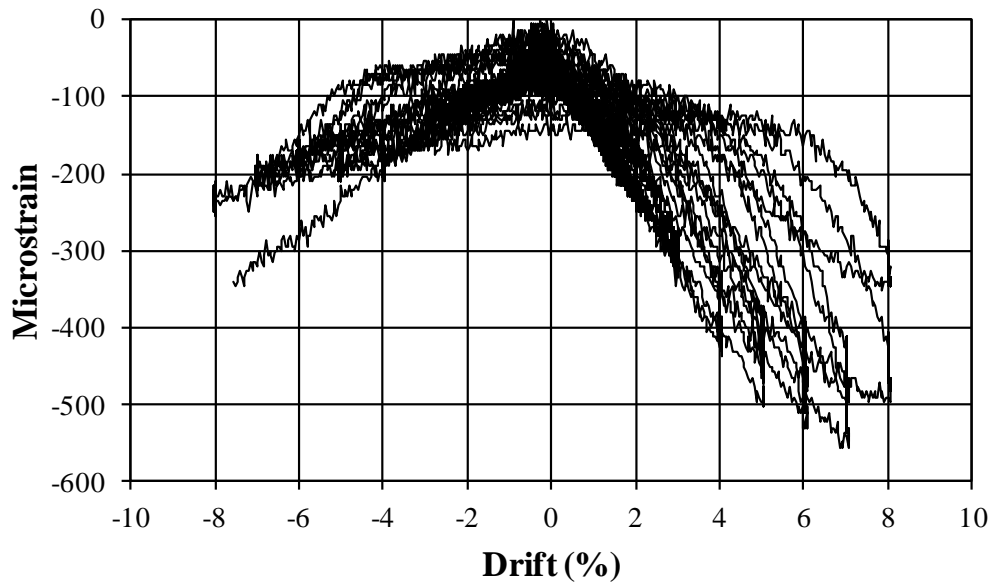
Figure A-70: PT-HL Strain vs. Drift, Strain Gauge 34
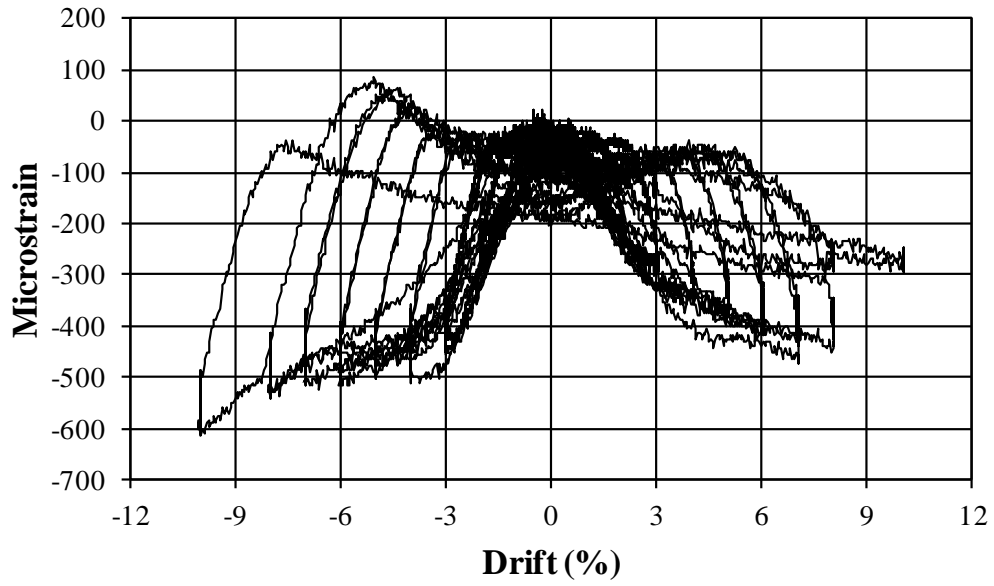
Figure A-71: PT-HL Strain vs. Drift, Strain Gauge 35
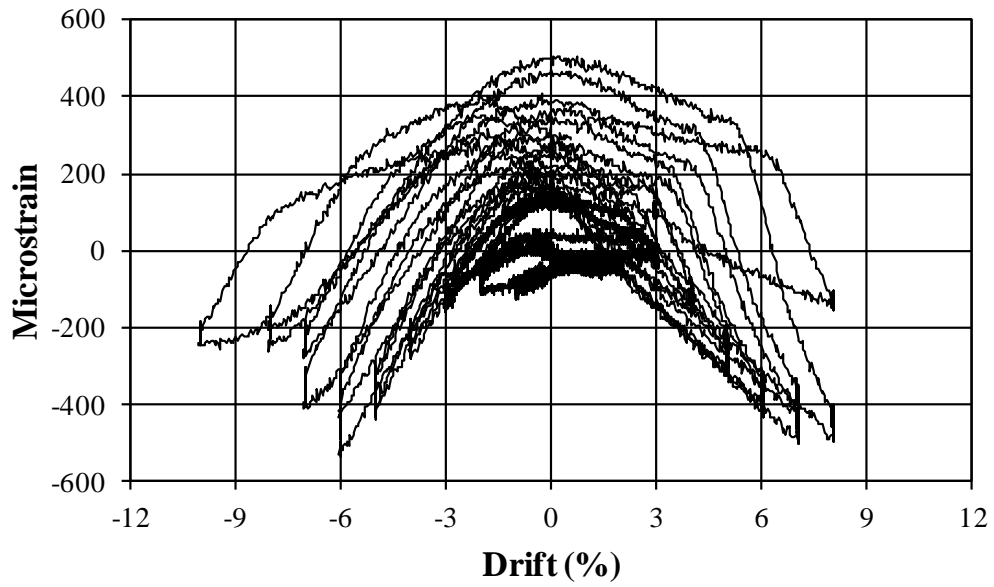
Figure A-72: PT-HL Strain vs. Drift, Strain Gauge 36
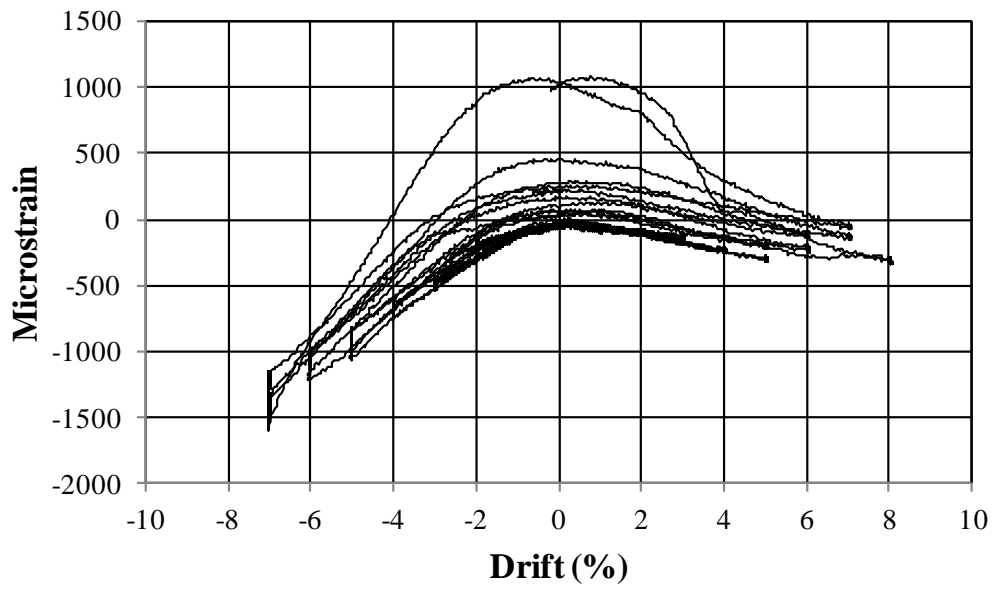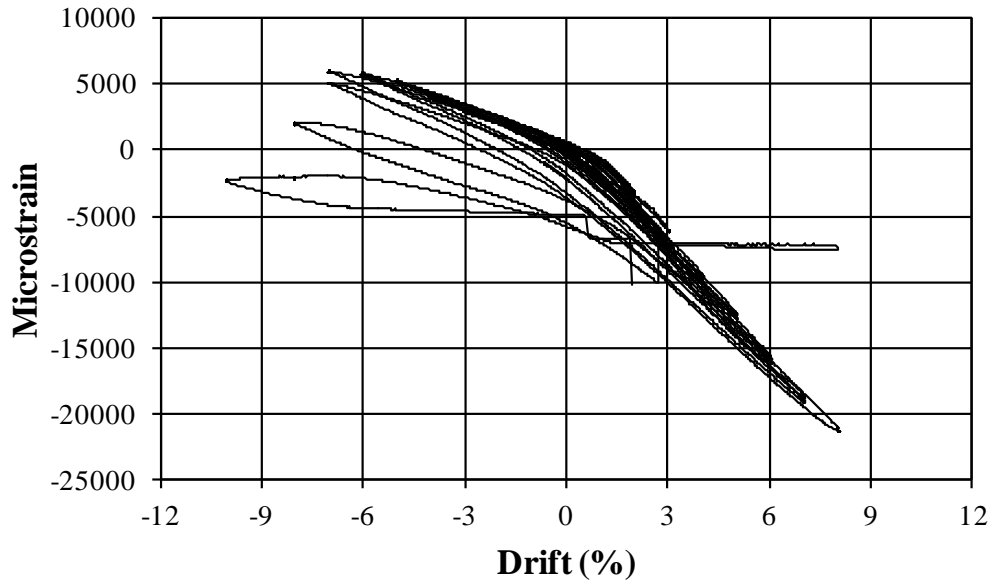
Figure A-73: PT-HL Strain vs. Drift, Strain Gauge 37
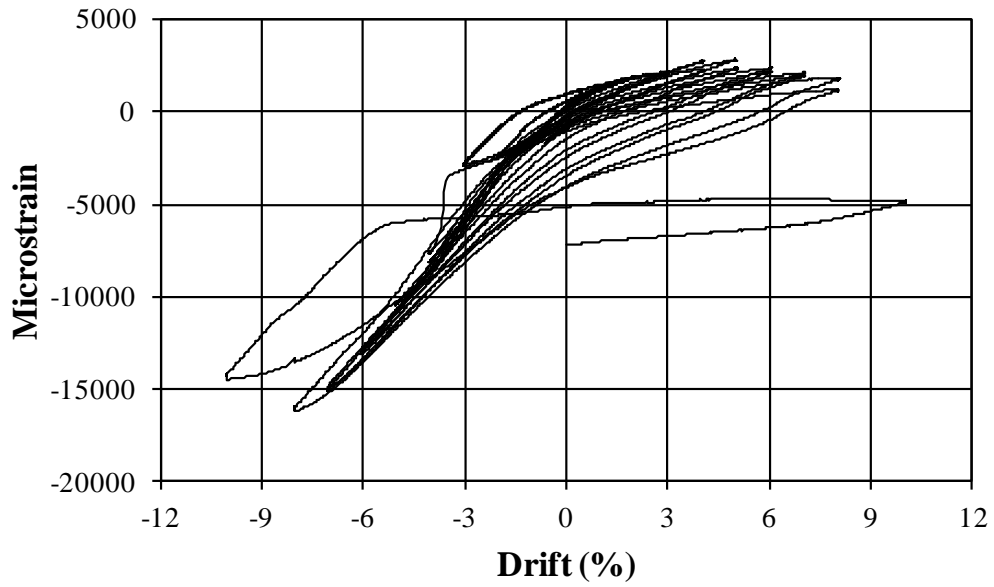
Figure A-74: PT-HL Strain vs. Drift, Strain Gauge 39
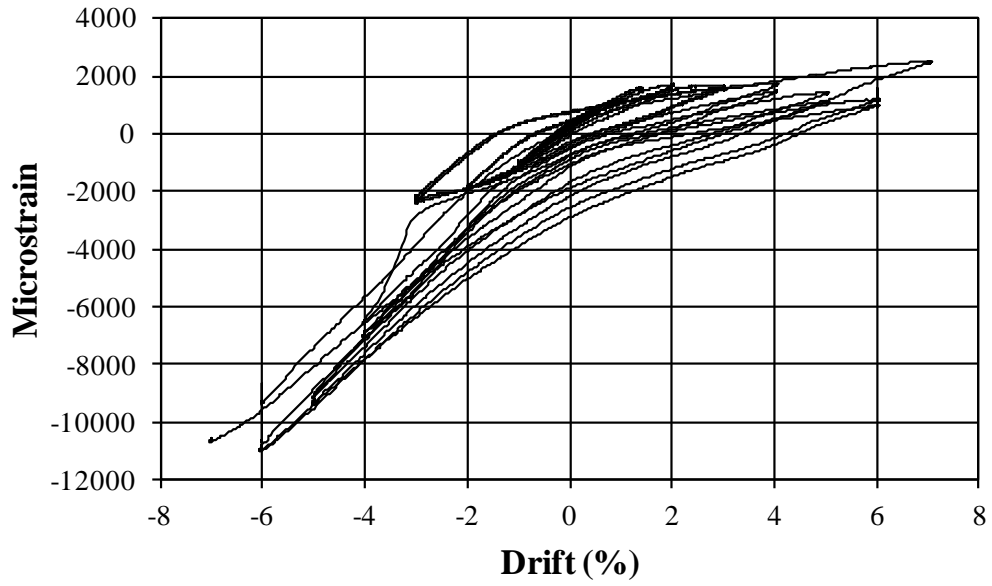
Figure A-75: PT-HL Strain vs. Drift, Strain Gauge 40
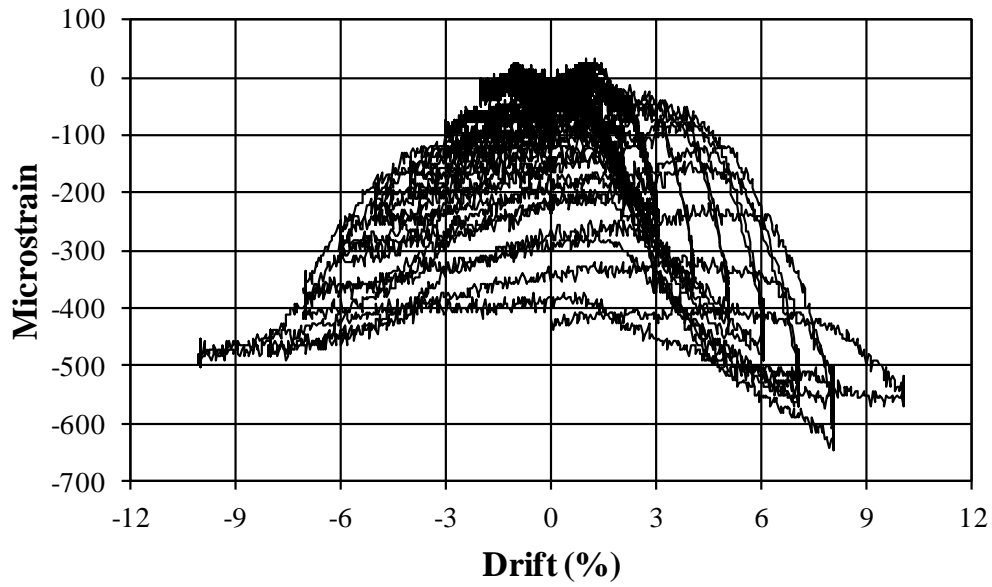
Figure A-76: PT-HL Strain vs. Drift, Strain Gauge 41
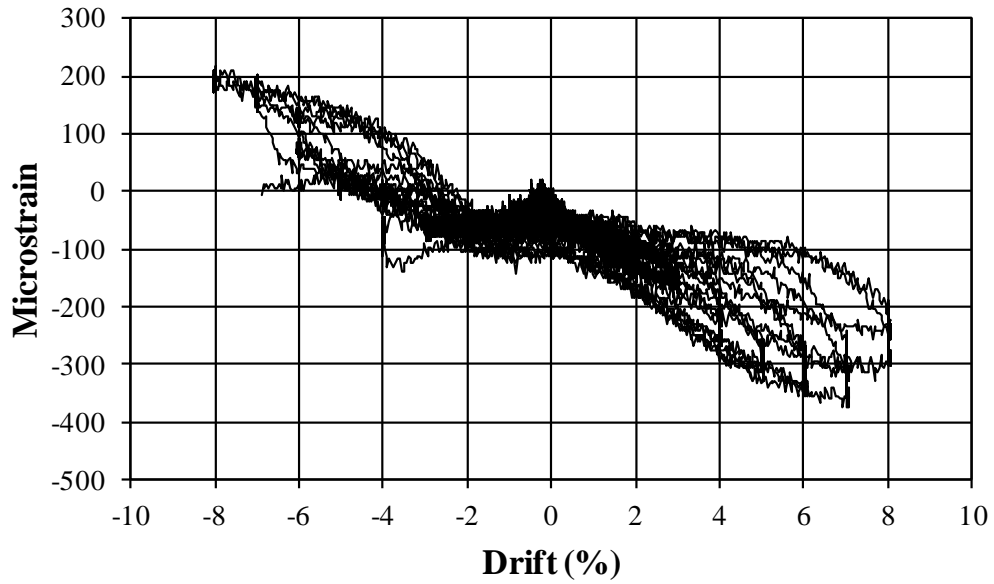
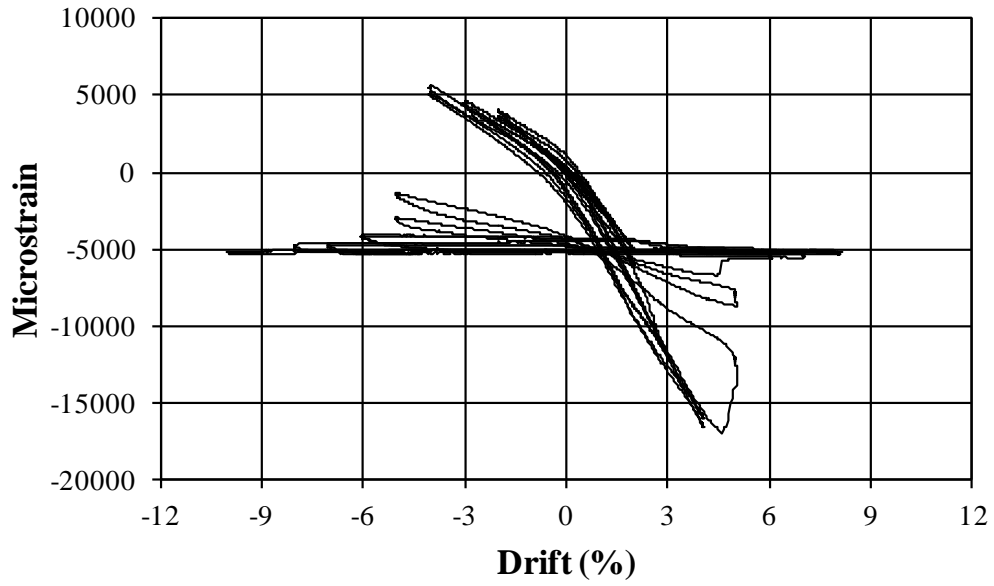**Figure A-77: PT-HL Strain vs. Drift, Strain Gauge 42**
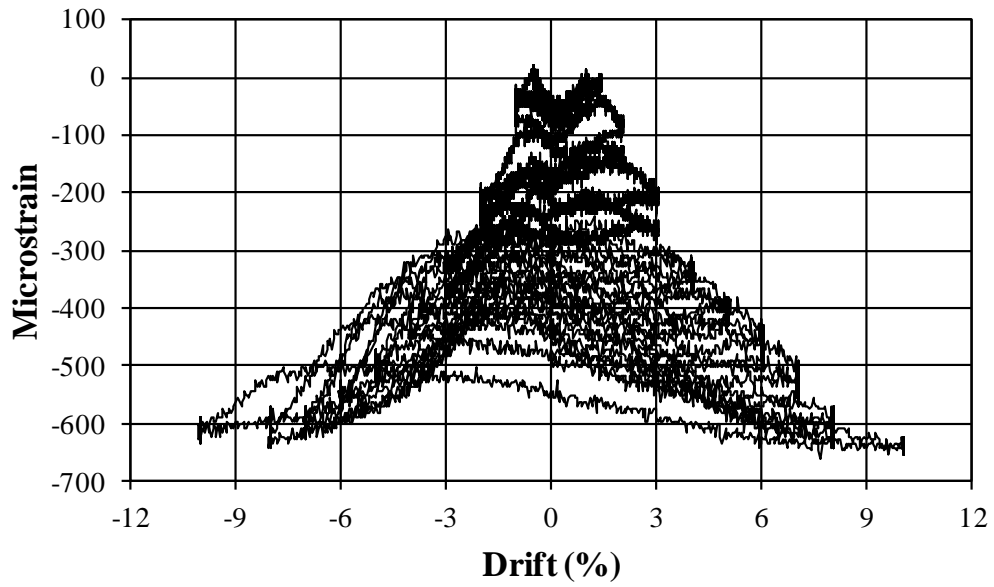
Figure A-78: PT-HL Strain vs. Drift, Strain Gauge 43
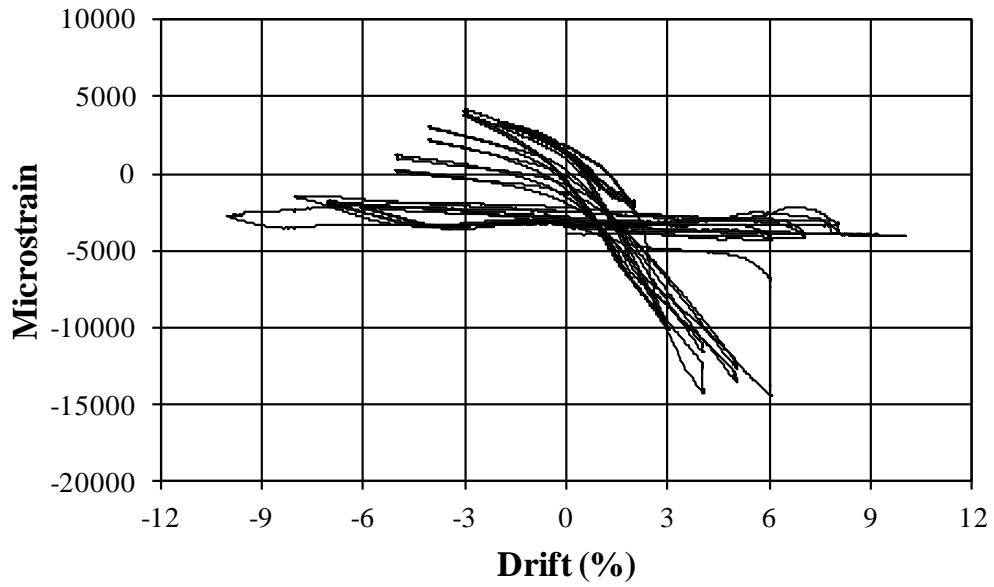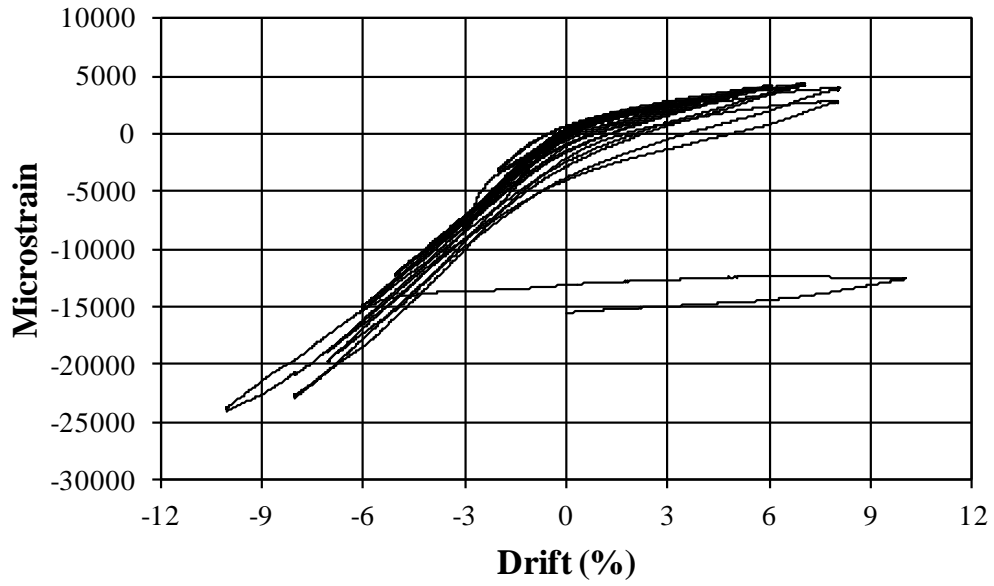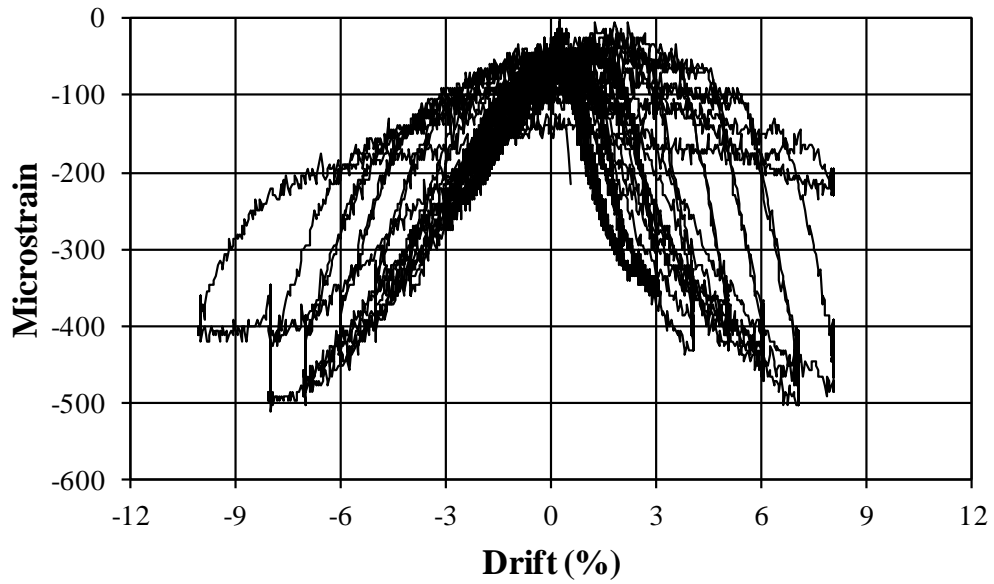
Figure A-79: PT-HL Strain vs. Drift, Strain Gauge 44
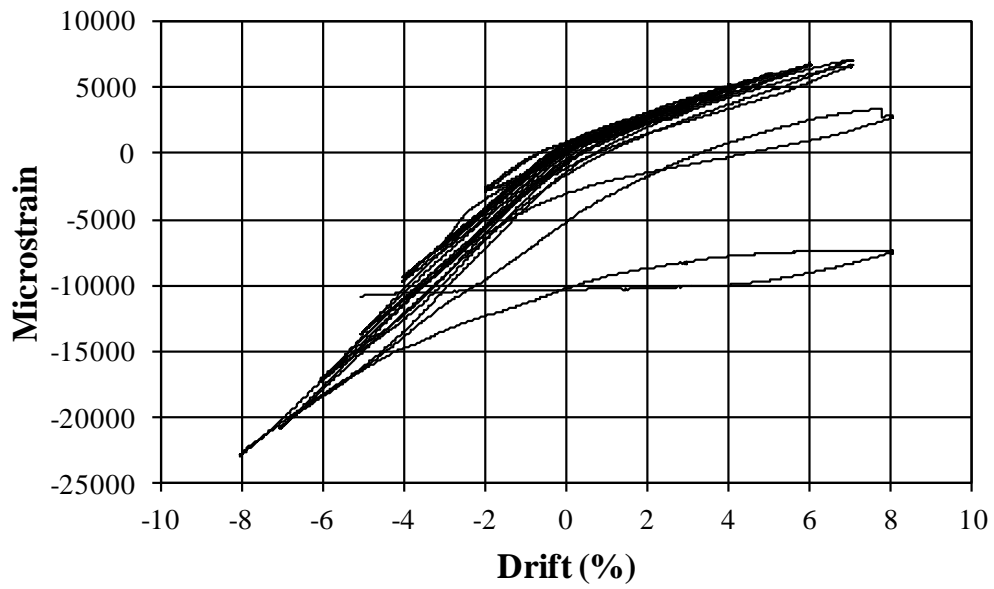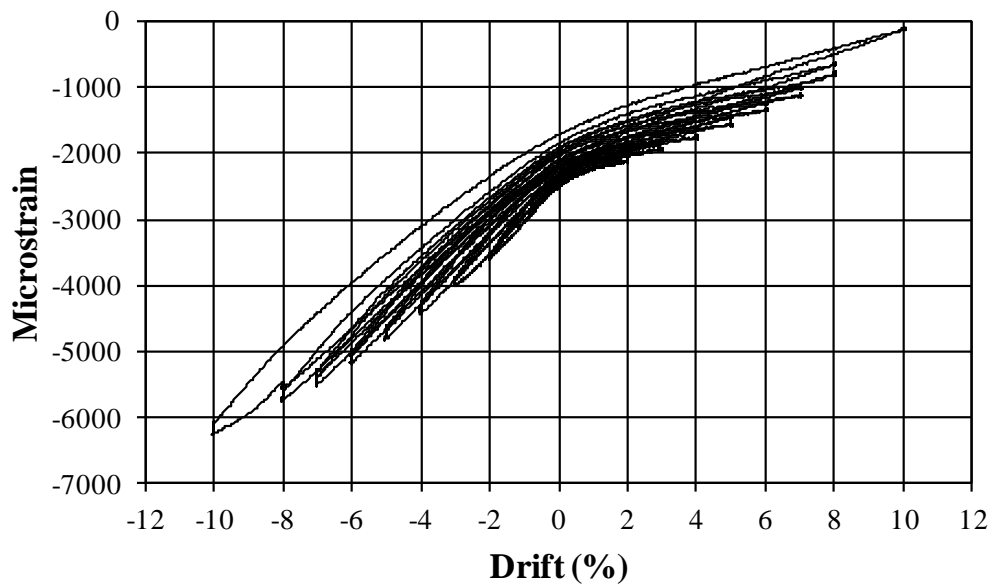

Figure A-80: PT-HL Strain vs. Drift, Strain Gauge PT-13, Tendon 3
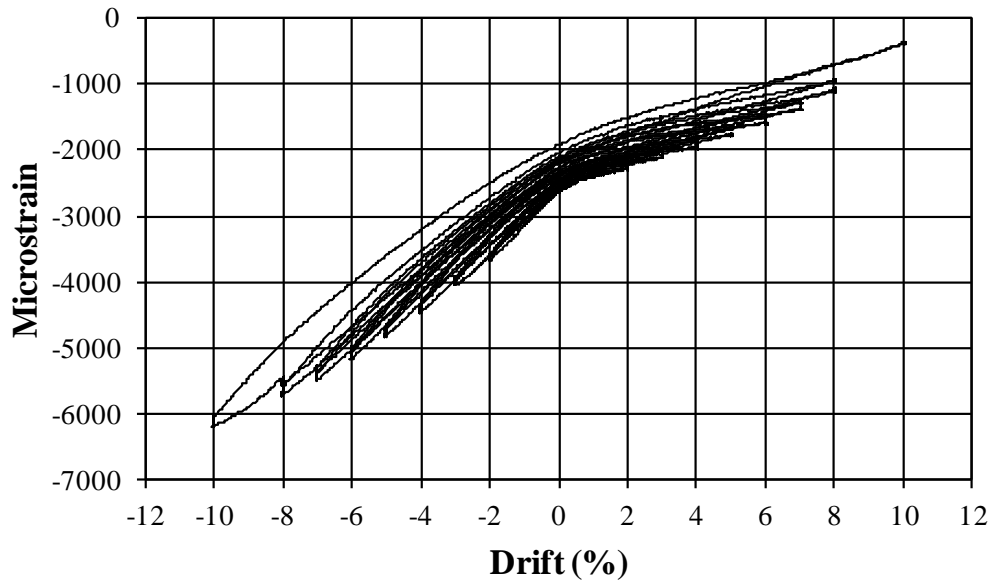
Figure A-81: PT-HL Strain vs. Drift, Strain Gauge PT-14, Tendon 3
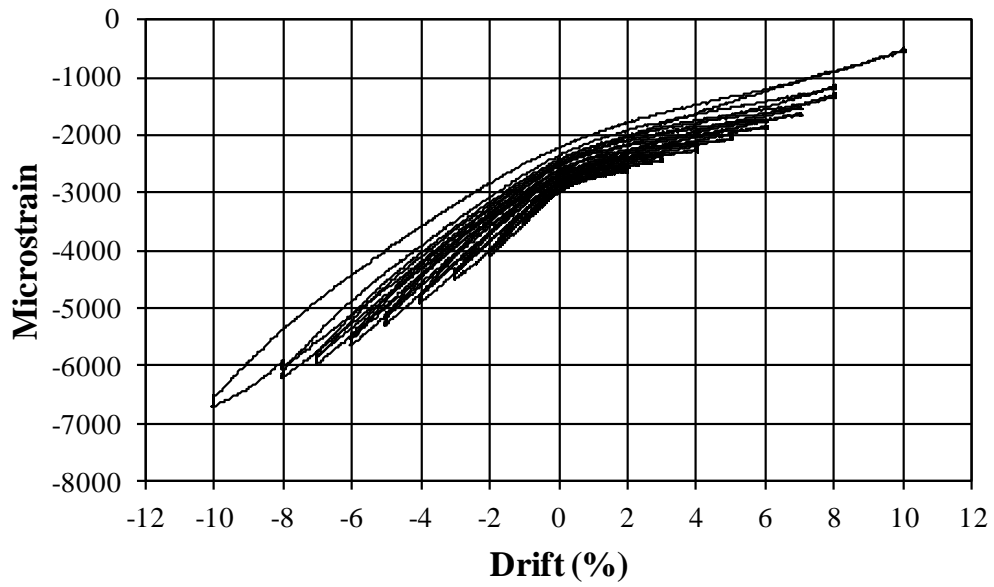
Figure A-82: PT-HL Strain vs. Drift, Strain Gauge PT-15, Tendon 3

223
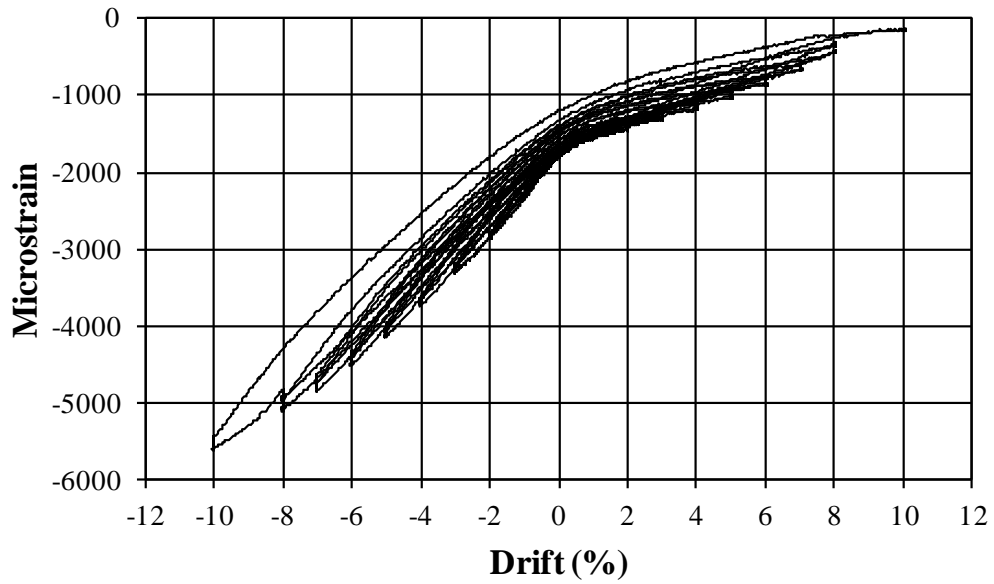
Figure A-83: PT-HL Strain vs. Drift, Strain Gauge PT-16, Tendon 3
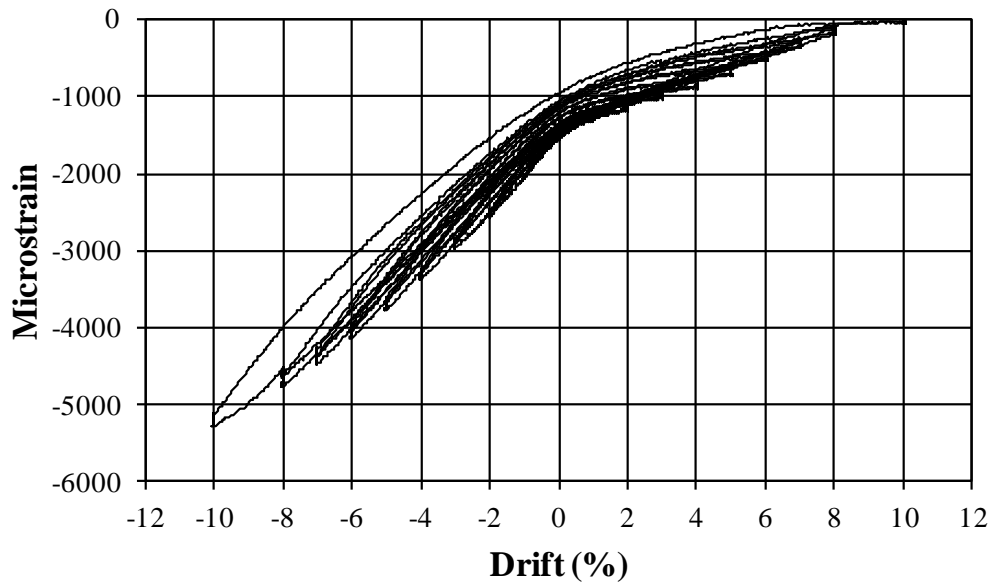
Figure A-84: PT-HL Strain vs. Drift, Strain Gauge PT-17, Tendon 3
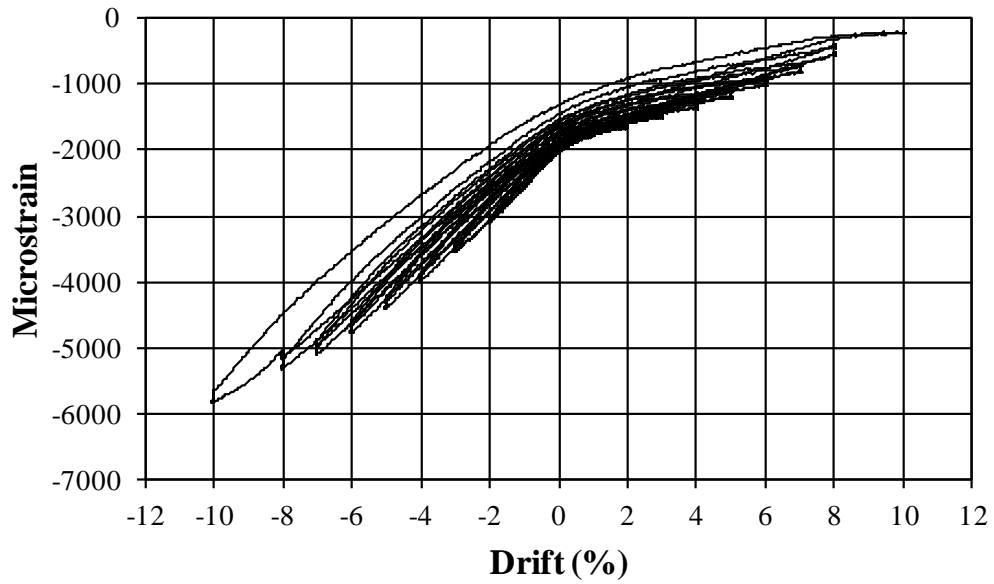
Figure A-85: PT-HL Strain vs. Drift, Strain Gauge PT-18, Tendon 3
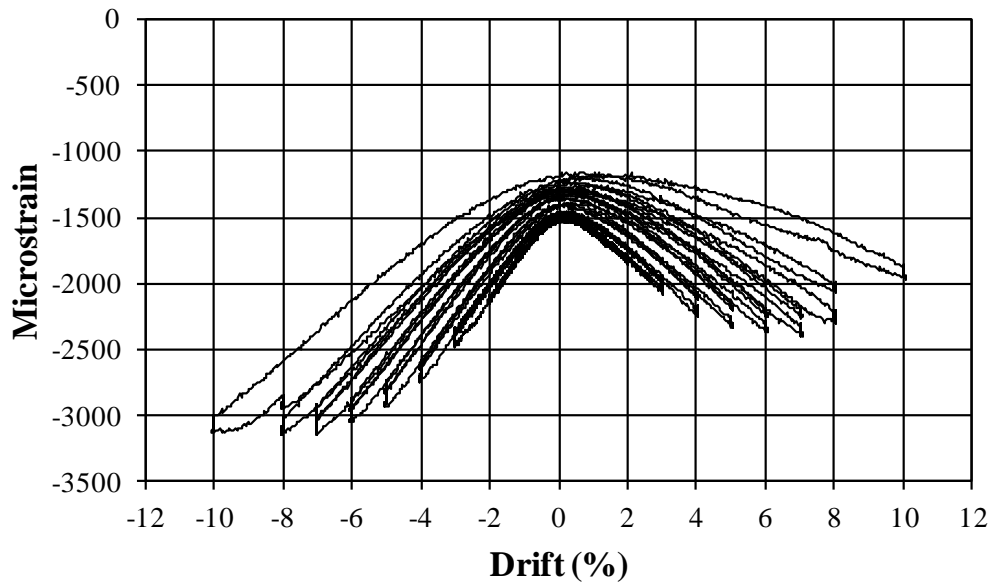
Figure A-86: PT-HL Strain vs. Drift, Strain Gauge PT-20, Tendon 2
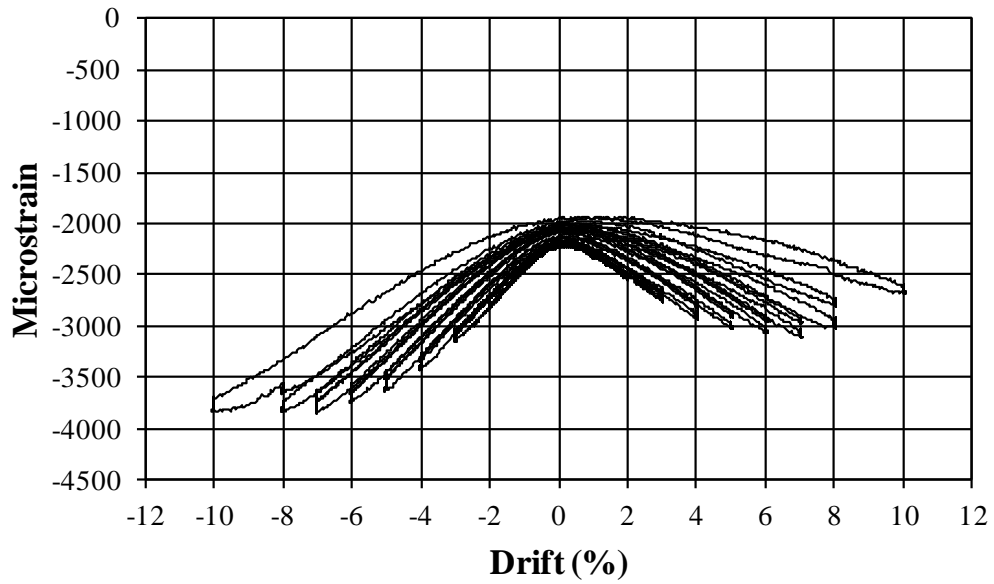
Figure A-87: PT-HL Strain vs. Drift, Strain Gauge PT-21, Tendon 2
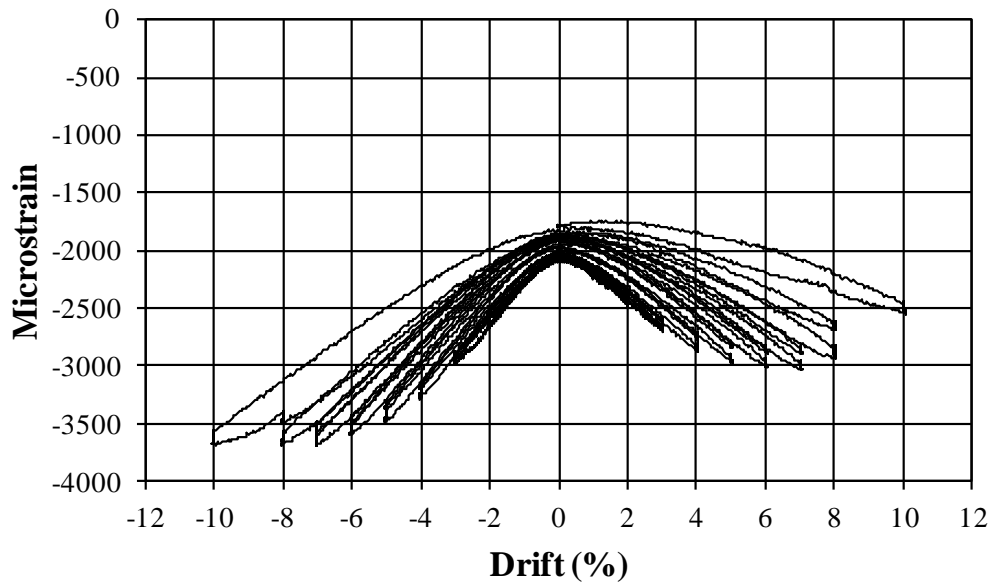
Figure A-88: PT-HL Strain vs. Drift, Strain Gauge PT-22, Tendon 2
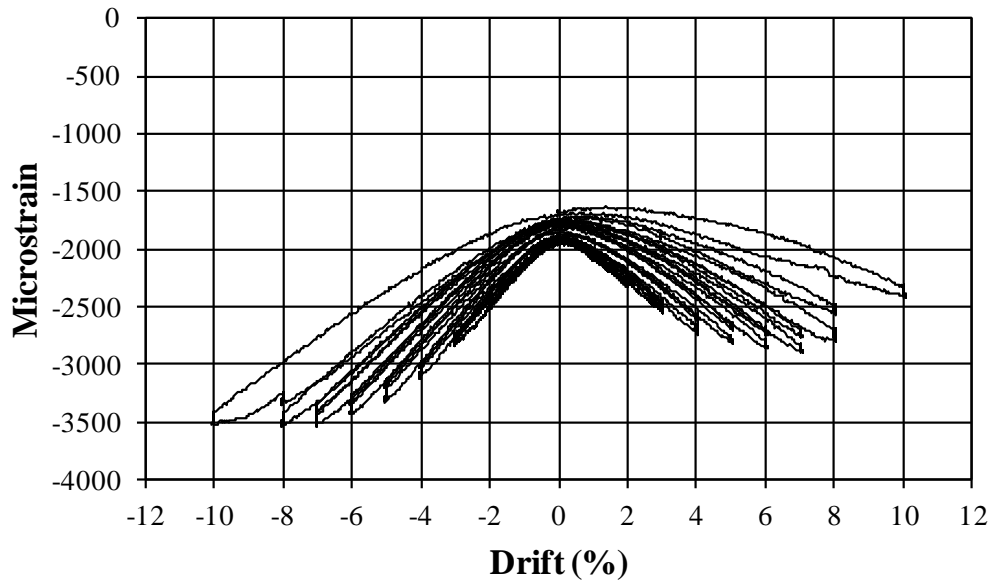
Figure A-89: PT-HL Strain vs. Drift, Strain Gauge PT-23, Tendon 2

LIST OF CCEER PUBLICATIONS

Report No.	Publication

CCEER-84-1   Saiidi, M., and R. Lawver, "User's Manual for LZAK-C64, A Computer Program to Implement the Q-Model on Commodore 64," Civil Engineering Department, Report No. CCEER-84-1, University of Nevada, Reno, January 1984.

CCEER-84-1 Reprint   Douglas, B., Norris, G., Saiidi, M., Dodd, L., Richardson, J. and Reid, W., "Simple Bridge Models for Earthquakes and Test Data," Civil Engineering Department, Report No. CCEER-84-1 Reprint, University of Nevada, Reno, January 1984.

CCEER-84-2   Douglas, B. and T. Iwasaki, "Proceedings of the First USA-Japan Bridge Engineering Workshop," held at the Public Works Research Institute, Tsukuba, Japan, Civil Engineering Department, Report No. CCEER-84-2, University of Nevada, Reno, April 1984.

CCEER-84-3   Saiidi, M., J. Hart, and B. Douglas, "Inelastic Static and Dynamic Analysis of Short R/C Bridges Subjected to Lateral Loads," Civil Engineering Department, Report No. CCEER-84-3, University of Nevada, Reno, July 1984.

CCEER-84-4   Douglas, B., "A Proposed Plan for a National Bridge Engineering Laboratory," Civil Engineering Department, Report No. CCEER-84-4, University of Nevada, Reno, December 1984.

CCEER-85-1   Norris, G. and P. Abdollaholiaee, "Laterally Loaded Pile Response: Studies with the Strain Wedge Model," Civil Engineering Department, Report No. CCEER-85-1, University of Nevada, Reno, April 1985.

CCEER-86-1   Ghusn, G. and M. Saiidi, "A Simple Hysteretic Element for Biaxial Bending of R/C in NEABS-86," Civil Engineering Department, Report No. CCEER-86-1, University of Nevada, Reno, July 1986.

CCEER-86-2   Saiidi, M., R. Lawver, and J. Hart, "User's Manual of ISADAB and SIBA, Computer Programs for Nonlinear Transverse Analysis of Highway Bridges Subjected to Static and Dynamic Lateral Loads," Civil Engineering Department, Report No. CCEER-86-2, University of Nevada, Reno, September 1986.

CCEER-87-1   Siddharthan, R., "Dynamic Effective Stress Response of Surface and Embedded Footings in Sand," Civil Engineering Department, Report No. CCEER-86-2, University of Nevada, Reno, June 1987.

CCEER-87-2   Norris, G. and R. Sack, "Lateral and Rotational Stiffness of Pile Groups for Seismic Analysis of Highway Bridges," Civil Engineering Department, Report No. CCEER-87-2, University of Nevada, Reno, June 1987.

CCEER-88-1   Orie, J. and M. Saiidi, "A Preliminary Study of One-Way Reinforced Concrete Pier Hinges Subjected to Shear and Flexure," Civil Engineering Department, Report No. CCEER-88-1, University of Nevada, Reno, January 1988.

CCEER-88-2   Orie, D., M. Saiidi, and B. Douglas, "A Micro-CAD System for Seismic Design of Regular Highway Bridges," Civil Engineering Department, Report No. CCEER-88-2, University of Nevada, Reno, June 1988.

CCEER-88-3   Orie, D. and M. Saiidi, "User's Manual for Micro-SARB, a Microcomputer Program for Seismic Analysis of Regular Highway Bridges," Civil Engineering Department, Report No. CCEER-88-3, University of Nevada, Reno, October 1988.

CCEER-89-1   Douglas, B., M. Saiidi, R. Hayes, and G. Holcomb, "A Comprehensive Study of the Loads and Pressures Exerted on Wall Forms by the Placement of Concrete," Civil Engineering Department, Report No. CCEER-89-1, University of Nevada, Reno, February 1989.

CCEER-89-2   Richardson, J. and B. Douglas, "Dynamic Response Analysis of the Dominion Road Bridge Test Data," Civil Engineering Department, Report No. CCEER-89-2, University of Nevada, Reno, March 1989.

CCEER-89-2   Vrontinos, S., M. Saiidi, and B. Douglas, "A Simple Model to Predict the Ultimate Response of R/C Beams with Concrete Overlays," Civil Engineering Department, Report NO. CCEER-89-2, University of Nevada, Reno, June 1989.

CCEER-89-3   Ebrahimpour, A. and P. Jagadish, "Statistical Modeling of Bridge Traffic Loads - A Case Study," Civil Engineering Department, Report No. CCEER-89-3, University of Nevada, Reno, December 1989.

CCEER-89-4   Shields, J. and M. Saiidi, "Direct Field Measurement of Prestress Losses in Box Girder Bridges," Civil Engineering Department, Report No. CCEER-89-4, University of Nevada, Reno, December 1989.

CCEER-90-1   Saiidi, M., E. Maragakis, G. Ghusn, Y. Jiang, and D. Schwartz, "Survey and Evaluation of Nevada's Transportation Infrastructure, Task 7.2 - Highway Bridges, Final Report," Civil Engineering Department, Report No. CCEER 90-1, University of Nevada, Reno, October 1990.

CCEER-90-2   Abdel-Ghaffar, S., E. Maragakis, and M. Saiidi, "Analysis of the Response of Reinforced Concrete Structures During the Whittier Earthquake 1987," Civil Engineering Department, Report No. CCEER 90-2, University of Nevada, Reno, October 1990.

CCEER-91-1   Saiidi, M., E. Hwang, E. Maragakis, and B. Douglas, "Dynamic Testing and the Analysis of the Flamingo Road Interchange," Civil Engineering Department, Report No. CCEER-91-1, University of Nevada, Reno, February 1991.

CCEER-91-2   Norris, G., R. Siddharthan, Z. Zafir, S. Abdel-Ghaffar, and P. Gowda, "Soil-Foundation-Structure Behavior at the Oakland Outer Harbor Wharf," Civil Engineering Department, Report No. CCEER-91-2, University of Nevada, Reno, July 1991.

CCEER-91-3   Norris, G., "Seismic Lateral and Rotational Pile Foundation Stiffnesses at Cypress," Civil Engineering Department, Report No. CCEER-91-3, University of Nevada, Reno, August 1991.

CCEER-91-4   O'Connor, D. and M. Saiidi, "A Study of Protective Overlays for Highway Bridge Decks in Nevada, with Emphasis on Polyester-Styrene Polymer Concrete," Civil Engineering Department, Report No. CCEER-91-4, University of Nevada, Reno, October 1991.

CCEER-91-5   O'Connor, D.N. and M. Saiidi, "Laboratory Studies of Polyester-Styrene Polymer Concrete Engineering Properties," Civil Engineering Department, Report No. CCEER-91-5, University of Nevada, Reno, November 1991.

CCEER-92-1   Straw, D.L. and M. Saiidi, "Scale Model Testing of One-Way Reinforced Concrete Pier Hinges Subject to Combined Axial Force, Shear and Flexure," edited by D.N. O'Connor, Civil Engineering Department, Report No. CCEER-92-1, University of Nevada, Reno, March 1992.

CCEER-92-2   Wehbe, N., M. Saiidi, and F. Gordaninejad, "Basic Behavior of Composite Sections Made of Concrete Slabs and Graphite Epoxy Beams," Civil Engineering Department, Report No. CCEER-92-2, University of Nevada, Reno, August 1992.

CCEER-92-3   Saiidi, M. and E. Hutchens, "A Study of Prestress Changes in A Post-Tensioned Bridge During the First 30 Months," Civil Engineering Department, Report No. CCEER-92-3, University of Nevada, Reno, April 1992.

CCEER-92-4   Saiidi, M., B. Douglas, S. Feng, E. Hwang, and E. Maragakis, "Effects of Axial Force on Frequency of Prestressed Concrete Bridges," Civil Engineering Department, Report No. CCEER-92-4, University of Nevada, Reno, August 1992.

CCEER-92-5   Siddharthan, R., and Z. Zafir, "Response of Layered Deposits to Traveling Surface Pressure Waves," Civil Engineering Department, Report No. CCEER-92-5, University of Nevada, Reno, September 1992.

CCEER-92-6   Norris, G., and Z. Zafir, "Liquefaction and Residual Strength of Loose Sands from Drained Triaxial Tests," Civil Engineering Department, Report No. CCEER-92-6, University of Nevada, Reno, September 1992.

CCEER-92-6-A Norris, G., Siddharthan, R., Zafir, Z. and Madhu, R. "Liquefaction and Residual Strength of Sands from Drained Triaxial Tests," Civil Engineering Department, Report No. CCEER-92-6-A, University of Nevada, Reno, September 1992.

CCEER-92-7   Douglas, B., "Some Thoughts Regarding the Improvement of the University of Nevada, Reno's National Academic Standing," Civil Engineering Department, Report No. CCEER-92-7, University of Nevada, Reno, September 1992.

CCEER-92-8   Saiidi, M., E. Maragakis, and S. Feng, "An Evaluation of the Current Caltrans Seismic Restrainer Design Method," Civil Engineering Department, Report No. CCEER-92-8, University of Nevada, Reno, October 1992.

CCEER-92-9   O'Connor, D., M. Saiidi, and E. Maragakis, "Effect of Hinge Restrainers on the Response of the Madrone Drive Undercrossing During the Loma Prieta Earthquake," Civil Engineering Department, Report No. CCEER-92-9, University of Nevada, Reno, February 1993.

CCEER-92-10   O'Connor, D., and M. Saiidi, "Laboratory Studies of Polyester Concrete: Compressive Strength at Elevated Temperatures and Following Temperature Cycling, Bond Strength to Portland Cement Concrete, and Modulus of Elasticity," Civil Engineering Department, Report No. CCEER-92-10, University of Nevada, Reno, February 1993.

CCEER-92-11   Wehbe, N., M. Saiidi, and D. O'Connor, "Economic Impact of Passage of Spent Fuel Traffic on Two Bridges in Northeast Nevada," Civil Engineering Department, Report No. CCEER-92-11, University of Nevada, Reno, December 1992.

CCEER-93-1   Jiang, Y., and M. Saiidi, "Behavior, Design, and Retrofit of Reinforced Concrete One-way Bridge Column Hinges," edited by D. O'Connor, Civil Engineering Department, Report No. CCEER-93-1, University of Nevada, Reno, March 1993.

230

CCEER-93-2   Abdel-Ghaffar, S., E. Maragakis, and M. Saiidi, "Evaluation of the Response of the Aptos Creek Bridge During the 1989 Loma Prieta Earthquake," Civil Engineering Department, Report No. CCEER-93-2, University of Nevada, Reno, June 1993.

CCEER-93-3   Sanders, D.H., B.M. Douglas, and T.L. Martin, "Seismic Retrofit Prioritization of Nevada Bridges," Civil Engineering Department, Report No. CCEER-93-3, University of Nevada, Reno, July 1993.

CCEER-93-4   Abdel-Ghaffar, S., E. Maragakis, and M. Saiidi, "Performance of Hinge Restrainers in the Huntington Avenue Overhead During the 1989 Loma Prieta Earthquake," Civil Engineering Department, Report No. CCEER-93-4, University of Nevada, Reno, June 1993 (in final preparation).

CCEER-93-5   Maragakis, E., M. Saiidi, S. Feng, and L. Flournoy, "Effects of Hinge Restrainers on the Response of the San Gregorio Bridge during the Loma Prieta Earthquake," (in final preparation) Civil Engineering Department, Report No. CCEER-93-5, University of Nevada, Reno.

CCEER-93-6   Saiidi, M., E. Maragakis, S. Abdel-Ghaffar, S. Feng, and D. O'Connor, "Response of Bridge Hinge Restrainers during Earthquakes -Field Performance, Analysis, and Design," Civil Engineering Department, Report No. CCEER-93-6, University of Nevada, Reno, May 1993.

CCEER-93-7   Wehbe, N., Saiidi, M., Maragakis, E., and Sanders, D., "Adequacy of Three Highway Structures in Southern Nevada for Spent Fuel Transportation," Civil Engineering Department, Report No. CCEER-93-7, University of Nevada, Reno, August 1993.

CCEER-93-8   Roybal, J., Sanders, D.H., and Maragakis, E., "Vulnerability Assessment of Masonry in the Reno-Carson City Urban Corridor," Civil Engineering Department, Report No. CCEER-93-8, University of Nevada, Reno, May 1993.

CCEER-93-9   Zafir, Z. and Siddharthan, R., "MOVLOAD: A Program to Determine the Behavior of Nonlinear Horizontally Layered Medium Under Moving Load," Civil Engineering Department, Report No. CCEER-93-9, University of Nevada, Reno, August 1993.

CCEER-93-10   O'Connor, D.N., Saiidi, M., and Maragakis, E.A., "A Study of Bridge Column Seismic Damage Susceptibility at the Interstate 80/U.S. 395 Interchange in Reno, Nevada," Civil Engineering Department, Report No. CCEER-93-10, University of Nevada, Reno, October 1993.

CCEER-94-1   Maragakis, E., B. Douglas, and E. Abdelwahed, "Preliminary Dynamic Analysis of a Railroad Bridge," Report CCEER-94-1, January 1994.

CCEER-94-2   Douglas, B.M., Maragakis, E.A., and Feng, S., "Stiffness Evaluation of Pile Foundation of Cazenovia Creek Overpass," Civil Engineering Department, Report No. CCEER-94-2, University of Nevada, Reno, March 1994.

CCEER-94-3   Douglas, B.M., Maragakis, E.A., and Feng, S., "Summary of Pretest Analysis of Cazenovia Creek Bridge," Civil Engineering Department, Report No. CCEER-94-3, University of Nevada, Reno, April 1994.

CCEER-94-4   Norris, G.M., Madhu, R., Valceschini, R., and Ashour, M., "Liquefaction and Residual Strength of Loose Sands from Drained Triaxial Tests," Report 2, Vol. 1&2, Civil Engineering Department, Report No. CCEER-94-4, University of Nevada, Reno, August 1994.

CCEER-94-5   Saiidi, M., Hutchens, E., and Gardella, D., "Prestress Losses in a Post-Tensioned R/C Box Girder Bridge in Southern Nevada," Civil Engineering Department, CCEER-94-5, University of Nevada, Reno, August 1994.

CCEER-95-1   Siddharthan, R., El-Gamal, M., and Maragakis, E.A., "Nonlinear Bridge Abutment , Verification, and Design Curves," Civil Engineering Department, CCEER-95-1, University of Nevada, Reno, January 1995.

CCEER-95-2   Ashour, M. and Norris, G., "Liquefaction and Undrained Response Evaluation of Sands from Drained Formulation," Civil Engineering Department, Report No. CCEER-95-2, University of Nevada, Reno, February 1995.

CCEER-95-3   Wehbe, N., Saiidi, M., Sanders, D. and Douglas, B., "Ductility of Rectangular Reinforced Concrete Bridge Columns with Moderate Confinement," Civil Engineering Department, Report No. CCEER-95-3, University of Nevada, Reno, July 1995.

CCEER-95-4   Martin, T.., Saiidi, M. and Sanders, D., "Seismic Retrofit of Column-Pier Cap Connections in Bridges in Northern Nevada," Civil Engineering Department, Report No. CCEER-95-4, University of Nevada, Reno, August 1995.

CCEER-95-5   Darwish, I., Saiidi, M. and Sanders, D., "Experimental Study of Seismic Susceptibility Column-Footing Connections in Bridges in Northern Nevada," Civil Engineering Department, Report No. CCEER-95-5, University of Nevada, Reno, September 1995.

CCEER-95-6   Griffin, G., Saiidi, M. and Maragakis, E., "Nonlinear Seismic Response of Isolated Bridges and Effects of Pier Ductility Demand," Civil Engineering Department, Report No. CCEER-95-6, University of Nevada, Reno, November 1995.

CCEER-95-7   Acharya, S.., Saiidi, M. and Sanders, D., "Seismic Retrofit of Bridge Footings and Column-Footing Connections," Civil Engineering Department, Report No. CCEER-95-7, University of Nevada, Reno, November 1995.

CCEER-95-8   Maragakis, E., Douglas, B., and Sandirasegaram, U., "Full-Scale Field Resonance Tests of a Railway Bridge," A Report to the Association of American Railroads, Civil Engineering Department, Report No. CCEER-95-8, University of Nevada, Reno, December 1995.

CCEER-95-9   Douglas, B., Maragakis, E. and Feng, S., "System Identification Studies on Cazenovia Creek Overpass," Report for the National Center for Earthquake Engineering Research, Civil Engineering Department, Report No. CCEER-95-9, University of Nevada, Reno, October 1995.

CCEER-96-1   El-Gamal, M.E. and Siddharthan, R.V., "Programs to Computer Translational Stiffness of Seat-Type Bridge Abutment," Civil Engineering Department, Report No. CCEER-96-1, University of Nevada, Reno, March 1996.

CCEER-96-2   Labia, Y., Saiidi, M. and Douglas, B., "Evaluation and Repair of Full-Scale Prestressed Concrete Box Girders," A Report to the National Science Foundation, Research Grant CMS-9201908, Civil Engineering Department, Report No. CCEER-96-2, University of Nevada, Reno, May 1996.

CCEER-96-3   Darwish, I., Saiidi, M. and Sanders, D., "Seismic Retrofit of R/C Oblong Tapered Bridge Columns with Inadequate Bar Anchorage in Columns and Footings," A Report to the Nevada Department of Transportation, Civil Engineering Department, Report No. CCEER-96-3, University of Nevada, Reno, May 1996.

232

CCEER-96-4   Ashour, M., Pilling, R., Norris, G. and Perez, H., "The Prediction of Lateral Load Behavior of Single Piles and Pile Groups Using the Strain Wedge Model," A Report to the California Department of Transportation, Civil Engineering Department, Report No. CCEER-96-4, University of Nevada, Reno, June 1996.

CCEER-97-1-A   Rimal, P. and Itani, A.   "Sensitivity Analysis of Fatigue Evaluations of Steel Bridges," Center for Earthquake Research, Department of Civil Engineering, University of Nevada, Reno, Nevada Report No. CCEER-97-1-A, September, 1997.

CCEER-97-1-B   Maragakis, E., Douglas, B., and Sandirasegaram, U. "Full-Scale Field Resonance Tests of a Railway Bridge," A Report to the Association of American Railroads, Civil Engineering Department, University of Nevada, Reno, May, 1996.

CCEER-97-2   Wehbe, N., Saiidi, M., and D. Sanders, "Effect of Confinement and Flares on the Seismic Performance of Reinforced Concrete Bridge Columns," Civil Engineering Department, Report No. CCEER-97-2, University of Nevada, Reno, September 1997.

CCEER-97-3   Darwish, I., M. Saiidi, G. Norris, and E. Maragakis, "Determination of In-Situ Footing Stiffness Using Full-Scale Dynamic Field Testing," A Report to the Nevada Department of Transportation, Structural Design Division, Carson City, Nevada, Report No. CCEER-97-3, University of Nevada, Reno, October 1997.

CCEER-97-4-A   Itani, A. "Cyclic Behavior of Richmond-San Rafael Tower Links," Center for Civil Engineering Earthquake Research, Department of Civil Engineering, University of Nevada, Reno, Nevada, Report No. CCEER-97-4, August 1997.

CCEER-97-4-B   Wehbe, N., and M. Saiidi, "User's Manual for RCMC v. 1.2 : A Computer Program for Moment-Curvature Analysis of Confined and Unconfined Reinforced Concrete Sections," Center for Civil Engineering Earthquake Research, Department of Civil Engineering, University of Nevada, Reno, Nevada, Report No. CCEER-97-4, November, 1997.

CCEER-97-5   Isakovic, T., M. Saiidi, and A. Itani, "Influence of new Bridge Configurations on Seismic Performance," Department of Civil Engineering, University of Nevada, Reno, Report No. CCEER-97-5, September, 1997.

CCEER-98-1   Itani, A., Vesco, T. and Dietrich, A., "Cyclic Behavior of "as Built" Laced Members With End Gusset Plates on the San Francisco Bay Bridge," Center for Civil Engineering Earthquake Research, Department of Civil Engineering, University of Nevada, Reno, Nevada Report No. CCEER-98-1, March, 1998.

CCEER-98-2   G. Norris and M. Ashour, "Liquefaction and Undrained Response Evaluation of Sands from Drained Formulation," Center for Civil Engineering Earthquake Research, Department of Civil Engineering, University of Nevada, Reno, Nevada, Report No. CCEER-98-2, May, 1998.

CCEER-98-3   Qingbin, Chen, B. M. Douglas, E. Maragakis, and I. G. Buckle, "Extraction of Nonlinear Hysteretic Properties of Seismically Isolated Bridges from Quick-Release Field Tests," Center for Civil Engineering Earthquake Research, Department of Civil Engineering, University of Nevada, Reno, Nevada, Report No. CCEER-98-3, June, 1998.

CCEER-98-4   Maragakis, E., B. M. Douglas, and C. Qingbin, "Full-Scale Field Capacity Tests of a Railway Bridge," Center for Civil Engineering Earthquake Research, Department of Civil Engineering, University of Nevada, Reno, Nevada, Report No. CCEER-98-4, June, 1998.

CCEER-98-5   Itani, A., Douglas, B., and Woodgate, J., "Cyclic Behavior of Richmond-San Rafael Retrofitted Tower Leg," Center for Civil Engineering Earthquake Research, Department of Civil Engineering, University of Nevada, Reno. Report No. CCEER-98-5, June 1998

CCEER-98-6   Moore, R., Saiidi, M., and Itani, A., "Seismic Behavior of New Bridges with Skew and Curvature," Center for Civil Engineering Earthquake Research, Department of Civil Engineering, University of Nevada, Reno. Report No. CCEER-98-6, October, 1998.

CCEER-98-7   Itani, A and Dietrich, A, "Cyclic Behavior of Double Gusset Plate Connections," Center for Civil Engineering Earthquake Research, Department of Civil Engineering, University of Nevada, Reno, Nevada, Report No. CCEER-98-5, December, 1998.

CCEER-99-1   Caywood, C., M. Saiidi, and D. Sanders, "Seismic Retrofit of Flared Bridge Columns with Steel Jackets," Civil Engineering Department, University of Nevada, Reno, Report No. CCEER-99-1, February 1999.

CCEER-99-2   Mangoba, N., M. Mayberry, and M. Saiidi, "Prestress Loss in Four Box Girder Bridges in Northern Nevada," Civil Engineering Department, University of Nevada, Reno, Report No. CCEER-99-2, March 1999.

CCEER-99-3   Abo-Shadi, N., M. Saiidi, and D. Sanders, "Seismic Response of Bridge Pier Walls in the Weak Direction," Civil Engineering Department, University of Nevada, Reno, Report No. CCEER-99-3, April 1999.

CCEER-99-4   Buzick, A., and M. Saiidi, "Shear Strength and Shear Fatigue Behavior of Full-Scale Prestressed Concrete Box Girders," Civil Engineering Department, University of Nevada, Reno, Report No. CCEER-99-4, April 1999.

CCEER-99-5   Randall, M., M. Saiidi, E. Maragakis and T. Isakovic, "Restrainer Design Procedures For Multi-Span Simply-Supported Bridges," Civil Engineering Department, University of Nevada, Reno, Report No. CCEER-99-5, April 1999.

CCEER-99-6   Wehbe, N. and M. Saiidi, "User's Manual for RCMC v. 1.2, A Computer Program for Moment-Curvature Analysis of Confined and Unconfined Reinforced Concrete Sections," Civil Engineering Department, University of Nevada, Reno, Report No. CCEER-99-6, May 1999.

CCEER-99-7   Burda, J. and A. Itani, "Studies of Seismic Behavior of Steel Base Plates," Civil Engineering Department, University of Nevada, Reno, Report No. CCEER-99-7, May 1999.

CCEER-99-8   Ashour, M. and G. Norris, "Refinement of the Strain Wedge Model Program," Civil Engineering Department, University of Nevada, Reno, Report No. CCEER-99-8, March 1999.

CCEER-99-9   Dietrich, A., and A. Itani, "Cyclic Behavior of Laced and Perforated Steel Members on the San Francisco-Oakland Bay Bridge," Civil Engineering Department, University, Reno, Report No. CCEER-99-9, December 1999.

CCEER 99-10   Itani, A., A. Dietrich, "Cyclic Behavior of Built Up Steel Members and their Connections," Civil Engineering Department, University of Nevada, Reno, Report No. CCEER-99-10, December 1999.

CCEER 99-10-A Itani, A., E. Maragakis and P. He, "Fatigue Behavior of Riveted Open Deck Railroad Bridge Girders," Civil Engineering Department, University of Nevada, Reno, Report No. CCEER-99-10-A, August 1999.

234

CCEER 99-11   Itani, A., J. Woodgate, "Axial and Rotational Ductility of Built Up Structural Steel Members," Civil Engineering Department, University of Nevada, Reno, Report No. CCEER-99-11, December 1999.

CCEER-99-12   Sgambelluri, M., Sanders, D.H., and Saiidi, M.S., "Behavior of One-Way Reinforced Concrete Bridge Column Hinges in the Weak Direction," Department of Civil Engineering, University of Nevada, Reno, Report No. CCEER-99-12, December 1999.

CCEER-99-13   Laplace, P., Sanders, D.H., Douglas, B, and Saiidi, M, "Shake Table Testing of Flexure Dominated Reinforced Concrete Bridge Columns", Department of Civil Engineering, University of Nevada, Reno, Report No. CCEER-99-13, December 1999.

CCEER-99-14   Ahmad M. Itani, Jose A. Zepeda, and Elizabeth A. Ware "Cyclic Behavior of Steel Moment Frame Connections for the Moscone Center Expansion," Department of Civil Engineering, University of Nevada, Reno, Report No. CCEER-99-14, December 1999.

CCEER 00-1   Ashour, M., and Norris, G. "Undrained Lateral Pile and Pile Group Response in Saturated Sand," Civil Engineering Department, University of Nevada, Reno, Report No. CCEER-00-1, May 1999. January 2000.

CCEER 00-2   Saiidi, M. and Wehbe, N., "A Comparison of Confinement Requirements in Different Codes for Rectangular, Circular, and Double-Spiral RC Bridge Columns," Civil Engineering Department, University of Nevada, Reno, Report No. CCEER-00-2, January 2000.

CCEER 00-3   McElhaney, B., M. Saiidi, and D. Sanders, "Shake Table Testing of Flared Bridge Columns With Steel Jacket Retrofit," Civil Engineering Department, University of Nevada, Reno, Report No. CCEER-00-3, January 2000.

CCEER 00-4   Martinovic, F., M. Saiidi, D. Sanders, and F. Gordaninejad, "Dynamic Testing of Non-Prismatic Reinforced Concrete Bridge Columns Retrofitted with FRP Jackets," Civil Engineering Department, University of Nevada, Reno, Report No. CCEER-00-4, January 2000.

CCEER 00-5   Itani, A., and M. Saiidi, "Seismic Evaluation of Steel Joints for UCLA Center for Health Science Westwood Replacement Hospital," Civil Engineering Department, University of Nevada, Reno, Report No. CCEER-00-5, February 2000.

CCEER 00-6   Will, J. and D. Sanders, "High Performance Concrete Using Nevada Aggregates," Civil Engineering Department, University of Nevada, Reno, Report No. CCEER-00-6, May 2000.

CCEER 00-7   French, C., and M. Saiidi, "A Comparison of Static and Dynamic Performance of Models of Flared Bridge Columns," Civil Engineering Department, University of Nevada, Reno, Report No. CCEER-00-7, October 2000.

CCEER 00-8   Itani, A., H. Sedarat, "Seismic Analysis of the AISI LRFD Design Example of Steel Highway Bridges," Civil Engineering Department, University of Nevada, Reno, Report No. CCEER 00-08, November 2000.

CCEER 00-9   Moore, J., D. Sanders, and M. Saiidi, "Shake Table Testing of 1960's Two Column Bent with Hinges Bases," Civil Engineering Department, University of Nevada, Reno, Report No. CCEER 00-09, December 2000.

CCEER 00-10   Asthana, M., D. Sanders, and M. Saiidi, "One-Way Reinforced Concrete Bridge Column Hinges in the Weak Direction," Civil Engineering Department, University of Nevada, Reno, Report No. CCEER 00-10, April 2001.

CCEER 01-1   Ah Sha, H., D. Sanders, M. Saiidi, "Early Age Shrinkage and Cracking of Nevada Concrete Bridge Decks," Civil Engineering Department, University of Nevada, Reno, Report No. CCEER 01-01, May 2001.

CCEER 01-2   Ashour, M. and G. Norris, "Pile Group program for Full Material Modeling a Progressive Failure," Civil Engineering Department, University of Nevada, Reno, Report No. CCEER 01-02, July 2001.

CCEER 01-3   Itani, A., C. Lanaud, and P. Dusicka, "Non-Linear Finite Element Analysis of Built-Up Shear Links," Civil Engineering Department, University of Nevada, Reno, Report No. CCEER 01-03, July 2001.

CCEER 01-4   Saiidi, M., J. Mortensen, and F. Martinovic, "Analysis and Retrofit of Fixed Flared Columns with Glass Fiber-Reinforced Plastic Jacketing," Civil Engineering Department, University of Nevada, Reno, Report No. CCEER 01-4, August 2001

CCEER 01-5   Not Published

CCEER 01-6   Laplace, P., D. Sanders, and M. Saiidi, "Experimental Study and Analysis of Retrofitted Flexure and Shear Dominated Circular Reinforced Concrete Bridge Columns Subjected to Shake Table Excitation," Civil Engineering Department, University of Nevada, Reno, Report No. CCEER 01-6, June 2001.

CCEER 01-7   Reppi, F., and D. Sanders, "Removal and Replacement of Cast-in-Place, Post-tensioned, Box Girder Bridge," Civil Engineering Department, University of Nevada, Reno, Report No. CCEER 01-7, December 2001.

CCEER 02-1   Pulido, C., M. Saiidi, D. Sanders, and A. Itani, "Seismic Performance and Retrofitting of Reinforced Concrete Bridge Bents," Civil Engineering Department, University of Nevada, Reno, Report No. CCEER 02-1, January 2002.

CCEER 02-2   Yang, Q., M. Saiidi, H. Wang, and A. Itani, "Influence of Ground Motion Incoherency on Earthquake Response of Multi-Support Structures," Civil Engineering Department, University of Nevada, Reno, Report No. CCEER 02-2, May 2002.

CCEER 02-3   M. Saiidi, B. Gopalakrishnan, E. Reinhardt, and R. Siddharthan, "A Preliminary Study of Shake Table Response of A Two-Column Bridge Bent on Flexible Footings," Civil Engineering Department, University of Nevada, Reno, Report No. CCEER 02-03, June 2002.

CCEER 02-4   Not Published

CCEER 02-5   Banghart, A., Sanders, D., Saiidi, M., "Evaluation of Concrete Mixes for Filling the Steel Arches in the Galena Creek Bridge," Civil Engineering Department, University of Nevada, Reno, Report No. CCEER 02-05, June 2002.

CCEER 02-6   Dusicka, P., Itani, A., Buckle, I. G., "Cyclic Behavior of Shear Links and Tower Shaft Assembly of San Francisco – Oakland Bay Bridge Tower," Civil Engineering Department, University of Nevada, Reno, Report No. CCEER 02-06, July 2002.

CCEER 02-7   Mortensen, J., and M. Saiidi, "A Performance-Based Design Method for Confinement in Circular Columns," Civil Engineering Department, University of Nevada, Reno, Report No. CCEER 02-07, November 2002.

CCEER 03-1   Wehbe, N., and M. Saiidi, "User's manual for SPMC v. 1.0 : A Computer Program for Moment-Curvature Analysis of Reinforced Concrete Sections with Interlocking Spirals," Center for Civil Engineering Earthquake Research, Department of Civil Engineering, University of Nevada, Reno, Nevada, Report No. CCEER-03-1, May, 2003.

CCEER 03-2   Wehbe, N., and M. Saiidi, "User's manual for RCMC v. 2.0 : A Computer Program for Moment-Curvature Analysis of Confined and Unconfined Reinforced Concrete Sections," Center for Civil Engineering Earthquake Research, Department of Civil Engineering, University of Nevada, Reno, Nevada, Report No. CCEER-03-2, June, 2003.

CCEER 03-3   Nada, H., D. Sanders, and M. Saiidi, "Seismic Performance of RC Bridge Frames with Architectural-Flared Columns," Civil Engineering Department, University of Nevada, Reno, Report No. CCEER 03-3, January 2003.

CCEER 03-4   Reinhardt, E., M. Saiidi, and R. Siddharthan, "Seismic Performance of a CFRP/ Concrete Bridge Bent on Flexible Footings," Civil Engineering Department, University of Nevada, Reno, Report No. CCEER 03-4, August 2003.

CCEER 03-5   Johnson, N., M. Saiidi, A. Itani, and S. Ladkany, "Seismic Retrofit of Octagonal Columns with Pedestal and One-Way Hinge at the Base," Center for Civil Engineering Earthquake Research, Department of Civil Engineering, University of Nevada, Reno, Nevada, and Report No. CCEER-03-5, August 2003.

CCEER 03-6   Mortensen, C., M. Saiidi, and S. Ladkany, "Creep and Shrinkage Losses in Highly Variable Climates," Center for Civil Engineering Earthquake Research, Department of Civil Engineering, University of Nevada, Reno, Report No. CCEER-03-6, September 2003.

CCEER 03- 7   Ayoub, C., M. Saiidi, and A. Itani, "A Study of Shape-Memory-Alloy-Reinforced Beams and Cubes," Center for Civil Engineering Earthquake Research, Department of Civil Engineering, University of Nevada, Reno, Nevada, Report No. CCEER-03-7, October 2003.

CCEER 03-8   Chandane, S., D. Sanders, and M. Saiidi, "Static and Dynamic Performance of RC Bridge Bents with Architectural-Flared Columns," Center for Civil Engineering Earthquake Research, Department of Civil Engineering, University of Nevada, Reno, Nevada, Report No. CCEER-03-8, November 2003.

CCEER 04-1   Olaegbe, C., and Saiidi, M., "Effect of Loading History on Shake Table Performance of A Two-Column Bent with Infill Wall," Center for Civil Engineering Earthquake Research, Department of Civil Engineering, University of Nevada, Reno, Nevada, Report No. CCEER-04-1, January 2004.

CCEER 04-2   Johnson, R., Maragakis, E., Saiidi, M., and DesRoches, R., "Experimental Evaluation of Seismic Performance of SMA Bridge Restrainers," Center for Civil Engineering Earthquake Research, Department of Civil Engineering, University of Nevada, Reno, Nevada, Report No. CCEER-04-2, February 2004.

CCEER 04-3   Moustafa, K., Sanders, D., and Saiidi, M., "Impact of Aspect Ratio on Two-Column Bent Seismic Performance," Center for Civil Engineering Earthquake Research, Department of Civil Engineering, University of Nevada, Reno, Nevada, Report No. CCEER-04-3, February 2004.

CCEER 04-4   Maragakis, E., Saiidi, M., Sanchez-Camargo, F., and Elfass, S., "Seismic Performance of Bridge Restrainers At In-Span Hinges," Center for Civil Engineering Earthquake Research, Department of Civil Engineering, University of Nevada, Reno, Nevada, Report No. CCEER-04-4, March 2004.

CCEER 04-5   Ashour, M., Norris, G. and Elfass, S., "Analysis of Laterally Loaded Long or Intermediate Drilled Shafts of Small or Large Diameter in Layered Soil," Center for Civil Engineering Earthquake Research, Department of Civil Engineering, University of Nevada, Reno, Nevada, Report No. CCEER-04-5, June 2004.

CCEER 04-6   Correal, J., Saiidi, M. and Sanders, D., "Seismic Performance of RC Bridge Columns Reinforced with Two Interlocking Spirals," Center for Civil Engineering Earthquake Research, Department of Civil Engineering, University of Nevada, Reno, Nevada, Report No. CCEER-04-6, August 2004.

CCEER 04-7   Dusicka, P., Itani, A. and Buckle, I., "Cyclic Response and Low Cycle Fatigue Characteristics of Plate Steels," Center for Civil Engineering Earthquake Research, Department of Civil Engineering, University of Nevada, Reno, Nevada, Report No. CCEER-04-7, November 2004.

CCEER 04-8   Dusicka, P., Itani, A. and Buckle, I., "Built-up Shear Links as Energy Dissipaters for Seismic Protection of Bridges," Center for Civil Engineering Earthquake Research, Department of Civil Engineering, University of Nevada, Reno, Nevada, Report No. CCEER-04-8, November 2004.

CCEER 04-9   Sureshkumar, K., Saiidi, S., Itani, A. and Ladkany, S., "Seismic Retrofit of Two-Column Bents with Diamond Shape Columns," Center for Civil Engineering Earthquake Research, Department of Civil Engineering, University of Nevada, Reno, Nevada, Report No. CCEER-04-9, November 2004.

CCEER 05-1   Wang, H. and Saiidi, S., "A Study of RC Columns with Shape Memory Alloy and Engineered Cementitious Composites," Center for Civil Engineering Earthquake Research, Department of Civil Engineering, University of Nevada, Reno, Nevada, Report No. CCEER-05-1, January 2005.

CCEER 05-2   Johnson, R., Saiidi, S. and Maragakis, E., "A Study of Fiber Reinforced Plastics for Seismic Bridge Restrainers," Center for Civil Engineering Earthquake Research, Department of Civil Engineering, University of Nevada, Reno, Nevada, Report No. CCEER-05-2, January 2005.

CCEER 05-3   Carden, L.P., Itani, A.M., Buckle, I.G, "Seismic Load Path in Steel Girder Bridge Superstructures," Center for Civil Engineering Earthquake Research, Department of Civil Engineering, University of Nevada, Reno, Nevada, Report No. CCEER-05-3, January 2005.

CCEER 05-4   Carden, L.P., Itani, A.M., Buckle, I.G, "Seismic Performance of Steel Girder Bridge Superstructures with Ductile End Cross Frames and Seismic Isolation," Center for Civil Engineering Earthquake Research, Department of Civil Engineering, University of Nevada, Reno, Nevada, Report No. CCEER-05-4, January 2005.

CCEER 05-5   Goodwin, E., Maragakis, M., Itani, A. and Luo, S., "Experimental Evaluation of the Seismic Performance of Hospital Piping Subassemblies," Center for Civil Engineering Earthquake Research, Department of Civil Engineering, University of Nevada, Reno, Nevada, Report No. CCEER-05-5, February 2005.

CCEER 05-6   Zadeh M. S., Saiidi, S, Itani, A. and Ladkany, S., "Seismic Vulnerability Evaluation and Retrofit Design of Las Vegas Downtown Viaduct," Center for Civil Engineering Earthquake Research, Department of Civil Engineering, University of Nevada, Reno, Nevada, Report No. CCEER-05-6, February 2005.

CCEER 05-7   Phan, V., Saiidi, S. and Anderson, J., "Near Fault (Near Field) Ground Motion Effects on Reinforced Concrete Bridge Columns," Center for Civil Engineering Earthquake Research, Department of Civil Engineering, University of Nevada, Reno, Nevada, Report No. CCEER-05-7, August 2005.

CCEER 05-8   Carden, L., Itani, A. and Laplace, P., "Performance of Steel Props at the UNR Fire Science Academy subjected to Repeated Fire," Center for Civil Engineering Earthquake Research, Department of Civil Engineering, University of Nevada, Reno, Nevada, Report No. CCEER-05-8, August 2005.

CCEER 05-9   Yamashita, R. and Sanders, D., "Shake Table Testing and an Analytical Study of Unbonded Prestressed Hollow Concrete Column Constructed with Precast Segments," Center for Civil Engineering Earthquake Research, Department of Civil Engineering, University of Nevada, Reno, Nevada, Report No. CCEER-05-9, August 2005.

CCEER 05-10   Not Published

CCEER 05-11   Carden, L., Itani., A., and Peckan, G., "Recommendations for the Design of Beams and Posts in Bridge Falsework," Center for Civil Engineering Earthquake Research, Department of Civil Engineering, University of Nevada, Reno, Nevada, Report No. CCEER-05-11, October 2005.

CCEER 06-01   Cheng, Z., Saiidi, M., and Sanders, D., "Development of a Seismic Design Method for Reinforced Concrete Two-Way Bridge Column Hinges," Center for Civil Engineering Earthquake Research, Department of Civil Engineering, University of Nevada, Reno, Nevada, Report No. CCEER-06-01, February 2006.

CCEER 06-02   Johnson, N., Saiidi, M., and Sanders, D., "Large-Scale Experimental and Analytical Studies of a Two-Span Reinforced Concrete Bridge System," Center for Civil Engineering Earthquake Research, Department of Civil Engineering, University of Nevada, Reno, Nevada, Report No. CCEER-06-02, March 2006.

CCEER 06-03   Saiidi, M., Ghasemi, H. and Tiras, A., "Seismic Design and Retrofit of Highway Bridges," Proceedings, Second US-Turkey Workshop, Center for Civil Engineering Earthquake Research, Department of Civil Engineering, University of Nevada, Reno, Nevada, Report No. CCEER-06-03, May 2006.

CCEER 07-01   O'Brien, M., Saiidi, M. and Sadrossadat-Zadeh, M., "A Study of Concrete Bridge Columns Using Innovative Materials Subjected to Cyclic Loading," Center for Civil Engineering Earthquake Research, Department of Civil Engineering, University of Nevada, Reno, Nevada, Report No. CCEER-07-01, January 2007.

CCEER 07-02   Sadrossadat-Zadeh, M. and Saiidi, M., "Effect of Strain rate on Stress-Strain Properties and Yield Propagation in Steel Reinforcing Bars," Center for Civil Engineering Earthquake Research, Department of Civil Engineering, University of Nevada, Reno, Nevada, Report No. CCEER-07-02, January 2007.

CCEER 07-03   Sadrossadat-Zadeh, M. and Saiidi, M., "Analytical Study of NEESR-SG 4-Span Bridge Model Using OpenSees," Center for Civil Engineering Earthquake Research, Department of Civil Engineering, University of Nevada, Reno, Nevada, Report No. CCEER-07-03, January 2007.

CCEER 07-04   Nelson, R., Saiidi, M. and Zadeh, S., "Experimental Evaluation of Performance of Conventional Bridge Systems," Center for Civil Engineering Earthquake Research, Department of Civil Engineering, University of Nevada, Reno, Nevada, Report No. CCEER-07-04, October 2007.

CCEER 07-05   Bahen, N. and Sanders, D., "Strut-and-Tie Modeling for Disturbed Regions in Structural Concrete Members with Emphasis on Deep Beams," Center for Civil Engineering Earthquake Research, Department of Civil Engineering, University of Nevada, Reno, Nevada, Report No. CCEER-07-05, December 2007.

CCEER 07-06   Choi, H., Saiidi, M. and Somerville, P., "Effects of Near-Fault Ground Motion and Fault-Rupture on the Seismic Response of Reinforced Concrete Bridges," Center for Civil Engineering Earthquake Research, Department of Civil Engineering, University of Nevada, Reno, Nevada, Report No. CCEER-07-06, December 2007.

CCEER 07-07   Ashour M. and Norris, G., "Report and User Manual on Strain Wedge Model Computer Program for Files and Large Diameter Shafts with LRFD Procedure," Center for Civil Engineering Earthquake Research, Department of Civil Engineering, University of Nevada, Reno, Nevada, Report No. CCEER-07-07, October 2007.

CCEER 08-01   Doyle, K. and Saiidi, M., "Seismic Response of Telescopic Pipe Pin Connections," Center for Civil Engineering Earthquake Research, Department of Civil Engineering, University of Nevada, Reno, Nevada, Report No. CCEER-08-01, February 2008.

CCEER 08-02   Taylor, M. and Sanders, D., "Seismic Time History Analysis and Instrumentation of the Galena Creek Bridge," Center for Civil Engineering Earthquake Research, Department of Civil Engineering, University of Nevada, Reno, Nevada, Report No. CCEER-08-02, April 2008.

CCEER 08-03   Abdel-Mohti, A. and Pekcan, G., "Seismic Response Assessment and Recommendations for the Design of Skewed Post-Tensioned Concrete Box-Girder Highway Bridges," Center for Civil Engineering Earthquake Research, Department of Civil and Environmental Engineering, University of Nevada, Reno, Nevada, Report No. CCEER-08-03, September 2008.

CCEER 08-04   Saiidi, M., Ghasemi, H. and Hook, J., "Long Term Bridge Performance Monitoring, Assessment & Management," Proceedings, FHWA/NSF Workshop on Future Directions," Center for Civil Engineering Earthquake Research, Department of Civil and Environmental Engineering, University of Nevada, Reno, Nevada, Report No. CCEER 08-04, September 2008.

CCEER 09-01   Brown, A., and Saiidi, M., "Investigation of Near-Fault Ground Motion Effects on Substandard Bridge Columns and Bents," Center for Civil Engineering Earthquake Research, Department of Civil and Environmental Engineering, University of Nevada, Reno, Nevada, Report No. CCEER-09-01, July 2009.

CCEER 09-02   Linke, C., Pekcan, G., and Itani, A., "Detailing of Seismically Resilient Special Truss Moment Frames," Center for Civil Engineering Earthquake Research, Department of Civil and Environmental Engineering, University of Nevada, Reno, Nevada, Report No. CCEER-09-02, August 2009.

CCEER 09-03   Hillis, D., and Saiidi, M., "Design, Construction, and Nonlinear Dynamic Analysis of Three Bridge Bents Used in a Bridge System Test," Center for Civil Engineering Earthquake Research, Department of Civil and Environmental Engineering, University of Nevada, Reno, Nevada, Report No. CCEER-09-03, August 2009.

CCEER 09-04   Bahrami, H., Itani, A., and Buckle, I., "Guidelines for the Seismic Design of Ductile End Cross Frames in Steel Girder Bridge Superstructures," Center for Civil Engineering Earthquake Research, Department of Civil and Environmental Engineering, University of Nevada, Reno, Nevada, Report No. CCEER-09-04, September 2009.

CCEER 10-01   Zaghi, A. E., and Saiidi, M., "Seismic Design of Pipe-Pin Connections in Concrete Bridges," Center for Civil Engineering Earthquake Research, Department of Civil and Environmental Engineering, University of Nevada, Reno, Nevada, Report No. CCEER-10-01, January 2010.

CCEER 10-02   Pooranampillai, S., Elfass, S., and Norris, G., "Laboratory Study to Assess Load Capacity Increase of Drilled Shafts through Post Grouting," Center for Civil Engineering Earthquake Research, Department of Civil and Environmental Engineering, University of Nevada, Reno, Nevada, Report No. CCEER-10-02, January 2010.

CCEER 10-03   Itani, A., Grubb, M., and Monzon, E, "Proposed Seismic Provisions and Commentary for Steel Plate Girder Superstructures," Center for Civil Engineering Earthquake Research, Department of Civil and Environmental Engineering, University of Nevada, Reno, Nevada, Report No. CCEER-10-03, June 2010.

CCEER 10-04   Cruz-Noguez, C., Saiidi, M., "Experimental and Analytical Seismic Studies of a Four-Span Bridge System with Innovative Materials," Center for Civil Engineering Earthquake Research, Department of Civil and Environmental Engineering, University of Nevada, Reno, Nevada, Report No. CCEER-10-04, September 2010.

CCEER 10-05   Vosooghi, A., Saiidi, M., "Post-Earthquake Evaluation and Emergency Repair of Damaged RC Bridge Columns Using CFRP Materials," Center for Civil Engineering Earthquake Research, Department of Civil and Environmental Engineering, University of Nevada, Reno, Nevada, Report No. CCEER-10-05, September 2010.

CCEER 10-06   Ayoub, M., Sanders, D., "Testing of Pile Extension Connections to Slab Bridges," Center for Civil Engineering Earthquake Research, Department of Civil and Environmental Engineering, University of Nevada, Reno, Nevada, Report No. CCEER-10-06, October 2010.

CCEER 10-07   Builes-Mejia, J. C. and Itani, A., "Stability of Bridge Column Rebar Cages during Construction," Center for Civil Engineering Earthquake Research, Department of Civil and Environmental Engineering, University of Nevada, Reno, Nevada, Report No. CCEER-10-07, November 2010.

CCEER 10-08   Monzon, E. V., "Seismic Performance of Steel Plate Girder Bridges with Integral Abutments," Center for Civil Engineering Earthquake Research, Department of Civil and Environmental Engineering, University of Nevada, Reno, Nevada, Report No. CCEER-10-08, November 2010.

CCEER 11-01   Motaref, S., Saiidi, M., and Sanders, D., "Seismic Response of Precast Bridge Columns with Energy Dissipating Joints," Center for Civil Engineering Earthquake Research, Department of Civil and Environmental Engineering, University of Nevada, Reno, Nevada, Report No. CCEER-11-01, May 2011.

CCEER 11-02   Harrison, N. and Sanders, D., "Preliminary Seismic Analysis and Design of Reinforced Concrete Bridge Columns for Curved Bridge Experiments," Center for Civil Engineering Earthquake Research, Department of Civil and Environmental Engineering, University of Nevada, Reno, Nevada, Report No. CCEER-11-02, May 2011.

CCEER 11-03   Vallejera, J. and Sanders, D., "Instrumentation and Monitoring the Galena Creek Bridge," Center for Civil Engineering Earthquake Research, Department of Civil and Environmental Engineering, University of Nevada, Reno, Nevada, Report No. CCEER-11-03, September 2011.

CCEER 11-04   Levi, M., Sanders, D., and Buckle, I., "Seismic Response of Columns in Horizontally Curved Bridges," Center for Civil Engineering Earthquake Research, Department of Civil and Environmental Engineering, University of Nevada, Reno, Nevada, Report No. CCEER-11-04, December 2011.

CCEER 12-01   Saiidi, M., "NSF International Workshop on Bridges of the Future – Wide Spread Implementation of Innovation," Center for Civil Engineering Earthquake Research, Department of Civil and Environmental Engineering, University of Nevada, Reno, Nevada, Report No. CCEER-12-01, January 2012.

CCEER 12-02   Larkin, A. S., Sanders, D., and Saiidi, M., "Unbonded Prestressed Columns for Earthquake Resistance," Center for Civil Engineering Earthquake Research, Department of Civil and Environmental Engineering, University of Nevada, Reno, Nevada, Report No. CCEER-12-02, January 2012.